FORMATION AND STABILITY OF NANOCRYSTALLINE ALLOYS SYNTHESIZED BY MECHANICAL MILLING

Thesis by

Yoshio Abe

In Partial Fulfillment of the Requirements

for the Degree of

Doctor of Philosophy

California Institute of Technology

Pasadena, California

1993

(Submitted May 20th, 1993)

To Ritsuko,

Hidetoshi and Kyoko.

Acknowledgments

I would like to acknowledge the support and assistance from the many people who contributed to this thesis in various manner.

First of all, I express my heartfelt gratitude to Professor William L. Johnson. I appreciate his kindness, generosity and patience. Bill's genius breaks down various complicated phenomena like milling balls and reduces them into a set of formulae. He taught me Science is simple and beautiful. His sharp and deep insight comes up in his words and flies around my brain like a photon with lightning speed. In my first year at Caltech, my brain rarely interact with his words and they passed through my ears. As I acquired knowledge and experience, English comprehension skill as well, my brain expanded its *cross section* gradually, and I could finally grasp some essence of his idea, and reflect it with my own originality. It took quite a while until I reach that stage , but he was so patient and generous as to keep teaching and instructing me.

I am grateful to Professor Tasuku Fuwa for his "spiritual" instruction. I also thank to Professors Yasuhiro Tani and Takaaki Nagao, who taught me the very basics of research in my senior year. Without the assistance of Professors Paul Hideo Shingu and Michihiko Nagumo, I could not have had opportunity to study at Caltech.

I would like to acknowledge the warm support from my colleagues with Nippon Steel Corporation. They provided me precious assistance and aid in various way. I am grateful to Drs. Ken-ichi Miyazawa and Tooru Inoue for making my study possible. The kindest assistance of Yoshimichi Ohara, Yasushi

Murakami and Jun-ichi Inoue for making my days in the U. S. comfortable and meaningful is deeply appreciated. I am also indebted to Drs. Tooru Matsumiya, Toyotaka Manabe, Tomomi Murata, Masakazu Nakamura, Shigehiro Yamaguchi, Tetsuro Ohashi, Wataru Ohashi, Atsushi Nogami, Wataru Yamada and many other people. The technical assistance by Toshihiro Kitamura in chemical analysis and by Yoichi Ikematsu, Dr. Toshihiro Hanamura in TEM observation is appreciated.

During my residence in Pasadena, especially when my family was in trouble, a lot of people helped us. I am grateful to Koichiro and Emiko Ikudome, Dr. and Mrs. Yasuhito Uezono, Atsuko Kobayashi - Kirschvink and Prof. Joseph Kirschvink, Mr. and Mrs. Kazuyuki Orita, Profs. Hiroshi Kubota and Toshiro Tanimoto. Without their assistance, my work could not have been completed.

The days in Keck Laboratories will be unforgettable. I am grateful to Reiner Birringer, Zezhong Fu, Carl E. Krill, III, Mo Li, David Lee, Jürgen Eckert, Joseph Holzer, Philip Askenazy, Hans Fecht, Jorge Kittl, Brent Fultz, Mohit Jain, Ken-ichi Ohsaka, Hao Ouyang, Channing Ahn, Laurence Anthony, Egon Hellstern, Yuichi Seki, Hideki Tonda, Hisashi Kuwano, Zheng - Qiang Gao, Charles Musgrave, Cho - Jen Tsai, Hideyuki Suzuki and Rajesh Panchanathan. I thank to Carol Garland for her great assistance and instruction in TEM observation. Not only I was indebted to them very much in technical assistance and precious advices, but I shared good time with them in fruitful discussions and collaborations, and exchanging nice friendship each other. They made my memory more colorful.

I appreciate various assistance by Pamera Albertson, Necia Parr, Louis Johnson and Mike Gerfen. Their help was indispensable for the completion of my

thesis. I am thankful to Nisshin Giken Corporation, Tokyo, for assistance in high temperature ball milling. This research was supported by the U. S. Department of Energy, contract No. DE - FG03 - 86ER45242. I am grateful to my financial support provided by California Institute of Technology and Nippon Steel Corporation.

At last, my appreciation goes to my family. I thank to my parents, for their constant support. I express my deepest gratitude to Ritsuko, for her everlasting dedication. Hidetoshi and Kyoko have never allowed me undisturbed sleep, however their innocent smile always makes me happy and relaxed. Their love made this thesis possible. To them I dedicate my thesis.

Abstract

Nanocrystalline materials are expected to have quite different physical properties from both conventional polycrystalline materials and amorphous materials, particularly due to high fraction of grain boundaries. For their application, to improve the stability is of great concern. In this study, nanocrystalline Ti - Cu, Ti - Zr - Cu and Nb - Cu alloys were synthesized by the mechanical alloying technique. Macroscopically, supersaturated single-phase solid solutions were obtained in the form of powder after certain duration of ball milling. The powders obtained were characterized by X - ray diffraction, differential scanning calorimetry, transmission electron microscopy and small angle X-ray scattering. In Ti - Cu and Ti - Zr - Cu systems, crystal grains do not grow by heating until the intermetallic $Cu(Ti, Zr)_2$ phase nucleates, while in Nb - Cu system, grain growth follows the clustering of elemental Cu. These result lead to the hypothesis that grain growth is suppressed due to the segregation of Cu atoms in grain boundaries. Furthermore, the mechanisms of solute segregation in grain boundaries and the stability of the nanocrystalline structure are discussed in terms of the hypothesis that grain boundaries consist of a liquid-like disordered phase. Finally, based on the above argument, we have proposed a new technology, high temperature ball milling, to synthesize nanocrystalline alloys with finer grain size and more stability and to control grain size as desired.

Contents

List of Figures

Chapter 1

Chapter 2

Chapter 3

Chapter 4

Chapter 5

Chapter 6

Chapter 1 Introduction and Background

1.1 Introduction

Nanostructured materials include materials such as ultrafine particles, nanometer-scale crystalline solids and nanoglasses. They are made of metals, alloys, ceramics, glasses and their composites. Nanostructured materials exhibit quite different physical properties from conventional materials due to surface and interface effects. The terminology *"nanostructured materials"* is quite new, and has just been accepted a few years ago [1].

Ultrafine particles and their dispersion have been utilized in human society for a long time. Submicron metal particles dispersed in stained glasses scatter light of certain wavelengths and display colors. Fe, Co and Cr, as oxides or metals, have been used for magnetic recording tapes. As the achievable particle size goes down to a nanometer size, the applications of ultrafine particles have broadened.

However, it has also been found that ultrafine particles are so surface-active that metallic powders oxidize instantly, or even pyrophoric. Therefore, they have to undergo gradual oxidation in a controlled atmosphere, sacrificing some of the properties originally expected. Bulk nanostructured materials can retain fresh surfaces inside as interfaces, so the surface effect still remains.

The demand for high-performance materials always encourages progress in materials science. Physical properties such as strength,

superplasticity, ductility and high-temperature creep resistivity require scaling down in grain size. Consequently it was not an abrupt leap that an attempt to consolidate ultrafine particles into bulk shapes was made and a novel field in materials science, the study of nanostructured materials, was developed.

Polycrystalline materials of the grain size of less than 25 $\overline{nm}$ are called *nanocrystalline materials* [2 - 8]. Nanocrystalline materials demonstrate quite different physical properties from both conventional polycrystalline materials and amorphous materials. As depicted schematically in Fig. 1-1 [3], the characteristic of nanocrystalline materials is a very high grain boundary volume fraction, reaching 20 - 50 % of the total volume. In such materials, bulk properties are no longer dominant, instead the characteristics of interfaces control the overall properties. Therefore it is essential for our understanding of these materials to study the structure and properties of grain boundaries. However, the structure of grain boundaries has long been a major topic of research. Studying nanocrystalline materials may also be helpful for understanding the grain boundary structure and the interaction of grain boundaries with the crystalline lattice.

To apply nanocrystalline materials to the real world, the stability of these materials is the most important. As discussed later, the nanocrystalline structure is a non-equilibrium state. Several questions arise. Are the materials unstable or somehow metastable, and do they continuously evolve to an equilibrium structure? Or is it possible to equilibrate the nanocrystalline structure chemically with other phases and stabilize it?

Furthermore, since the characteristics of nanocrystalline materials are governed by grain boundaries, one may be able to fabricate materials with

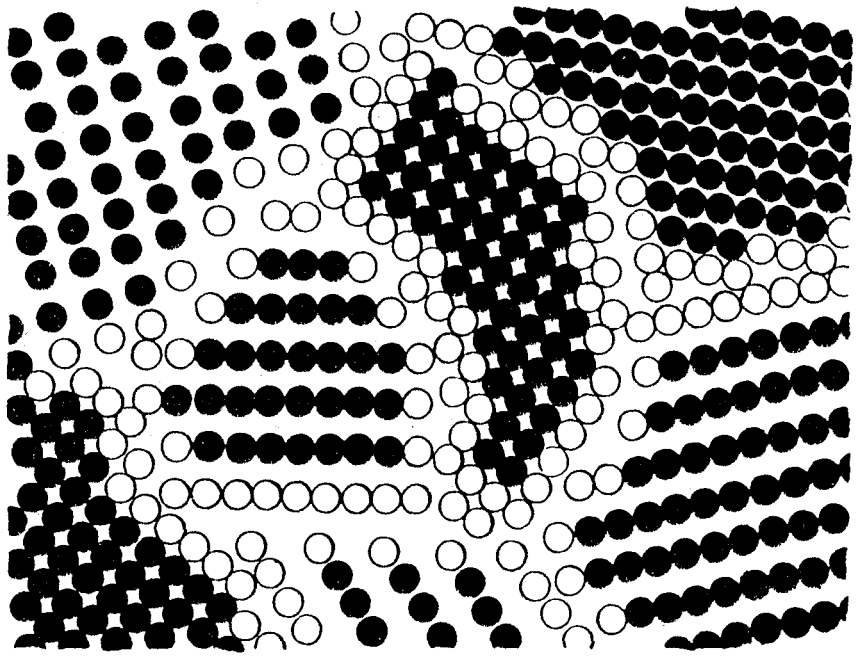

Fig. 1-1 Schematic picture of nanocrystalline structure by Gleiter [3]. The white circles represent atoms involved in grain boundaries, while the black circles forms perfect lattices and behave as bulk.

desired properties by controling grain size. The questions are what determines the grain size of nanocrystalline materials, and how to control it.

This thesis focuses on the study of the structure and thermodynamic stability of nanocrystalline materials. Two major topics constitute this thesis research. The first topic is the study of the synthesis of nanocrystalline materials by the mechanical milling. The nanocrystalline structure was studied by means of X-ray diffraction, transmission electron microscopy. The details of experiments and results are mentioned. In addition, small angle X-ray scattering experiments to investigate the microstructure of the grain boundaries of nanocrystalline materials are described.

As the second topic, the thermal stability of nanocrystalline materials and the mechanism of grain growth are investigated and discussed. Furthermore, the thermodynamic stability of a non-equilibrium nanocrystalline structure is discussed in terms of grain boundary segregation. The mechanism of solid-state amorphization is also discussed briefly.

A novel high-temperature ball milling technique will then be mentioned. The effect of milling temperature was investigated, and it was found that at high temperatures, grain boundary segregation is enhanced and the grain boundaries are stabilized, so that the grain size is reduced.

Finally, a general discussion will be given. The topics include the mechanism of mechanical alloying, and the structure of grain boundaries of nanocrystalline materials. Solid-state amorphization reaction will be mentioned.

In this chapter, after the thermodynamic background of the non-

equilibrium state and metastable state is introduced, the basic concept of nanocrystalline materials will be described. Finally the synthesis of nanocrystalline materials and their physical properties will be discussed.

1.2 Non-equilibrium State and Metastable State

An equilibrium state is defined by thermodynamics as the global free energy minimum of the system. Gibbs' stability criteria state that the system in equilibrium must be stable against perturbation. Multiple phases may coexist in equilibrium. Gibbs' phase rule determines the allowed degrees of freedom. In the solid or liquid state, the pressure usually is constant, therefore a unique combination of phases and compositions of these phases is allowed at a given temperature for a binary system. The compositions of the phases present are obtained by a common tangent on the free energy diagram. However, systems of more components carry more degrees of freedom, therefore additional constraints such as tie lines are needed to determine the composition of existing phases. Finally, the lever rule determines the mole fraction of existing phases. When matter is in a state different from the equilibrium state, the free energy associated is always higher, and it is called a non-equilibrium state.

The Gibbs' stability criteria can be satisfied at a local free energy minimum. Such a state is stable against *small* perturbations but may possibly "leap" to a more stable -- equilibrium -- state, hence is referred to as metastable equilibrium state. As this state is a non-equilibrium state, it will evolve to an equilibrium state after a finite lifetime, when a large perturbation takes place. Assuming a relatively long lifetime, the thermodynamic functions can be defined in a metastable state [9].

Kinetics determines the lifetime of metastable states. The fluctuation to equilibrium is usually thermally activated, and the probability of a perturbation large enough to overcome the related energy barrier is given by Arhenius-type equation. However if such external fluctuation is kinetically suppressed, the lifetime of the metastable state is extended.

A state may appear to be metastable even if it is unstable. If a structure evolves very slowly due to kinetic constraints, the time required for an unstable state to reach a metastable or stable state may be so long that the initial state appears metastable. Such conditions may not be accessible by experimental investigation, but only by a computational approach. A new concept of a *pseudostable state* deals with such a phenomenon: a non-equilibrium state may evolve to a state, then stay for a while until another decay takes place. As such, it is difficult to distinguish a metastable state and a kinetically stabilized, long-life unstable state. The term "metastable" often applies to an unstable state, provided its lifetime is long enough.

For example, an amorphous solid is one of the typical metastable states. As it evolves to a stable state crystalline solid via nucleation, it is metastable. Not all amorphous materials are in metastable states, however. Amorphous alloys synthesized by solid-state reaction are often obtained as a mixture with a crystalline state, and hence thought to be in metastable equilibrium with it. Therefore they are truly metastable [10]. On the other hand, rapidly quenched amorphous alloys relax to a more ordered amorphous structure continuously and sometimes even undergo spinodal decomposition to two amorphous phases [11]. Thus they must be unstable. After all, artificial non-equilibrium materials often carry higher energy than their metastable states, and thus incorporate instability. This is mainly because of the method of production,

the so-called *"energize and quench"* method.

In order to obtain a non-equilibrium state, one has to *"energize"* the material. A material can be energized in various ways, *e. g.*, thermally, mechanically or chemically. One can equilibrate a material in a high energy state, in other words, energize it well above the desired state. However, when it is "cooled down" to the normal state, the material relaxes toward equilibrium and releases energy. Therefore the material has to be quenched with the energy release to preserve high energy state kinetically. Turnbull described this method to achieve non-equilibrium states of matter as *"energize and quench* [12]."

The required quenching conditions depend on the energy release rate. To obtain amorphous states by rapid quenching of liquid alloys, the cooling rate must be at least 10^2 °C/*s* [13]. In a solid-state reaction, the energy release rate is so low that no physical quenching is necessary.

1.3 Thermodynamics of Nanocrystalline Structure

Various types of defects in a crystalline solids such as grain boundaries, phase boundaries, anti-phase boundaries, stacking faults, twins, dislocations and point defects carry extra energy compared to a perfect crystal lattice. The equilibrium state of a single phase solid is a single crystal. In multiphase materials, defects reorganize themselves to the lowest energy configuration. For example, the area of phase/grain boundaries decreases toward equilibrium to minimize the total free energy. As a nanocrystalline structure contains many more grain boundaries than a conventional polycrystalline structure or a single crystal, it is obvious that the nanocrystalline structure is

in a high energy state, and thus a non-equilibrium state.

It has not been clear whether a nanocrystalline structure is a metastable or a kinetically stabilized unstable state. Nanocrystalline materials undergo grain growth by heating. However, nanocrystalline metals of high melting temperature are relatively stable against grain growth [3]. Nanocrystalline alloys also show significant resistance against grain growth [14]. Birringer showed that a pure nanocrystalline metal is thermodynamically unstable [15]. However, it is yet to be determined if nanocrystalline alloys can be metastable. Also it has been known that nanocrystalline structure formation often precedes amorphization [16]. Therefore it is assumed that the stability of grain boundaries and crystalline lattices is strongly related to amorphous structure formation.

Nanocrystalline materials are produced by several different methods as described later. The structures and properties of nanocrystalline materials synthesized by vapor condensation have been well studied [3, 5]. However these results may not be directly applicable to nanocrystalline materials formed by mechanical milling, since the microstructure may depend on the process of synthesis. In the case of mechanical milling, the defects introduced to form grain boundaries are mainly dislocations, while in the case of vapor condensation, due to loose atomic packing, volumetric defects are created.

This thesis discusses the structure and properties of nanocrystalline materials produced by mechanical milling is discussed.

1.4 Production of Nanocrystalline Materials

Since the earliest work by Gleiter *et al.* [2], nanocrystalline materials

have been produced by consolidating vapor-condensed nanostructured powder, with no innovative technique involved. Recently various methods have been developed to obtain nanocrystalline solids. In some cases a bulk sample is produced directly. The details of various production methods are described in literature [3]. In this section, the major methods to synthesize ultrafine particles and direct production of bulk solids are briefly mentioned. In addition, recent developments on the consolidation of non-equilibrium materials will be discussed.

Nanostructured materials are usually fabricated by assembling atomic clusters and condensing them into solid. A variety of techniques are used depending on the products and initial states as shown in Fig. 1-2. Starting materials may be in gas, liquid and solid states.

1.4.1 Vapor Condensation Methods

The vapor condensation processes are the most common techniques to deposit a thin film on a substrate. They are known as *physical vapor deposition* (PVD), *chemical vapor deposition* (CVD) and *activated reactive evaporation* (ARE). By the use of a cooling device with a scraper or using fluid as a substrate instead of a solid substrate, the accumulation of clusters into a solid film can be prevented, and powder is obtained. This technique has many advantages such as cleanliness, ease of particle size control and uniformity in particle shape.

Starting materials are heated or sputtered by high energy beams, and evaporated in a chamber, thus thermally energized. Electron beam, ion beam, laser, arc, plasma, electric oven, infrared rays, ultraviolet rays and so on can be employed as energy sources. Starting materials may be pure metals, alloys,

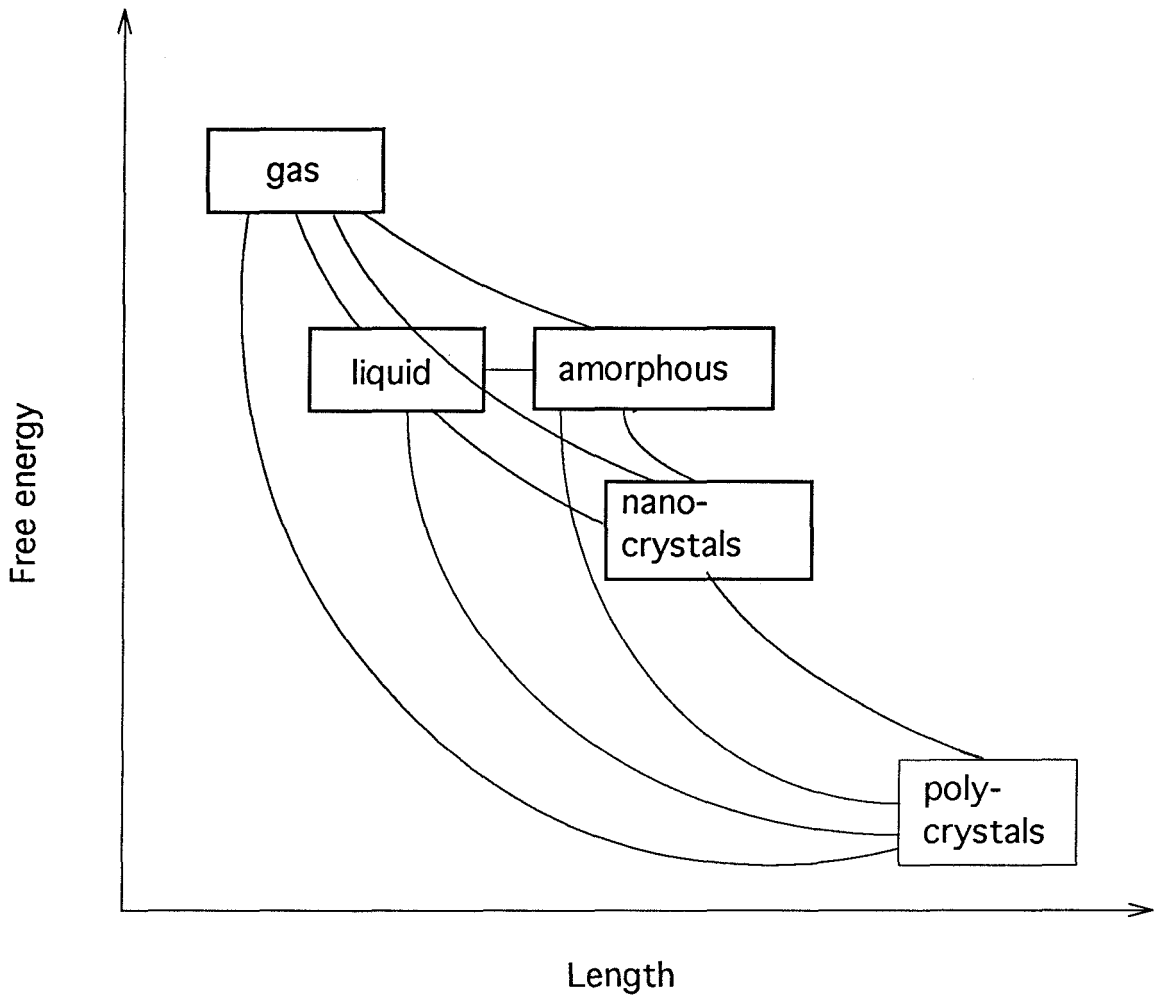

Fig. 1-2 Schematic energy hierarchy for the production of metastable materials. Amorphous and nanocrystalline phases are not states of extremely high energy, therefore they can be reached from gas, liquid and solid-state by various techniques.

salts, compounds or organic materials. The atmosphere may be vacuum, inert gases or reactive gases.

In PVD process, pure metals or alloys are evaporated in a vacuum or inert gas atmosphere. Evaporated atoms collide with gas molecules and lose energy, or atoms collide with one another and form a cluster. A vacuum atmosphere is used when the kinetic energy of the vapor is very low, since cluster formation from vapor is prevented by gas molecules. Salts are evaporated at relatively low temperatures. In CVD process, a vapor phase precursor is introduced into a reactive gas atmosphere, and then reacted to form a different compound or pure metal. The production rate of vapor condensation techniques is relatively low. However, recent development enabled the production of $100\,g/h$ of powder with the hydrogen thermal plasma process [17]. Today, the hybrid processes of CVD and PVD are in practical use, known as ARE [18]. The product is obtained as powder in this method. Therefore it has to be consolidated or compacted into a bulk form after production.

Aerosol synthesis is a good way for mass-production of uniform and spherical ultrafine particles [19, 20]. Various materials such as carbon black, silicon, TiO_2, SiO_2, SiN_4 powders are synthesized commercially by this method. Organic, non-metallic, or organometallic substances are often used. For example, to synthesize SiO_2, silane is mixed with oxygen, and sprayed into the heated reactor to form oxide. In some cases, the products have a nanocrystalline structure.

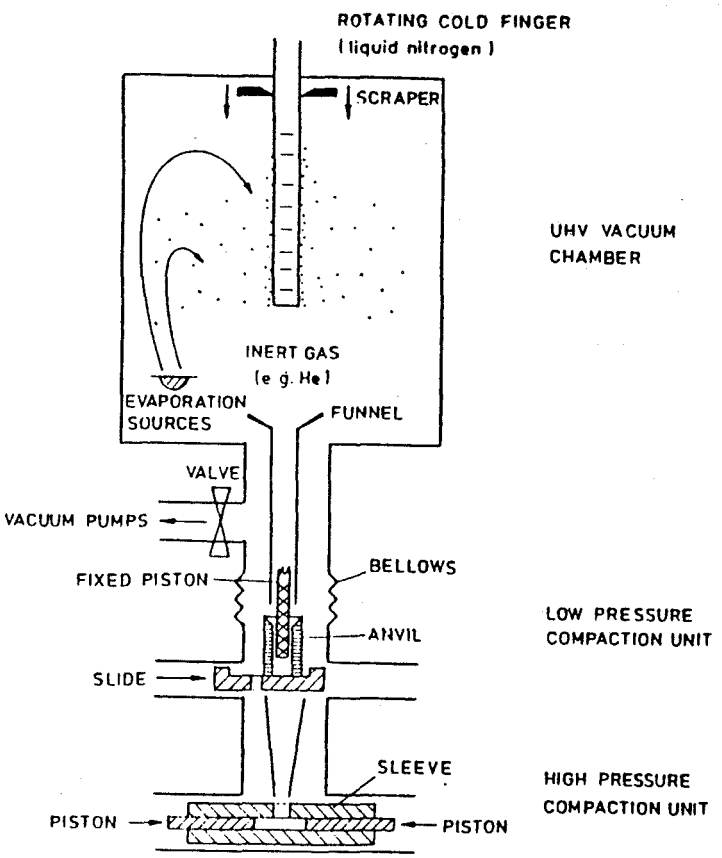

Fig. 1-3 Schematic picture of vapor condensation apparatus [3].

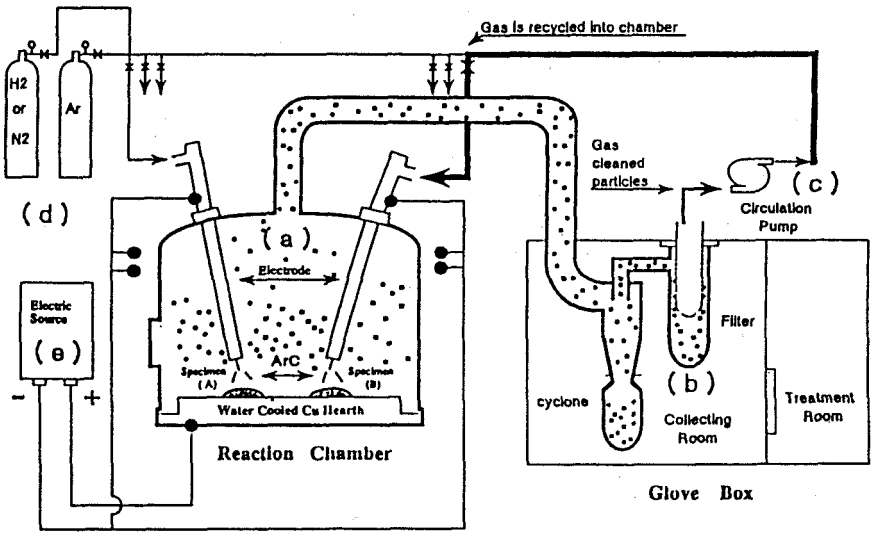

Fig. 1-4 Hydrogen thermal plasma apparatus by Uda [17].

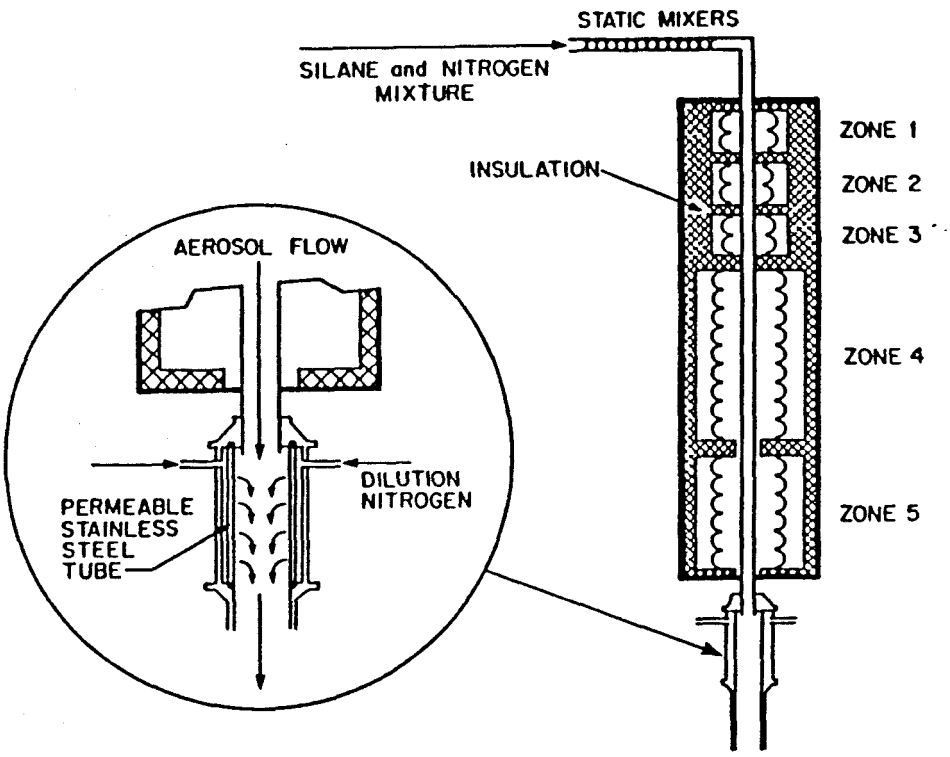

Fig. 1-5 Aerosol reactor for ultrafine powder synthesis [19].

1.4.2 Solid-state Reaction

There are two major types of solid-state reactions that can be used to obtain nanocrystalline materials.

1. Crystallization of Amorphous Materials

Amorphous materials can be crystallized into the nanocrystalline state. Since amorphous solid is regarded as frozen undercooled liquid, it has already been energized and quenched at a higher energy level. When an amorphous solid evolves to the equilibrium structure, one may expect homogeneous crystal nucleation: the larger the undercooling is, the higher is the nucleation rate, while the lower is the crystal growth rate. Thus one may expect highly uniformly distributed nanocrystals on crystallization of amorphous structure [21]. Rapidly quenched amorphous foils can be employed as starting materials, thus a nanocrystalline sheet is obtained immediately. However in order to obtain a bulk sample, usually one has to pulverize the foils and compact them.

2. Intense Plastic Deformation

When solid materials undergo plastic deformation, mechanical energy is consumed to create dislocations and cause plastic deformation, or create cracks and let them open to fracture. This energy is dissipated away when dislocations go out to surfaces or cracks propagate to break the material into pieces, however a part of the input energy remains in materials. Usually the energy is stored as atomic strain and defects such as dislocations, grain boundaries, stacking faults, twins, antiphase domains and atomic disordering. Since plastic deformation is approximately an isothermal process, materials

are energized due to entropic contribution.

In order to establish a nanocrystalline structure, it is necessary to build up a large density of grain boundaries, or antiphase domain boundaries for ordered alloys. In other words, enormous numbers of defects should be supplied. Accordingly, the total strain and strain rate must be extremely high. Note that it is inevitable that the product will become powder, because a part of input energy is used for pulverization as previously mentioned. Thus qualified processes are limited: even high-speed hot rolling can only provide $d\varepsilon/dt \sim 5$ /s. In a practical sense, the only available choice is mechanical attrition.

Mechanical attrition is considered to be good for industrial application because of the simple mechanism, feasibility to scale up, and cost efficiency. Its biggest drawback is the lack of cleanliness (due to wear processes involved) which may limit the quality of products. On the other hand, the nanocrystalline material obtained in this method is usually powder of particle size of 1 - 100 μm, which implies that each particle contains 10^4 - 10^8 crystal grains. Therefore, surfaces of nanocrystals are not exposed to the outside, and it may be possible to preserve their chemical nature.

The most serious problem in this method is contamination. As will be discussed in Chapter 3, it is supposed that the impurities play a big role in forming nanocrystalline or amorphous structure. Since contamination from milling device is inevitable in conventional ball mills, various attempts to avoid contamination have been conducted. Asai *et al.* invented a mortar-and-pestle type powder synthesizer that consists of Ti rods (pestles) rotating in a Cu mortar to produce Ti - Cu metastable alloys [22].

1.4.3 Other Methods

There are several methods to produce nanoparticles or nanocrystalline materials other than mentioned above, such as electrochemical precipitation from solution [23] and biosynthesis [24]. However the production rate is very low comparing to the physical methods.

1.4.4 Consolidation of Nanocrystalline Materials

As discussed above, in order to preserve surface effects in the material, in-line consolidation or compaction immediately following powder production has to be considered. The facility used by Gleiter *et al.* [3] has a cold press equipment beneath the evaporation chamber, however only less than one gram of powder can be processed at one time. Also various techniques such as sheath warm rolling of powder [25], Pseudo-HIP [26] or CIP [27], extrusion [28], electro-discharge compaction [29] and shock-wave compaction [30] have been applied for consolidation of nanocrystalline materials.

1.5 Properties of Nanocrystalline Materials

As Gleiter [3] addressed in his excellent review article, the characteristics of nanocrystalline materials may be mostly the result of (1) high density of grain boundaries, (2) crystalline regions finely divided by grain boundaries, (3) the grain boundary network. High density of free volume associated with grain boundaries may influence various properties. The remaining question is whether those properties are just the extrapolation of normal polycrystalline materials as the extremity of grain size refinement, and whether there is any new properties only expected for nanocrystalline

materials.

1.5.1 *Heat Capacity*

The fact that non-equilibrium states have higher free energy than the equilibrium states in spite of larger entropy suggests that they have a high heat capacity. In fact, an amorphous phase has higher heat capacity than a crystalline phase. Nanocrystalline materials are also known to have higher heat capacities compared with their polycrystalline states with larger grain sizes. These phenomena are interpreted as the increase of vibrational and configurational entropies in such states with more free volumes associated with grain boundaries. In nanocrystalline materials, therefore, the increase of the heat capacity is attributed to the large fraction of grain boundaries. Accordingly, the heat capacity drops closer to the value of conventional materials by grain growth, as the clasical limits indicates.

1.5.2 *Diffusion*

Mori *et al.* [31] recently found the spontaneous alloying of Cu into gold clusters of the diameter of several nanometer to form Au - Cu solid solution. The diffusion coefficient of Cu in Au clusters was estimated about 9 orders higher than in bulk polycrystalline Au. This phenomenon has been attributed to the lattice softening, namely, the instability of atomic clusters and lowering Debye temperature. They argue that bulk nanocrystalline materials may show such instability if the grain boundaries provide enough free volume for the lattice softening.

Schumacher *et al.* [32] measured the diffusivity of Ag in nanocrystalline Cu to obtain higher values than that of bulk Ag - Cu by

several order of magnitude. Gleiter [33] stated in the recent review that the diffusivity for substitutional atoms are very high in the nanocrystalline structure due to high volume fraction of grain boundaries. Furthermore, he pointed out that the overall diffusion coefficient in the nanocrystalline structure is larger than that for grain boundary diffusion in the polycrystalline structure by several orders of magnitude. Hence it is suspected that the grain boundary region is less dense than normal grain boundaries.

On the contrary, the diffusivity for interstitial atoms is compatible to that in the conventional polycrystalline state, because the mechanism for the atomic movement *in* the lattice remains the same even as crystals are scaled down to nanometer size. This implies that lattice softening is limited to the neighborhood of grain boundaries, and does not extend deep inside the lattice. Thus it is proved that the nanocrystalline structure is less resistant against heating with respect to grain growth, even compared with amorphous structure.

1.5.3 Solid Solubility

As was Pol E. Duwez's original objective in his epoch-making rapid quenching experiments [34], a solute trapping during rapid solidification is expected to result in enhanced solid solubility. This is also common in vapor quench techniques, and accordingly nanocrystalline materials synthesized by gas condensation method exhibit remarkably extended solid solubility [3]. In mechanical milling, the strong atomic mixing overcomes slow diffusion in low temperature and leaves the system in a mixed state, far from equilibrium. However, the microscopic distribution of solute atoms, *i. e.*, the segregation behavior has not been well understood.

1.5.4 *Chemical Properties*

The specific interface area and surface area are larger by orders of magnitude than that in conventional polycrystalline materials due to intersecting grain boundaries to the surface. Therefore nanocrystalline materials may be good catalyst due to very high surface activity. In addition, good adsorption capability is expected in these materials [3].

1.5.5 *Mechanical Properties*

Superplasticity phenomenon is usually observed in materials with grain size smaller than 1 μm [35]. For very brittle materials, it is expected that the nanocrystalline state will help improving their ductility.

The Hall - Petch relation states that the ultimate strength goes as $d^{-1/2}$, where d is grain size. It holds down to a certain grain size, however in nanocrystalline materials, it is reported that the relation does not hold, and the material softens under a certain grain size due to diffusional creep [36, 37].

1.5.6 *Electric Properties*

High electrical resistivity is expected in nanocrystalline materials due to the lack of periodicity. This is useful when used as magnetic materials since Eddy currents are suppressed.

1.5.7 *Magnetic Properties*

Grain boundaries divide magnetic domains. Nanostructured materials are expected to provide very fine magnetic domains, which allows easy magnetic moment rotation, thus low coersive force and high magnetization at low applied field. High saturation magnetic flux density B and high

permeability μ can be achieved simultaneously [21]. These properties are appropriate for soft magnetic materials.

1.6 Summary

Nanostructured materials are relatively new materials, which have been studied for only several years. Nanocrystalline materials are among those materials attracting commercial attention. Because of the large volume fraction of grain boundaries, the nanocrystalline materials exhibit quite different properties from both conventional polycrystalline and amorphous materials. However, it has been unknown yet whether they are thermodynamically metastable or unstable, and how one can stabilize them enough for real applications.

Chapter 2 Experimental Procedures

2.1 Introduction

In this thesis research, nanocrystalline materials were prepared from the mixture of pure elemental powders by the mechanical alloying technique. The powder obtained was then characterized with X-ray diffraction (XRD), differential scanning calorimetry (DSC) and transmission electron microscopy (TEM). On the other hand, the powder was consolidated into a foil and thinned to 10 - 30 μm thick, then provided for small angle X-ray scattering (SAXS) experiments.

This chapter will serve as a detailed description of experimental methods. The first part is dedicated to the ball milling technique, and the second part is for the small angle scattering technique. Since the techniques employed for characterization are so common that most of them will not be mentioned.

2.2 Ball Milling

2.2.1 Introduction

The ball milling technique has been known for more than thirty years. Benjamin and coworkers [38, 39] first developed this technique for producing oxide dispersion-strengthened (ODS) alloys. Since ball milling is probably the one and only practical method of mechanical alloying, the term *mechanical alloying* usually refers to the ball milling. The milling of a single component

is sometimes called *mechanical grinding* or *mechanical milling*, since no alloying is involved.

The phenomena expected in ball milling are schematically depicted in Fig. 2-1. The sample is first sealed into a vial with hard balls, and agitated together. During milling, many collisions between balls or a ball and the vial take place. The sample is sandwiched and crushed to powder. The powder particles are then elongated to be flakes, and cold-welded into a layered structure. If the starting material is a mixture of two or more kinds of powders, a multilayered structure is obtained. Since fast diffusion is expected due to high dislocation density in spite of low temperature, strong chemical reactions such as alloying and amorphous formation are expected by further milling. Vials and crushing balls are usually made of hard materials such as stainless steel, tool steel or cobalt-bound tungsten-carbide (WC). Nevertheless a certain amount of contamination from the milling device is usually anticipated.

There are three types of ball mills. Fig. 2-2 (a) exhibits the most common one, a *vibratory mill*. A vial containing the sample and balls is shaken violently. This mill is widely employed for crushing and mixing in the real world. The high intensity and simple mechanism are among the characteristics of this mill. Since the vial movement is almost unidirectional, a very strong thrust force at each collision is expected.

Szegvari invented a mechanical attritor illustrated in Fig. 2-2 (b), referred to as *Szegvari Attritor* or simply *attritor* [40]. Many balls in the container are agitated by a rotary mixer bar with arms. Powder particles are crushed and alloyed due to a shear force between two rotating balls or a

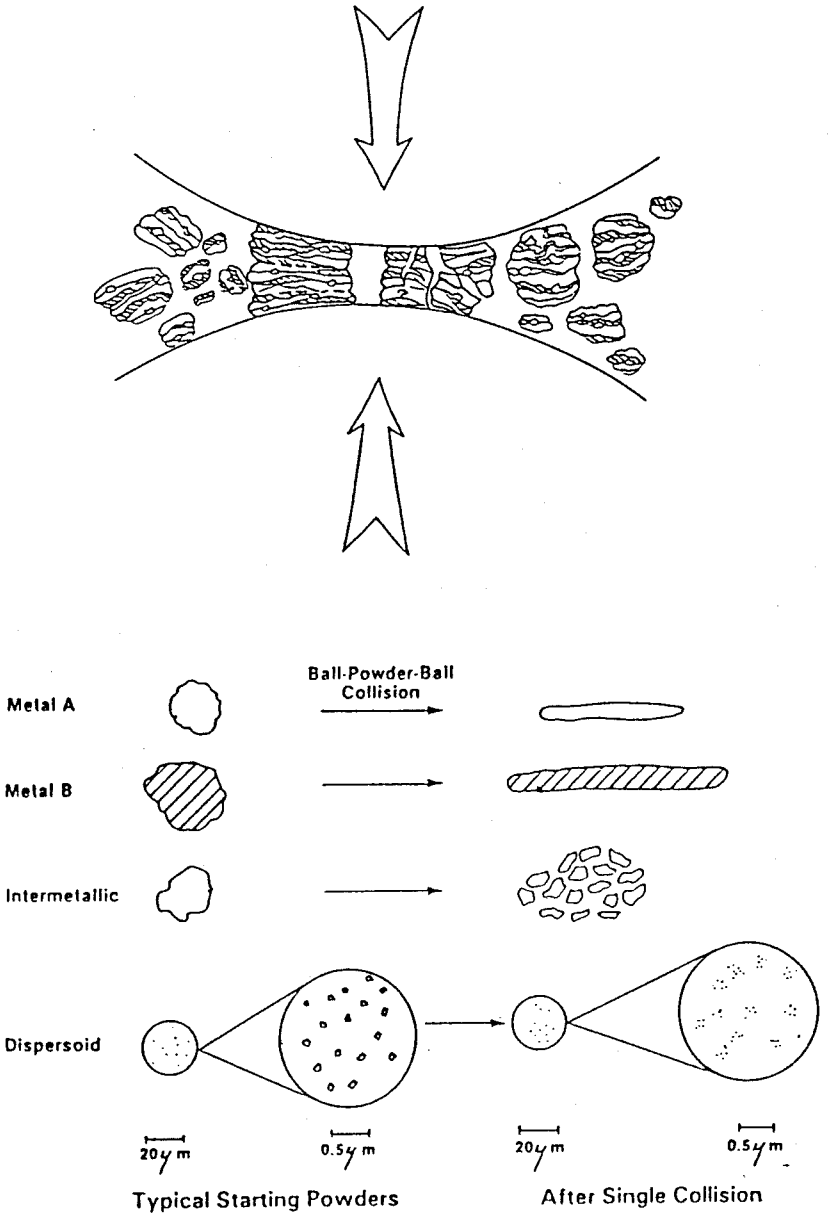

Fig. 2-1 Schematic drawing of the mechanism of ball milling. Powder particles are sandwiched between balls or a ball and the vial wall, and flattened. Layered structure is then formed. Alloying can accompany if particles of different species are sandwiched together [39].

ball and the inside wall of the container. Although the energy input is relatively small in this technique, this method allows an open architecture. Therefore it is capable of scale-up and continuous feeding of raw materials and extraction of products. Thus this technique is conveniently employed for industrial milling and alloying.

Another type of ball mill is called a *planetary ball mill*, drawn in Fig. 2-2 (c). This mill has a revolving table with several vial stages also rotating individually. The difference from the shaker mill is that shear forces are rather dominant to thrust force in this technique. Its variation is a *rotary ball mill*, which has a rotating vial put horizontally positioned on two drive rollers. The planetary mill is less intense than the vibratory mill, however generally more intense than the attritor.

Although ball-milled materials are apparently driven away from thermodynamic equilibrium even in Benjamin's time, the deviation was not extraordinary, and the products were still categorized in "conventional" materials. Hence, the significance of this technique had not long been recognized.

In 1981, Yermakov *et al.* accidentaly synthesized amorphous phases by mechanical grinding of intermetallic compounds [41]. They thought this as melting and subsequent rapid solidification, and much attention had not been paid. However, since Koch *et al.* [42] applied mechanical alloying for synthesizing amorphous alloys from elemental powders, this technique has attracted much attention as one of the methods to synthesize non-equilibrium materials other than rapid quenching.

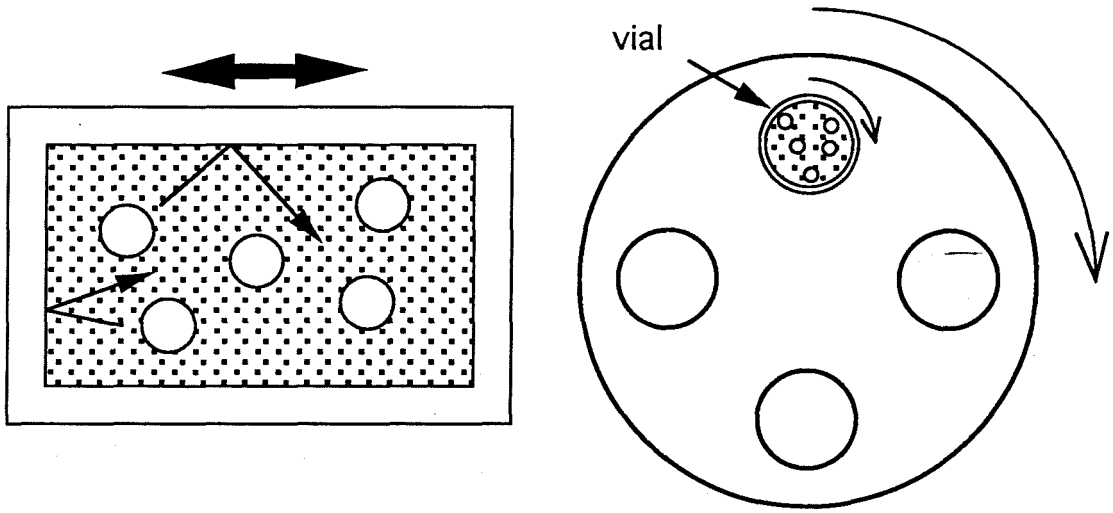

(a) vibratory mill

(b) planetary mill

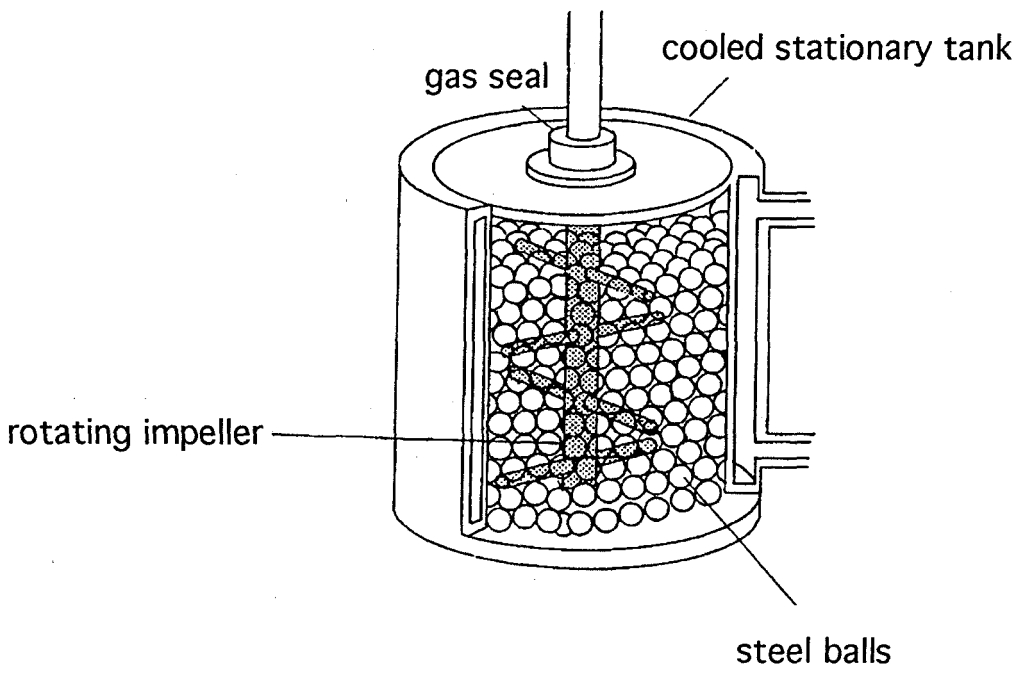

(c) attritor mill

Fig. 2-2 Schematic drawing of typical ball mills. (a) vibratory mill, (b) planetary mill, (c) attritor mill [38].

Phenomenological studies have shown that the amorphization follows the grain refinement into nanocrystalline structures. After Gleiter and coworkers [2 - 7] synthesized nanocrystalline materials by inert-gas condensation method and observed special properties described in the previous chapter, a variety of techniques have been attempted for the production of nanocrystalline materials Hellstern *et al.* [43] produced nanocrystalline Ru and AlRu with ball milling. Fecht *et al.* [44] prepared *bcc* and *hcp* pure metals. Eckert *et al.* [45] synthesized nanocrystalline *fcc* metals with ball milling. Fecht *et al.* [46] reported the formation of Zr - Al metastable nanocrystalline solid solution by mechanical alloying. Suzuki and colleagues prepared Al - Ni alloys by mechanical alloying, then eliminated Al by leaching in KOH solution to obtain nanocrystalline *bcc* Ni [47] porous materials.

2.2.2 *Mechanisms of ball milling*

1 Deformation Behavior

The mechanism of deformation introduced by ball milling has been well studied by many researchers, however no comprehensive overall description of the process has been proposed. Hellstern *et al.* [48] performed mechanical attrition experiments using CsCl - type intermetallic compounds. They found that the atomic-level strain increases with decreasing of grain size, reaches a maximum, and then decreases. They argue that the dislocation density saturates at a certain level as the grain size decreases. Dislocations are then absorbed into grain boundaries to form high angle grain boundaries. Hellstern *et al.* [49] observed that the deformation of ball milled AlRu powder is strongly localized in thin shear bands of about 1 μm width which separate

the material into narrow regions. They propose three stages of deformation in ball milling:

(1) shear band formation due to very high strain rates and strain concentration,

(2) evolution of shear band regions to form new grain boundaries, and subsequent grain size refinement,

(3) grain size reaches a steady state.

The same tendency was later observed in TiCu intermetallic compound by Seki and Johnson [16]. On the other hand, the authors [50] and Eckert *et al.* [45] observed that atomic strain increases monotonically in the Ti - Cu system and *fcc* metals, respectively.

2 The Mechanism of Energy Storage

Mechanical alloying is capable of increasing the free energy of the materials so that they deviate from equilibrium state to form the nanocrystalline structure or transform to amorphous state. One of major questions to be yet solved is the mechanism of energy storage in materials by ball milling. Neither elasticity nor plasticity theory has provided successful interpretation of the energy storage sufficient to transform the crystalline phase to the amorphous phase.

Fecht *et al.* [51] argue that most of energy input is stored in grain boundary regions. On the other hand, Seki and Johnson [16] estimated enthalpy stored in TiCu and Ti_2Cu intermetallic compounds by ball milling, and concluded that the antiphase boundaries play a major role in energy storage, while grain boundaries do not contribute very much.

It is not always the case that the more intense milling produces non-equilibrium phases of the higher energy. Eckert *et al.* reported the effect of milling intensity on the final structure of milling products [52]. It has been thought that too much intensity generates enough heat for a stable phase to nucleate. Also the influence of milling power has been investigated by Burgio *et al.* [53]. Stable crystalline phases occur when the milling is too intense, although amorphous phases were obtained with an appropriate milling intensity. Hashimoto et *al* [54] demonstrated that the ball charge fraction is an important factor for the progress of reaction in ball milling.

3 Simulational Study

Simulating ball milling has been attempted recently by a few researchers. Mazzone *et al.* simulated mechanical alloying with deformation of a bulk metallic diffusion couple and found that interdiffusion is activated by plastic deformation [55]. Furthermore they observed that the reaction is enhanced with increasing strain rate. These phenomena were interpreted in terms of increasing free volume due to plastic deformation.

Hashimoto *et al.* performed mathematical simulation on mechanical alloying [56]. In order to express energy consumption by collision and plastic deformation of powder, a 1 - dimension viscoelastic ball model was considered. A certain fraction of energy consumed by the viscosity is supposed to be accumulated in the powder. The effect of milling power, ball diameter and ball charge volume fraction on the microstructure was studied along with ball milling experiments of the Cu - C system. Their results include the following findings:

(1) The averageous impact energy is inversely proportional to the

impact frequency.

(2) The volume fraction of ball charge is the impact force at each collision.

(3) The total energy consumed is proportional to the ball charge volume fraction.

(4) The energy input into the material is proportional to the total energy consumption by the ball mill.

2.2.3 *Description of Ball Mills*

Two types of mechanical alloying apparatus were employed in this research: a SPEX 8000 high intensity shaker ball mill (SPEX Industries, Inc., New Jersey) and a Super - Misuni NEV-MA-8 vibratory ball mill (Nisshin Giken, Japan).

1 SPEX Shaker Mill

The SPEX mill shown in Fig. 2-3 is much more intense than Misuni, and is mainly used for investigating the microstructure evolution during milling and for forming products at a final stable stage. The steady state is usually reached within 10 hours of milling time. The powder is sealed into the vial with balls under an argon gas atmosphere. Although it is impossible to control the milling temperature accurately, the vial is air-cooled to prevent it from heating. The temperature outside vial during milling is about 40 - 50°C. A ball to powder ratio is usually set to 10 - 5 : 1.

2 Misuni Vibratory Mill

The characteristics of Super-Misuni ball mill are accurate controllability of atmosphere and temperature. The vials are connected to a vacuum pump

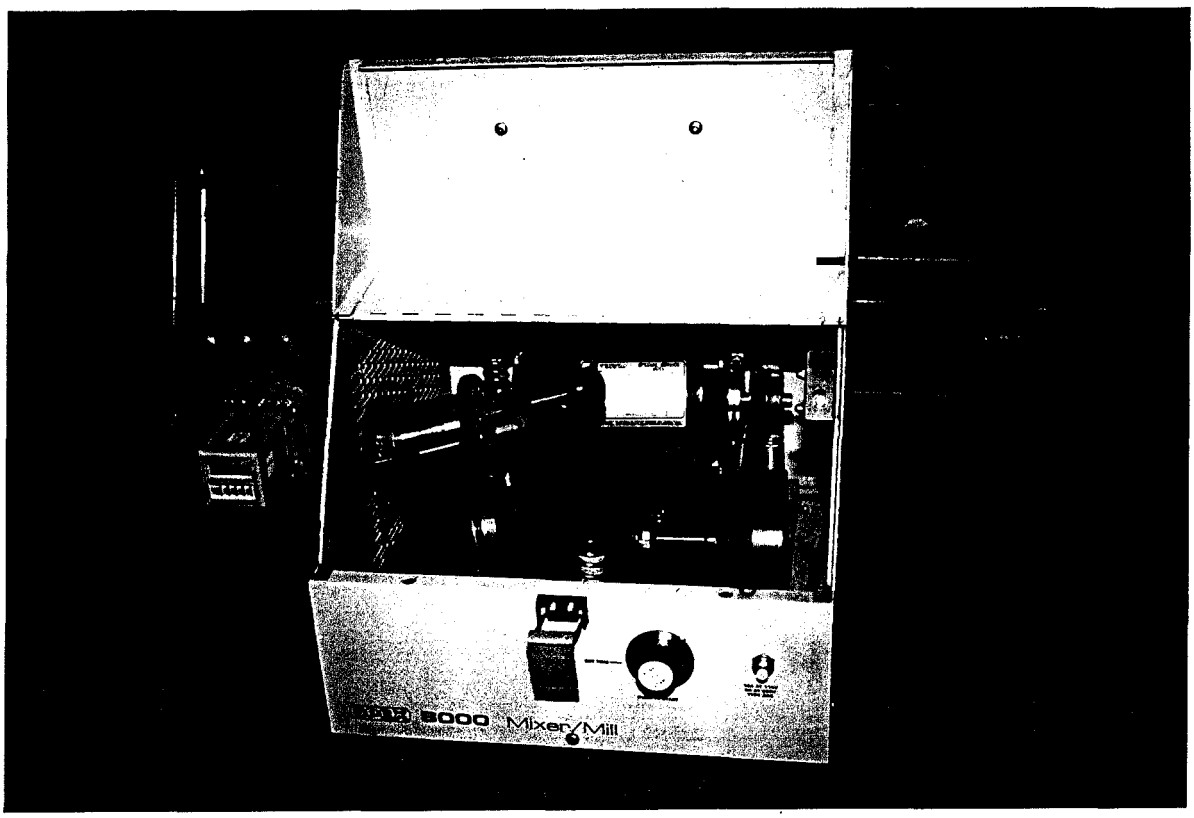

Fig. 2-3 SPEX shaker mill type 8000.

and inert gas inlet, which allow one to perform ball milling under gas-flow and to eliminate influence of gaseous impurities. In addition, a heating apparatus can be attached to the vibrating table so that one of the vials is kept at high temperature (up to 300 °C) during milling.

The milling temperature is feed-back controlled by measuring the temperature between the vial and the heater with a thermocouple. In addition, the vial is cooled by flowing water during room temperature milling experiments. Although not used in this study, the cooling equipment can also be attached, with which one can carry out low temperature milling down to - 196 °C, the boiling temperature of nitrogen. However the container must be refilled with liquid nitrogen in every 15 minutes, and in addition, the temperature cannot be as constant and accurate as on heating, since no control is possible. The milling intensity is less than SPEX mill, therefore longer milling time is required to obtain the same result.

For room temperature ball-milling, both in the SPEX mill and the Misuni mill, the vial is sealed with a viton gasket. However at higher temperature than 200 °C, viton O - rings cannot be used. Therefore an alternate way to seal the vial was needed. In this study, sealing with a Cu gasket for ultra-high vacuum equipment was contrived. The schematic picture of the vial for high temperature milling is drawn in Fig. 2-5. The vial lid and bottom are made of type 304 stainless steel. The lid is tightened to the bottom with bolts and nuts. An oxygen-free Cu gasket deforms plastically at room temperature under inert gas atmosphere by two notches. Although there is no way to control the atmosphere during milling, this vial shuts out the intrusion of foreign gas from outside.

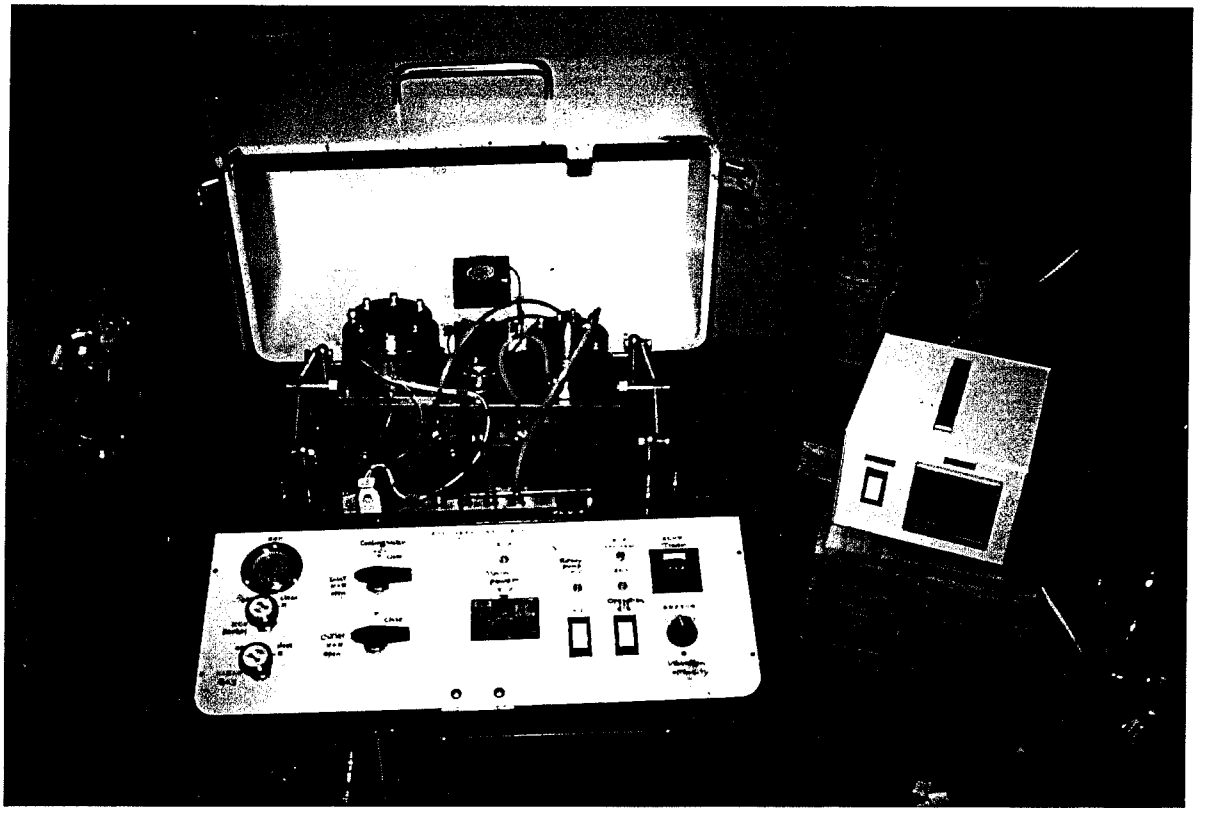

Fig. 2-4 Super-Misuni NEV-MA8 shaker mill.

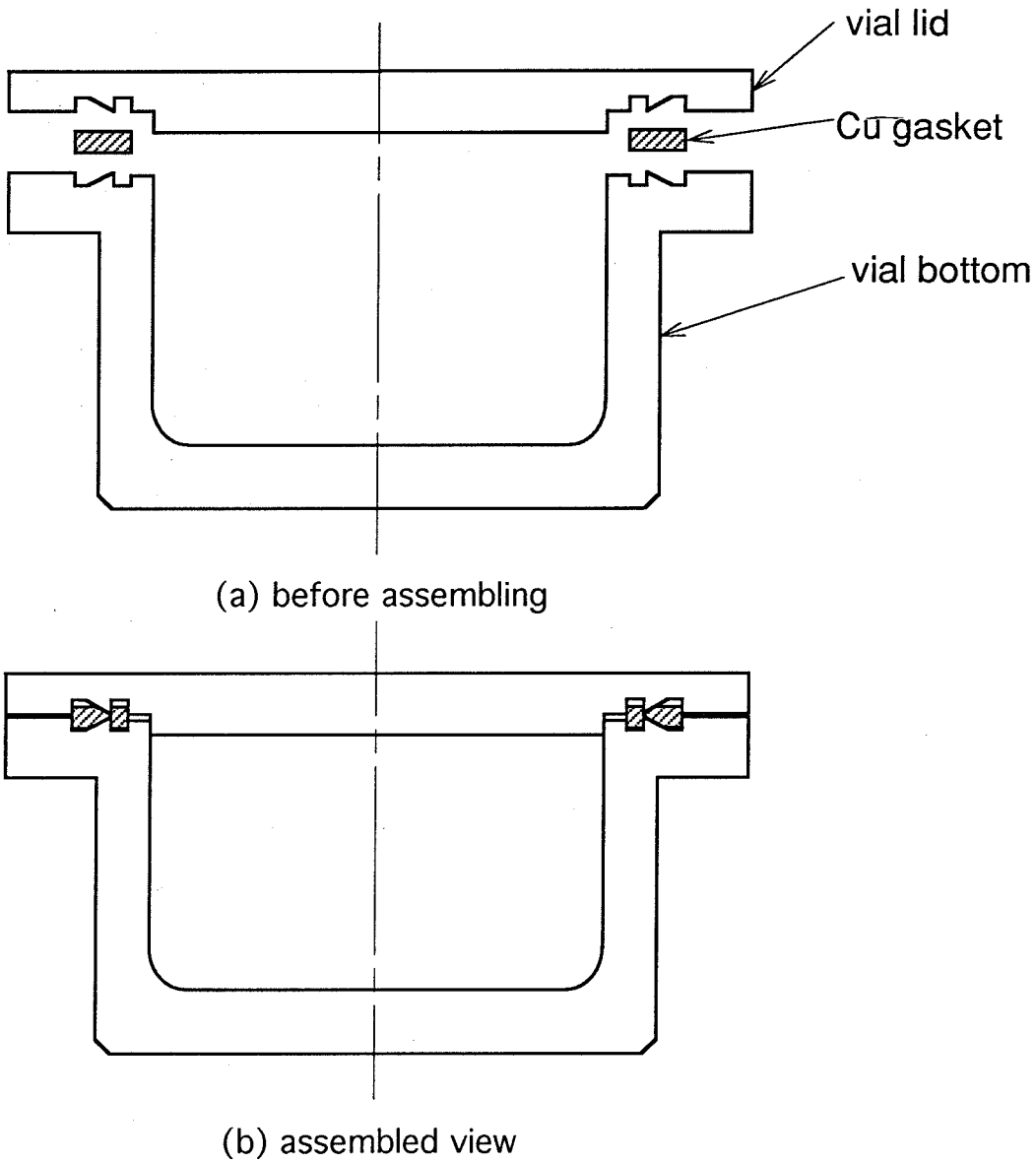

Fig. 2-5 Schematic picture of a vial for high-temperature milling.

After an experiment is completed, milled powder is cooled in the vial to avoid oxidation at high temperature. Since the vial cannot be removed from the mill while it is hot, and no quenching device is available, the powder is annealed for an hour during cooling.

It is not clear if the contamination level is different from the SPEX or not. While the wear rate of the milling equipment must be less, the longer milling time enhances contamination.

2.2.4 *Characterization*

1 Chemical Analysis

Ball-milled powder was subjected to various chemical analysis methods with which the impurities are quantitatively measured: the infra-red absorption for C and O, the thermal conductivity method for N and the fluorescence X-ray method for metallic elements.

The effect of Fe has not been studied. Fecht *et al.* [51] reported that Fe contamination is below 2 at.% after 24 hours of milling regardless of alloy systems. Also a previous study shows that 0.32 wt.% of Fe is found in Ti - Cu alloys after 10 hours of milling with a steel vial and (WC + 6 wt.% Co) balls [57]. In Chapter 3, an attempt to avoid Fe contamination by using a pure Ti milling device will be discussed.

2 Grain Size/Strain Estimation

Bragg peaks in X-ray diffraction spectra have finite width due to the grain size and atomic-level strain. If one may neglect the strain effect to estimate grain size, the Scherrer formula [58] can be applied.

$$L \approx \frac{K\lambda}{B\cos\theta_B}, \tag{2-1}$$

where L is the grain size, λ is the wave length of X-rays, B is the full width at half maximum of the Bragg peak at diffraction angle $2\theta_B$. K is a constant, usually set to 0.9.

However, in the present experiment, atomic strain is expected to be presumed to be large. Therefore the two mechanisms of broadening of the diffraction peaks were separated in the following manner [59]:

The peak broadening profile is usually assumed to be a Cauchy (Lorenzian) or Gaussuan function. To separate grain size and strain effects from a Bragg peak, it is essential to assume each contribution to have one of these forms. The peak broadening δs is related to the diffraction vector s as,

$$(\delta s) = \frac{1}{L} + 2es \qquad \text{for Cauchy/Cauchy approximation,} \tag{2-2}$$

$$(\delta s)^2 = \left(\frac{1}{L}\right)^2 + (2es)^2 \qquad \text{for Gaussian/Gaussian approximation,} \tag{2-3}$$

for Cauchy grain size broadening and Gaussian strain broadening,

$$\frac{K}{(\delta s)L} = 1 - \left(\frac{2es}{(\delta s)}\right)^2, \tag{2-4}$$

where e is atomic-level strain.

Although it has been believed that strain broadening tends to obey Gaussian and that grain size broadening is approximated by Lorenzian [59], the combination that makes the error least is usually adapted. In the present study, Gaussian approximation was applied for both grain size and strain

broadenings.

3 Lattice Parameter Calculation [58]

From Bragg's law one derives for the cubic system,

$$\frac{\Delta d}{d} = \frac{\Delta a}{a} = K \cos^2 \theta, \tag{2-5}$$

where d is spacing and a is lattice parameter and K is a constant. The diffraction angle θ should be measured with a Debye - Scherrer camera.. Eqn. (2-5) becomes,

$$\frac{\Delta \sin^2 \theta}{\sin^2 \theta} = \frac{2\Delta d}{d}. \tag{2-6}$$

Also, one has

$$\sin^2 \theta = \frac{\lambda^2}{4a^2}\left(h^2 + k^2 + l^2\right). \tag{2-7}$$

From Eqns. (2-5) - (2-7), one can estimate K, and thus the lattice parameter a. Practically, one has to apply least square methods to find K from measurements on several Bragg diffraction peaks.

4 Thermal Analysis

DSC experiments were carried out using Perkin - Elmer DSC - 4 and SETARAM DSC - 2000K. The latter utilizes an alumina crucible as a sample container so that samples can be heated to 2000 K, while in the former apparatus, the maximum temperature is 600 °C. However the former apparatus is capable of quick heating/quenching up to the rate of 100 K/sec. In the present study, Ti - Cu and Nb - Cu samples were examined with the Perkin - Elmer and SETARAM, respectively.

2.3 Small Angle X - ray Scattering (SAXS)

2.3.1 Introduction

Small angle scattering (SAS) is a useful technique to observe the structure of mid-range order (10 - 1000 Å) in condensed matter. Therefore SAS has been regarded as a complement of optical and electron microscopy techniques.

SAS is the elastic scattering of the light by the material. X - rays and neutrons are the sources employed. In small angle X - ray scattering (SAXS), photons are scattered by electrons, therefore from SAXS the electron density fluctuation in the material is measured. Similarly, small angle neutron scattering (SANS) is the elastic scattering of neutrons by atomic nuclei, and the atomic density fluctuation is obtained.

The results from SAXS and SANS are expected to show little difference, however this is not always the case. The reason is because X - rays are less sensitive to light atoms than neutrons. However the discrepancy is still under discussion [60].

SAS is a relatively "classic" technology. Back to 1930's, Guinier first developed SAXS to apply to metallurgy. The Guinier-Preston zones, fine planar cluster-like precipitates of Cu in Al - Cu alloys, were discovered by SAXS [61]. Since then, the SAS technique has been applied widely in various fields such as biology, inorganic or organic chemistry, and geology. Since neutrons are much more penetrating than X - rays, SANS is more effective for metallic materials, however due to the limited availability of neutron

sources, SAXS is used commonly in the field of metallurgy. Topics in metallurgy investigated with SAXS and SANS include spinodal decomposition, nucleation, defects, interfaces, magnetic properties and superconductivity [62]. In recent years, studies on metallic glasses using SAS technique have been conducted vividly [60]. Also nanocrystalline materials have been investigated with SAXS and SANS techniques [63].

In this section, the SAXS apparatus at Caltech is described. A brief introduction to the principle of SAXS will be given in the appendix. However SANS will not be mentioned.

2.3.2 *Experimental Apparatus*

We have constructed a SAXS apparatus at Caltech. The schematic picture is shown in Figs. 2-6 and 2-7. X - rays are generated by a sealed-anode type X - ray tube with a power supply of 40 kV, 25 mA. Cu - $K\alpha$ radiation is utilized. After removing $K\beta$ radiation by Ni filters, X - rays are focused onto the position sensitive detector (PSD) with the aid of two Johannson focusing crystals. Most of the light paths are enclosed in a vacuum chamber to prevent from air scattering. The detail principles are described in the following sections.

1. X - ray Source

In general, for SAXS experiments, a rotating anode X - ray generator is employed because the intensity of the scattered beam is much lower than that of the diffracted beam by lattice planes. Today's rapid technological development has allowed us to make use of ultra-high intensity X - ray beams. For example, for Cu - $K\alpha$ radiation, systems operated at 60 kV, 300 mA

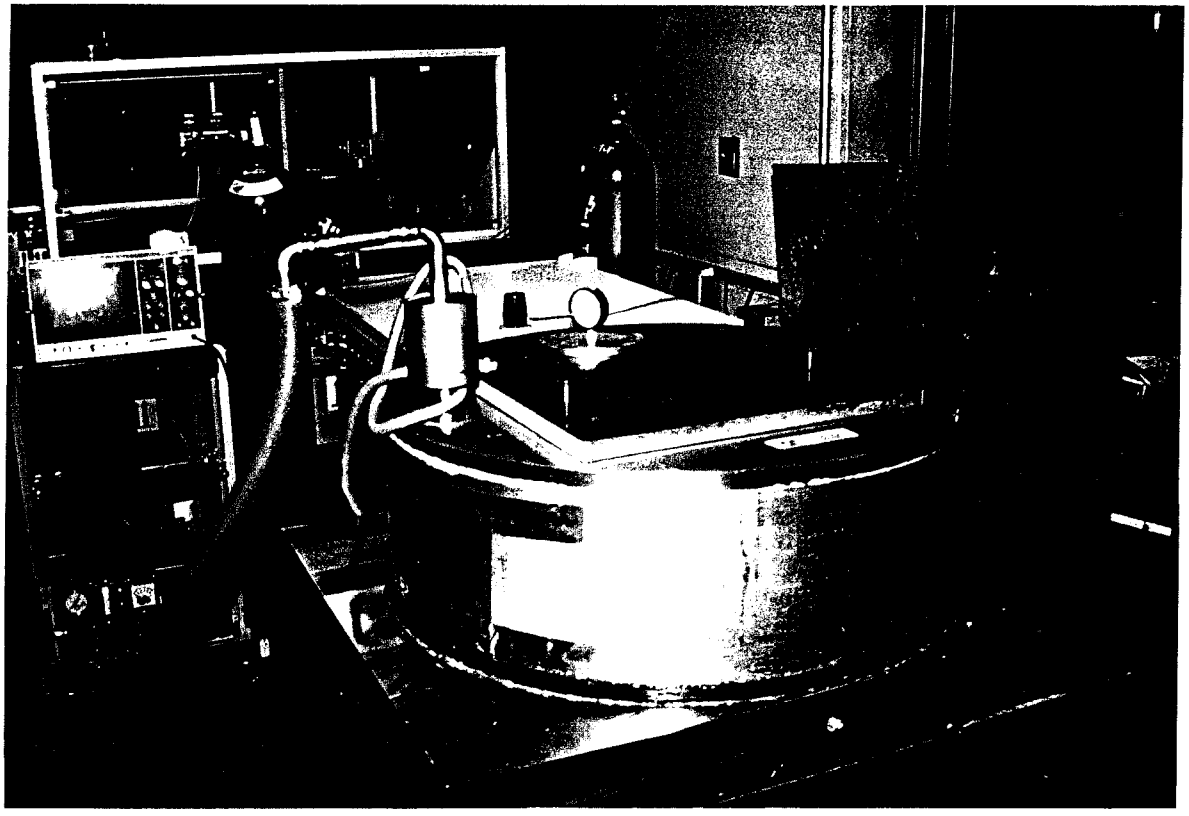

Fig. 2-6 Caltech SAXS apparatus.

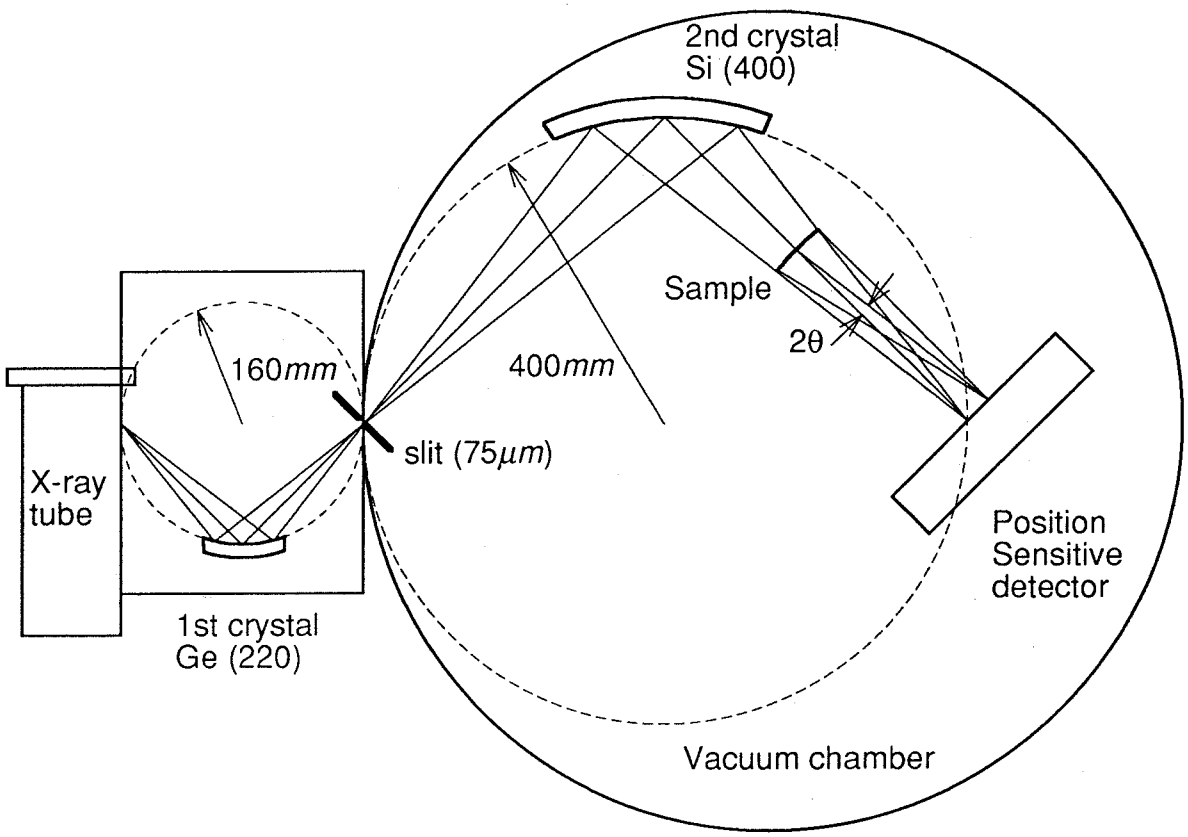

Fig. 2-7 Schematic picture of Caltech SAXS apparatus.

are now in practical use.

Caltech SAXS system makes use of a small power supply, the Rigaku Geigerflex X - ray generator (40 kV 25 mA), however the double curved-crystal monochromator configuration allows us to measure SAXS with good accuracy and efficiency. Cu - $K\alpha$ radiation (λ=1.54 Å) is used in our system. Mo - $K\alpha$, Ni - $K\alpha$, Co - $K\alpha$, Cr - $K\alpha$ are among alternative choices. As mentioned previously, the width of the scattered peak from a small object is proportional to the wavelength of the incident beam. On the other hand, as will be discussed later, the optimum sample thickness increases for longer wavelength radiation. In studies on metals and alloys, Mo and Cu radiations are used commonly. After all, the most appropriate system must be chosen according to the purpose and physical constraints.

2. Optical System

A SAXS system requires X - rays of a single wavelength in a sharply collimated beam. For this purpose, monochromators and collimators are utilized. There are three common methods to measure SAXS, namely Kratky camera, double curved-crystal method and multiple reflection diffractometer.

As shown in Fig. 2-8, the primary beam in the Kratky method is collimated into a line by a set of slits. A film or a position sensitive detector (PSD) is placed at the screen. Instead of slits, pinholes may be used for point collimation. The parasitic scattering of width a in Fig. 2-8 is expected due to the non-parallel component of the beam passing through slits. Consequently, long slit intervals and narrow slits are essential for precise SAXS measurement.

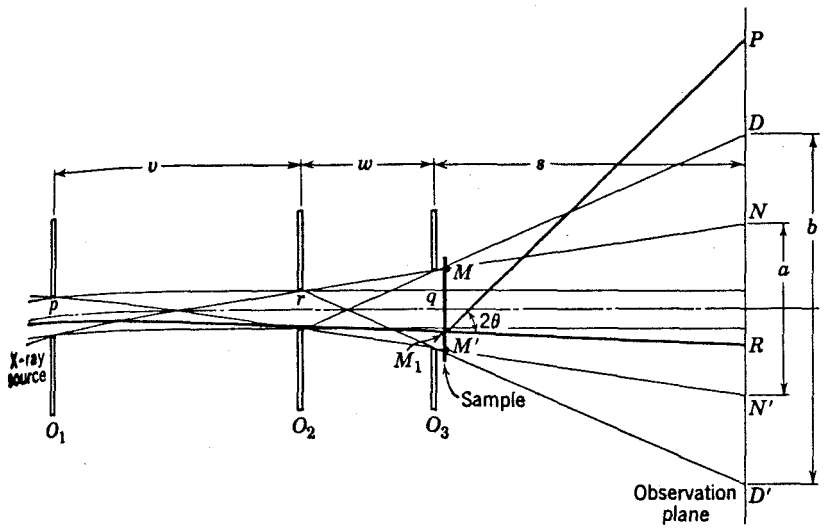

Fig. 2-8 Schematic picture of line collimation by double slit configuration [61].

Bonse and Hart [64] proposed a method to make use of a grooved monolithic crystal. When the X - ray beam passes the grooved crystal it undergoes multiple diffractions and is well monochromated. Their system is a modification of the Beeman configuration, where the slit systems are replaced by grooved crystals. No separate collimators are needed since the beams are parallel after passing through the first crystal. Although the intensity loss is very large, the parasitic scattering is eliminated almost perfectly, and the width of the direct beam of 5 seconds is achieved. Thus scattering near the direct beam is now measurable. This method is called *Ultra Small Angle X - ray Scattering* (USAXS) and has recently been applied to polymers and colloids to study structures of the order of 5000 Å [65].

The biggest drawback of the crystal monochromatization/collimation is the tremendous loss of intensity. To compensate this disadvantage, curved crystal monochromators were devised. DuMond and Kirkpatrick were the first to apply this idea as in Fig. 2-9 [66]. Since Johann [67] and Johansson [68] independently developed such crystals earlier, these crystals are often referred to as Johann or Johansson crystals. A crystal is bent elastically by the radius R and then has the surface polished by the radius $R/2$. The genius of this idea is that a spherical primary beam at A is diffracted on the crystal surface and focuses at B coherently. A simple SAXS system with this configuration is schematically drawn in Fig. 2-10. However, since the primary beam is not monochromatic, the crystal may diffract X - rays of various wavelengths. Thus the parasitic scattering can be enormous as seen in Fig. 2-10 [61]. The combination of two curved crystals can solve this problem. Fournet [69] showed that the antiparallel setting shown in Fig. 2-11 can eliminate parasitic scattering almost completely without any slit collimator.

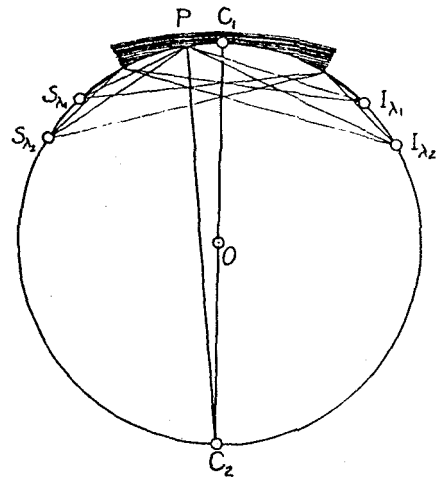

Fig. 2-9 Schematic drawing of double-bent crystal (Johannson crystal) [66].

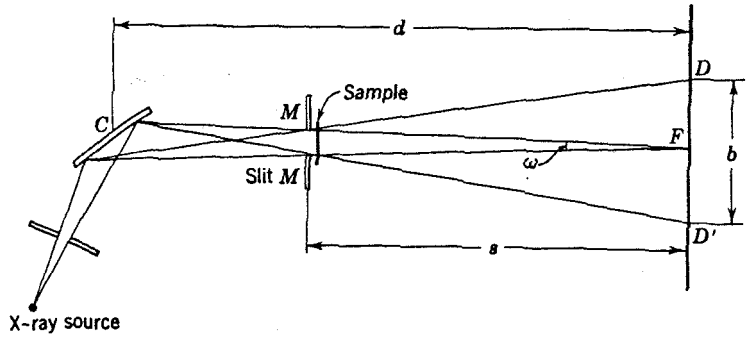

Fig. 2-10 SAXS system using one Johannson crystal [61].

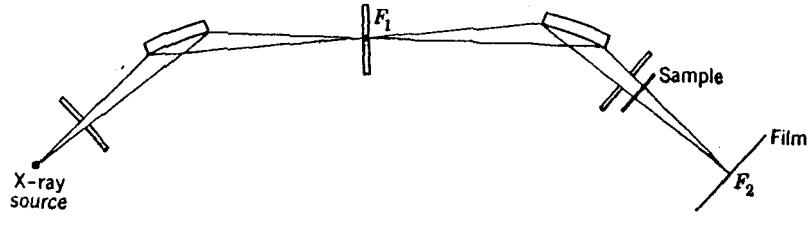

Fig. 2-11 SAXS system using two Johannson crystals in antiparallel geometry [61].

Therefore the intensity loss is relatively small. Also the direct beam intensity falls off so quickly that usually the parasitic scattering is almost negligible at 10′ from the beam center in such a system [61]. Thus one may conclude this configuration is suitable for a SAXS apparatus.

The Caltech SAXS apparatus adapted this double curved-crystal monochromator configuration with positioning two Johannson crystals in parallel. A Ge (220) single crystal with surface radius 160 mm (*i. e.*, R = 320 mm) is used as the first monochromator, and A Si (400) single crystal with surface radius 400 mm is employed as the second monochromator. These crystals are 1 inch high. The antiparallel positioning was not taken due to the spatial restriction. Although Fournet [69] suggested that this geometry allows some undesired wavelengths to remain, the performance of our system is satisfactory. The measured FWHM of the direct beam is about 4.7′, thus the parasitic scattering is suppressed below 10′ in this system. The intensity of the direct beam is theoretically estimated to be as high as 2×10^8 counts per second, however usually the alignment is far from perfect, therefore the obtained intensity is several times 10^7 c/s.

1. Position Sensitive Detector

A position sensitive detector OED-50-M (M. Braun GmbH, Germany) is employed for detection of scattered photons. It is a gas proportional counter operated under a 10 vol. % CH_4 - Ar atmosphere, with a 50 mm wide and 10 mm high detection window. This range is divided into 1024 channels. Thus each channel constitutes a 48.8 μm wide independent counter.

Since this detector does not operate under vacuum, it was enclosed in a small pressure chamber connected to the laboratory atmosphere. A window

of 1/4 mil thick mylar foil allows the X - ray entrance to the detector with negligible intensity loss.

The sensitivity of the position sensitive detector must be calibrated in a separate experiment. The calibration is carried out with a radioactive source at the position of the sample with the X - ray power supply turned off. Usually the nonuniformity of the detector sensitivity may range up to 10 %.

2. Experimental Data Correction

The real scattering intensity function $I(q)$ has only scattering angle dependence, therefore X - rays scattered by the sample with a scattering angle θ form a cone with a conic angle 2θ. (Note that q is defined by $q = 4\pi/\lambda \sin\theta$).) However, due to the equipment and experimental conditions, usually the measured scattering intensity $J(q)$ is the result of the convolution of such a circular source and the slit geometry functions.

The double curved-crystal monochromator geometry allows us to treat the incident beam as infinitely narrow vertical lines. Therefore the beam width correction is not necessary. However, the incident beam is linearly collimated and regarded as a row of point sources, and a beam height correction is required.

A complicated analytical expression for $J \rightarrow I$ conversion has been derived [61]. However, assuming the infinite beam height, the expression can be simplified. Guinier [61] showed that if the real scattering intensity is Gaussian, the observed scattering intensity must be Gaussian, too. Hence near the beam center,

$$J(q) \propto I(q) \tag{2-8}$$

Also shown is in high q limit,

$$J(q) = \frac{\pi}{2} qI(q). \tag{2-9}$$

Thus, Porod law becomes $J(q) \sim q^{-3}$ for a system with sharp interfaces. Schmidt [70] derived a general relation between the measured scattering intensity and the correlation function:

$$\gamma(r) = \frac{1}{2\pi^2} \int_0^\infty q J_0(qr) J(q) dq, \tag{2-10}$$

where, J_0 is Bessel function of the first kind, as shown in Eqn. (2-11),

$$J_0(x) = \sum_{k=0}^{\infty} \frac{(-1)^k (x/2)^{2k}}{k! \Gamma(k+1)}, \tag{2-11}$$

and Γ is Gamma function, given by $\Gamma(k) = \int_0^\infty t^{k-1} e^{-t} dt$. Using (2-10), one can convert the measured intensity to the real intensity. Thus one can calculate real scattering intensity without complex computation, even using measured quantities only.

3. Data Collection and Processing

A Canberra 1024 channel multi-channel analyzer (MCA) has been used for Caltech SAXS apparatus. Analog input data of 0 - 5 V are converted to 10 bit digital data and stored in the corresponding channels. It has an input energy discriminator, with which a fluorescent radiation and inelastic scattering component with less energy can be removed effectively.

4. Capability of This System

Since the distance between the sample and detector can be varied from

150 to 370 *mm*, this system is capable of covering the scattering angle ranging from 6.6×10^{-5} to $0.16\,rad$. Usually for the better resolution, the sample/detector distance is set to 370 *mm*.

5. Data processing in This System

The scattering intensity measured with the position sensitive detector was counted and accumulated with the multichannel analyzer, which has a data transfer protocol to the data-logging computer. The collected data were converted to a function, the intensity vs. scattering angle, then sent to the processing computer. In the computer the data were processed and analyzed.

2.3.3 *Sample Preparation and Data Collection Procedures*

In order to investigate the structure of grain boundaries of nanocrystalline materials synthesized by ball milling, SAXS experiments of mechanical alloyed powder were conducted.

1. Optimum Sample Thickness/Absorption

The term "absorption" is somehow misleading when used for X - rays: when X - rays are absorbed, they do not transmit, but they are reemitted by the sample as fluorescent radiation. The fluorescent X - rays can be collected as SAXS.

From an experimental observation, the absorption behavior of matter is expressed by:

$$-\frac{dI}{I} = \mu\, dx, \tag{2-12}$$

where I is the intensity and μ is referred to as the linear absorption coefficient.

Integrating Eqn. (2-12) yields, at the depth x in the sample,

$$I = I_0 \exp(-\mu x), \tag{2-13}$$

where I_0 is the intensity of the incident beam. The linear absorption coefficient μ is not a material constant but dependent of its state, while a quantity mass absorption coefficient μ/ρ. is a material constant, and found in references. Using the mass absorption coefficient, Eqn. (2-13) becomes:

$$I(x) = I_0 \exp\left(-\left(\frac{\mu}{\rho}\right)\rho x\right). \tag{2-14}$$

The absorption coefficient is given approximately by:

$$\frac{\mu}{\rho} = k\lambda^3 Z^3, \tag{2-15}$$

where k is a constant, Z is atomic number. k varies for each absorption branch, *K, L, M...*, and lowers as passing absorption edges. Hence, in general, the longer the wavelength is and the heavier the atoms are, the more X - rays are absorbed.

For compounds or alloys, total mass absorption coefficient $(\mu/r)_{tot}$ is given by the weighed sum of mass absorption coefficient of each element $(\mu/r)_i$ as,

$$\left(\frac{\mu}{\rho}\right)_{tot} = \sum_i n_i \left(\frac{\mu}{\rho}\right)_i, \tag{2-16}$$

so that,

$$\mu_{tot} = \rho \cdot \sum_i n_i \left(\frac{\mu}{\rho}\right)_i, \tag{2-17}$$

where μ_{tot} is total linear absorption coefficient, ρ is overall sample density, n_i is the molar fraction of each element.

From Eqn. (2-12), one can derive the maximum scattering condition [59]. Assume a sample of thickness t. For incident X - rays scattered at depth x, Eqn. (2-12) becomes:

$$dI = I_0 \exp(-\mu t) dx, \tag{2-18}$$

since all the scattered beam passes the sample and is attenuated by $\exp(-\mu t)$. Integrating Eqn. (2-18) with respect to the depth, the total scattered intensity becomes,

$$I = \int_0^t dI = \int_0^t I_0 \exp(-\mu t) dx = I_0 t \exp(-\mu t). \tag{2-19}$$

Equating $dI/dt = 0$ yields the optimum sample thickness t_0 as follows:

$$\left.\frac{dI}{dt}\right|_{t=t_0} = I_0 \exp(-\mu t_0)(1-\mu t_0) = 0, \tag{2-20}$$

thus, $t_0 = 1/\mu$. As shown here, the optimum thickness is a function of wavelength and the state of the material. Usually for metals, absorption coefficients are fairly big, so the sample thickness must be of the order of 1-10 μm.

2. Practical Sample Preparation

The procedure of SAXS sample preparation is schematically shown in Fig. 2-12. (a) Mechanical alloyed $Ti_{95}Cu_5$ and $Ti_{90}Cu_{10}$ powders were loaded and sealed into a sheath (a piece of steel tube of 6.25 mm diameter.) (b) Then the sheath underwent cold rolling to the total thickness of 0.625 mm.

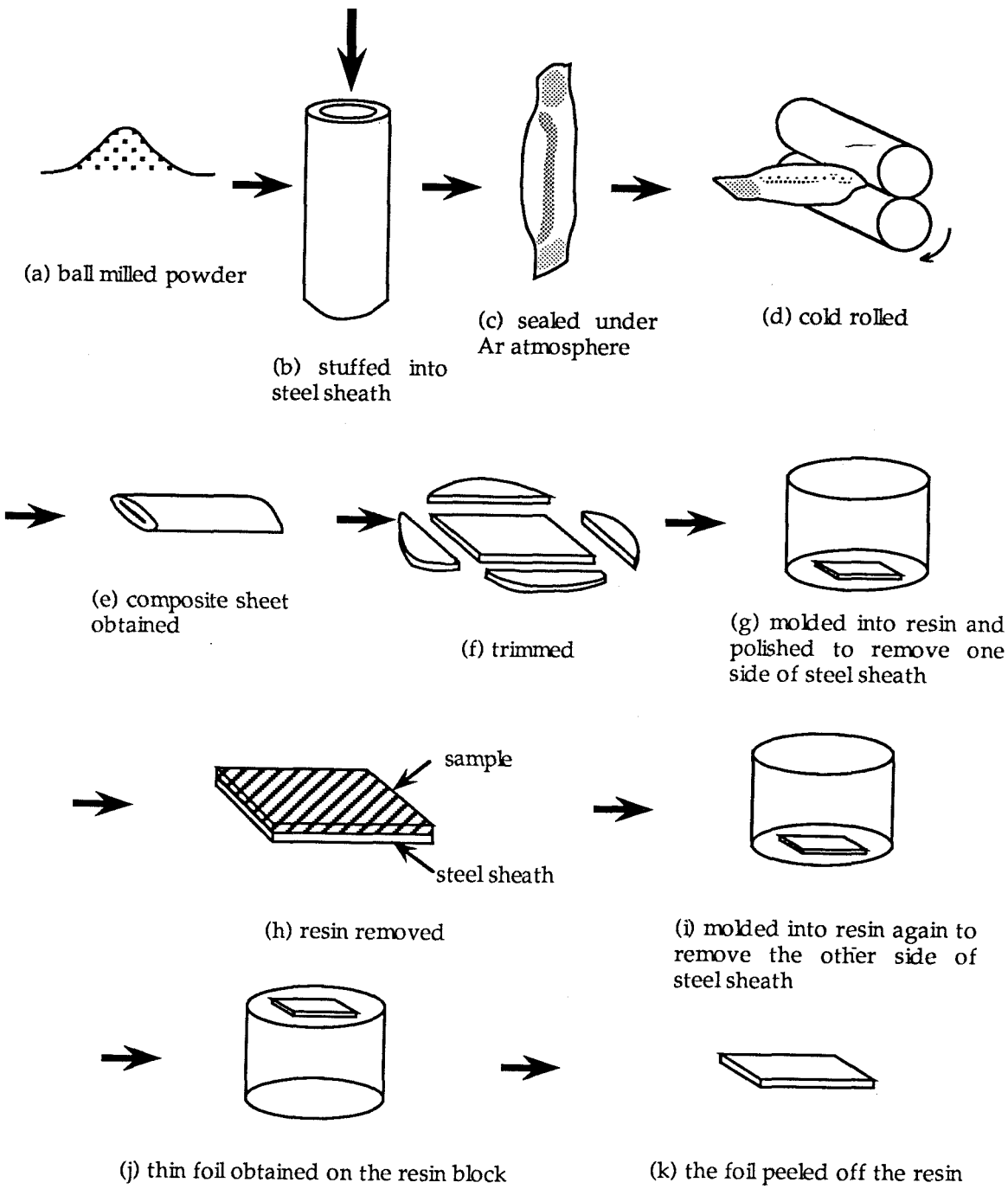

Fig. 2-12 SAXS sample preparation procedure

The reduction rate in each pass was limited less than 5 % to prevent heating of the sample. (c) The rolled sample was cut short and molded into resin. (d) After solidification, the sample was mechanically polished from one side until the steel tube was removed and the consolidated material was exposed and the final surface roughness was below 0.25 *mm*. (e) Then the sample was molded in resin again and mechanically polished from the opposite side. (f) Finally, when the desired thickness was achieved, the sample was peeled off the resin and fixed on a kapton foil.

Because of the brittleness of consolidated material and limited thinning, the final thickness reached was much more than the desired thickness, and the effect of multiple scattering could not be eliminated completely. In addition, the uniformity of the sample thickness was not guaranteed.

3. Actual Data Collection Procedure

A series of experiments on one sample consists of the following measurements:

(1) measuring transmitting beam intensity through the sample holder I_0,

(2) measuring scattering intensity by the sample holder, called "background" B,

(3) measuring scattering intensity by the sample and sample holder I,

(4) measuring transmitting beam intensity through by the sample and sample holder I_S,

(5) measuring transmitting beam intensity through the sample

holder I_0'.

The final objective of SAXS experiment is to measure the difference between Expts. (2) and (3), with appropriate calibration. One can calculate the incident beam intensity, and absorption by the sample from Expts. (1) and (4). Transmitting beam intensity measurements are carried out using stacked nickel foils as absorbers. Since the absorption coefficient and thickness of nickel foils are known, one can calculate the true intensity of the incident beam.

SAXS signals are usually very small, especially in high q range. In addition, near $q \sim 0$, around the center of the incident beam, the transmitting beam and scattering beam coexist, and they are inseparable. Therefore direct measurement with nickel absobers does not provide accurate results. Instead, a direct beam trap is used to protect the detector from the strong central beam. A tungsten beam trap is used in this study, which is designed not to lead any stray beam reflecting on the trap surface into the detector.

The SAXS $J(q)$ is calculated in the following fashion.

Usually the absorption coefficient of the sample or its thickness may be unknown, therefore the absorption must be estimated experimentally. Fraction of transmitting beam through the sample A is computed from Expts. (1) and (4) as,

$$A = I_s / I_0 , \tag{2-21}$$

Then, the measured SAXS $J(q)$ is obtained as,

$$J(q) = \frac{I(q) - (B - D) \times A}{A} = \frac{I}{A} - (B - D), \tag{2-22}$$

where, I is measured scattering from (sample + background), B is measured background scattering , and D is dark current. The dark current is due to stray X - rays from outside the system and noise in the detector. It must be measured separately with the X - ray power supply in the system turned off.

The X - ray intensity from an X - ray tube varies in time. It has been found that two hours of preliminary "warm-up" of the X - ray tube in full power is sufficient to stabilize the output. In our measurement, the transmitting beam intensity through the sample holder (Expts. (1) and (5)) is compared to confirm that the intensity change is less than 2 %.

If the sample is a powder and needs a substrate for support, then the scattering from the substrate must be counted. The SAXS from the substrate is measured as if the substrate were the sample, and it is then subtracted from SAXS from the sample on the substrate. The substrated was a kapton foil (hydrocarbonate) since it is transparent to X - rays, namely, absorbs X - rays quite little (less than 1 %.) Due to the strong absorption of metals, the intensity of the scattered X - ray beam is very low. Therefore it may take 10 hours for measurement (3) in order to obtain reliable data.

2.3.4 *Calibration Experiment*

1. Glassy Carbon

In order to confirm the functionality of Caltech SAXS apparatus, SAXS from amorphous carbon was measured. The sample is 2 mm thick glassy carbon specimen and has a porous structure. The porosity is measured as a "inhomogeneity" in the experiment. Fig. 2-13 demonstrates the result. The Porod plot gives slope of -3 at high q region. This implies a very sharp carbon-

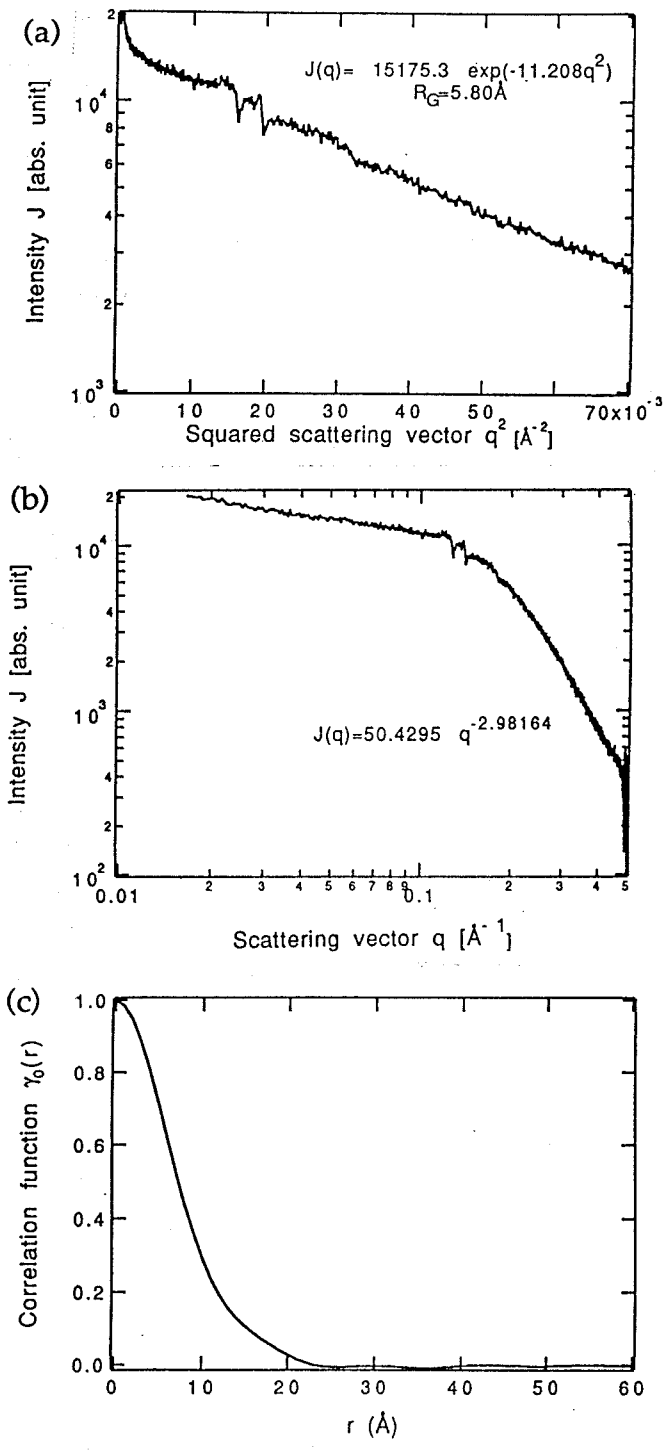

Fig. 2-13 SAXS signal from glassy carbon sample. Parasitic scattering and other noises have already been removed. (a) Guinier plot, (b) Porod plot, (c) correlation function. Guinier radius and Porod exponent agree well with the typical values for glassy carbon.

porosity interface, as is anticipated. The Guinier plot estimates the radius of gyration as 8.80 Å, while the correlation length is 10 Å, which agrees with typical reported values, 5 - 9Å and 10 - 12 Å, respectively [71].

2. Sputtered Film

Fe and Er have been co-sputtered onto kapton foil to form a crystalline $Fe_{50}Er_{50}$ alloy thin film. The film was investigated with Caltech SAXS. The results are shown in Fig. 2-14. The Porod plot indicates that the slope is about -1.86 and is constant throughout all q range. This implies that there is a fractal-like structure in the film. The characteristic length is computed from correlation function as about 10 Å. TEM observation on this sample columnar crystals growing along the direction of deposition and form elongated grains in such sputtered alloy films [72]. This is common in such sputtered alloy films [73]. These results have been interpreted as diffuse boundaries, detected as inhomogeneities due to the electron density difference. Actually, the characteristic length corresponds well to the observed grain boundary width in TEM. Thus we conclude that Caltech SAXS system can provide reliable results.

2.4 Summary

In this chapter, the basic principles and experimental procedures of ball milling and small angle X - ray scattering (SAXS) were discussed. We have constructed a SAXS apparatus with parallel positioned double Johannson crystals. This system enables us to measure small angle scattering at angles less than 10^{-4} *rad*. Although the X - ray source is not strong enough to get strong SAXS signals from metallic materials, it has been demonstrated that

the system provides reliable results for thin films and carbon.

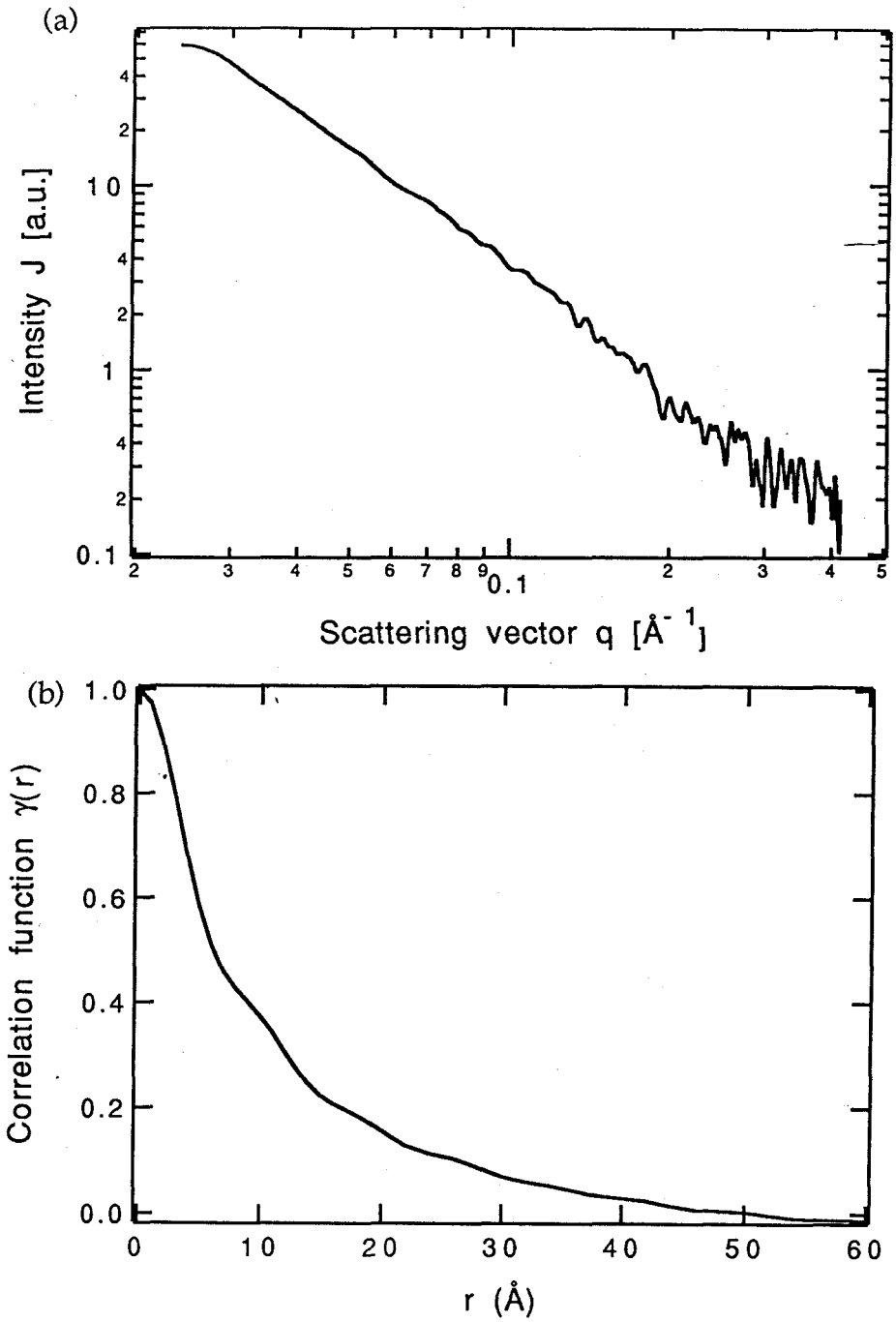

Fig. 2-14 SAXS signal from Fe-Er film sputtered on Kapton substrate. Parasitic scattering and other noises have already been removed. (a) Porod plot, (b) correlation function. Columnar structure is predicted from Porod exponent.

Chapter 3 Nanocrystalline Structure of Ti - Cu alloys

3.1 Introduction

The following chapters will be devoted to discussion on the results of ball milling experiments to produce nanocrystalline structure, and the study on the grain growth behavior of nanocrystalline materials synthesized by ball milling, by means of analytical approaches such as X-ray diffraction (XRD), differential scanning calorimetry (DSC), scanning electron microscopy (SEM), transmission electron microscopy (TEM) and small-angle X-ray scattering (SAXS). In Chapter 3, observation on Ti - Cu and (Ti ,Zr) - Cu will be discussed. In Chapter 4, experiments with Nb - Cu will be reported. In addition to conventional room temperature ball milling (later referred to as RTBM), a novel technique, high temperature ball milling (HTBM) was introduced, and the effect of milling temperature was investigated. The last topic will make up Chapter 5.

Mechanical alloying of Ti and Cu was conducted in this study. At first, the compositional effect on the phase transformation from nanocrystal to amorphous was investigated. Then the mechanism of nanocrystal formation by ball milling was studied. Mechanical alloying of intermetallic compound TiCu and pure elements (Ti or Cu) was also performed in comparison in order to investigate the effect of the starting state. Ti - Cu equilibrium binary phase diagram is shown in Fig. 3-1 for reference [74].

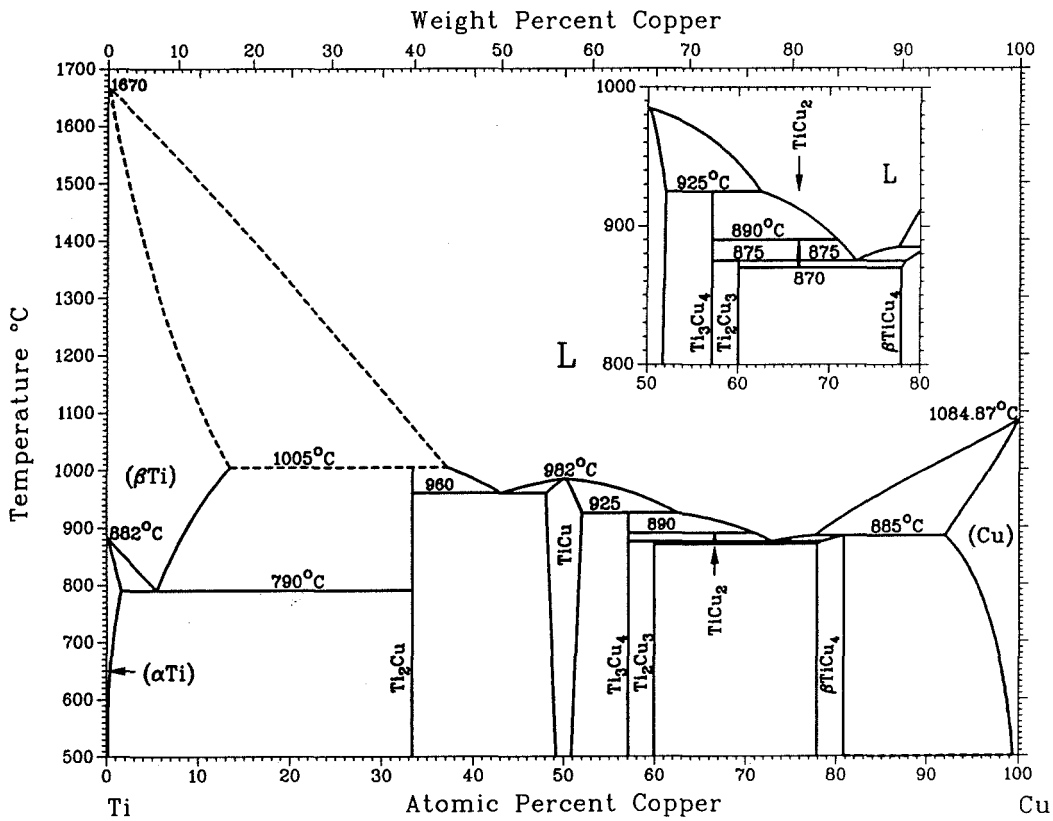

Fig. 3-1 Ti - Cu binary phase diagram [74].

3.2 Previous Study

The Ti - Cu system has been chosen in this research because of much previous study and abundant data available. The major results previously reported are presented for reference.

Ti - Cu alloys can be amorphized by various methods. Ray *et al.* were the first to report the vitrification of $Ti_{100-x}Cu_x$ ($65 \leq x \leq 70$) by the rapid quenching technique [75]. More works [76 - 78] proved that the glass forming range is as wide as 25 - 72 at.% Cu. Also Reeve *et al.* estimated the glass formability in terms of the critical thickness of ribbons [79]. Rizzo *et al.* [80] synthesized crystalline and amorphous Ti - Cu alloys by sputtering and reported compositional range of amorphization as 26 - 84 at.% Cu (single phase at 37 - 76 at.% Cu.) They also found the extended solubility in both terminal solid solutions. Luzzi *et al.* successfully vitrified intermetallic compounds TiCu and Ti_4Cu_3 by electron irradiation [81, 82]. Askenazy and Johnson found crystal-to-amorphous transformation of Ti_2Cu floating in amorphous matrix by rolling [83].

A controversial result was reported by von Allmen and Blatter [84]. They prepared various binary alloys of a high-temperature phase *m* by laser rapid heating and quenching, then annealed it at a certain temperature. $Ti_{40}Cu_{60}$ is among the materials that underwent amorphization: a mixture of a high-temperature phase *m* (unidentified) and the amorphous phase was produced by rapid quenching, then was annealed at 300 °C and completely vitrified. They call this *spontaneous vitrification*. Furthermore, they claim that this amorphization is reversible. However, their results have never been reproduced by any other workers. Theoretical study based on the thermodynamics proposes doubt on the feasibility of this phenomenon [85, 86].

The Ti - Cu system has been adopted by a lot of researchers for study of mechanical alloying. Politis and Johnson conducted mechanical alloying experiments of Ti - Cu system and obtained the amorphous state in the compositional range of 10 - 87 at.% Cu [57]. Cocco *et al.* prepared amorphous Ti - Cu alloys by mechanical alloying [87, 88]. Seki and Johnson [16] reported that TiCu intermetallic compound does not amorphize by mechanical milling, instead it forms nanocrystalline structure. They discussed this phenomena in terms of the energy associated with chemical disorder, and concluded that TiCu is unable to store enough energy to transform to metallic glass. In addition, they reported that in Ti_2Cu the grain size monotonically decreases to less than 10 *nm* before amorphization. Nagumo *et al.* conducted mechanical alloying of TiH_2 and Cu to find that no amorphization takes place after nanocrystalline structure formation [89]. In addition to studies of the materials themselves, milling and consolidation processes have also been investigated using this alloy system [22, 28].

Thermal stability and crystallization behavior of Ti - Cu amorphous alloys have been studied by many researchers [76, 78, 90 - 92]. Schwarz and Turnbull [93] discussed the thermodynamic models with respect to the T_0 curve, in other words, the compositional range for polymorphic transformation. However, they only found that no glass formation in Ti - Cu system was anticipated from any models ever proposed. Battezatti *et al.* [94] estimated free energy for solid solution and liquid phase and predicted amorphization in the composition range of 50 - 70 at. % Cu. Woychik and Massalski estimated the nucleation temperature of the Ti - Cu system with a mathematical model based on a classical nucleation theory [95]. The thermodynamic property of liquid Ti - Cu alloys have been studied by Sommer *et al.* [96]

3.3 Structure Evolution by Ball Milling

3.3.1 Study on the Transient Stage

1. Ball Milling

Previous reports revealed that the microstructure evolves with milling time as more energy is injected into the material. The structure evolution was investigated, and the steady state and the transient state were studied.

Pure elemental Ti (99.9% purity, -100 mesh) and Cu (99.9% purity, -200 +325 mesh) powders were mixed into the overall composition of $Ti_{90}Cu_{10}$ and subjected to the experiments with a SPEX ball mill. 2 - 4 g of powder is milled in one charge. The ball-to-powder mass ratio (BPR) was set to 10 - 5. Milled powder is collected under an argon atmosphere and used for further study. Intermetallic compound TiCu was prepared in the same fashion as Seki and Johnson [16].

The chemical analysis results indicate that the major impurities contained are less than 0.3 at.% for O, 0.1 at.% for N, 0.15 at.% for C and 0.25 at.% for Fe. Thus we judged that the impurities affect neither the microstructure formation behavior, nor the physical and chemical properties of ball-milled materials.

It takes several hours of milling until the system is completely mixed. By studying this transient stage, it is possible to acquire some knowledge about the mechanism of ball milling. The XRD spectra of $Ti_{90}Cu_{10}$ powders milled for various time spans are shown in Fig. 3-2. Significant peak broadening is observed owing to grain size reduction and atomic level strain accumulation. Nevertheless, the *hcp* structure of α - Ti is preserved. Peaks of nonreacted Cu disappear in 3 hours. Bragg peak from Ti (002) intensifies first, then attenuates in intensity. A slight diffuse halo from amorphous phase is recognizable in the powder milled

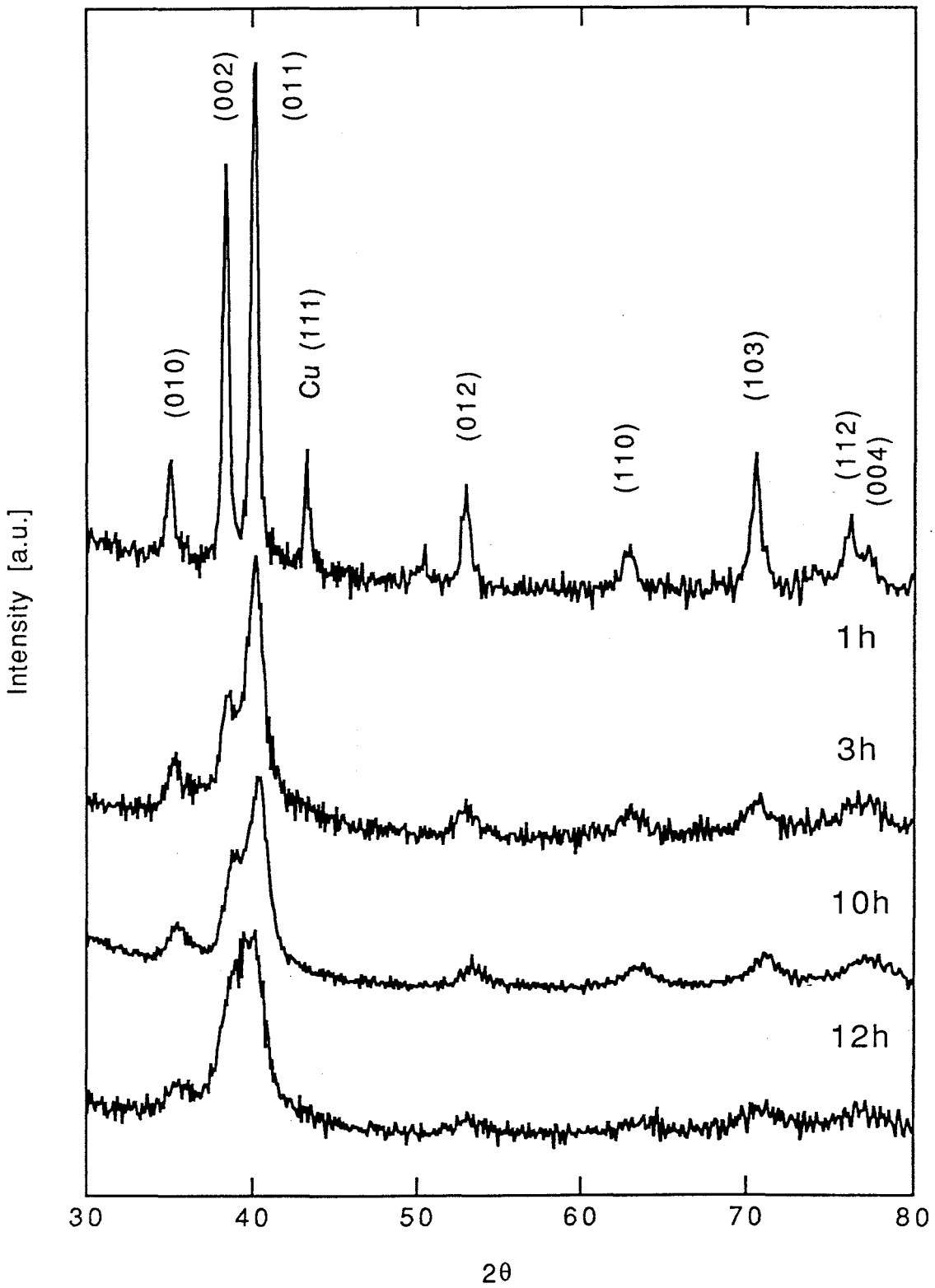

Fig. 3-2 XRD spectra of $Ti_{90}Cu_{10}$ synthesized by ball milling for the indicated duration.

for more than 10 hours. Extended solid solubility by mechanical alloying has been reported in many alloy systems [3, 97]. In the Ti - Cu system, a single-phase *hcp* structure is obtained at Ti - 10 at.% Cu composition although the equilibrium solid solubility of Cu in Ti at 300 K is negligibly small [79].

Macroscopically, ball-milled Ti - Cu alloys first form plate-like flakes of 1 - 2 *mm* diameter and 0.2 *mm* thickness in 1 hour of milling, then they are gradually pulverized into fine powder. Final particle size is nonuniform and system-dependent, of 1 - 100 μm in diameter. The change of appearance of ball-milled powder was observed with SEM as seen in Fig. 3-3. This change of mode from plastic deformation to fracture is interpreted as follows. In the first stage of milling, atomic mixing is not so remarkable that most of the matrix consists of pure titanium. Therefore dislocations are not pinned in the crystal lattice and the material is deformed plastically. After enough mixing, stress field occurs by atomic strain, therefore dislocations cannot march smoothly any longer, and they accumulate somewhere to cause cracking.

Fig. 3-4 indicates that grain size decreases with milling time and reaches a steady state value of 6 - 8 *nm* in 6 hours of milling, while atomic strain continuously increases. The change of lattice parameters and the nearest neighbor distance of α - Ti phase with milling time are shown in Fig. 3-5. The *c*-axis lattice parameter decreases quickly after 1 hour of milling, which results in a decrease of the nearest neighbor distance. This decrease may be due to diffusion of Cu into the Ti matrix. Lattice parameters reach constant values after 3 hours of milling.

It is implied above that strain is primarily stored in *c*-axis direction. This tendency agrees the observation that the Bragg peak intensity of Ti (002)

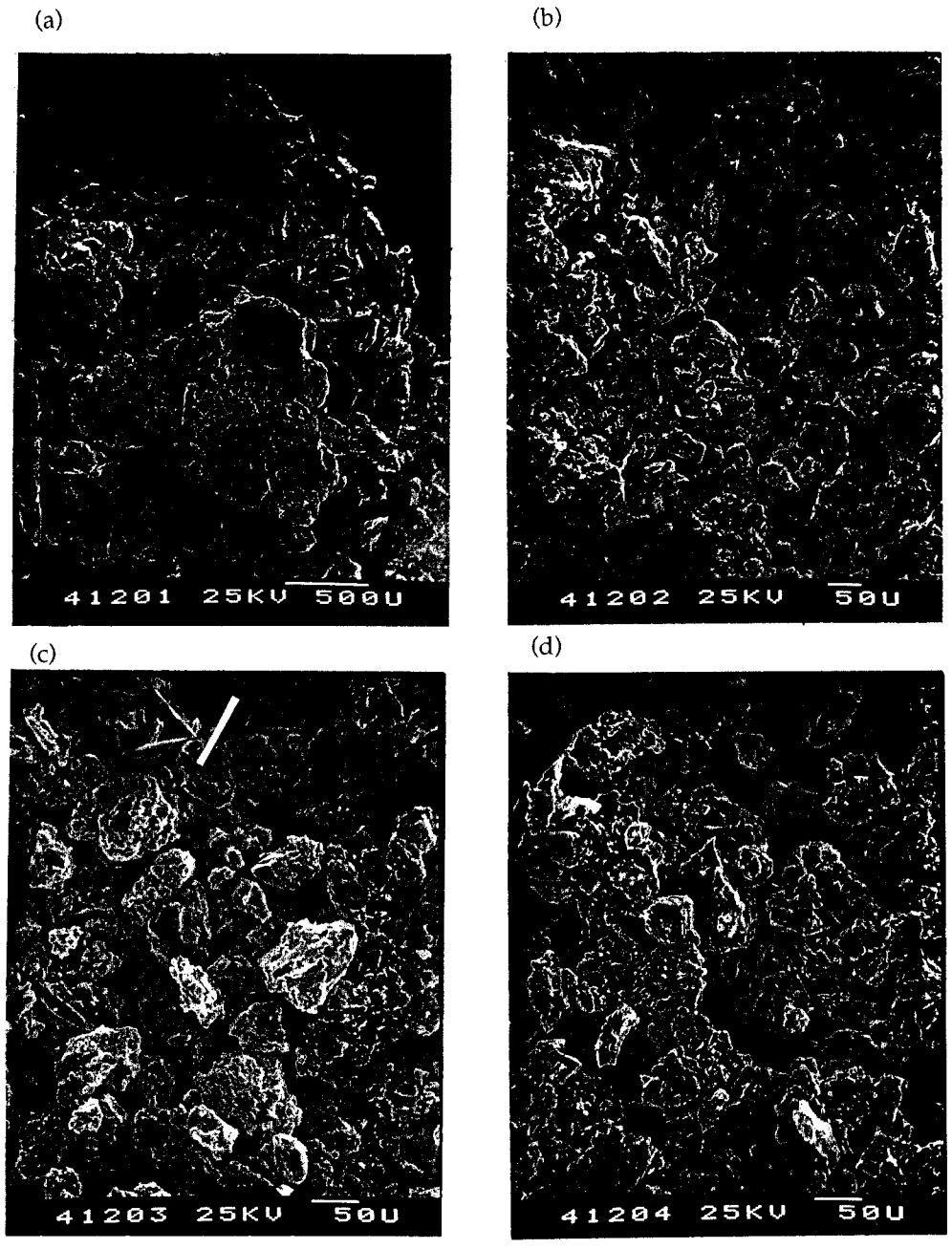

Fig. 3-3 SEM pictures of $Ti_{90}Cu_{10}$ powders synthesized by ball milling for various duration. After (a) 1 hr, (b) 3 hrs, (c) 6 hrs, (d) 10 hrs of milling. Ti particles are deformed ductile at first, then the deformation mode changes to brittle fracture.

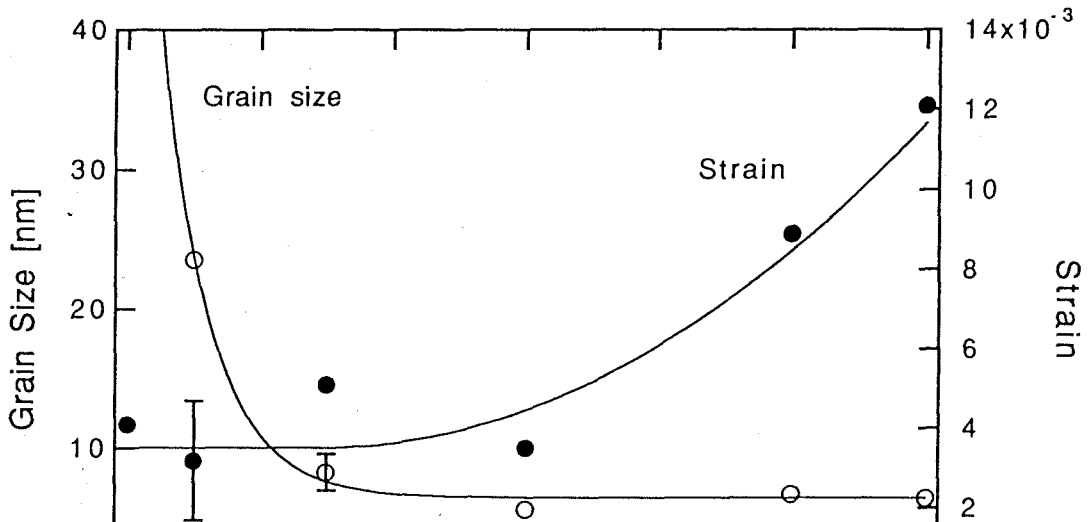

Fig. 3-4 Grain size and atomic strain of $Ti_{90}Cu_{10}$ synthesized by ball milling as a function of the milling time.

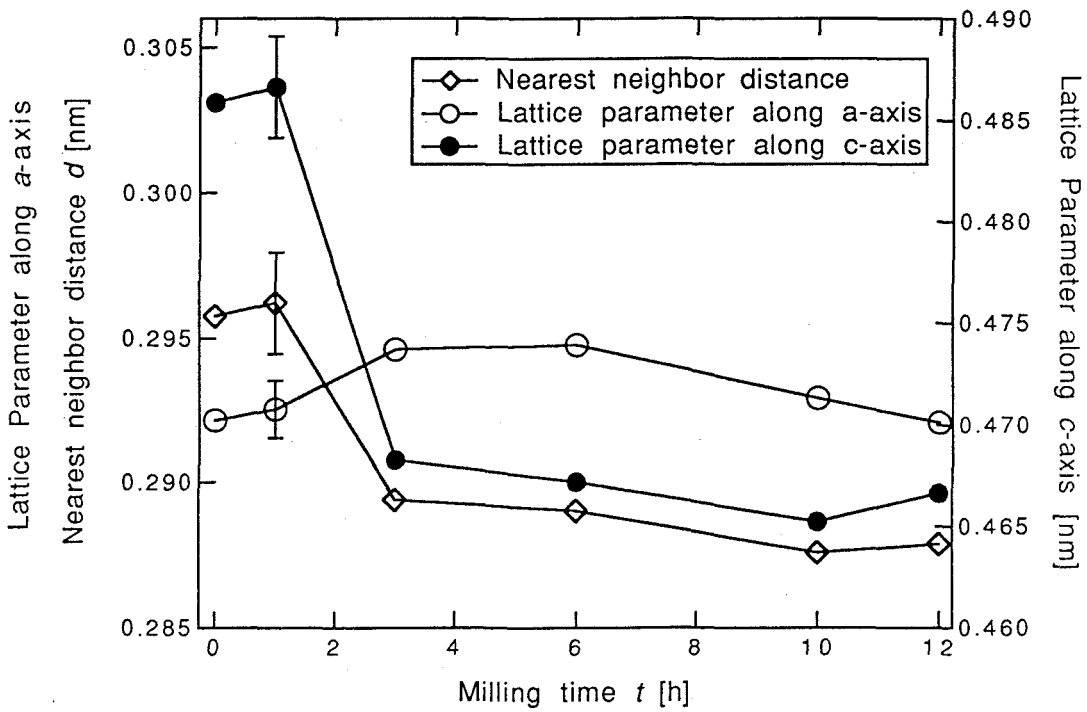

Fig. 3-5 Lattice parameters of $Ti_{90}Cu_{10}$ synthesized by ball milling as a function of the milling time.

diminishes after 1 hour of milling. The small increase of lattice parameters and nearest neighbor distance in the first hour of milling can be interpreted with decomposition of surface oxide layers of Ti powder and solution of the oxygen into Ti matrix.

The nearest neighbor distance of powder ball-milled for 10 hours is estimated to be 0.2876 *nm* by XRD analysis, which is larger than the value derived from Vegard's law by about 0.5 %. This deviation implies the solid solubility of Cu is less than overall concentration, *i. e.*, it is implied that the actual Cu in-grain concentration of nanocrystalline $Ti_{90}Cu_{10}$ is less than 10 at.%. The rest of Cu atoms are suspected to segregate at grain boundaries.

2. Thermal Analysis

To study the structural evolution, DSC experiments were carried out using $Ti_{90}Cu_{10}$ samples milled for various duration. DSC traces from Ti - Cu alloys ball-milled for various duration are shown in Fig 3-6. There is found a shallow exothermic reaction ranging from 100 to 200 °C, however no structural change corresponding this peak is seen from the XRD study. Probably this peak is due to the gradual structural relaxation. A blunt exothermic peak, apparently a superposition of multiple peaks, is observed in samples milled for less than 6 hours. However those small peaks reduce into a deep exothermic peak finally. These small peaks are interpreted from local region with high concentration of Cu, where amorphous or other non-equilibrium phases occur by mechanical alloying. Only one of the peaks survives after long time of milling. It is thought that the compositional fluctuation due to insufficient atomic mixing is gradually eliminated during long milling, and non-equilibrium phases again turn to equilibrium or metastable phases. Thus one may conclude that the completion of

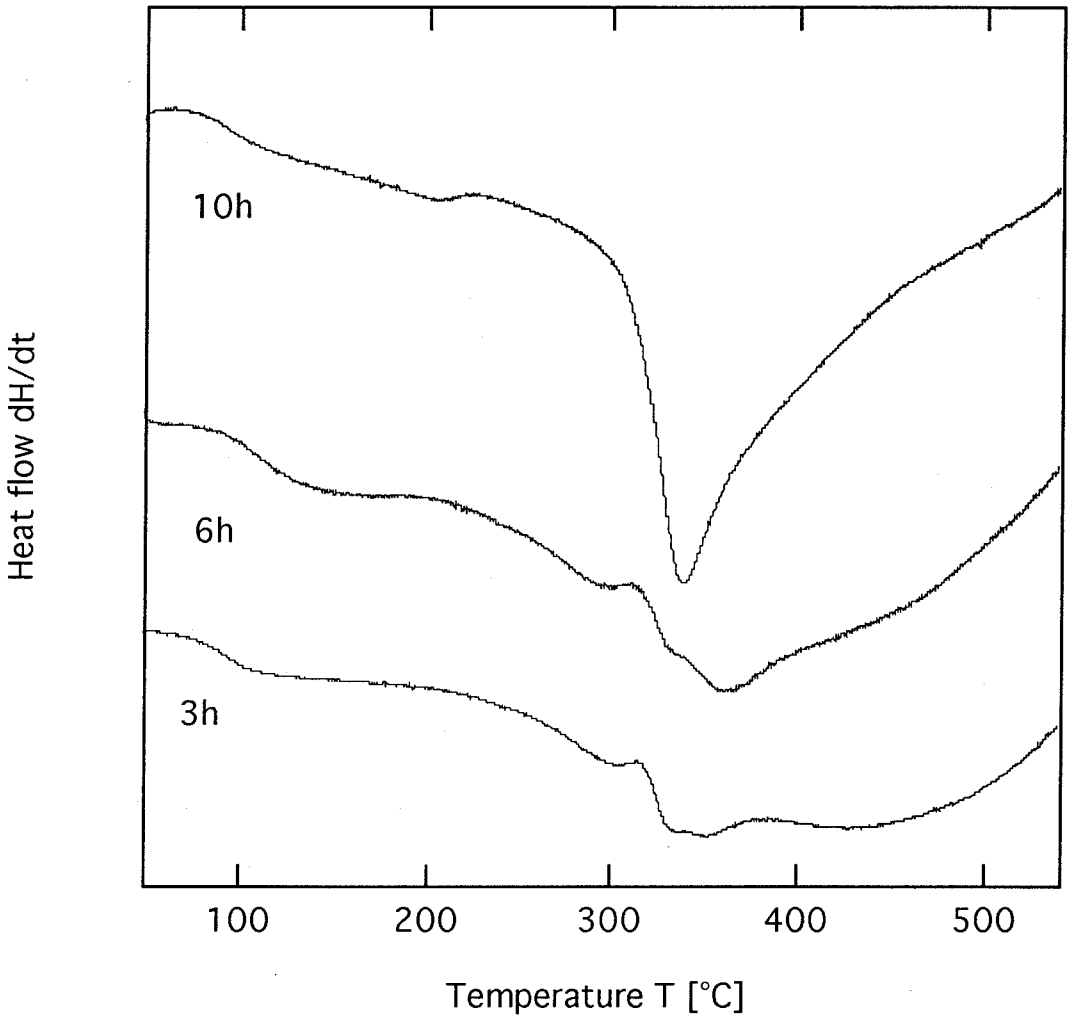

Fig. 3-6 DSC traces of $Ti_{90}Cu_{10}$ synthesized by ball milling for various duration.

atomic mixing can be determined by the DSC results. The critical milling time required for the DSC peaks reduces to a single peak is 6 hours, which agrees with the grain size reduction behavior.

In order to investigate the exothermic reaction, Kissinger analysis was carried out [98]. The following equation provides the activation energy E of the reaction, if E is well defined. The activation energy estimates the stability of the metastable structure.

$$\frac{d\left[\ln\left(\phi/T_m^2\right)\right]}{d(1/T)} = -\frac{E}{R}, \tag{3-1}$$

where ϕ is the heating rate, T_m is the peak temperature (*i. e.*, temperature at the maximum heat release rate), T is temperature and R is the gas constant. Although this treatment is valid only when the reaction is homogeneous, Criado and Ortega [99] demonstrated that the Kissinger analysis is applicable to any solid state reactions within negligible error.

An attempt was made to separate the blunt peaks in DSC spectra of samples milled for less than 6 hours. Two of these small peaks separated have a higher and lower peak temperature than the peak appearing by further milling as shown in Kissinger plot in Fig. 3-7. Activation energies are well defined, thus all the reactions observed are proved to be thermal activated reactions. Interestingly, the activation energies of the reactions are all the same, although the reason is not clear. Thus it is suspected that compositional nonunioformity causes interfaces with quite large composition difference which forms a highly non-equilibrium phase.

It has been commonly believed that the materials reach a metastable state with the highest energy by ball milling long enough. However in some reports

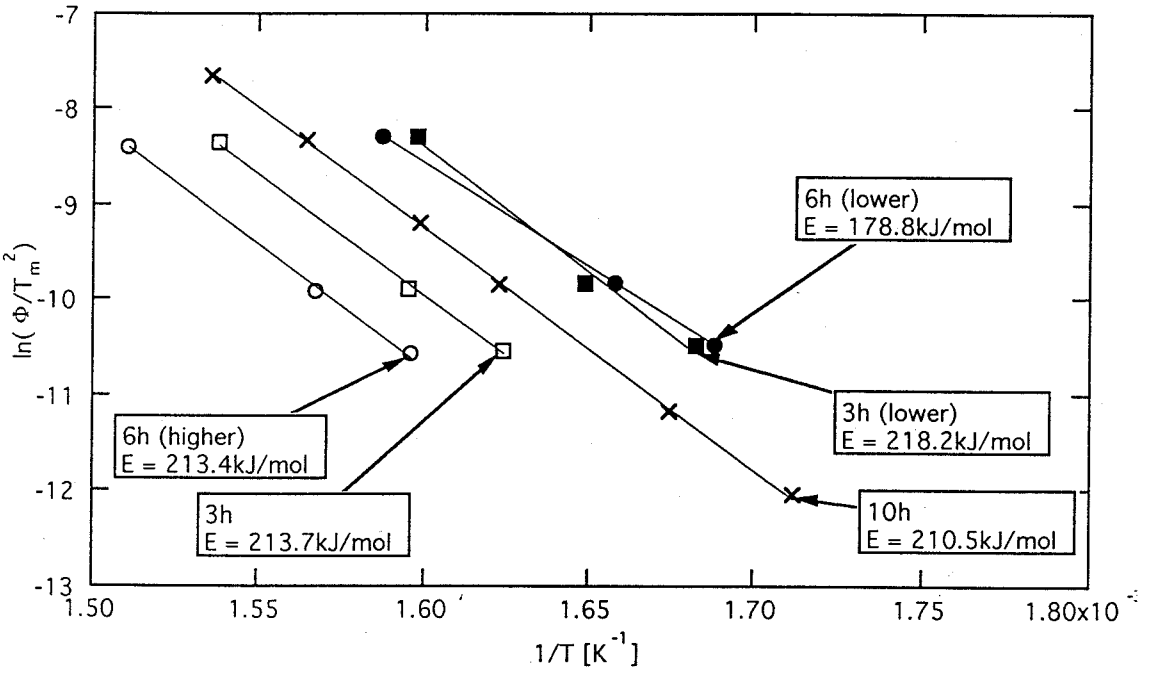

Fig. 3-7 Kissinger plot of $Ti_{90}Cu_{10}$ synthesized by ball milling for various duration.

the materials transform to more stable phases by extended milling. Nasu and Shingu [100] conducted Mössbauer measurement and reported that amorphous or other non-equilibrium phases occur during ball milling, which is destroyed by further milling. Their results include $FeSn_2$ formed near the grain boundaries in the early stage of mechanical alloying of Fe - Sn system.

Since contamination from a milling device increases with milling time, the changing effect of contamination along the microstructure evolution must be taken into account. In the Ti - Cu system, therefore, no attempt has been made to determine whether nanocrystalline structure is *metastable* or *pseudostable.*

3.3.2 *Compositional Effect on the Structure*

Phases and microstructure synthesized by ball milling strongly depends on the composition. The effect of Cu concentration on the final structure of Ti - Cu alloys, grain size and lattice parameter was investigated. Pure elemental Ti and Cu powders were mixed into the intended composition $Ti_{100-x}Cu_x$ ($0 \leq x \leq 15$) and subjected to the experiments. 2 g of powder is milled in one charge with BPR = 10.

XRD spectrum in Fig. 3-8 demonstrates that the amorphous phase occurs in samples with no less than 10 at.% Cu, and the fraction of the amorphous phase increases with increasing Cu content. The intensity ratio of remaining Bragg peaks, especially of Ti (002) to Ti (011), are close to the theoretical intensity of Ti (002)/Ti (011) in pure titanium, irrespective of the Cu concentration.

The change of grain size and the nearest neighbor distance is shown in Fig. 3-9. The grain size decreases with increasing Cu concentration. Although there is no reason that the grain size linearly decreases with Cu concentration, by

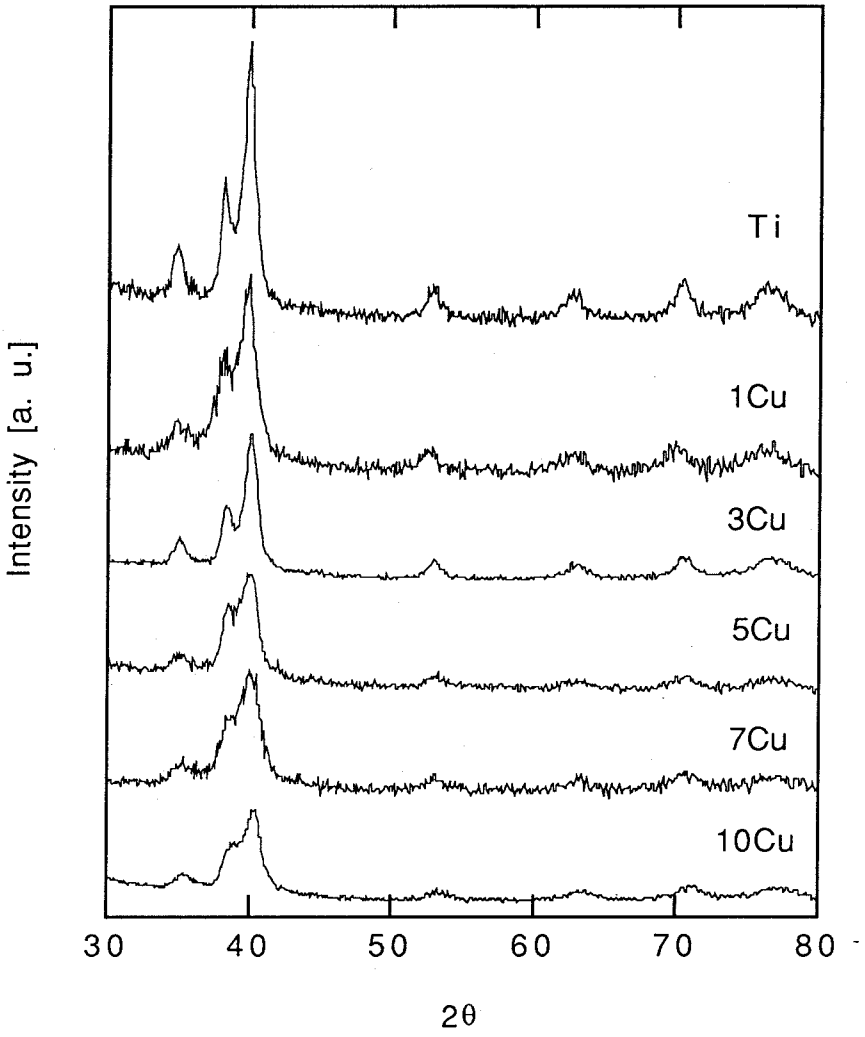

Fig. 3-8 XRD spectra of Ti - Cu alloys synthesized by ball milling.

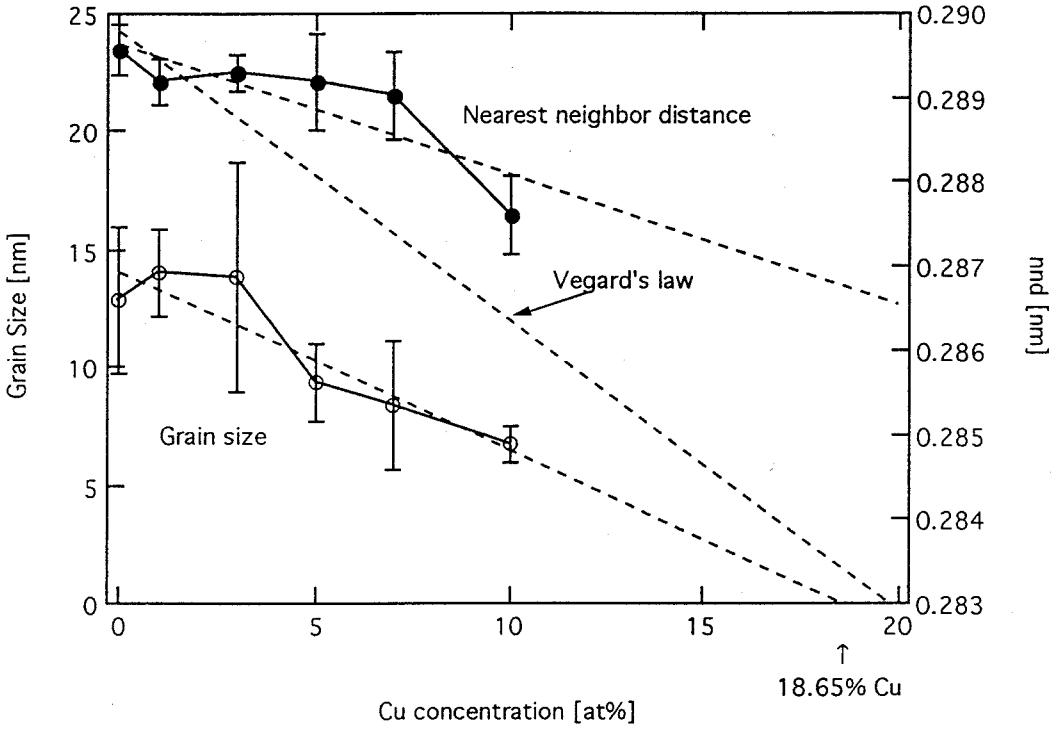

Fig. 3-9 The effect of Cu concentration on the grain size and nearest neighbor distance of Ti - Cu alloys synthesized by ball milling.

extrapolating the relation, one has Cu concentration of 18.65 at.% for zero grain size. In reality, for samples with more than 12 at.% Cu, the grain size cannot be estimated due to significant peak broadening by the amorphous phase. This tendency is found in some other systems such as Fe - Cu and Zr - Al [101, 102]. Interestingly, the final grain size of ball-milled pure Ti also obeys this relation. This topic will be discussed later. The nearest neighbor distance decreases also with increasing Cu concentration, however it deviates from Vegard's law in the positive direction. This infers that the real Cu concentration in the titanium lattice may be less than the nominal composition.

In the present study, grain boundary segregation is suspected on the basis of the deviation of nearest neighbor distance from Vegard's law. However, in reality, Vegard's law rarely holds for metallic systems [103]. Commonly observed deviation of interatomic distance from the Vegard's law in metallic systems is depicted in Fig. 3-10. The nearest neighbor distance tends to deviate toward negative side from Vegard's law by addition of smaller atoms, and positive by larger atoms. In the Ti - Cu system, Cu is smaller than Ti. Therefore negative deviation is expected.

The nearest neighbor distance of Ti - Cu alloys has been studied by a few researchers. Rizzo *et al.* [80] measured nearest neighbor distance in *fcc*, *hcp* and amorphous Ti - Cu alloys produced by sputtering, and compared them with data by other researchers. In the amorphous phase ranging from 16 to 74 at.% Cu, the nearest neighbor distance linearly decreases with increasing Cu concentration, and is about 1 - 3 % smaller than the values derived from Vegard's law, for compositions of more than 15 at.% of Cu. In metastable *fcc* solid solution, Vegard's law is obeyed in the composition range from 73 - 87 to 100 at.% Cu, depending on the target voltage. The behavior of the lattice parameter in *fcc* and

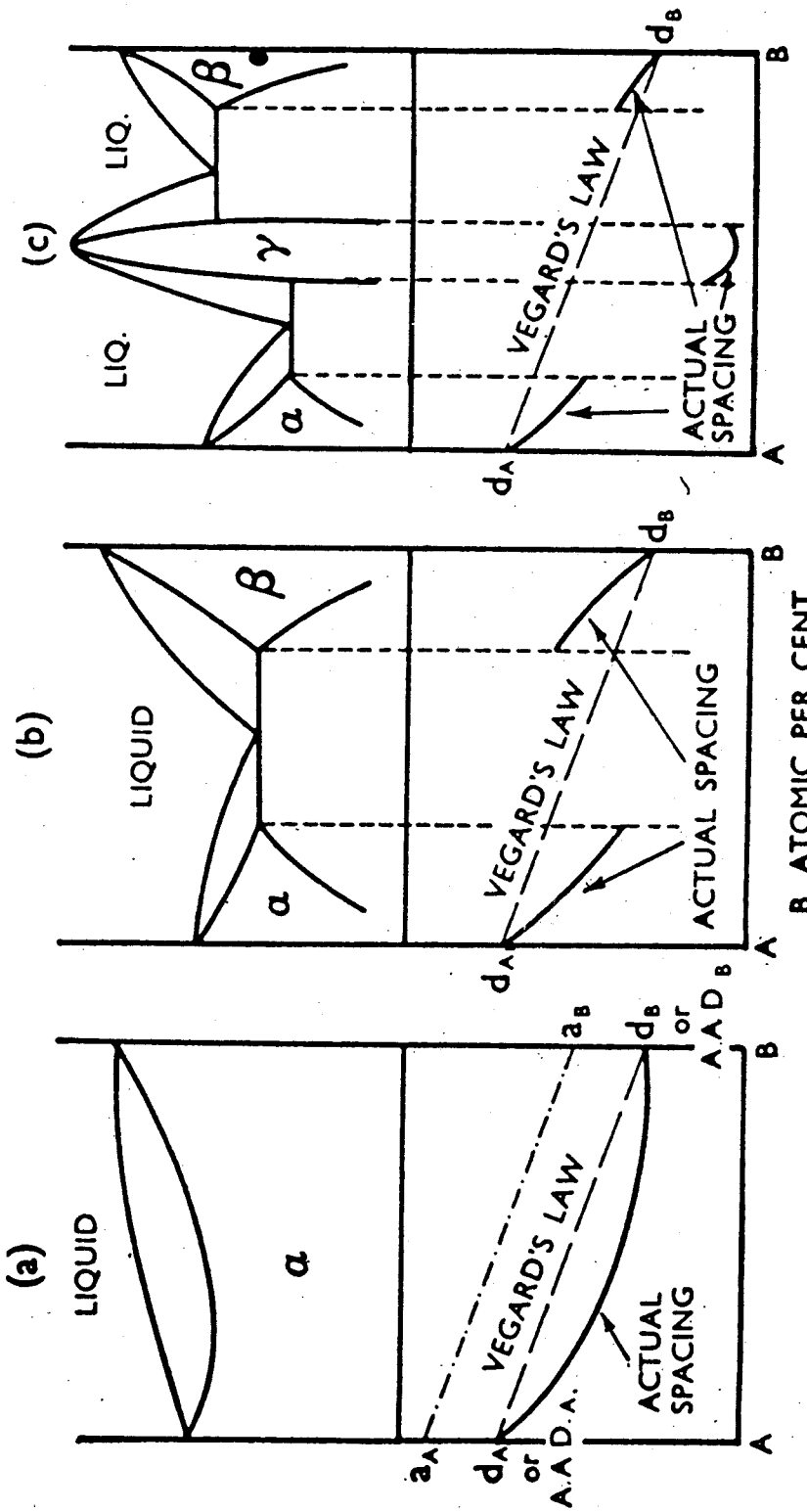

Fig. 3-10 The observed trends in the nearest neighbor distance of alloys [103].

nearest neighbor distance in amorphous are shown in Figs. 3-11 and 3-12, respectively. Outside this composition range, the nearest neighbor distance deviates from Vegard's law to the negative side by about 1.4 %. The lattice parameters of *hcp* phase in the mixture of amorphous and metastable *hcp* solid solution at 17 and 19 at.% Cu compositions deviate from those estimated by Vegard's law by ~1% to the positive side. This behavior may be attributed to the solute segregation in the amorphous phase. Tennover [104] showed that Fe concentration is higher in amorphous region than in crystalline region in rapidly quenched two-phase alloys.

The present study shows that the measured nearest neighbor distance is larger than those expected from Vegard's law bt about 1.5 %. Therefore, one may assume the real solute concentration is smaller than the overall concentration, so that the solute stoms segregate at grain boundaries.

3.3.3 *Effect of Starting State*

Seki and Johnson conducted ball-milling experiments of Ti - Cu intermetallic compounds [16]. The known facts include that $TiCu_2$ and Ti_4Cu_3 amorphize by ball-milling, but TiCu does not. Therefore an attempt to synthesize an amorphous phase by ball-milling mixture of intermetallic TiCu and pure Ti (or Cu) powders were performed in order to study the effect of grain boundary enrichment.

Pure elemental Ti or Cu and intermetallic compound TiCu powders (-100 mesh) were mixed into the intended composition $Ti_{100-x}Cu_x$ ($43 \leq x \leq 57$) and subjected to the experiments. 2 g of powder is milled in one charge with BPR= 10.

The time-transformation diagram of Ti - Cu alloys by ball milling is shown

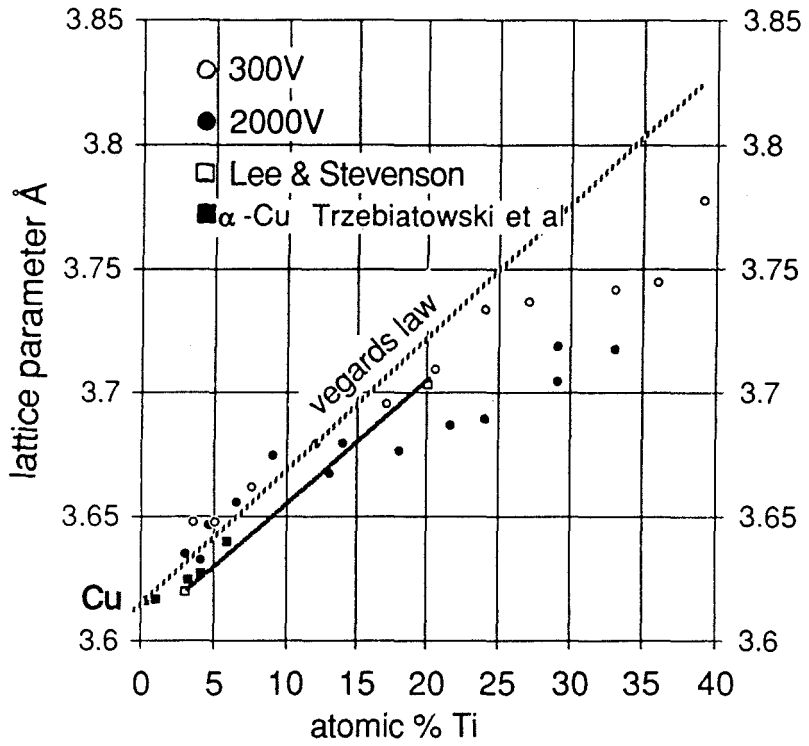

Fig. 3-11 Lattice parameter of *fcc* Ti - Cu alloys [80].

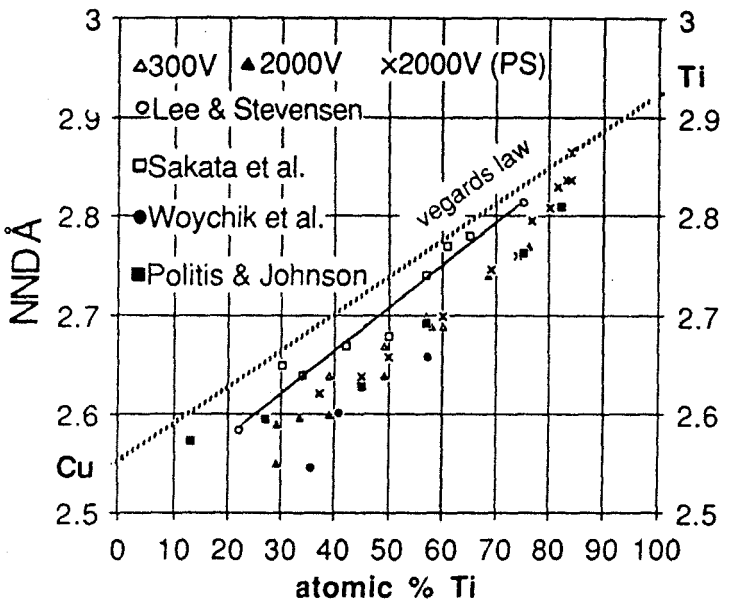

Fig. 3-12 Nearest neighbor distance of amorphous Ti - Cu alloys [80].

in Fig. 3-13 as a function of composition. The structure is supposed to settle down to a stable state in 20 hours of milling. The obtained structure was either amorphous or the mixture of amorphous and TiCu. Circles denote the first appearance of amorphous phase. Crystalline structure was preserved only for 48 at.% to 50 at.% Cu range.

It was found that even small amounts of additional Cu (or Ti) destabilizes the crystalline lattice of TiCu and causes crystal-amorphous transformation. Also the progress of amorphization strongly depends on the milling time and compositional deviation from TiCu: as the overall composition goes farther from $Ti_{50}Cu_{50}$, the structure reaches amorphous state faster. Therefore this amorphization reaction is thought to be diffusion-limited.

In addition, an interesting observation is that even in the compositional range where TiCu is thermodynamically stable, amorphous phase takes place by ball milling of the mixture. It should be noted here that $Ti_{50}Cu_{50}$ amorphizes by mechanical alloying of Ti and Cu [87], and intermetallic compounds TiCu never forms glass by mechanical grinding in spite of small compositional fluctuation so far as the overall composition is in the stoichiometry range, for more than 49 at.% and less than 51 at.% of Ti [105].

From this observation, it is suspected that the crystal - amorphous transformation in Ti - Cu is rather due to Cu (or Ti) enrichment at TiCu grain boundaries. In addition, since extra Cu is more effective than extra Ti for amorphization, it can be said that Cu enrichment destabilizes the lattice more effectively than Ti.

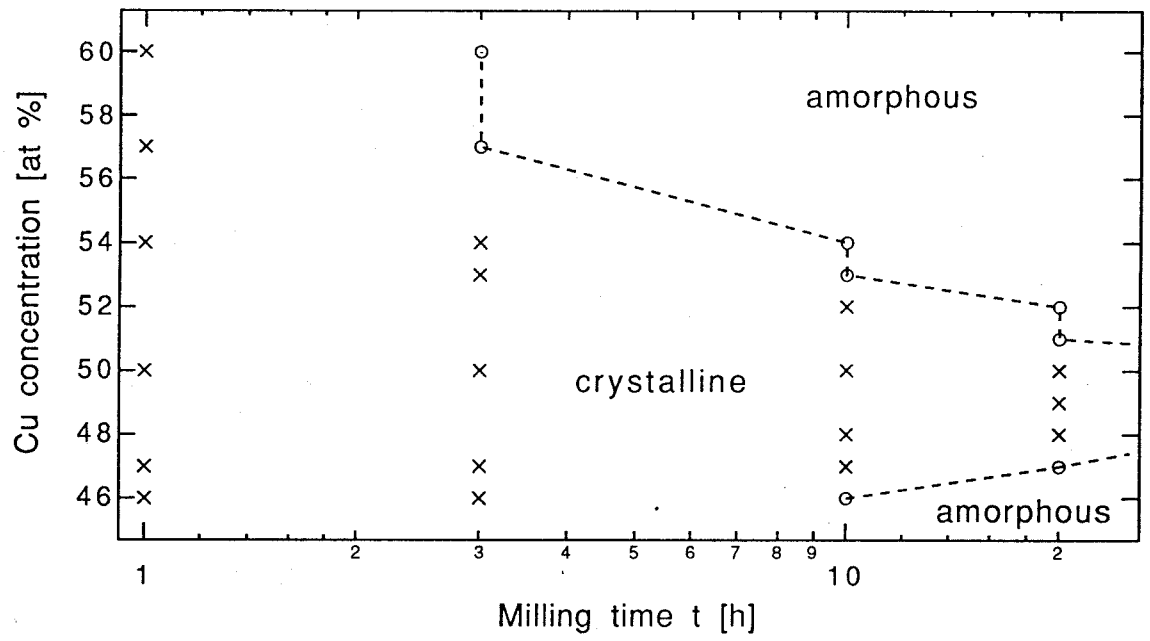

Fig. 3-13 Time-transformation diagram of Ti - Cu alloys by ball milling as a function of composition.

3.3.4 *Influence of Impurity*

As mentioned in the previous section, ball-milled Ti - Cu alloys contain about 0.25 at. % of Fe. Since Goldschmidt radius of Fe is about as large as Cu, the Fe atoms are supposed to behave as extra Cu. When the overall Cu content is as low as the impurity concentration, therefore, it is probable that the contamination affects the phenomenon.

In order to investigate the effect of contamination in the microstructure formation of the Ti - Cu system, a vial and balls made of pure titanium were prepared and employed for milling experiments of the Ti - Cu system. The vial was cut from commercial titanium bar, and the balls of about 12 *mm* diameter were prepared with a vacuum arc melter from 99.99% purity Ti chunks. Milling experiments were carried out under pure argon atmosphere with BPR = 5.

First, $Ti_{100-x}Cu_x$ ($0 \leq x \leq 20$) alloys were synthesized by mechanical alloying. Fig. 3-14 presents XRD spectra of as-milled powders. Chemical analysis indicates that typical ball-milled powder contains 0.005 at.% Fe. As such, metallic contamination is much less than milling in a steel vial. Grain size, atomic strain and the nearest neighbor distance are plotted in Figs. 3-15 and 3-16. The mechanism of alloying and microstructure formation is substantially the same as with steel milling device. Cu Bragg peaks diminish in 6 hours, and the grain size reaches a stable value of 10 *nm* in 6 hours. The nearest neighbor distance deviates from Vegard's law in positive direction, as seen in steel-vial experiments.

However, two significant differences were observed. At first, even after 40 hours of milling, no amorphous phase is seen in synthesized $Ti_{90}Cu_{10}$, while in steel-vial experiments with BPR = 10, a very small amount of amorphous phase occurs in 12 hours of milling. Second, although atomic strain continuously

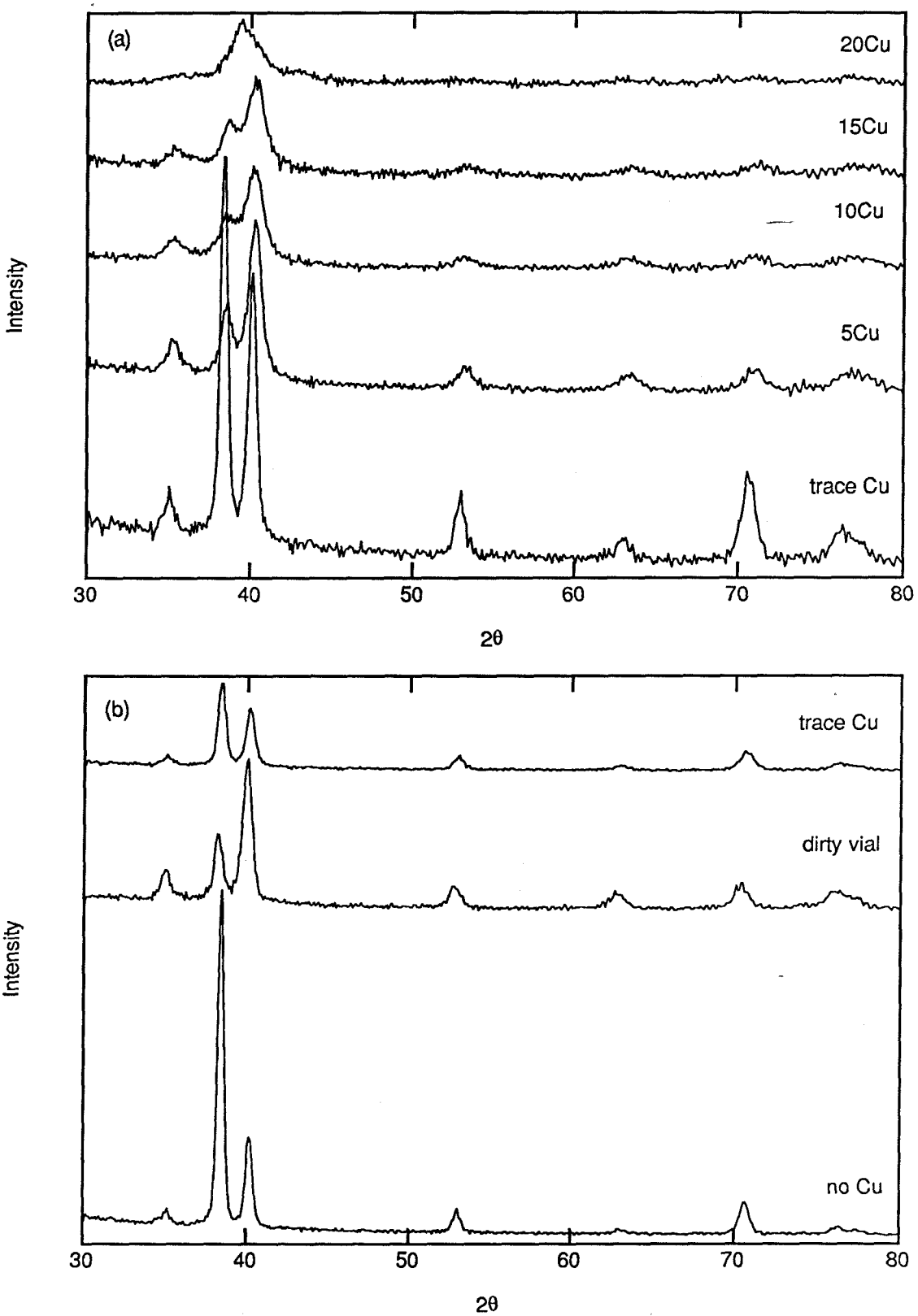

Fig. 3-14 XRD spectra of Ti - Cu alloys synthesized by ball milling processed for 10 hours with titanium milling device.

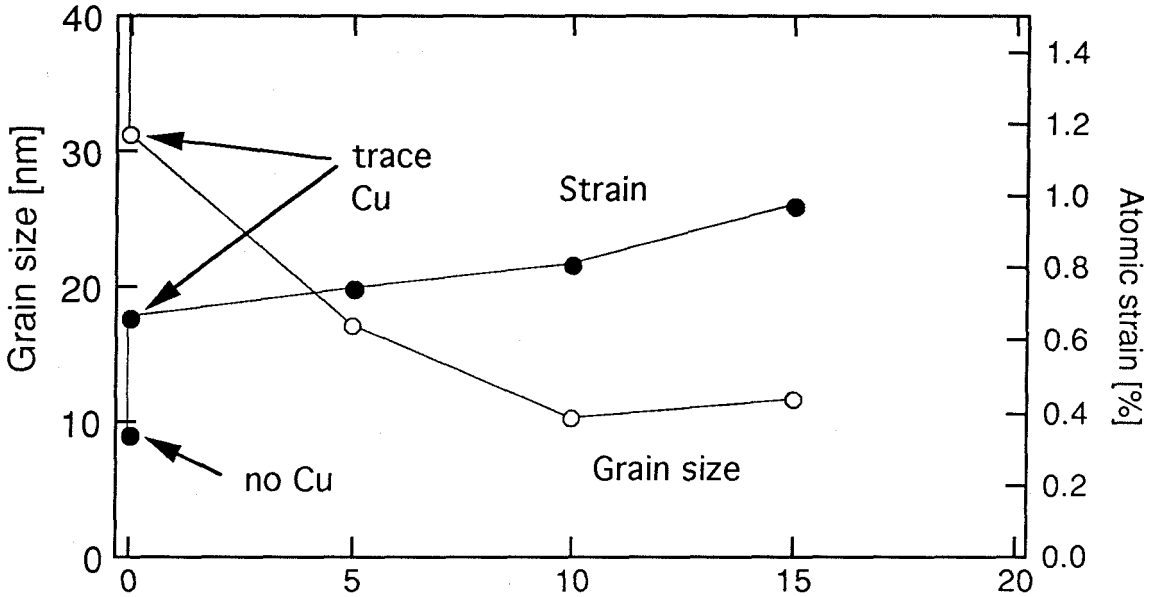

Fig. 3-15 Grain size and strain of $Ti_{90}Cu_{10}$ alloy synthesized by ball milling with a titanium device as functions of milling time.

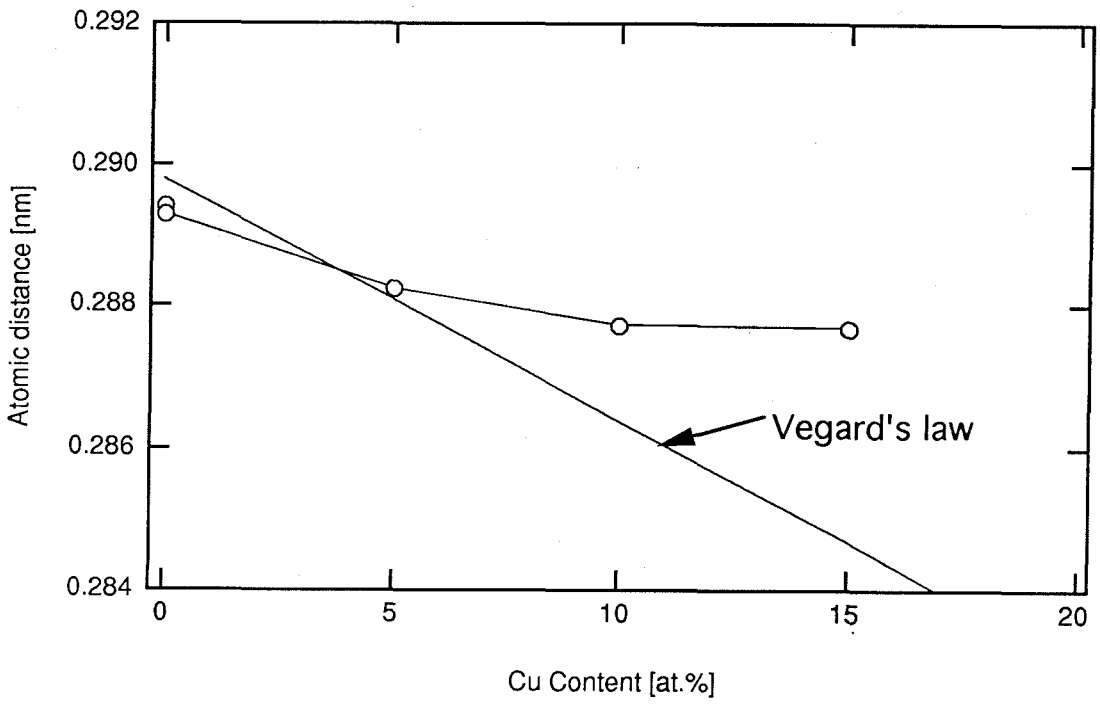

Fig. 3-16 Nearest neighbor distance of $Ti_{90}Cu_{10}$ alloy synthesized by ball milling with a titanium device as functions of milling time.

increases in steel-vial experiments, in Ti - vial experiments, it stays constant or gradually decreases after 10 hours of milling. This tendency agrees with the result of Hellstern *et al.* in the Ru - Al system [49]. The above differences are interpreted as follows:

(1) The overall composition tends to Ti - rich during milling because of wearing of titanium balls. On the contrary, in steel vial experiments, iron wear debris drives the system to Cu - rich side. Hence atomic strain decreases during milling in Ti vial, and increases in steel vial.

(2) Momentum transferred from balls to the material, namely impact energy by titanium balls are smaller than by steel balls due to the smaller density. Therefore the amorphizatiion of $Ti_{90}Cu_{10}$ becomes harder in titanium milling device, and easier in steel device.

Judging from the above, the effect of iron contamination is not critical in ball milling of Ti - Cu alloys.

However, it is not the case for ball milling of pure titanium. Milling experiments for Ti - Cu alloys with a very small amount of Cu (or *no* Cu) revealed quite different results. All the material was welded onto the vial wall, so that no powder was obtained. The stuck material peeled off the Ti vial indicating a large grain size: no nanocrystalline structure. Furthermore, when milled in a "dirty" atmosphere, such as with moist Ti vial or under air, nanocrystalline Ti powder was produced with no sticking.

Another interesting observation in Fig. 3-14 is that Ti (002) peak is very intense in ball milled pure Ti in a titanium vial, which is not the case with a steel vial. This reminds us of profound Ti (002) peak in the first hour of ball milling

(Fig. 3-2). This is due to the characteristic of deformation of titanium, since in the first hour of milling, not much atomic mixing is expected, and the deformation may be mainly inside pure titanium powder particles.

This phenomenon is interpreted that titanium is pretty rigid in (001) direction, and the deformation is highly concentrated in the hexagonal layers, which are the *close-packed* plane of *hcp* structure. Thus, due to stretch and curtail of atomic spacings in (001) plane, the Bragg peaks diffuse and lower, except for (002).

DSC spectra shown in Fig. 3-17 demonstrates that titanium powder ball milled in the titanium vial stores virtually no energy. As its grain size is as big as the starting state, no grain growth takes place. Comparing ball-milled pure Ti with ball-milled Ti - Cu, one finds the entropy contribution by adding small fraction of Cu atoms in pure Ti, and dislocation density. In pure metals, dislocation pinning is not likely because no atomic strain field exists in the crystal lattice. Dislocations march smoothly through the material to the surface, hence grain refinement hardly takes place. The entropic part is usually negligibly small, therefore it is inferred that the defect accumulation such as grain boundaries and dislocations is the most significant role in energy storing in ball milled powder.

Fecht *et al.* reported the formation of nanocrystalline structure of pure *bcc* and *hcp* metals such as Cr, Nb, W, Co, Zr, Hf and Ru using a steel vial and balls [44]. Eckert *et al.* [45] prepared nanocrystalline *fcc* metals using steel device. No study has been conducted to confirm the effect of iron contamination on the formation of nanocrystalline or amorphous structures.

However, Fecht *et al.* mention in the above study that pure nanocrystalline Fe can be produced using steel milling device. Also nanocrystalline Fe has been

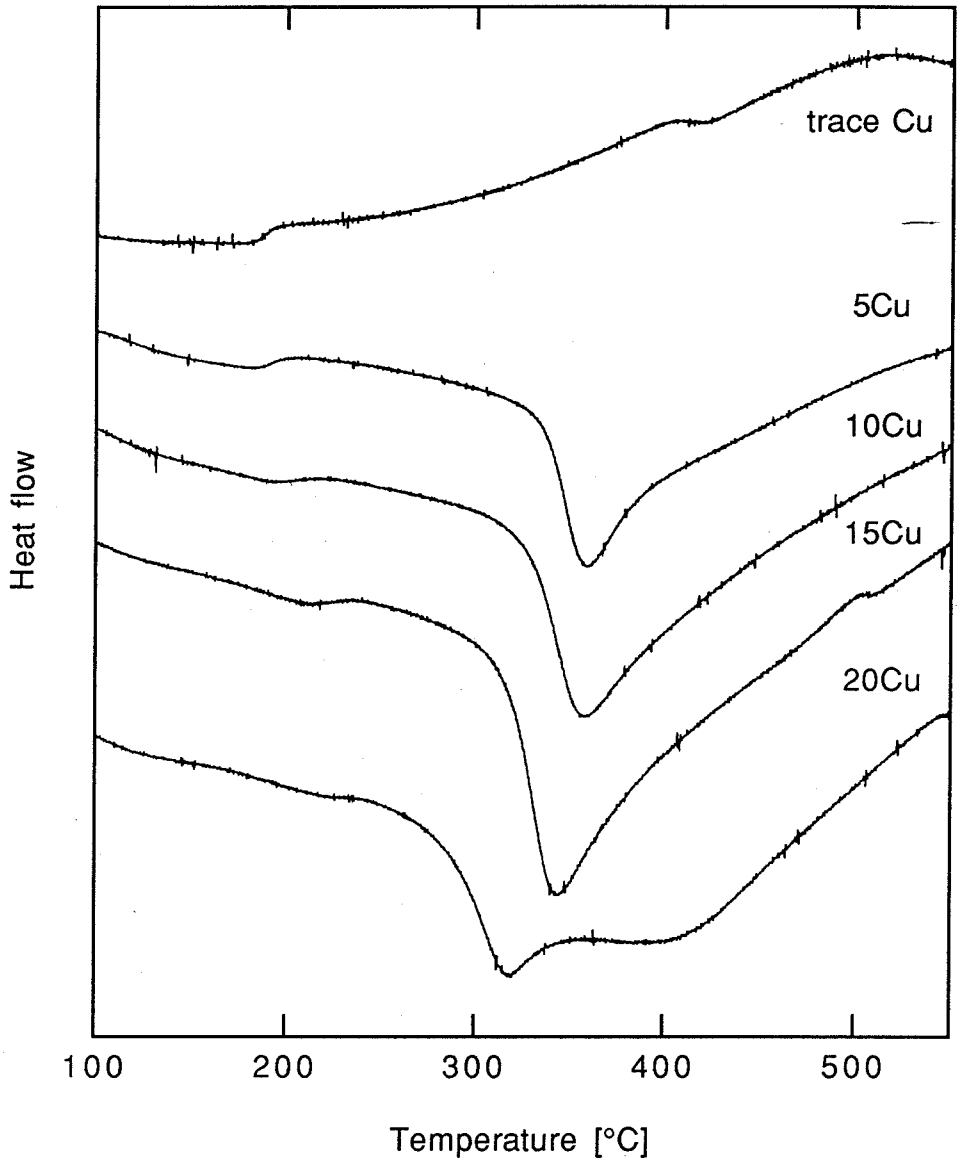

Fig. 3-17 DSC spectra of Ti - Cu alloys synthesized by ball milling with titanium milling device.

prepared by ball milling of Fe powder [100, 106]. Therefore the synthesis of nanocrystalline pure metals must be possible by ball milling. Nevertheless the present result implies that the contamination such as Fe, O, N is critical for nanocrystalline structure formation.

3.4 Nanocrystalline structure of $Ti_{90}Cu_{10}$

In order to investigate the property of nanocrystalline structure and its thermodynamic stability, nanocrystalline $Ti_{90}Cu_{10}$ was synthesized by mechanical alloying of Ti and Cu powders, and its microstructure was studied. Mechanical alloying was carried out by 10 hours of ball milling with SPEX mill. 2 g of powder was milled so that BPR was set to 10.

3.4.1 Microstructure Observation

1. TEM Study

Hitachi H-800 200kV STEM with EDAX was employed. As-milled $Ti_{90}Cu_{10}$ powder was crushed into finer particles using a mortar and a pestle, then scattered onto a Cu mesh coated with collodion. Then carbon was deposited on the mesh to prevent from charge-up. In addition, ball-milled powder was rolled to thin foil in the same fashion as preparing SAXS sample, then subjected to ion milling so that a large thin area was obtained.

As mentioned previously, XRD traces give the steady grain size of 6 - 8 nm in samples after 10 hours of milling. TEM pictures of as-milled powder shown in Fig. 3-18 indicate that the microstructure is relatively homogeneous and the grain size looks uniform, although the grains are not spherical. Fig. 3-19 shows the microstructure of typical annealed powder. Diffraction pattern indicates large

grains exist. Grain size appears bigger and relatively uniform after grain growth. The grain size measured from the TEM pictures of as-milled powder is compared with that from XRD analysis. Values derived by both methods yield reasonable agreement. Therefore it is assumed that the grain size calculated from XRD spectra reflects the real grain size.

2. SAXS Study

The Ti - Cu system is also adopted for SAXS experiments. The objective of these experiments is to study the structure of grain boundaries. The detail of experimental procedure has been discussed in the previous chapter.

1. Mechanically Alloyed Ti - Cu

Mechanically alloyed $Ti_{95}Cu_5$ powders were consolidated and polished into thin foils of about 50 μm thickness. The density of the foils were measured to be 90 - 95 % of the theoretical density of solid solution calculated from the specific volume. Therefore we assume that the prepared samples contain negligible porosity. Indeed, no visible porosity was found by optical microscope observation of the foil. Nanocrystalline structure is seen in the XRD spectrum in Fig. 3-20, which indicates that the microstructure is not altered by consolidation and polishing.

The Porod plot of SAXS of $Ti_{95}Cu_5$ ball milled for 10 hours is shown in Fig. 3-21. There are two distinct regions with respect to the slope. At lower q range, the slope is about -3, while at higher q range it is about -2.5. This result implies diffuse grain boundaries. Since the slope in the Porod plot changes around $q \sim 0.05$, it is suspected that the diffuse boundary ranges for narrower than $1/q$, namely, 20 Å.

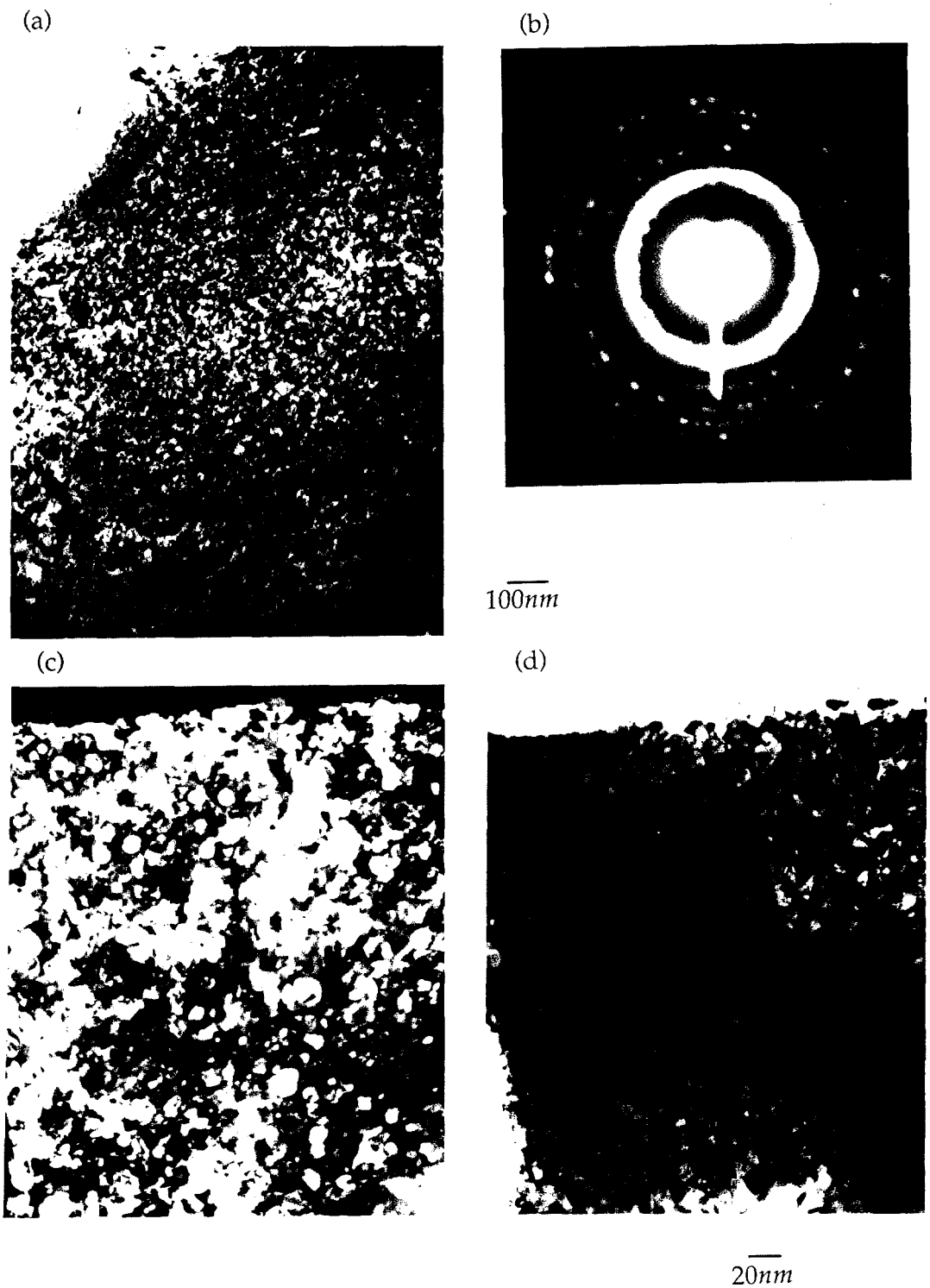

Fig. 3-18 TEM pictures of as-milled $Ti_{90}Cu_{10}$ powder. Fine uniform grains fill the space. Grain boundaries look relatively sharp in these pictures. (a), (b) bright field image, (c) diffraction pattern, (d) dark field image.

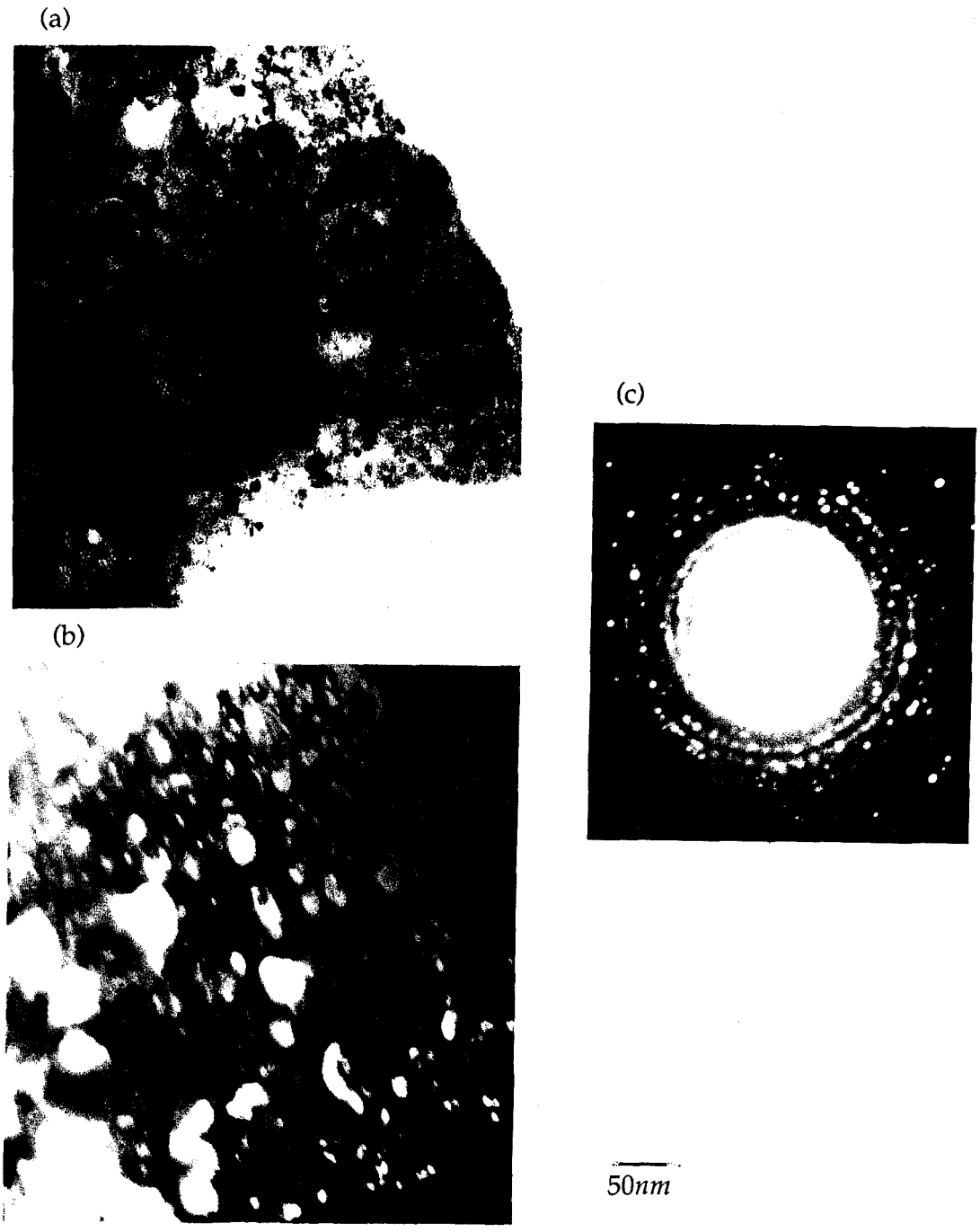

Fig. 3-19 TEM pictures of $Ti_{90}Cu_{10}$ powder after grain growth by heating at 600 °C. Most grains have uniformly grown. (a) bright field image, (b) dark field image, (c) diffraction pattern.

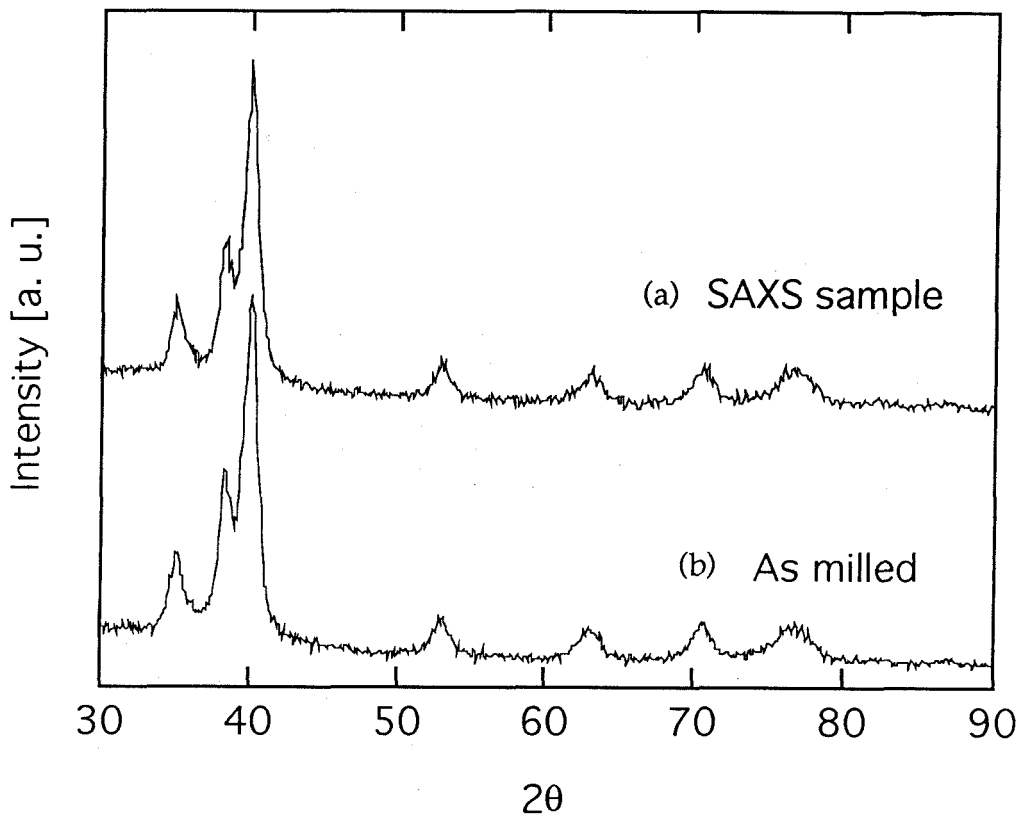

Fig. 3-20 XRD spectra of $Ti_{95}Cu_5$ alloy synthesized by mechanical alloying. (a) Consolidated and polished to thin film for SAXS experiment, (b) as milled, . The grain size is about 15nm and does not change by consolidation.

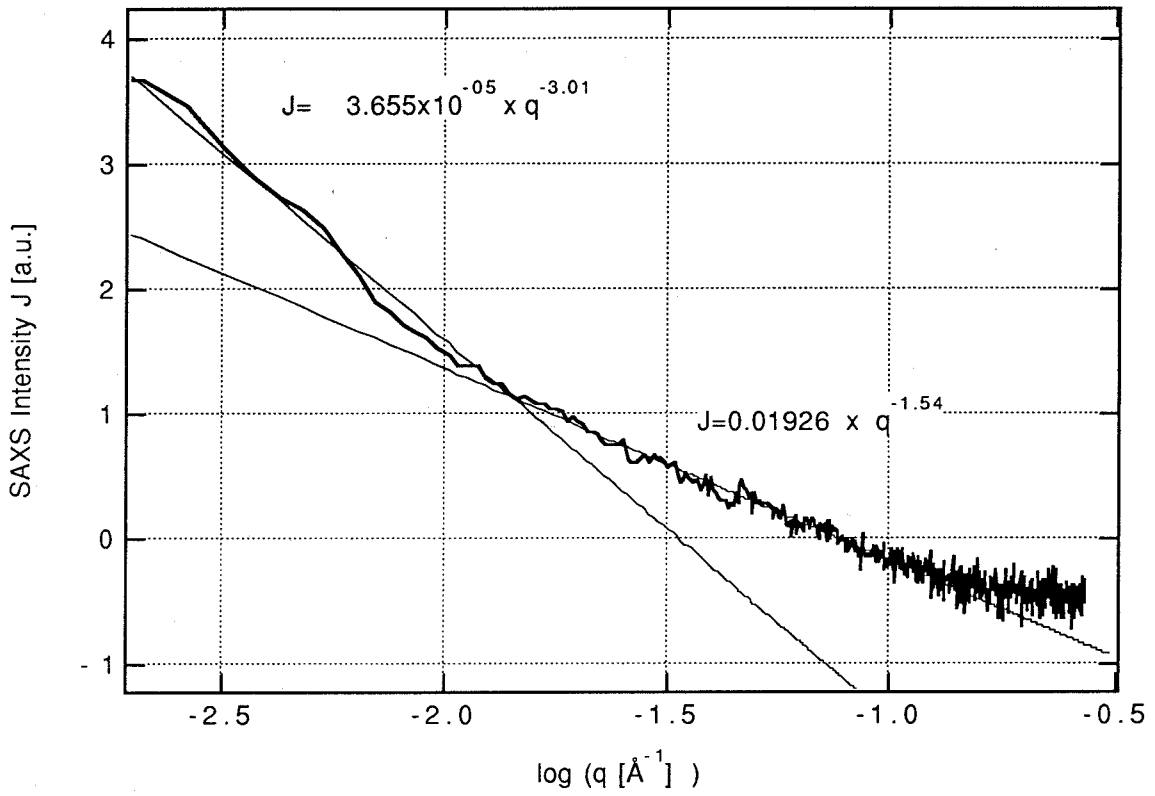

Fig. 3-21 SAXS spectra of $Ti_{95}Cu_5$ synthesized by ball milling.

2. Mechanically Ground Intermetallic Ti - Cu Compounds

Intermetallic compound TiCu and Ti_4Cu_3 are ball milled with a SPEX mill for 20 hours and SAXS experiments were carried out. SAXS spectra are shown in Figs. 3-22 and 3-23. Relatively higher slope is observed in the lower q region in both samples. This implies equiaxed grains, and probably the "*gaseous*" structure at grain boundaries suggested by Jorra *et al.* [63]. Again a steeper region with a slope of -3 is found in the higher q region of the spectrum of the TiCu samples. This demonstrates that the Porod law is obeyed and the interface of each crystal grains are quite sharp.

However, this characteristic is not seen in the Ti_4Cu_3 samples. This spectrum shows rather straight lines in mid-high q regions, with a slope of about -1.9. Therefore it is suspected that the interfaces between crystal grains form somehow diffuse boundaries in the Ti_4Cu_3 structure. Indeed, the XRD spectrum in Fig. 3-24 demonstrates that an amorphous phase exists in ball milled Ti_4Cu_3. Therefore it is suspected that the amorphous phase occurs at Ti_4Cu_3 grain boundaries.

The latter results may imply that an amorphous-like structure exists at grain boundaries of ball milled $Ti_{95}Cu_5$ nanocrystalline structure.

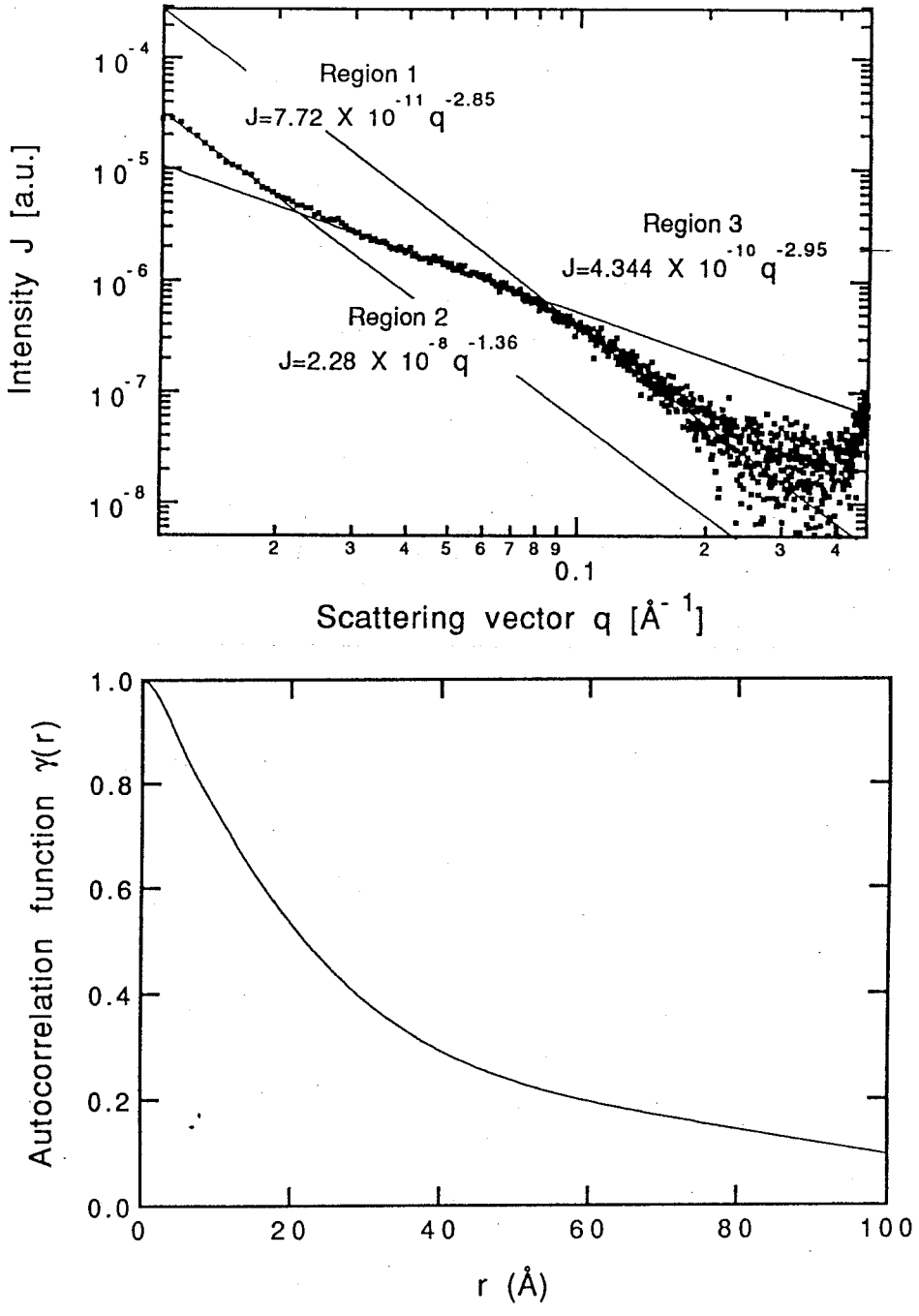

Fig. 3-22 SAXS spectra of ball-milled intermetallic TiCu. (a) Porod plot, (b) correlation function.

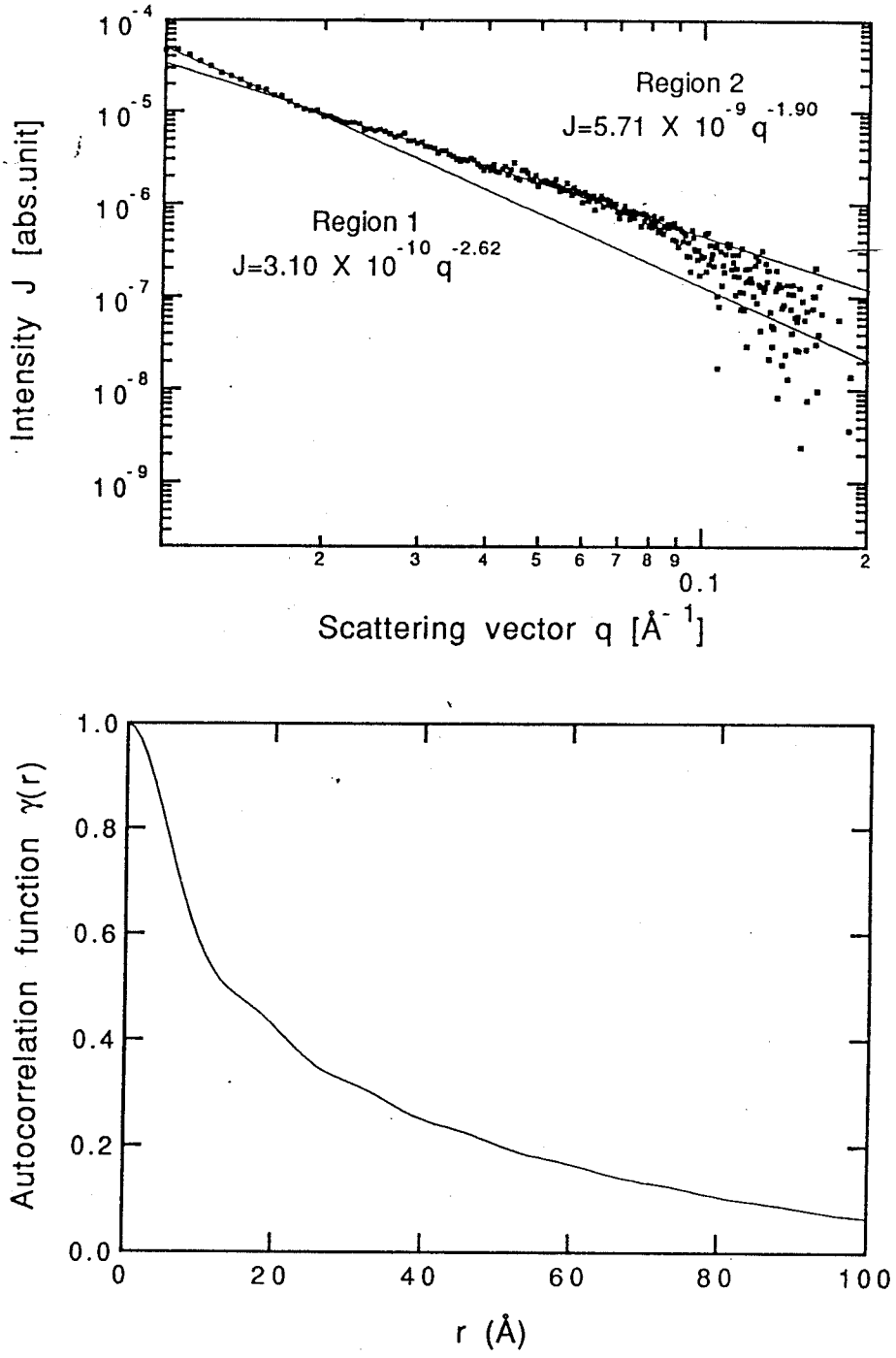

Fig.4 Correlation function

Fig. 3-23 SAXS spectra of ball-milled intermetallic Ti_4Cu_3. (a) Porod plot, (b) correlation function.

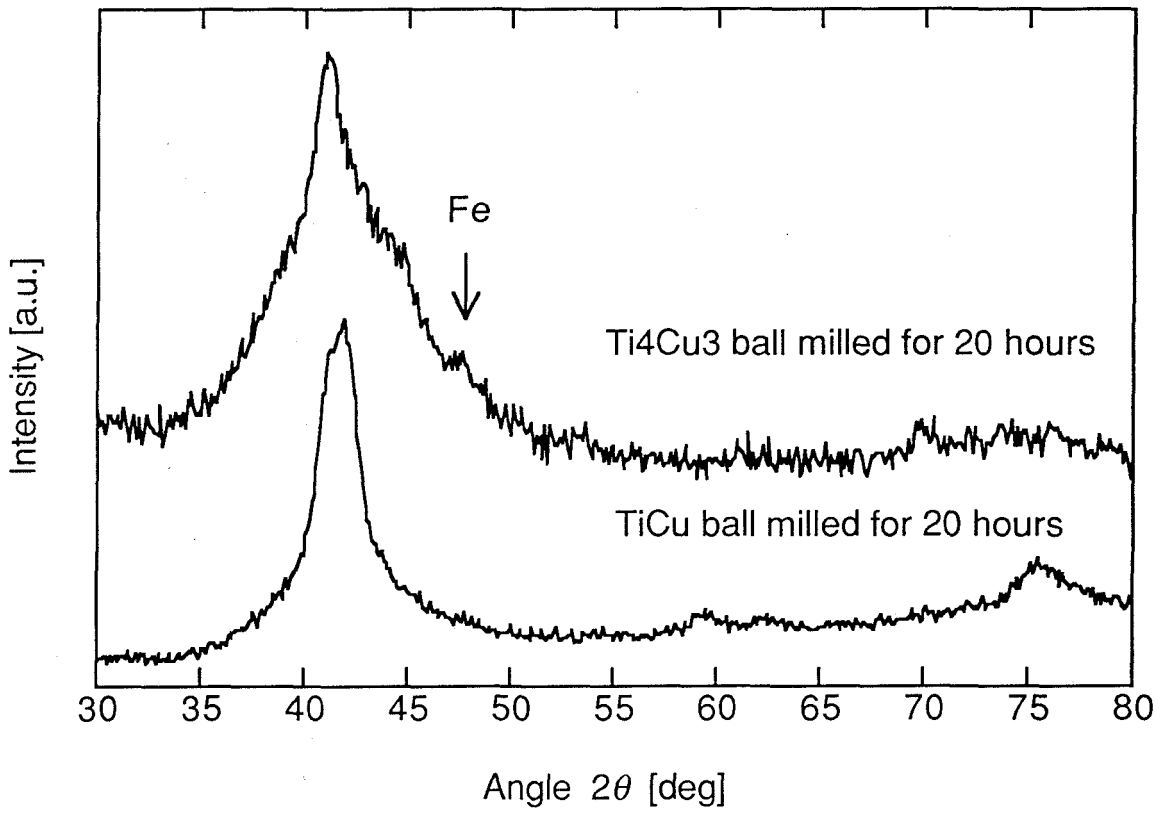

Fig. 3-24 XRD spectra of ball-milled TiCu and Ti_4Cu_3, consolidated and thinned for SAXS experiments.

3.4.2 *Grain Growth Behavior*

$Ti_{90}Cu_{10}$ powder synthesized by mechanical alloying was heated and annealed at various temperatures, and the thermal stability of nanocrystalline structure of $Ti_{90}Cu_{10}$ has been studied with XRD, thermal analysis and TEM.

1. Heating

Fig. 3-25 demonstrates the structural evolution of ball milled $Ti_{90}Cu_{10}$ heated at a heating rate of 20 °C/min to the indicated temperatures and quenched. The system tends to the equilibrium structure by heating. Broadened Bragg peaks by small grain size and large amount of strain sharpen. No structural transformation is observed. Only slight peak sharpening is seen in the spectra heated to temperatures below 450 °C. At 350 °C, peaks from intermetallic compound Ti_2Cu become visible. After heated to 600 °C, the structure goes to the equilibrium structure; the mixture of Ti and Ti_2Cu.

1. Grain Growth and Strain

Grain size and strain of ball milled $Ti_{90}Cu_{10}$ are plotted versus temperature heated in Fig. 3-26. Strain starts being relaxed by heating at a low temperature, and decreases monotonously. Then grain growth takes place at about 400 °C. Although the grain size remains at about 50 *nm*, this value is not reliable any longer since the Bragg peak width is too narrow. One should note that the nucleation of intermetallic compound Ti_2Cu precedes the grain growth.

2. Lattice Parameters

Lattice parameters of heated powders shown in Fig. 3-27 expand as the nucleation of Ti_2Cu starts, finally reaching to the value of pure Ti, as expected

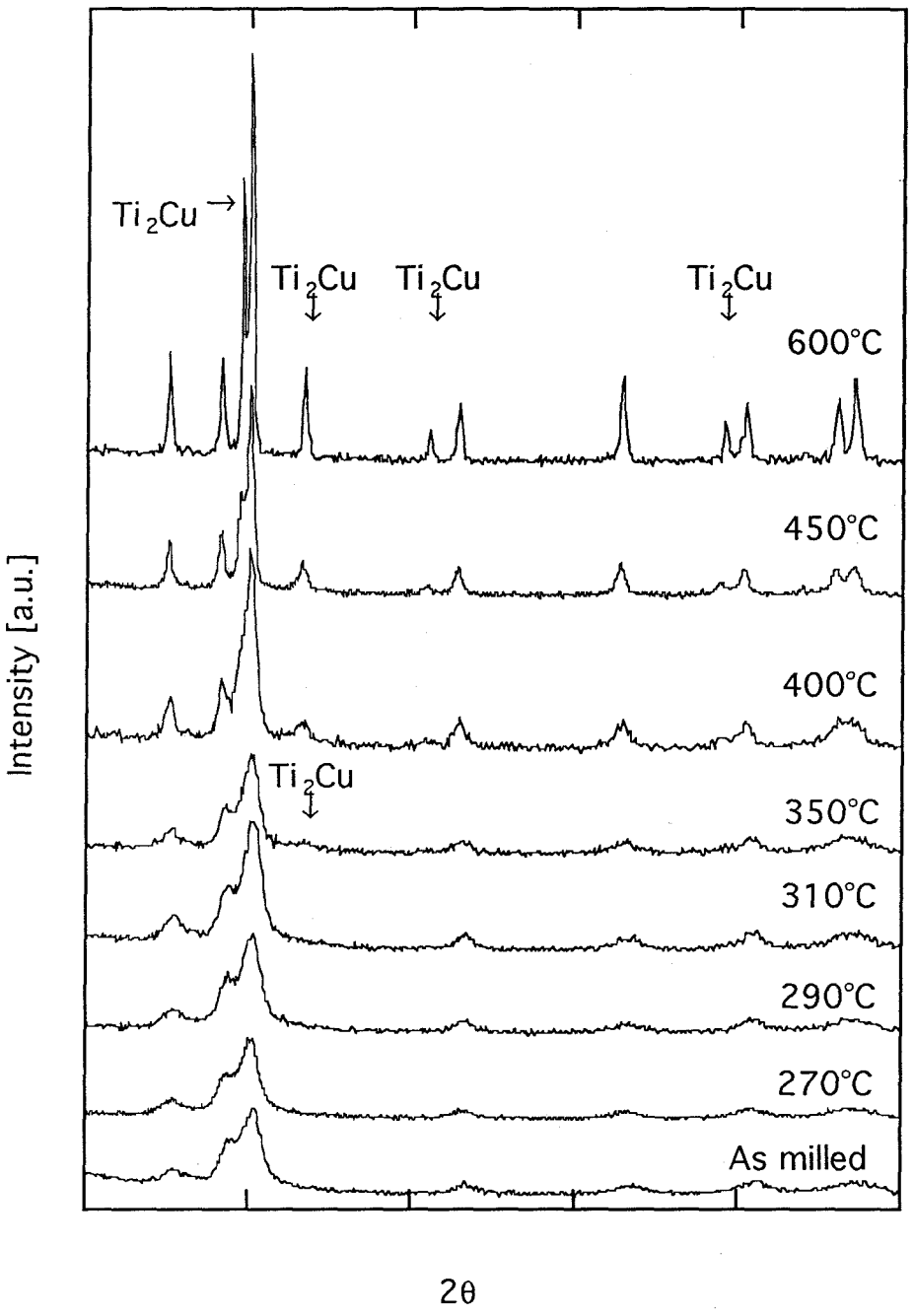

Fig. 3-25 XRD spectra of $Ti_{90}Cu_{10}$ powder synthesized by ball milling and heated to the indicated temperatures. Ti_2Cu is detected as the sample is heated at 350 °C.

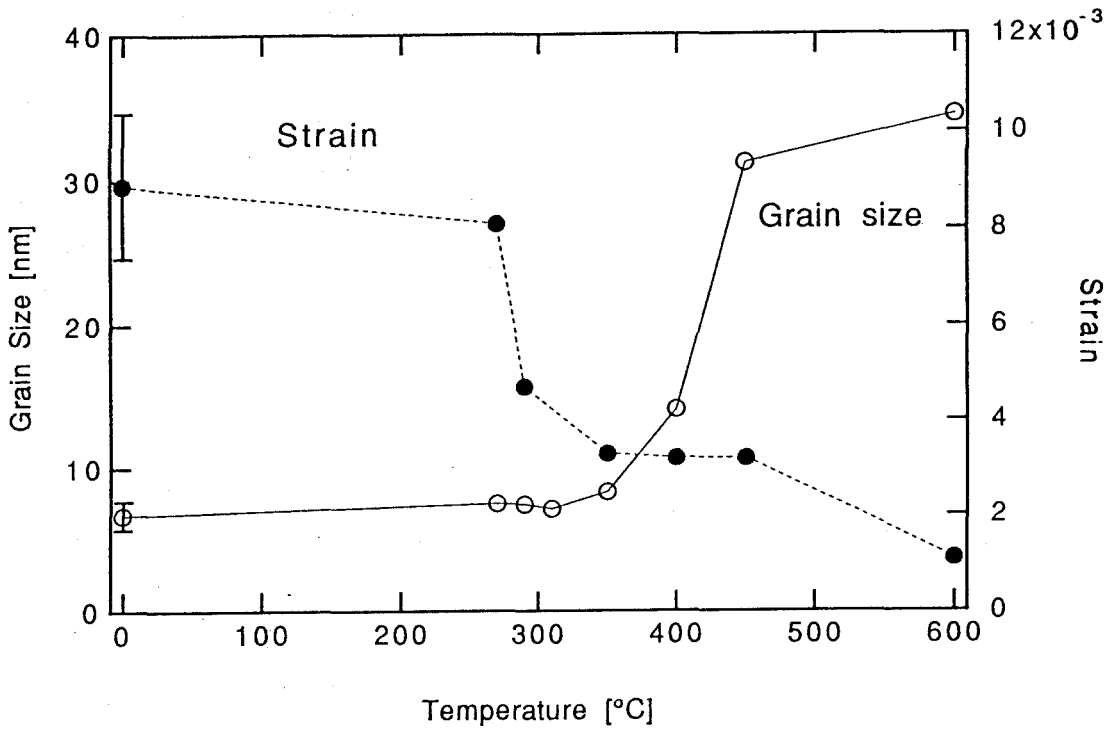

Fig. 3-26 Change of the grain size and strain of $Ti_{90}Cu_{10}$ powder produced by ball milling and heated to the indicated temperatures.

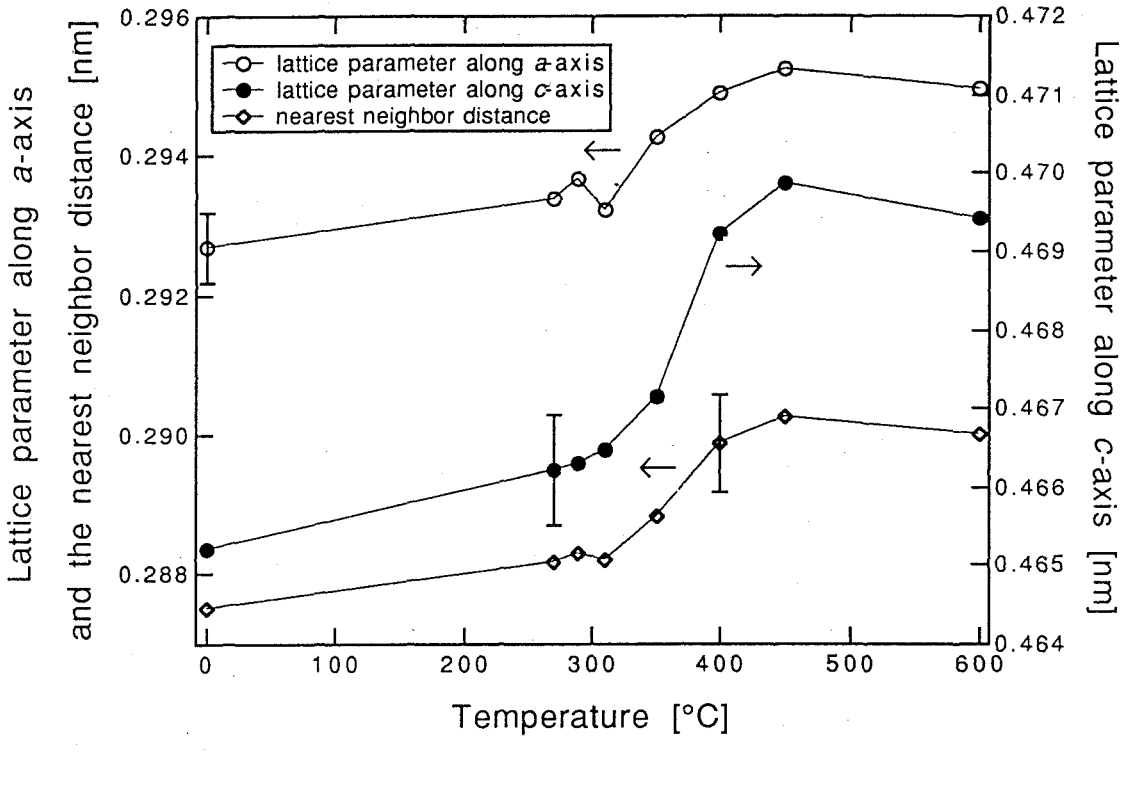

Fig. 3-27 Change of the nearest neighbor distance of $Ti_{90}Cu_{10}$ powder produced by ball milling and heated to the indicated temperatures.

from the small equilibrium solubility of Cu in α-Ti.

2. Annealing

Microstructural evolution with isothermal annealing is studied with XRD. Fig. 3-28 shows XRD spectra of annealed powders. The grain size change is estimated and shown in Fig. 3-29. Nanocrystals do not grow significantly at 250 °C and 270 °C even after 5 hours of annealing, and average grain size remains around 7 - 8 *nm*. At the higher temperatures, grain growth begins in 1 hour at 290 °C and in 0.5 hour at 310 °C. Ti_2Cu peaks are not observed in XRD spectra of samples annealed at 250 °C. Ti_2Cu peaks appear in 5 hours for samples annealed at 270 °C, in 1 hour at 290 °C and in 0.5 hour at 310 °C.

Thus the appearance of Ti_2Cu peaks and grain growth take place at the same time, or the latter follows the former. Again, it can be said that the nucleation of Ti_2Cu precedes the grain growth. Nearest neighbor distance, shown in Fig. 3-30, extends by annealing, in the similar fashion to the grain size, however in shorter time. It is implied that solute atoms are purged from crystal lattice ahead of grain growth.

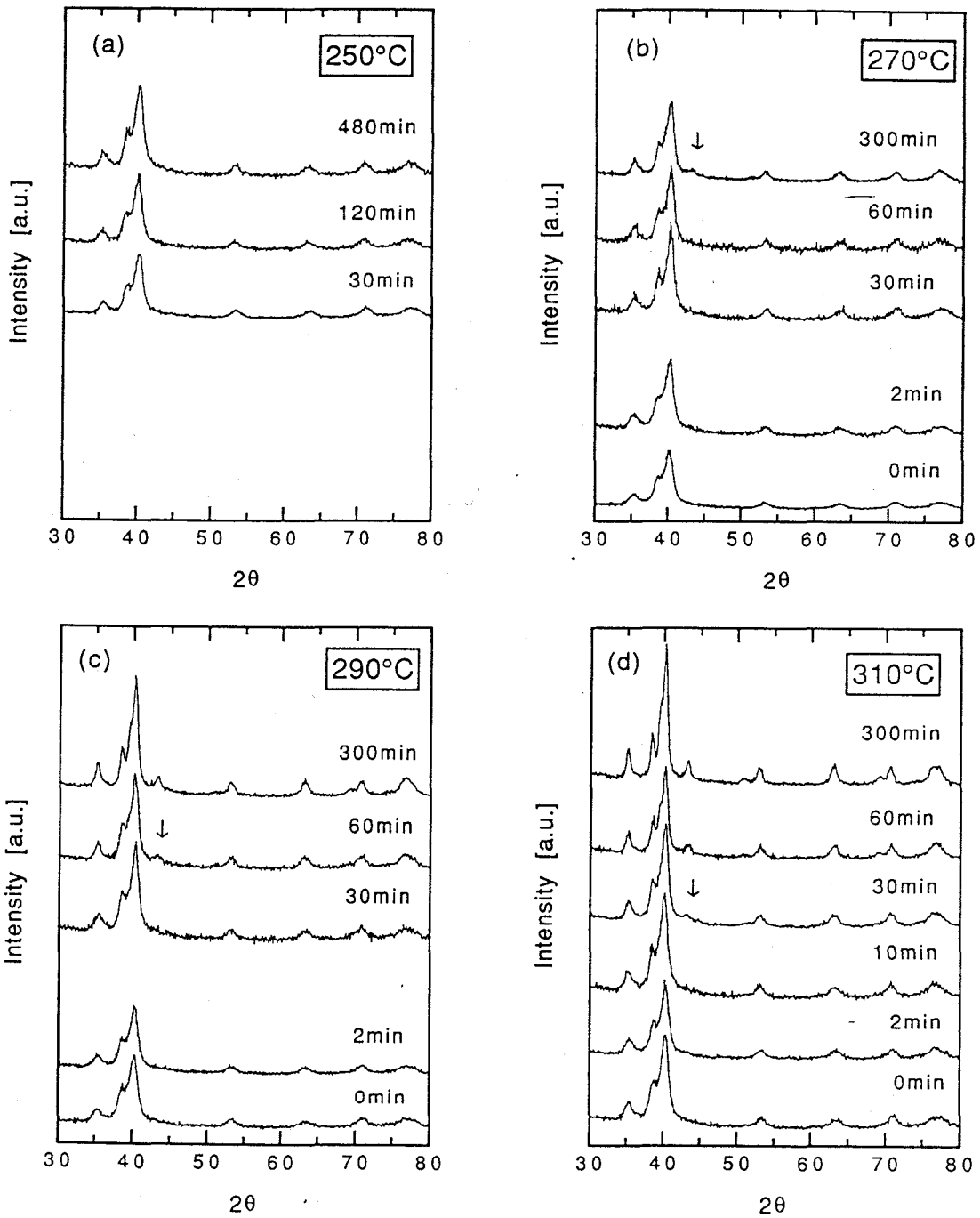

Fig. 3-28 XRD spectra of $Ti_{90}Cu_{10}$ powder produced by ball milling and annealed at the indicated temperatures for the indicated duration.

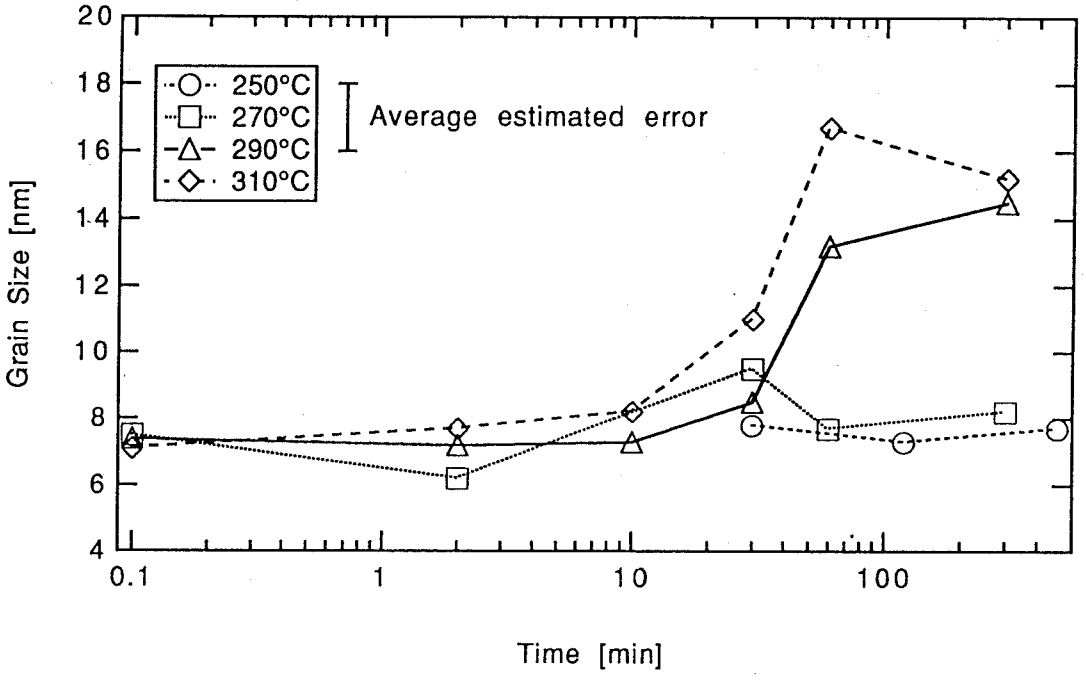

Fig. 3-29 Change of the grain size and strain of $Ti_{90}Cu_{10}$ powder produced by ball milling and annealed at the indicated temperatures for the indicated duration.

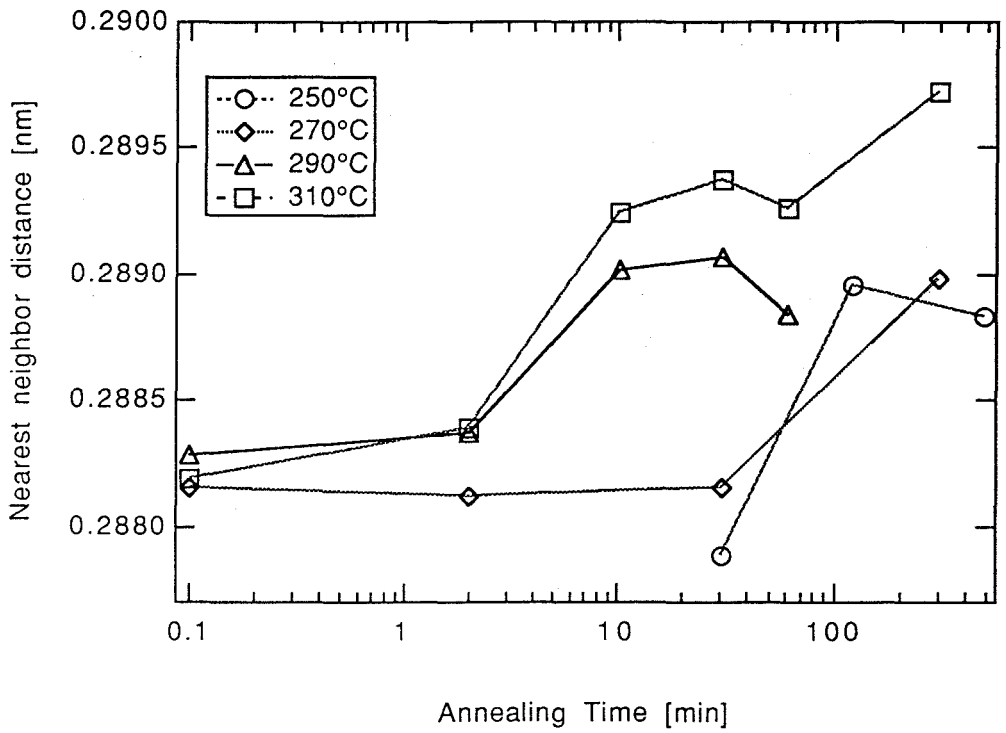

Fig. 3-30 Change of the nearest neighbor distance of $Ti_{90}Cu_{10}$ powder produced by ball milling and annealed at the indicated temperatures for the indicated duration.

3.5 Further Research -- Zr Addition

3.5.1 *Background*

Both Zr and Ti belong to group IV - B, therefore resemble in the physical properties such as the crystal structure. Ti and Zr form an approximately ideal solid solution exhibiting complete miscibility, also intermetallic compounds in Zr - Cu have the same structures as corresponding compounds in Ti - Cu. On the other hand, the Goldschmidt radius of Zr is bigger than that of Ti by about 9 %. Hence extra Zr atoms enhance size mismatch between the solute and the solvent. Therefore it is speculated that it becomes easier for the matrix to store more strain, and pin a larger number of dislocations, thus the nanocrystalline structure becomes more stable. Indeed, the glass formability of the Ti - Zr - Cu system by rapid quenching techniques is reported to be much wider than in the Ti - Cu system [107], which implies the Ti - Zr - Cu system stores higher energy than the Ti - Cu system, and the crystal lattice of the former system is less stable than the latter.

3.5.2 *Experimental*

The procedure for the synthesis of (Ti, Zr) - Cu alloys is just the same as for the Ti - Cu system, except that pure elemental Zr powder (99.9% purity, -200 mesh) was blended together. The molar fraction of Cu was kept to 10 at. % so that a part of Ti atoms are replaced by Zr. As such, the overall composition is $(Ti_{1-x}Zr_x)_{90}Cu_{10}$, where $0 < x \leq 0.15$.

3.5.3 *Effect of Zr Addition*

XRD spectra of (Ti, Zr) - Cu alloys synthesized by ball milling for 20 hours are shown in Fig. 3-31. Peak broadening is more significant than Ti - Cu alloys,

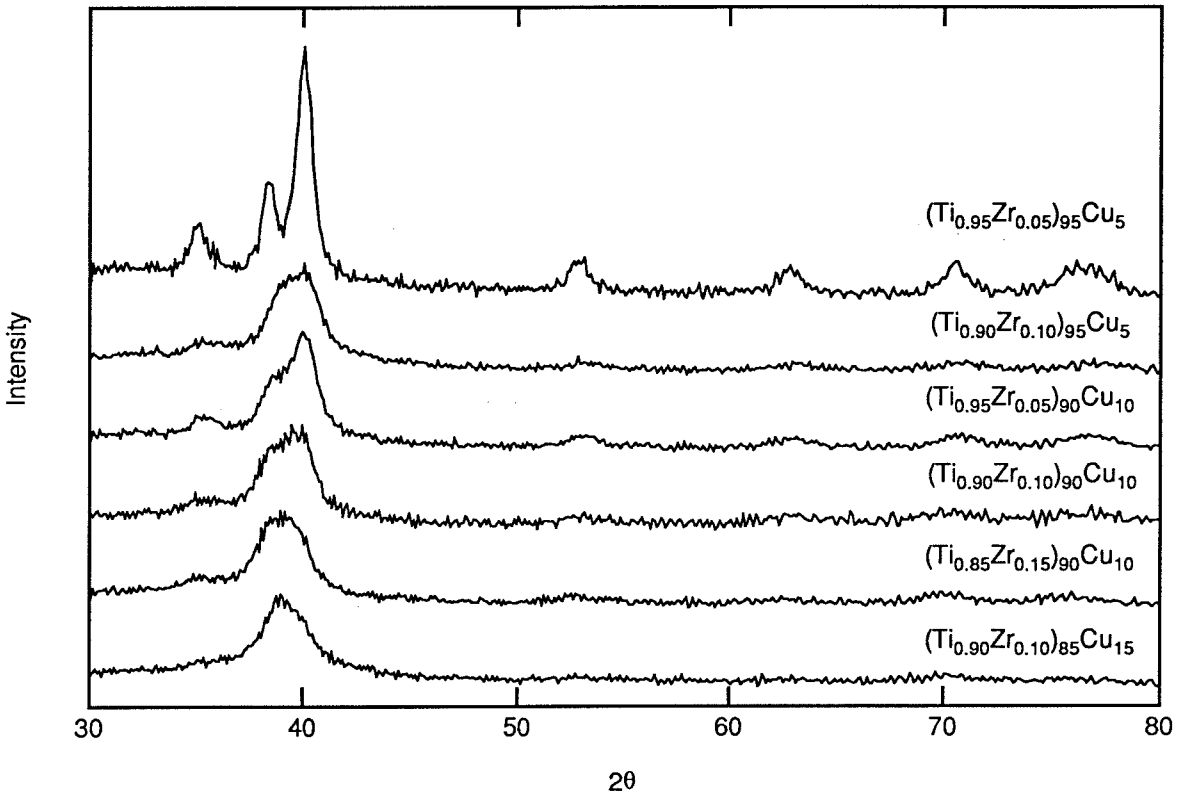

Fig. 3-31 XRD patterns of (Ti, Zr) - Cu alloys synthesized by ball milling.

demonstrating that some amount of amorphous phase exists. However, since Bragg peaks are still observed, the majority should be nanocrystalline structure.

Grain size and nearest neighbor distance of $(Ti_{1-x}Zr_x)_{90}Cu_{10}$ are shown in Figs. 3-32. Grain size decreases with increasing Zr concentration, while lattice parameter expands. These are interpreted due to more lattice mismatch. Thus the replacement of a part of Ti by Zr makes some effect on the formation of nanocrystalline structure. Since materials containing higher Zr tend to amorphize easier, more energy may be stored in the structure when Zr is added.

3.5.4 *Grain growth behavior*

DSC spectra of (Ti, Zr) - Cu samples in Fig. 3-33 show only one exothermic peak like Ti - Cu. Therefore Zr atoms are thought to be distributed uniformly and affect the formation and grain growth of nanocrystalline structure. However, the peak shift to higher temperature than Ti - Cu.

XRD spectra of heated $(Ti_{0.9}Zr_{0.1})_{90}Cu_{10}$ powder is shown in Fig. 3-34. α-Ti and an intermetallic compound phase occurs on heating. The latter has the same structure as Ti_2Cu, with expanded lattice spacing. This phase is supposed to be $(Ti, Zr)_2Cu$. The behavior of grain size, strain and nearest neighbor distance in Figs. 3-35 and 3-36 is about the same as in Ti - Cu system. However, the reaction temperatures shift up by about 100 °C. The activation energies were estimated by Kissinger analysis. The peak temperature and activation energy is the monotonically increasing function of Zr concentration, as shown in Fig. 3-37.

The replacement of a part of Ti by Zr affects the grain growth behavior. DSC experiments of ball-milled (Ti, Zr) - Cu samples revealed similar profile to Ti - Cu. That is, the nucleation of intermetallic compound and the grain growth

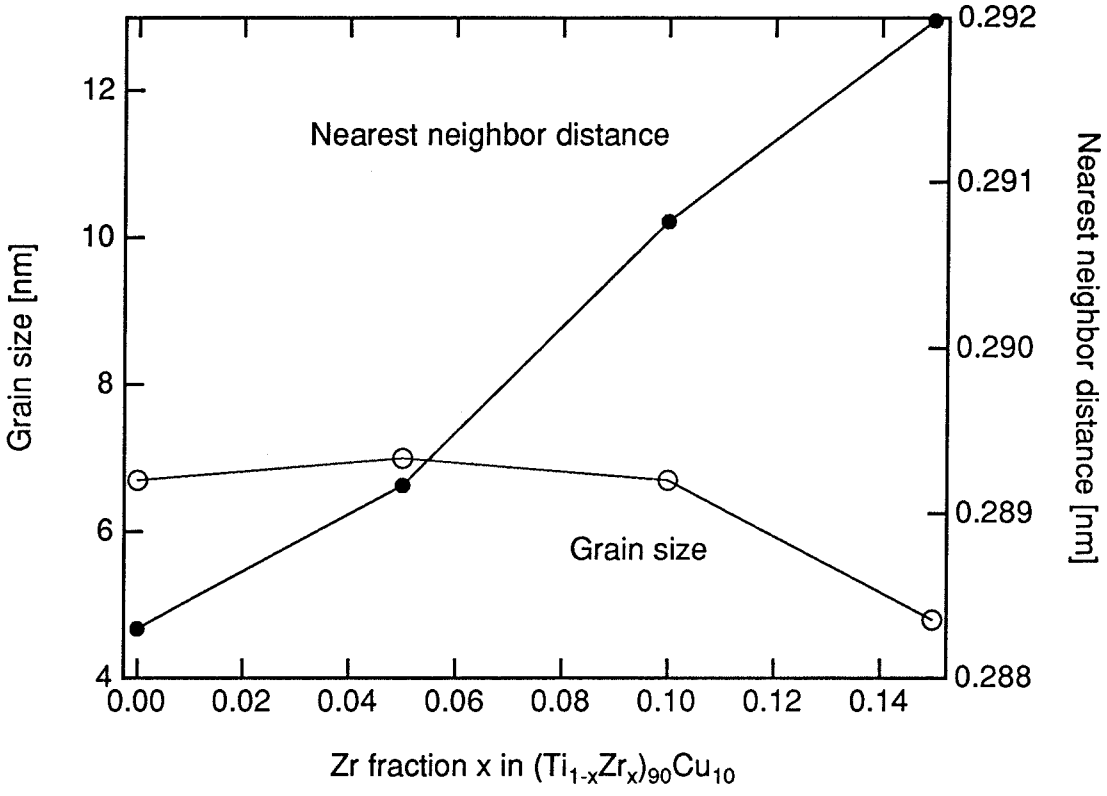

Fig. 3-32 Grain size and nearest neighbor distance of $(Ti_{1-x}Zr_x)_{90}Cu_{10}$ synthesized by ball milling.

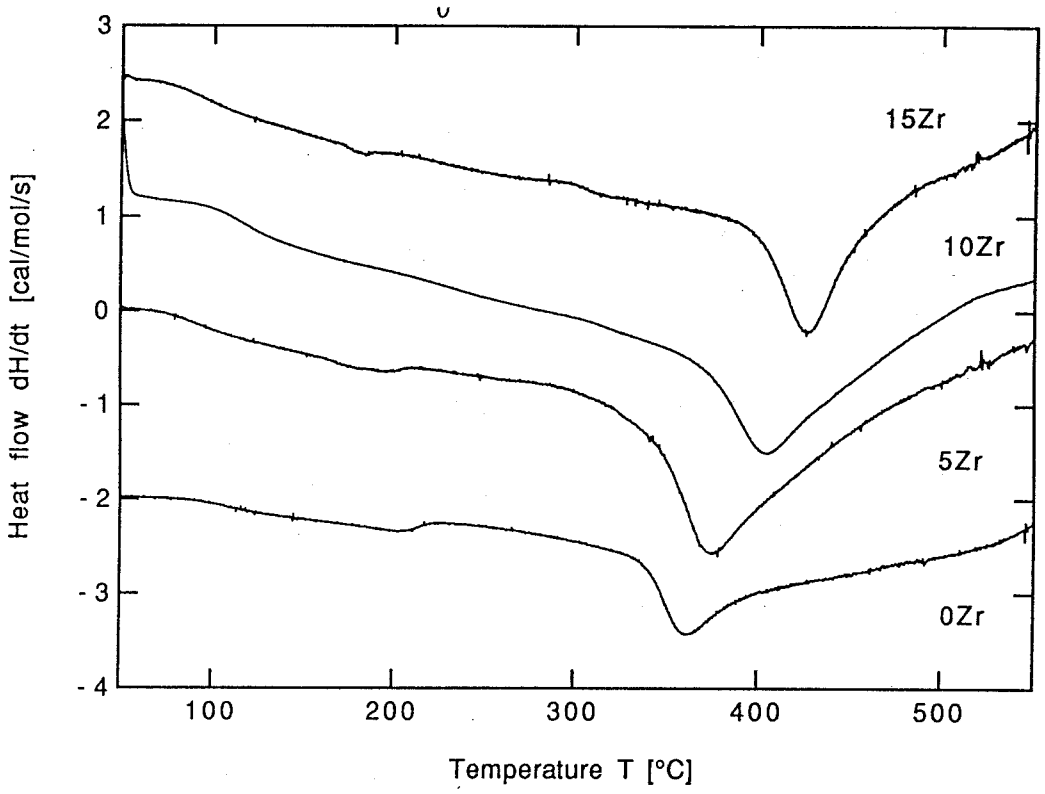

Fig. 3-33 DSC spectra of $(Ti, Zr)_{90}Cu_{10}$ alloys synthesized by ball milling.

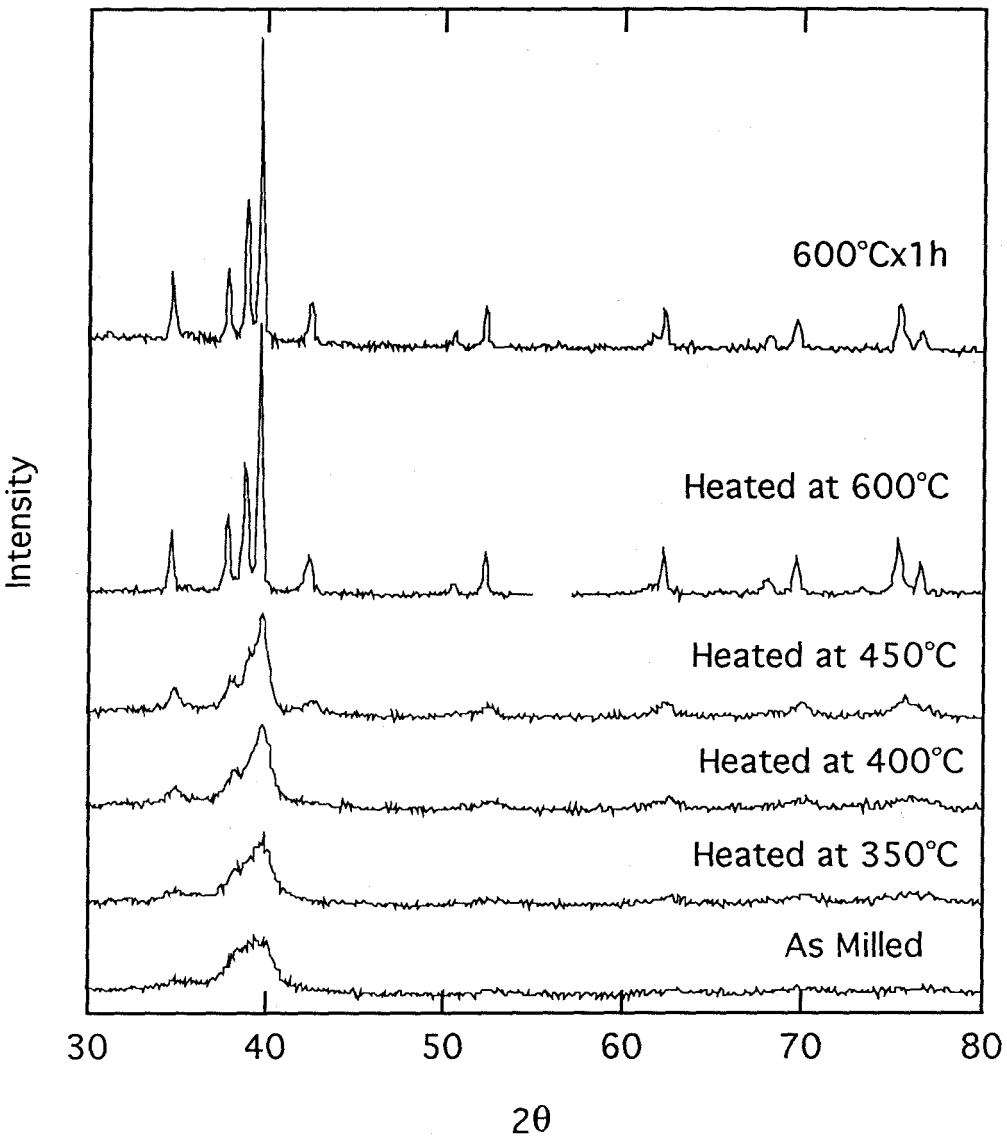

Fig. 3-34 XRD spectra of $(Ti_{0.9}Zr_{0.1})_{90}Cu_{10}$ powder synthesized by ball milling and heated to the indicated te,peratures.

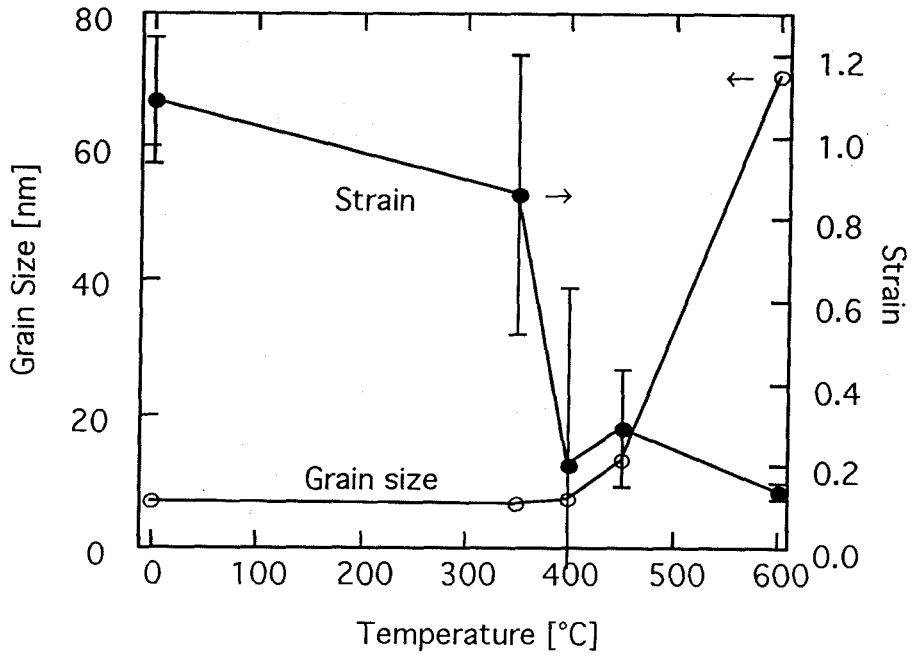

Fig. 3-35 Grain size and strain of $(Ti_{0.9}Zr_{0.1})_{90}Cu_{10}$ powder synthesized by ball milling and heated to the indicated temperatures.

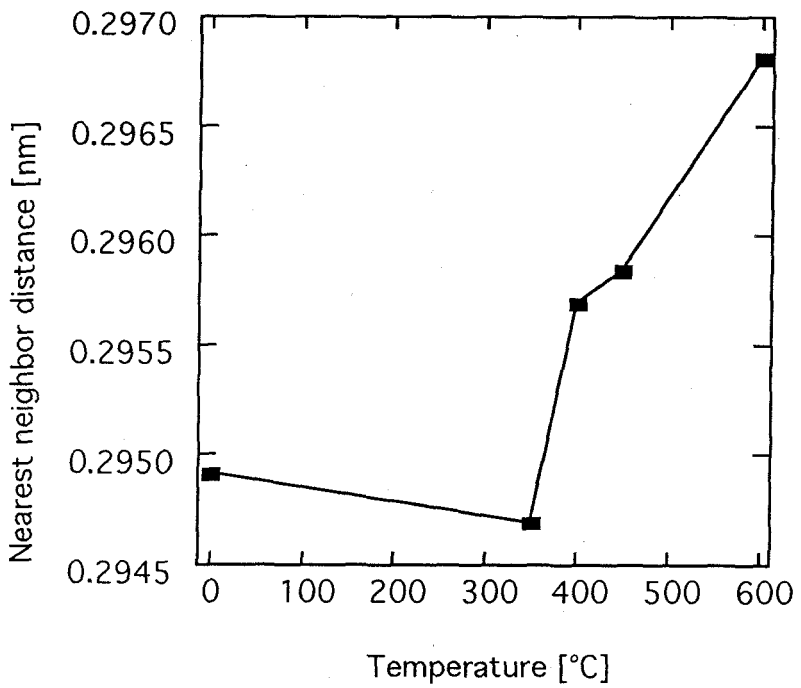

Fig. 3-36 Nearest neighbor distance of $(Ti_{0.9}Zr_{0.1})_{90}Cu_{10}$ powder synthesized by ball milling and heated to the indicated temperatures.

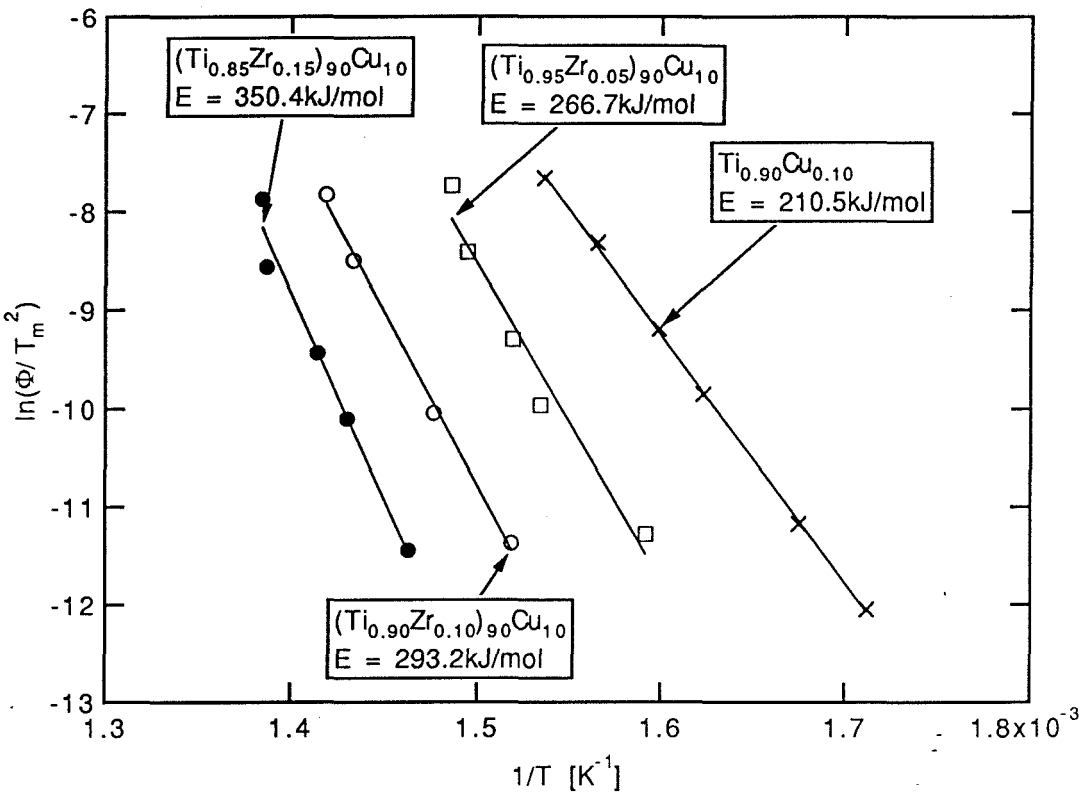

Fig. 3-37 Kissinger plot of $(Ti_{1-x}Zr_x)_{90}Cu_{10}$ powder synthesized by ball milling.

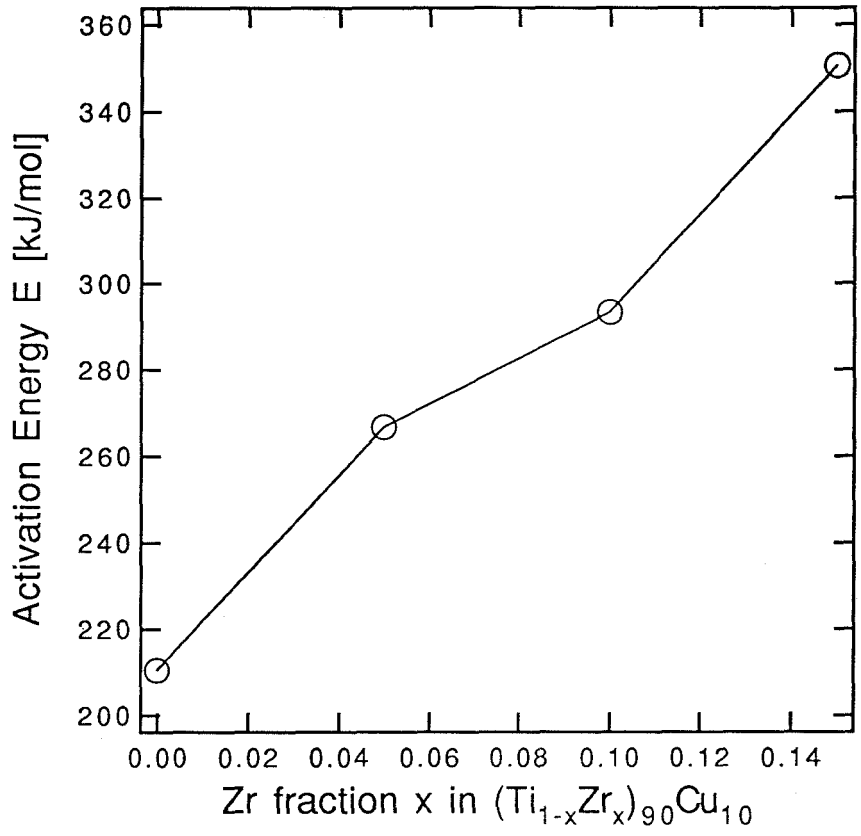

Fig. 3-38 Effect of Zr on the activation energy of the grain growth of $(Ti_{1-x}Zr_x)_{90}Cu_{10}$ powder synthesized by ball milling.

take place concurrently. On the other hand, the activation energies estimated by Kissinger analysis indicate that the reactions -- nucleation and grain growth -- become harder in samples with higher Zr concentration. The activation energy of the peak is plotted as a function of Zr concentration in Fig. 3-38.

It is suspected that the size mismatch between Zr and Ti make the nucleation of intermetallic compound difficult, hence the nanocrystalline structure be stabilized. As a result, the grain growth temperature was raised by 100 °C. Kissinger analysis revealed that the activation energy of the grain growth increased significantly. However, the migration of solute atoms were made difficult, too. Therefore there was no widening of the temperature range.

3.6 Discussion -- Mechanism of Grain Growth

Kissinger analysis estimated the activation energy of $Ti_{90}Cu_{10}$ synthesized by mechanical alloying as 209.5 kJ/mol. Furthermore, the study revealed that the replacement of part of Ti by Zr increases the activation energy and raises the peak temperature.

Both in Ti - Cu and Ti - Zr - Cu alloys, XRD study shows that the exothermic peak comes from the grain growth and the nucleation of the intermetallic compound Ti_2Cu or $(Ti, Zr)_2Cu$, respectively. However, it is not possible to separate the exothermic peak to distinguish two reactions. The XRD spectra of the powder heated up to the peak and quenched indicates no grain growth but does show the existence of Ti_2Cu or $(Ti, Zr)_2Cu$. Therefore it is supposed that the nucleation of the intermetallic compounds is responsible for this heat release.

The grain growth of nanocrystals and the nucleation of Ti_2Cu compete

with each other kinetically. In solid solutions, grain growth is often governed by solute diffusion. If this is true in the present case, the activation energy of grain growth would be that for solute (Cu) diffusion in Ti. Although this value is unknown, it may be close to the activation energy for self diffusion of Ti, 122.7 kJ/mol [108].

The activation energy of crystallization of amorphous $Ti_{67}Cu_{33}$ is reported to be 275.8 kJ/mol [109]. Also the activation energy of crystallization of amorphous $Ti_{85}Cu_{15}$ synthesized by mechanical alloying is known as 242.4 kJ/mol [110]. In these cases, the nucleation barrier for crystallization is associated with the homogeneous nucleation of Ti_2Cu. For Ti - Zr - Cu alloys, the activation energy of crystallization of amorphous is probably higher than that of Ti - Cu alloys, according to amorphous formability [107]. Consequently, at low temperatures, grain growth is kinetically favored over the nucleation of Ti_2Cu, while at high temperatures, the nucleation and growth of Ti_2Cu should prevail. However, the present results indicate that no grain growth occurs below 400 °C.

As discussed later, it is expected that Cu atoms in Ti - Cu alloys tend to grain boundaries due to the surface energy difference. Since the increase of grain size causes decrease of total grain boundary volume, Cu atoms in the boundaries have to move into grains, or precipitate to form a different phase so that grain growth occurs. Nevertheless, while the nucleation of Ti_2Cu is kinetically hindered by any reason, the nucleation of either Cu or Ti is thermodynamically prohibited. Thus Cu atoms cannot move from grain boundaries, as a result, grain growth is inhibited.

The results of heating and annealing experiments reveal that strain release, lattice parameter expansion, Ti_2Cu peak appearance in XRD spectra and

grain growth take place in that order. The starting of strain release indicates that the dislocation mobility increases so that solute Cu atoms start to diffuse. The following lattice parameter expansion corresponds to the migration of Cu atoms from Ti matrix. Since the grain growth is governed by diffusion, grain boundaries must be mobile at this temperature. Apparently, both grain growth boundary mobility and precipitation of Ti_2Cu are required for grain growth. Therefore the activation energy measured here is thought to be that of the heterogeneous nucleation of Ti_2Cu phase along Ti grain boundaries. The reason that the activation energy of the exothermic peak in Ti - Zr - Cu alloys is higher than that of Ti - Cu is probably due to the extra strain field by large zirconium atoms.

Hence, it is concluded that this exothermic reaction is governed by the nucleation of the intermetallic compound Ti_2Cu, and the grain growth follows immediately. This implies that crystal grains do not grow by heating until the intermetallic Ti_2Cu phase nucleates. Thus these results lead us to the conclusion that the grain growth is suppressed due to the segregation of Cu atoms in the grain boundaries.

3.7 Summary

Synthesis of Ti - Cu alloys by ball milling provided some new knowledge on the mechanism of structural refinement by mechanical milling. First, ultimate grain size by ball milling depends on the composition, and second, the grain size (or even formation) of nanocrystalline structure depends on the impurities such as oxygen.

Also an observation that the nucleation of Ti_2Cu triggers the grain growth

led us to a further idea in (Ti, Zr) - Cu ball milling experiments. As expected, Zr addition turned out to discourage grain growth. This effect is supposed to be due to the size mismatch of Zr and Ti and extra strain introduced. By those findings, a hypothesis that grain boundary segregation of Cu stabilizes the nanocrystalline structure was introduced.

It has been shown that the mechanically alloying process enables us to input so much energy that nanocrystalline and/or amorphous structures can be synthesized. Various research activity revealed that grain boundaries play an important role as energy storage, and the stored energy in grain boundaries may be much more than in conventional grain boundaries. This motivates us to assume that grain boundaries of nanocrystalline structure produced by ball milling may have somehow different structure from conventional polycrystalline materials. This topic will be discussed in Chapter 6.

Chapter 4 Nanocrystalline Structure of Nb - Cu Alloys

4.1 Background

In the previous section, it is speculated that the solute segregation in the grain boundaries helps nanocrystalline structure formation in Ti - Cu alloys. In order to enhance the effect of grain boundary segregation, we chose the Nb - Cu system, which has little equilibrium solubility in the solid state, hence Cu tends to segregate strongly at Nb grain boundaries. Furthermore, this system forms no equilibrium intermetallic compounds, as shown in the equilibrium binary phase diagram, in Fig. 4-1 [111]. Schänzer and Mehrer reported no vitrification by mechanical alloying of $Nb_{50}Cu_{50}$ and $Nb_{95}Cu_5$ [112], while amorphization by ion beam mixing has been demonstrated by Andersen *et al.* [113].

4.2 Experimental

Elemental Nb (99.8 % purity, –325mesh) and Cu (99.9 % purity, –200mesh) powders were blended to the designated composition and sealed into a hardened steel vial with steel balls under an argon atmosphere. Ball milling was carried out with a Spex 8000 shaker mill. BPR was set to 5. In a typical experiment, 4 *g* of powder was milled for 20 hours. Since the vial absorbs water during cleaning before milling, and some materials such as Nb tend to absorb water during milling, the milling device was dried up in a low-temperature furnace at about 80 °C for a few hours. In the present study, amorphization did not take place. Therefore the milling time was chosen such that the grain size no longer

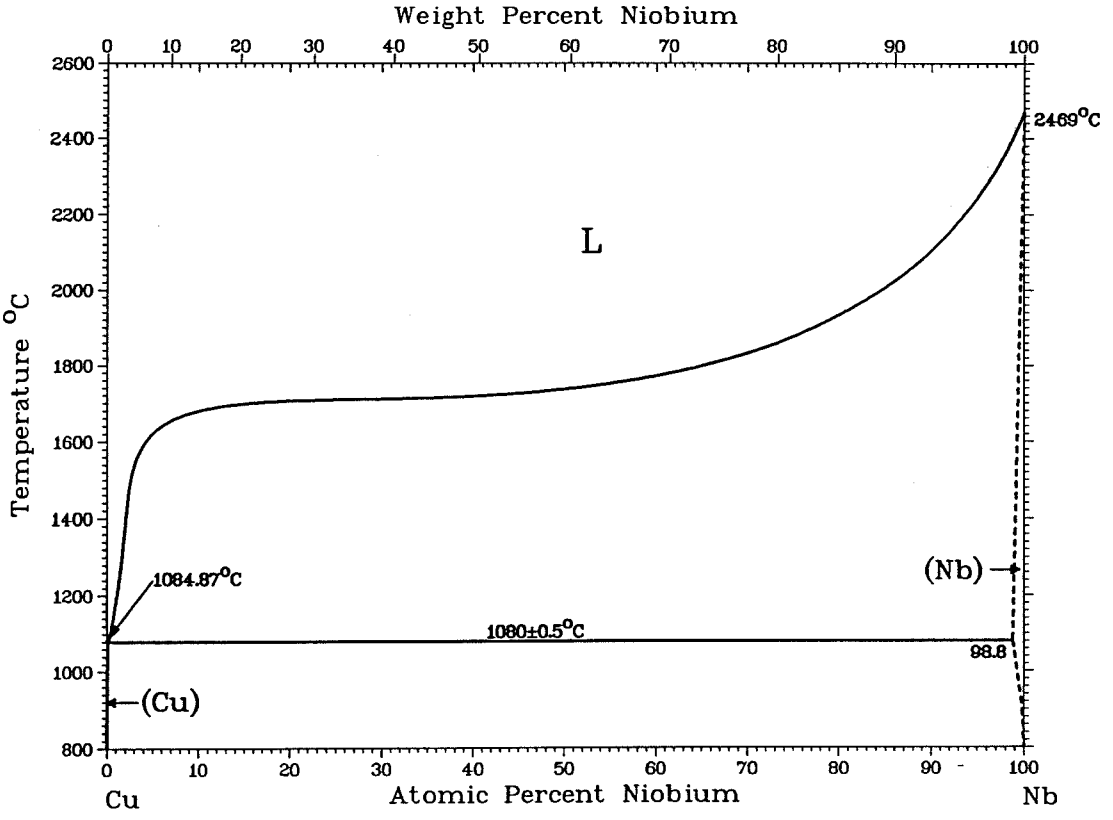

Fig. 4-1 Nb - Cu binary phase diagram [111].

decreased. Milled powder was collected under an argon atmosphere and used for further analysis.

4.3 Microstructure of As-milled Powder

4.3.1 Structural Evolution by Ball Milling

Nanocrystalline $Nb_{100-x}Cu_x$ ($0 \leq x \leq 30$) alloys of 8 - 25 *nm* grain size are synthesized with the mechanical alloying technique. Cu peaks diminish in the early stage of milling, and *bcc* Bragg peaks of Nb remain. Grain size, strain and nearest neighbor distance were estimated from XRD spectra and shown in Figs. 4-2 and 4-3. These figures demonstrate that the microstructure reaches stable state within 20 hours of milling.

4.3.2 Effect of Composition

The effect of Cu concentration on the structure of milling product was investigated. The XRD spectra of the as-milled powders shown in Fig. 4-4 indicate nanocrystalline $Nb_{100-x}Cu_x$ alloys of single-phase *bcc* structure for $x < 25$. The *fcc* Cu phase is detectable together with the *bcc* phase in $Nb_{75}Cu_{25}$ and $Nb_{70}Cu_{30}$. The grain size, strain and interatomic distance reach stable values in 20 hours of milling.

The relations between the grain size, strain, interatomic distance and Cu concentration are shown in Fig. 4-5. The data shown have been averaged over at least two samples at each composition. The grain size first increases with Cu concentration, then decreases and finally reaches a constant value of 8 - 12 *nm* for samples with more than 15 at.% Cu. The *fcc* Cu grain size in $Nb_{75}Cu_{25}$ and $Nb_{70}Cu_{30}$ are about 6 and 8 *nm*, respectively. Conversely, the strain and lattice

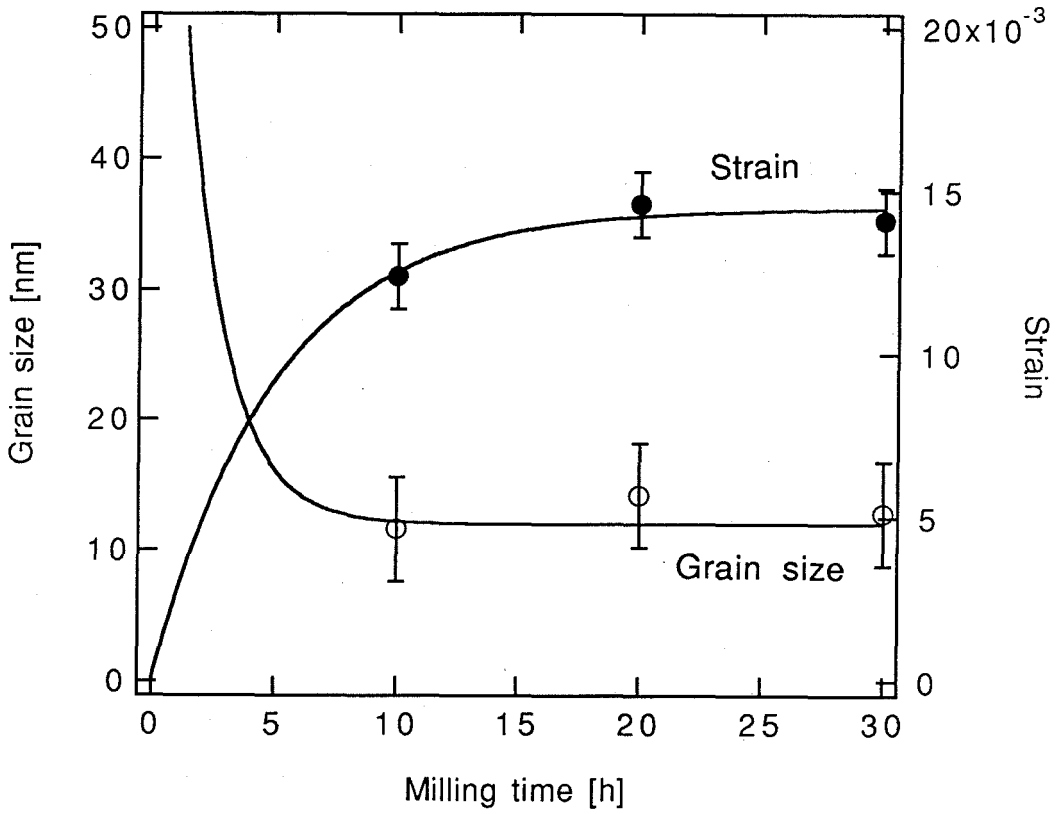

Fig. 4-2 Change of grain size and atomic strain of $Nb_{90}Cu_{10}$ by ball milling.

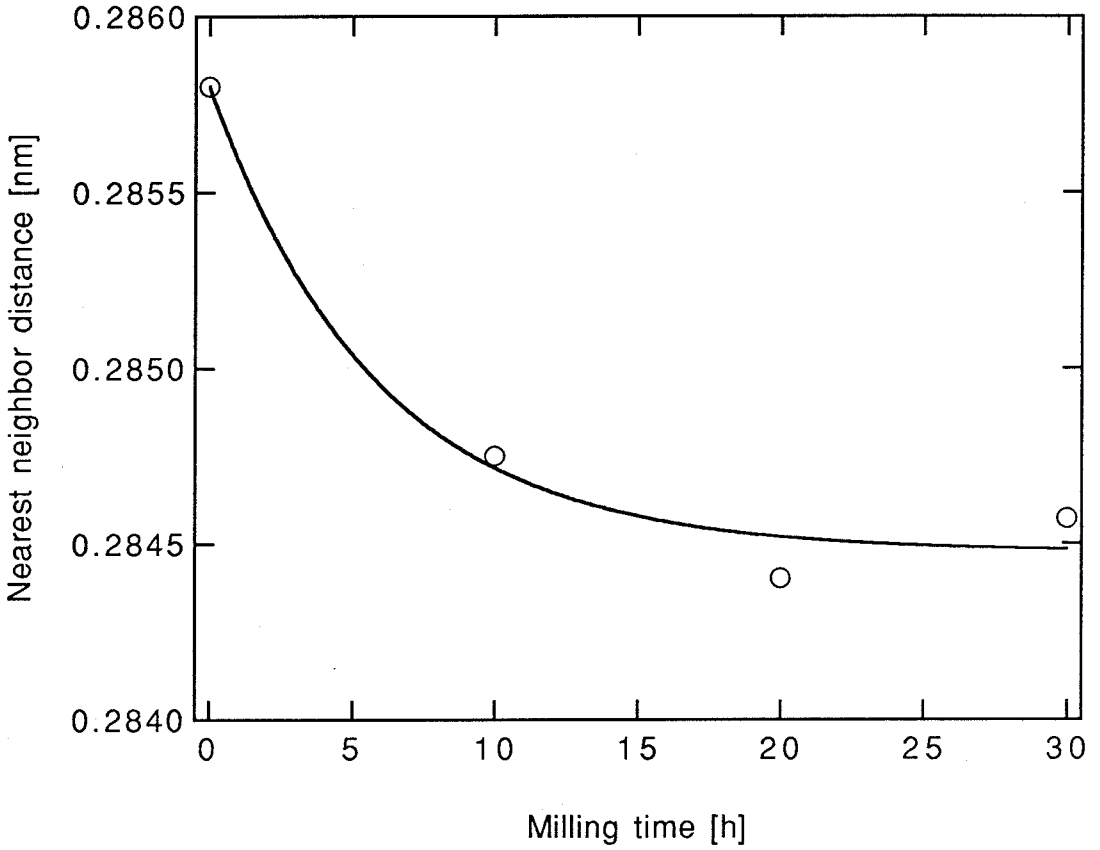

Fig. 4-3 Change of nearest neighbor distance of $Nb_{90}Cu_{10}$ by ball milling.

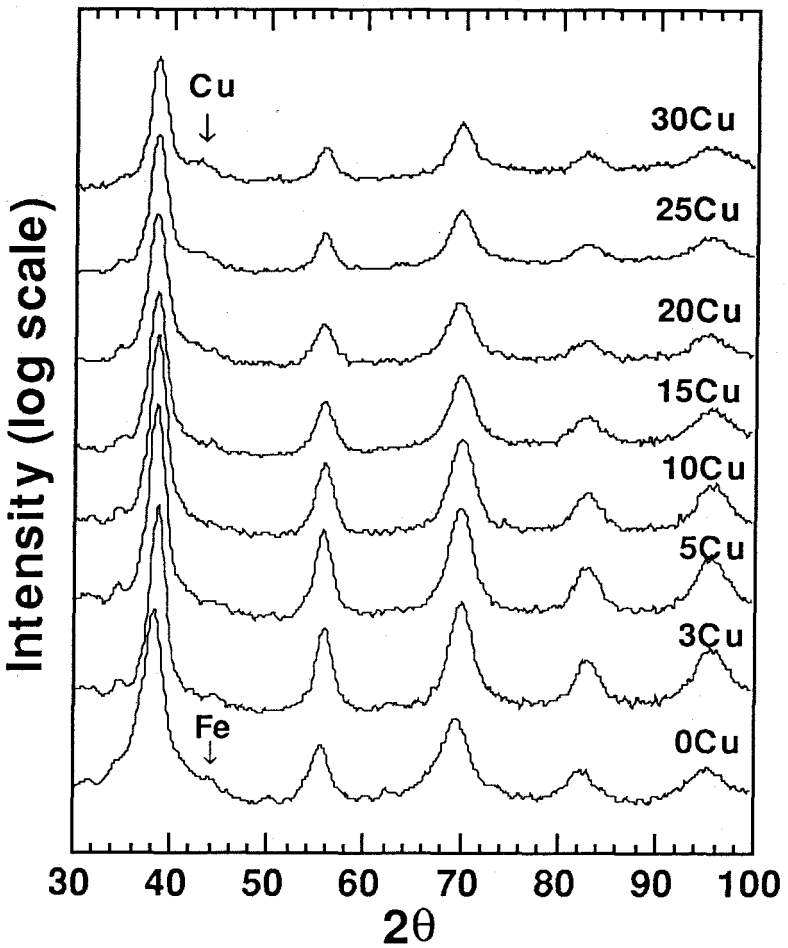

Fig. 4-4 XRD spectra of Nb - Cu alloys synthesized by ball milling for 20 hours.

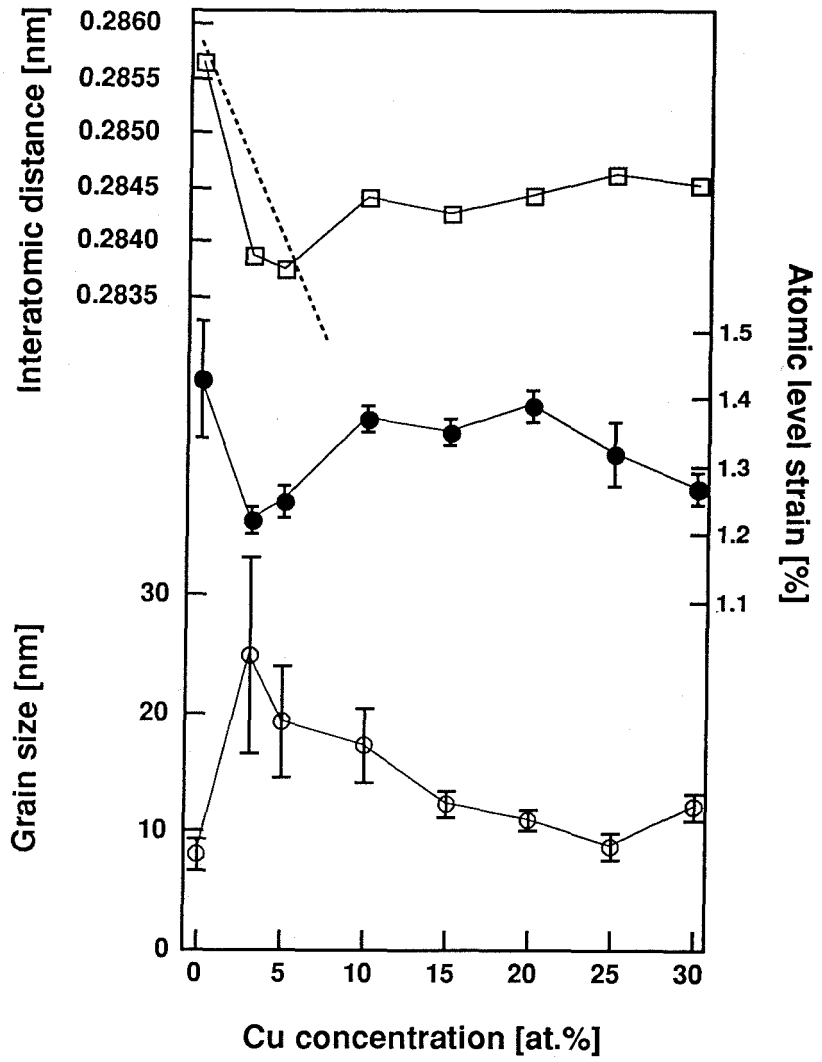

Fig. 4-5 Grain size, strain and nearest neighbor distance of Nb - Cu alloys synthesized by ball milling for 20 hours.

parameter decrease first, then increase to reach stable values. The grain size and strain of pure Nb obtained in this study agree with previous results [51]. XRD spectra also show a weak Fe peak due to wear debris from the milling devices. Chemical analysis proved that about 1 at.% O, 1 at.% Fe are the major contamination.

Grain size, strain and lattice parameters behave in a strange manner. At about 3 - 5 at.% Cu composition, the nearest neighbor distance and atomic strain take minimum, and the grain size takes maximum. It is suspected that Cu more than 5 at.% does not dissolve completely, remaining as fine particles. However, since no Bragg peaks are seen in XRD spectra, some Cu atoms may be segregated in the grain boundaries. Otherwise it is also possible that the microstructure looks similar to spinodal decomposition.

4.3.3 TEM Study

TEM observation was carried out with Hitachi H-800 analytical TEM. Ball-milled powder was crushed with a mortar and pessel, so that a small region thin enough for the observation was obtained. As seen in Fig. 4-6, the structure is not so uniform as Ti - Cu powder. Although the majority is small grains, large grains are also included. The grain size obtained by XRD Bragg peak width analysis is supposed to fit the grain size of the majority. Although pure Cu phase is supposed to remain in samples with high Cu concentration, EDAX study could not provide any information, mainly because fine grain structure and the usage of copper mesh for TEM sample preparation.

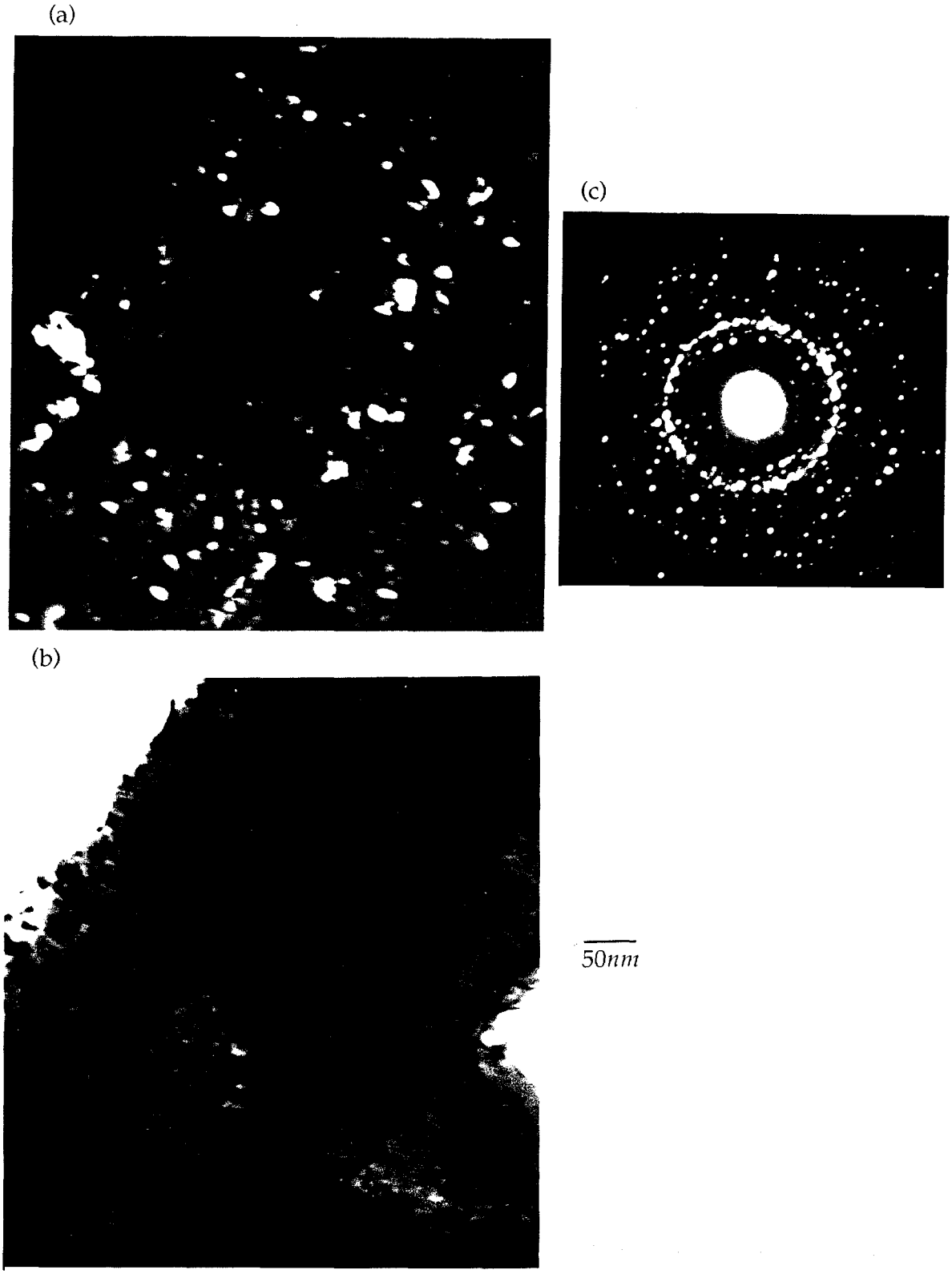

Fig. 4-6 TEM picture of mechanically-alloyed $Nb_{90}Cu_{10}$ alloy. Along with fine grains, big grains are observed. (a) bright field image, (b) dark field image, (c) diffraction pattern.

4.4 Grain Growth Behavior

4.4.1 DSC Study

DSC experiments were conducted with a CETARAM 2000K DSC apparatus. The trace of mechanically alloyed $Nb_{90}Cu_{10}$ is shown in Fig. 4-7 as a typical example. Two exothermic peaks, at about 630 °C and 830 °C, are present. The peak temperatures and stored enthalpies are nearly independent of Cu concentration. The two exothermic reactions were studied with a Kissinger analysis for $Nb_{90}Cu_{10}$. The measured activation energies are 2.6 ± 0.1 eV for the first reaction, and 2.79 ± 0.03 eV for the second reaction.

4.4.2 Heating Experiments

To investigate these two exothermic reactions in more detail, $Nb_{90}Cu_{10}$ powder was heated and annealed at various temperatures, then the microstructural change was studied.

Ball-milled powders were heated at 20 °C/*min* and quenched, then subjected to the observation. The XRD spectra in Fig. 4-8 indicate that the interatomic distance first decreases upon heating to 400°C, then increases monotonically to the value of pure Nb (0.2858 *nm*). Atomic strain release starts at 400°C. This temperature is much lower than the onset of the first exothermic peak. The Cu peak is visible in XRD after heating to 675 °C. Above the second peak, pure Nb and Cu are present, but no peaks of intermetallic compounds are found. Grain growth starts above 550 °C, during the first exothermic reaction. By heating above the first exothermic reaction, the grain size is almost twice of that of the as-milled powder. A tendency for the suspension of grain growth when the grain size doubles is seen in specimens of all compositions studied.

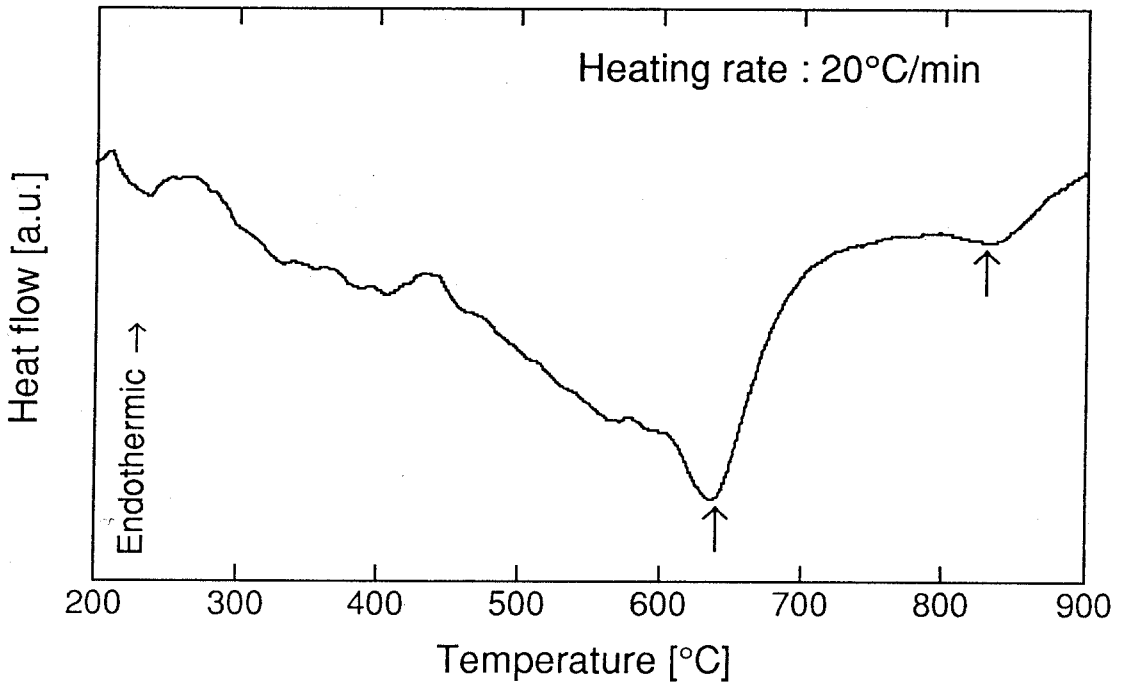

Fig. 4-7 DSC trace of mechanically-alloyed $Nb_{90}Cu_{10}$ alloy.

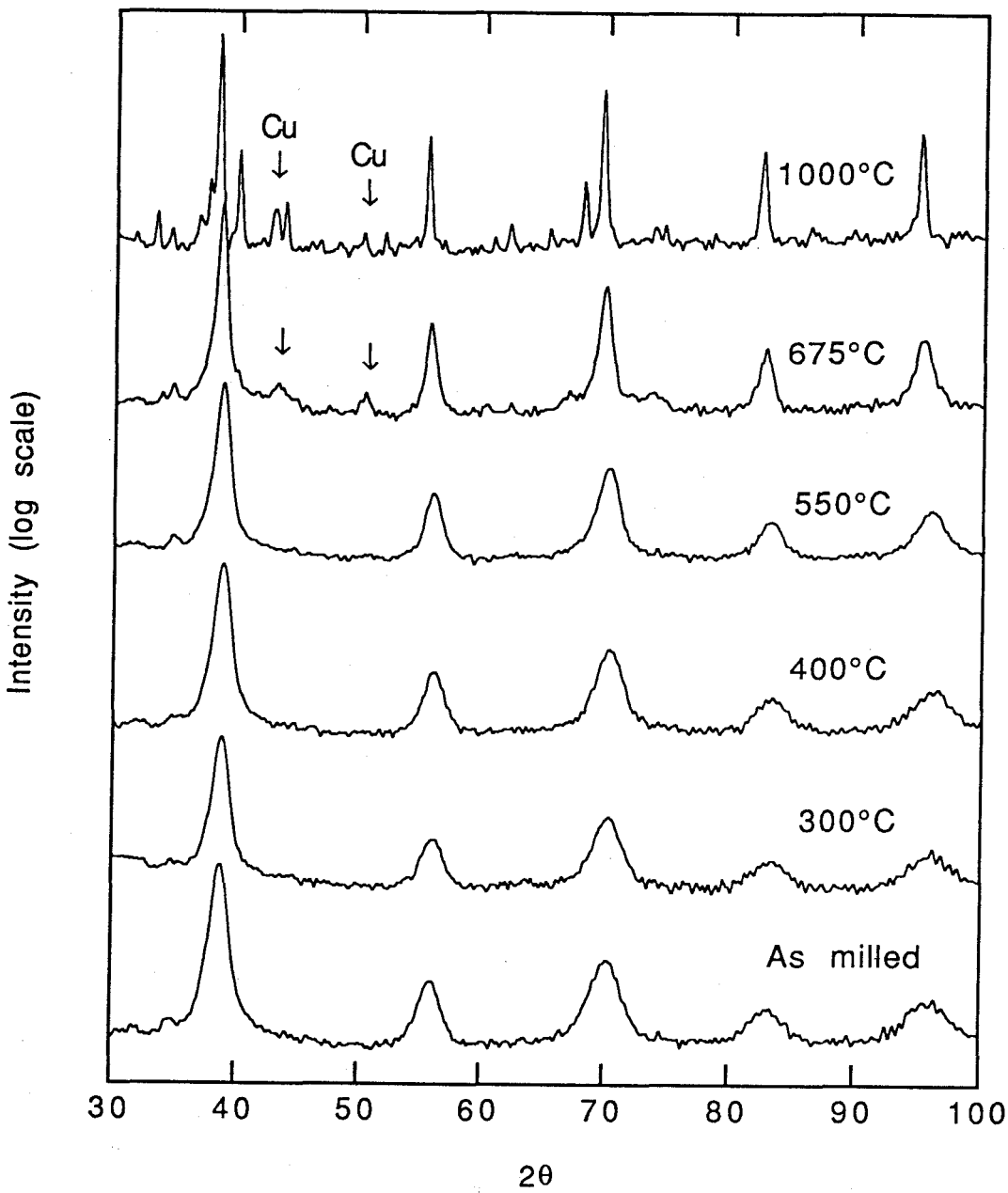

Fig. 4-8 XRD spectra of $Nb_{90}Cu_{10}$ heated to the indicated temperatures.

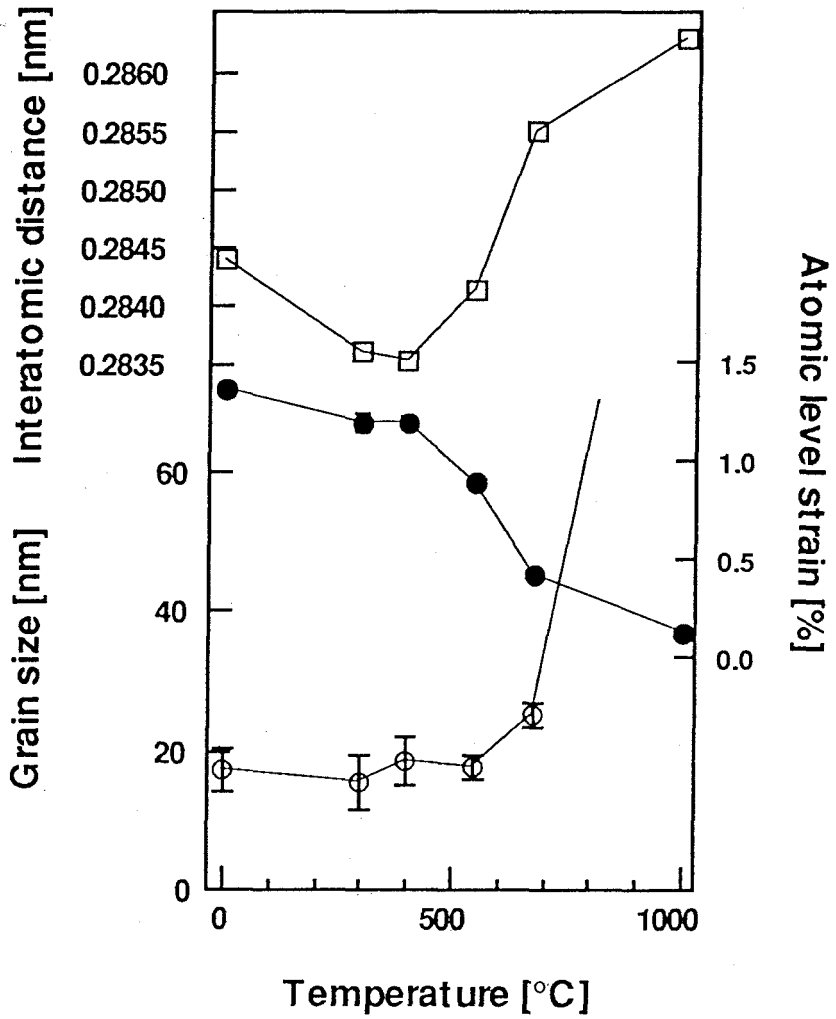

Fig. 4-9 Change of grain size, strain and nearest neighbor distance of mechanically-alloyed $Nb_{90}Cu_{10}$ alloy by heating to the indicated temperatures.

4.4.3 *Annealing Experiments*

Isothermal annealing experiments were carried out at 550 °C, around the onset of the first reaction, and at 675 °C, between the two exothermic peaks. Specimens annealed at 550 °C reveal that the atomic strain decreases and the interatomic distance increases rapidly with no associated grain growth in 5 hours of annealing, as shown in Figs. 4-10 and 4-11. A Cu peak becomes visible in XRD spectra after 18 hours of annealing. The Cu grain size is estimated to be less than 10 *nm*. The interatomic distance recovers to the value of pure niobium in 5 hours of annealing. The grain growth starts with more than 5 hours of delay, with the grain size reaching about 40 *nm* in 24 hours of annealing. Such an incubation period is not expected for a normal grain growth process.

At 675 °C, only slight grain growth is observed after 5 hours of annealing. However, the grain size increases to about 40 *nm* in 24 hours. A Cu peak appears in XRD spectra after 1 hour of annealing. This result again implies that it is not normal grain growth.

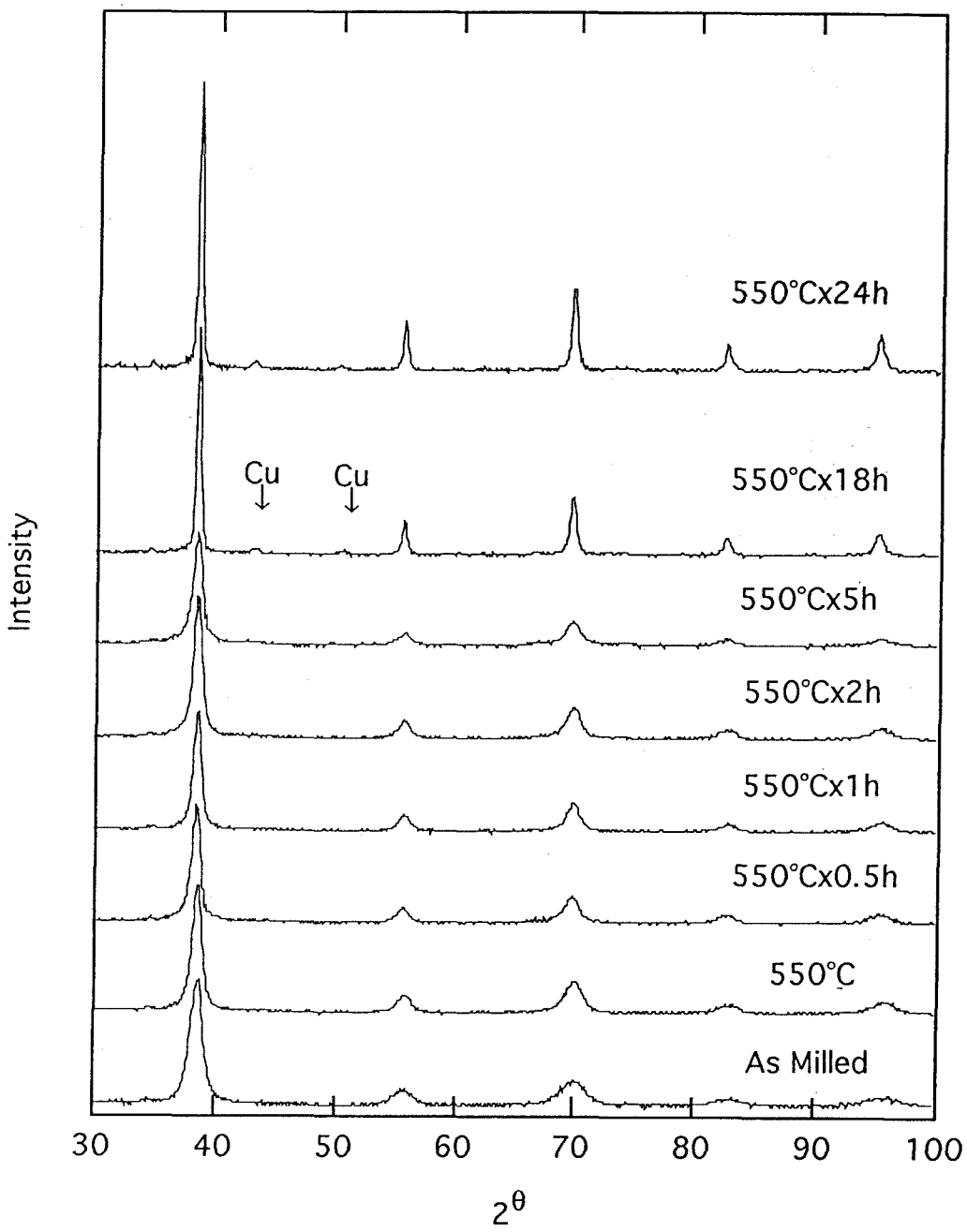

Fig. 4-10 XRD spectra of $Nb_{90}Cu_{10}$ annealed at 550 °C for the indicated duration.

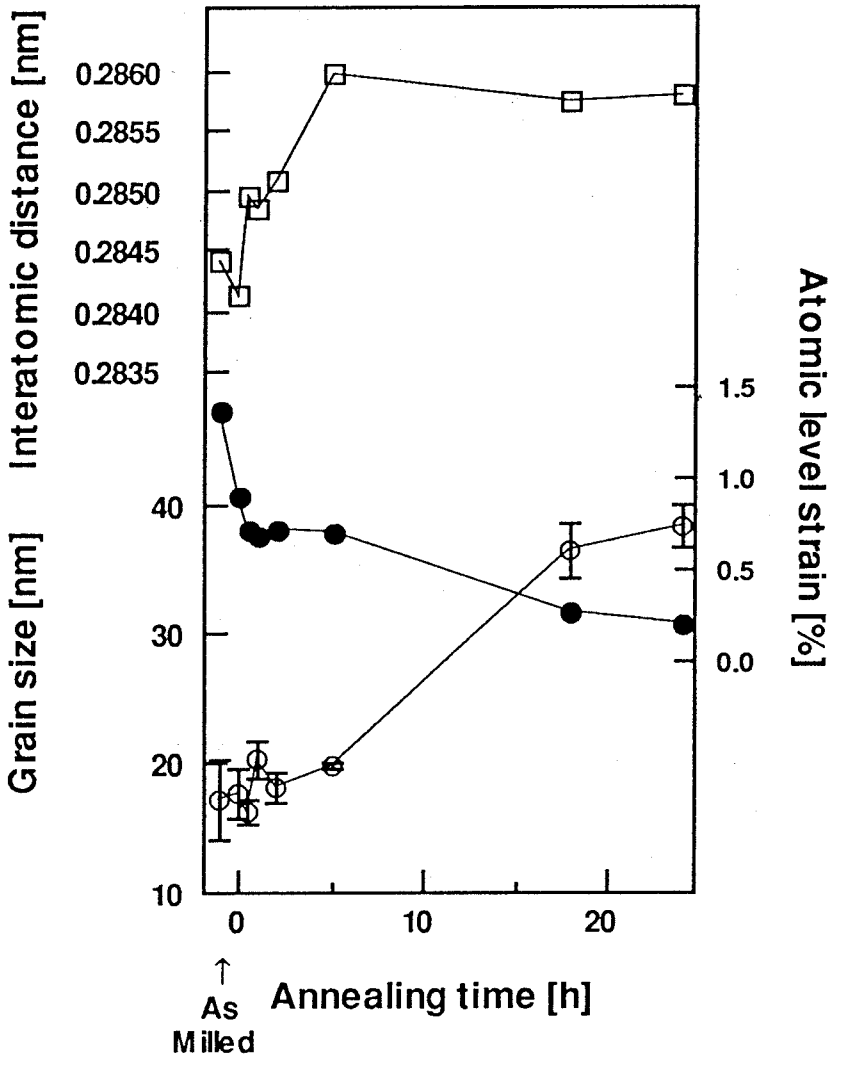

Fig. 4-11 Change of grain size, strain and nearest neighbor distance of mechanically-alloyed $Nb_{90}Cu_{10}$ alloy by annealing at 550 °C.

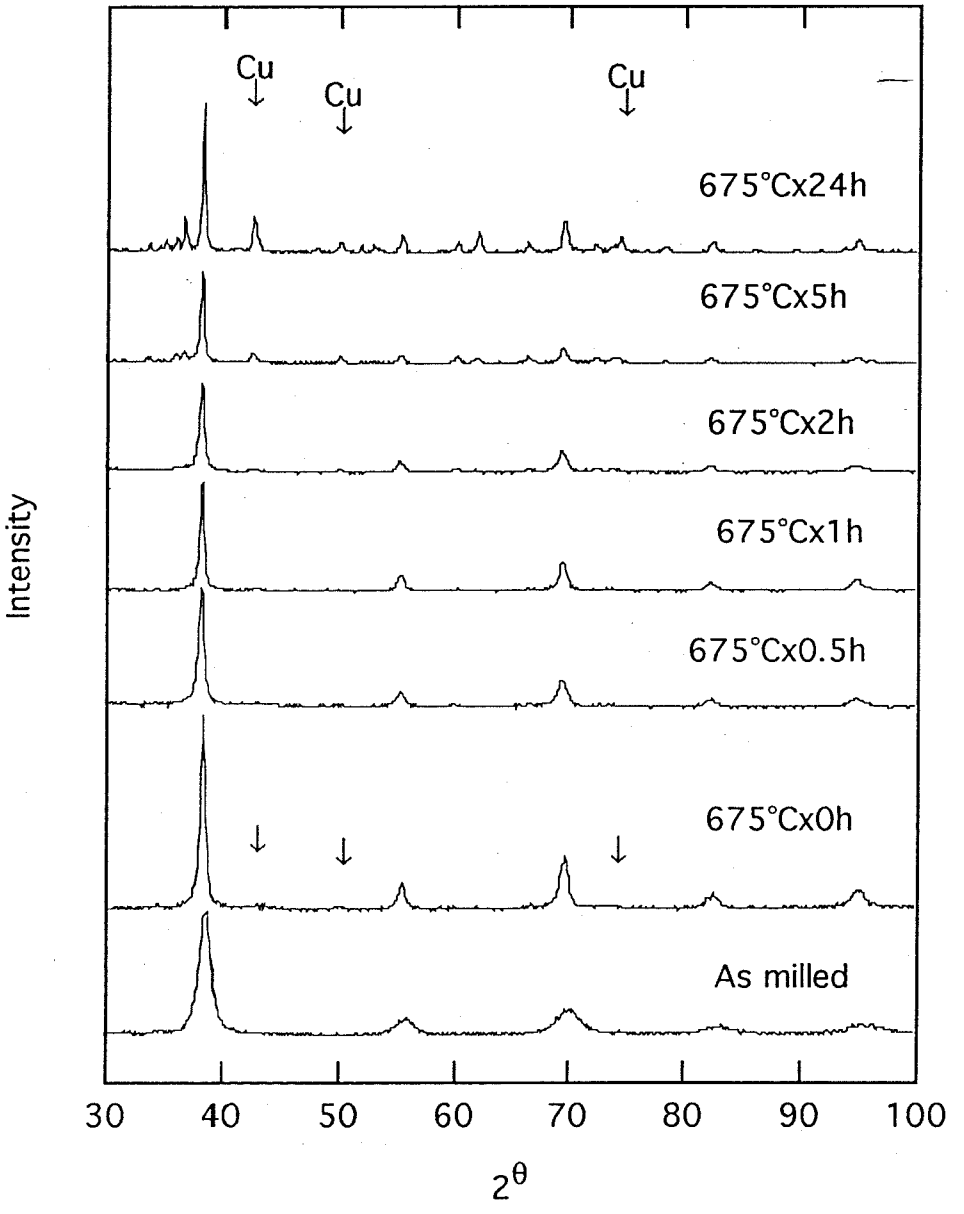

Fig. 4-12 XRD spectra of $Nb_{90}Cu_{10}$ annealed at 675 °C for the indicated duration.

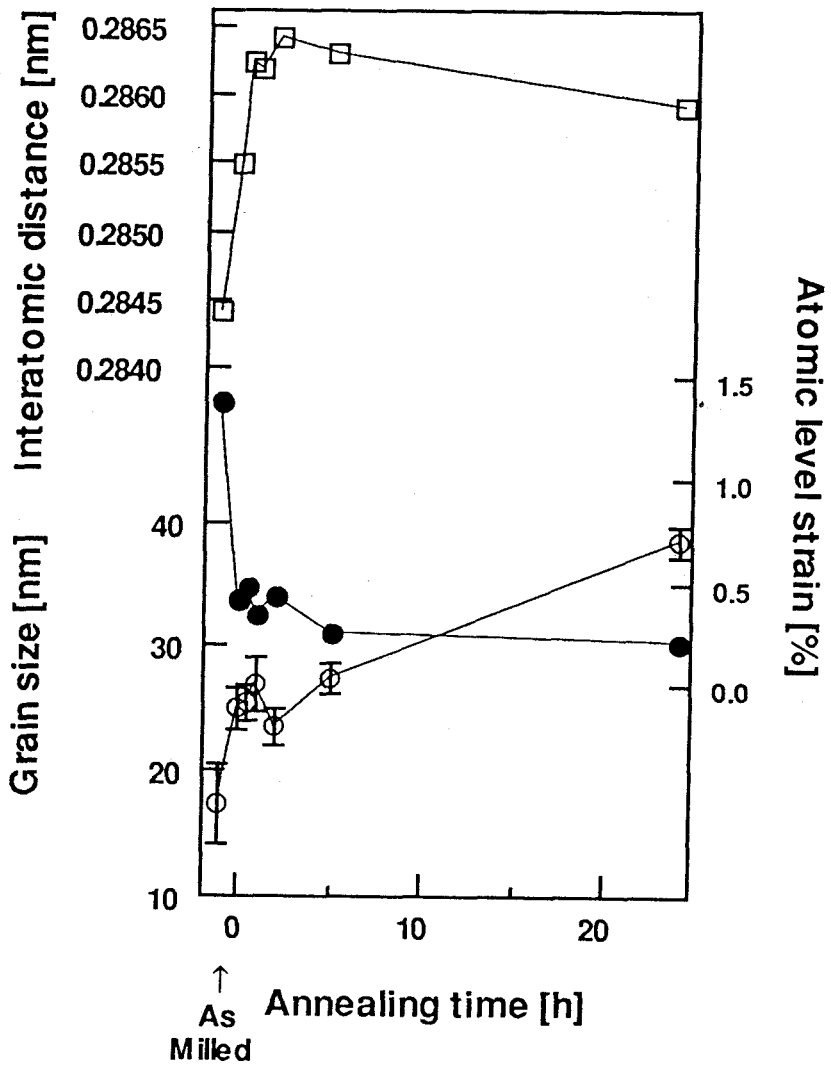

Fig. 4-13 Change of grain size, strain and nearest neighbor distance of mechanically-alloyed $Nb_{90}Cu_{10}$ alloy by annealing at 675 °C.

4.5 Discussion

In Nb - Cu system, particularly in 0 - 5 at.% Cu region, the grain size, strain and interatomic distance show a complex dependence on Cu concentration. Eckert *et al.* [114] have reported a similar tendency for Fe - rich Fe - Cu alloys. They have stated that for Cu - rich Fe - Cu solid solutions the grain size achieved by mechanical alloying decreases with increasing Cu concentration, which has been explained by solution hardening. This tendency is observed in other systems such as Ti - Cu. However, for Nb - Cu, this interpretation apparently does not apply.

4.5.1 Interpretation of Exothermic Reactions

In the first stage, the grain growth is associated with migration of solute Cu atoms to grain boundaries. Grain growth stops as the grain boundaries are saturated with Cu. The second reaction takes place either when the threshold for the nucleation of an *fcc* Cu phase in the grain boundary is overcome by thermal activation, or when segregating Cu atoms in the grain boundary are driven by diffusion to the growing Cu grains, and the Cu concentration in the grain boundary drops. This increases the grain boundary energy, and initiates a second stage of rapid grain growth.

4.5.2 Behavior of Cu Atoms

The equilibrium solubility of Cu in Nb at room temperature is less than 0.5 at.%. In the present study, no apparent signal of pure Cu is observed in XRD up to 25 at.% Cu. However, above 5 at.% of Cu, the measured interatomic distance is much larger than values derived from Vegard's law. This implies that the solute Cu concentration in the lattice may be less than the overall solute

concentration for samples with more than 5 at.% Cu.

4.5.3 *Grain Boundary Saturation*

The observation that both the final grain size and the interatomic distance become independent of Cu concentration implies that the grain boundaries become saturated with Cu. Since Cu peaks are not seen in XRD, the Cu atoms may either form very fine Cu particles or segregate to Nb grain boundaries. As Cu atoms are driven into the Nb lattice during ball-milling, they interact with the stress field of dislocations, and tend to be accommodated in the dislocation cores.

Accordingly, dislocations in Nb are expected to be decorated by Cu atoms. This phenomenon enhances solid solubility. As the solute Cu concentration increases, the chemical potential of Cu is raised as long as the nucleation of a pure Cu phase is inhibited. Hence the solid solubility is extended as shown in Fig. 4-14.

4.5.4 *Ultrafine Cu Particles Have Higher Free Energy*

The extended solid solubility is recognized by the interatomic distance decrease up to 5 at.%. The smallest atomic distance achieved by ball milling is at 5 at.% Cu composition. In samples containing 5 - 10 at.% of Cu, the nearest neighbor distance gradually recovers to the value of pure niobium. This is interpreted as follows. Ultrafine particles have higher energy than the bulk phase due to the surface contribution. When pure Cu nucleates as ultrafine particles, solid solubility gradually decreases as the Cu particles grow [115]. This solubility transition leads atomic distance to increase with increasing Cu concentration, as seen in 5 - 10 at.%. In samples containing more than 10 at.% Cu, Cu phase exists as relatively big grains, probably as big as the matrix, Nb - Cu solid solution. The

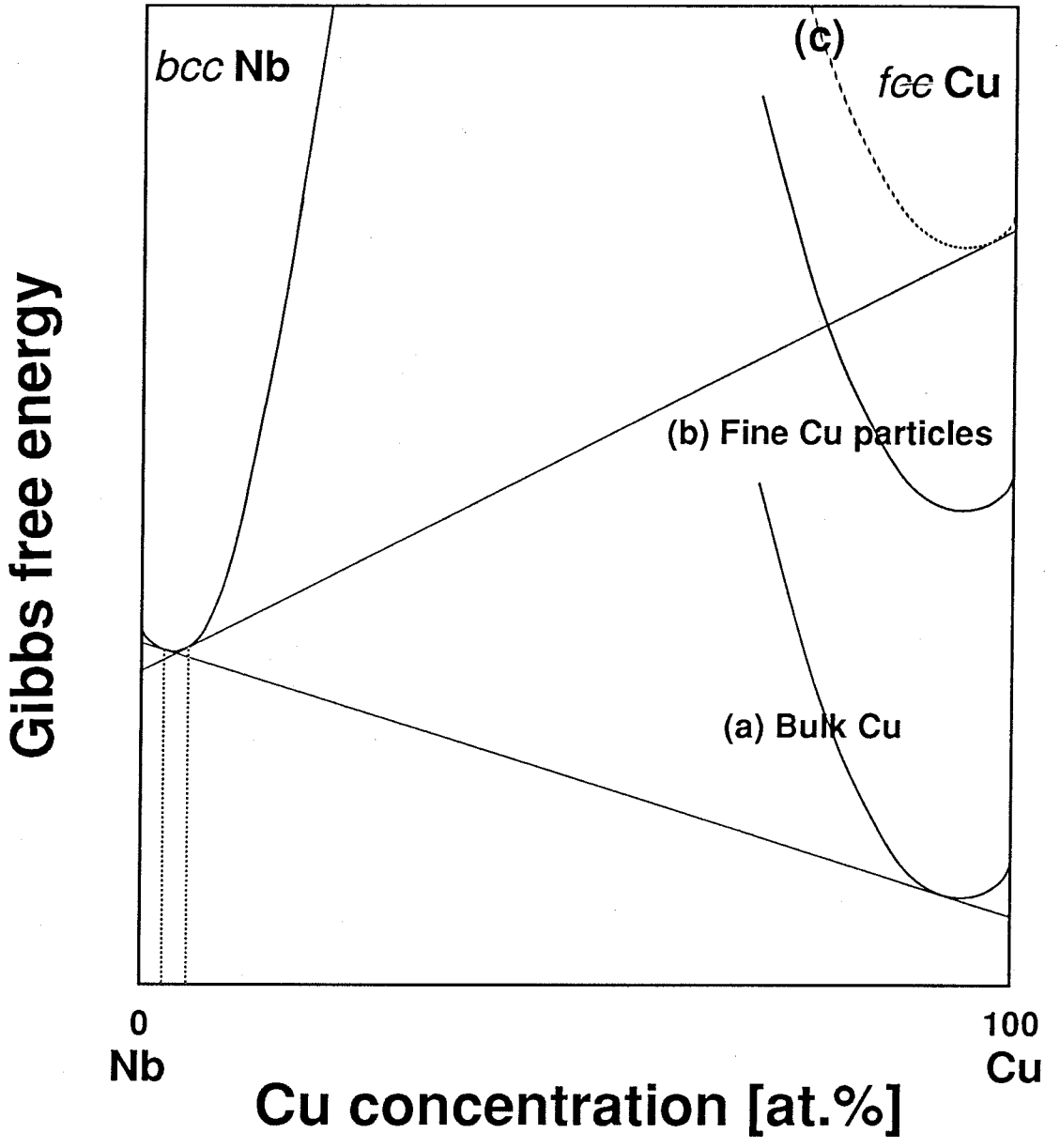

Fig. 4-14 Schematic Nb - Cu free energy diagram. Extended solid solubility of Cu in Nb - Cu alloy is explained.

above is also expressed in Fig. 4-14.

4.6 Summary

The grain size of the nanocrystalline structure obtained by mechanical alloying varies with Cu concentration in a complex manner. Grain growth of the nanocrystalline structure is apparently influenced by solute segregation of Cu to the Nb grain boundaries. We speculate that when grain boundaries are saturated and the grains and grain boundaries reach a metastable equilibrium, the grain growth stops. Further grain growth does not take place until Cu atoms in the grain boundary are removed by the nucleation and growth of a pure Cu phase. Thus, the initiation of normal grain growth is constrained by the nucleation of a Cu phase.

Chapter 5 High Temperature Ball Milling

5.1 Background

In the previous chapters it is argued that the grain boundary segregation stabilizes grain boundary structure, thus leads the system to a finer-grain and more stable nanocrystalline structure. It is suspected that there exists a metastable equilibrium between the crystalline phase and the grain boundary in the nanocrystalline structure produced by mechanical alloying. However, no clear evidence of a metastable equilibrium has been found, probably because mechanical alloying at room temperature yields only supersaturated structures which are quite far from such metastable equilibrium.

Recently a high temperature ball-milling (HTBM) technique was introduced, showing that the solid-state amorphization reaction during ball milling is accelerated in high ambient temperature, and nanocrystalline structure formation as the preliminary stage of amorphization was hastened also. These phenomena are attributed to enhanced interdiffusion [97, 116]. This technique has been applied to the synthesis of nanocrystalline Ti - Cu alloys anticipating that the system may be able to reach the metastable chemical equilibrium during ball milling [102]. The effect of the milling temperature on the microstructure of milling product has been investigated. It is speculated that by performing mechanical alloying at high ambient temperature, the diffusion of solute atoms are encouraged, thus solute atoms are driven to segregate into grain boundaries and stabilize the nanocrystalline structure.

5.2 Experimental

Pure elemental Ti and Cu powders were mixed into 95 at.% Ti - 5 at.% Cu composition and sealed into a type - 304 stainless steel vial with Cr steel balls (type 52100 equivalent). The vial was evacuated and filled with high-purity argon gas before milling. BPR was set to 5. High temperature ball milling experiments (HTBM) at 200 °C and 300 °C were carried out in this study, and the results were compared with those of milling experiments at room temperature (RTBM). The milling products were studied with XRD, DSC and TEM, and grain size and atomic strain are estimated from the broadening behavior of the Bragg peaks. Also the lattice parameters are calculated from the position of Bragg peaks. It should be noted that the intensity of the mill is quite lower than that used in the study presented in Chapter 3. Therefore it is meaningless to compare both results directly.

5.3 Chemical Analysis

In the ball milling process, contamination is inevitable. Typical chemical analysis results indicate a slight oxygen increase in HTBM process (0.5 - 0.6 at.% in HTBM above 200 °C, 0.3 - 0.4 at.% in RTBM), probably due to gas desorption from the vial. Other impurities include Fe ~ 0.25 at.% and N ~ 0.07 at.% regardless of the milling temperature. Since the solubility of oxygen in titanium is very large, it was assumed that all the oxigen atoms dissolves uniformly in the titanium lattice, and that the difference in oxygen amount between HTBM and RTBM samples does not have any effect on the physical, chemical or thermodynamic properties of nanocrystalline structure.

5.4 Microstructure Observation

Grain size, lattice parameters reach final and stable values quicker than in the room temperature. Atomic strain is so small that the absolute value may be erroneous and unreliable. No nucleation of the intermetallic compound during milling even at the temperatures where it nucleates on annealing. The XRD spectra of as-milled powders are shown in Fig. 5-1. The mechanism of the microstructure evolution seems independent of milling temperatures. Both in RTBM and HTBM, the obtained structure is a *hcp* α - Ti single phase. No trace of either amorphous or intermetallic compound phase is visible. Peak broadening is apparent, especially in samples processed longer and in higher temperature.

The grain size of as-milled powders are plotted in Fig. 5-2 as a function of milling time and temperature. The grain size reduces in HTBM much faster than in RTBM. There seems little effect of the milling temperate in HTBM at as high as 200°C. It should be noted that the smallest grain size achieved by HTBM is smaller than that by RTBM. The grain size achieved using a high-intensity ball mill at this composition was 9.3 *nm*, still 30% larger than the present result in HTBM, as presented in Chapter 3. This difference is significant since the volume fraction of grain boundaries in the HTBM sample is about twice that of the RTBM samples.

The other significant effect of HTBM is on the lattice parameters. Fig. 5-3 shows the change of the interatomic distance with milling in various temperatures. The interatomic distance in the RTBM samples decreases with milling time monotonously. On the other hand in HTBM, after a faster decrease than in RTBM in the early stage of milling, the lattice parameter gradually recovers and finally increases toward the value of pure titanium. By assuming

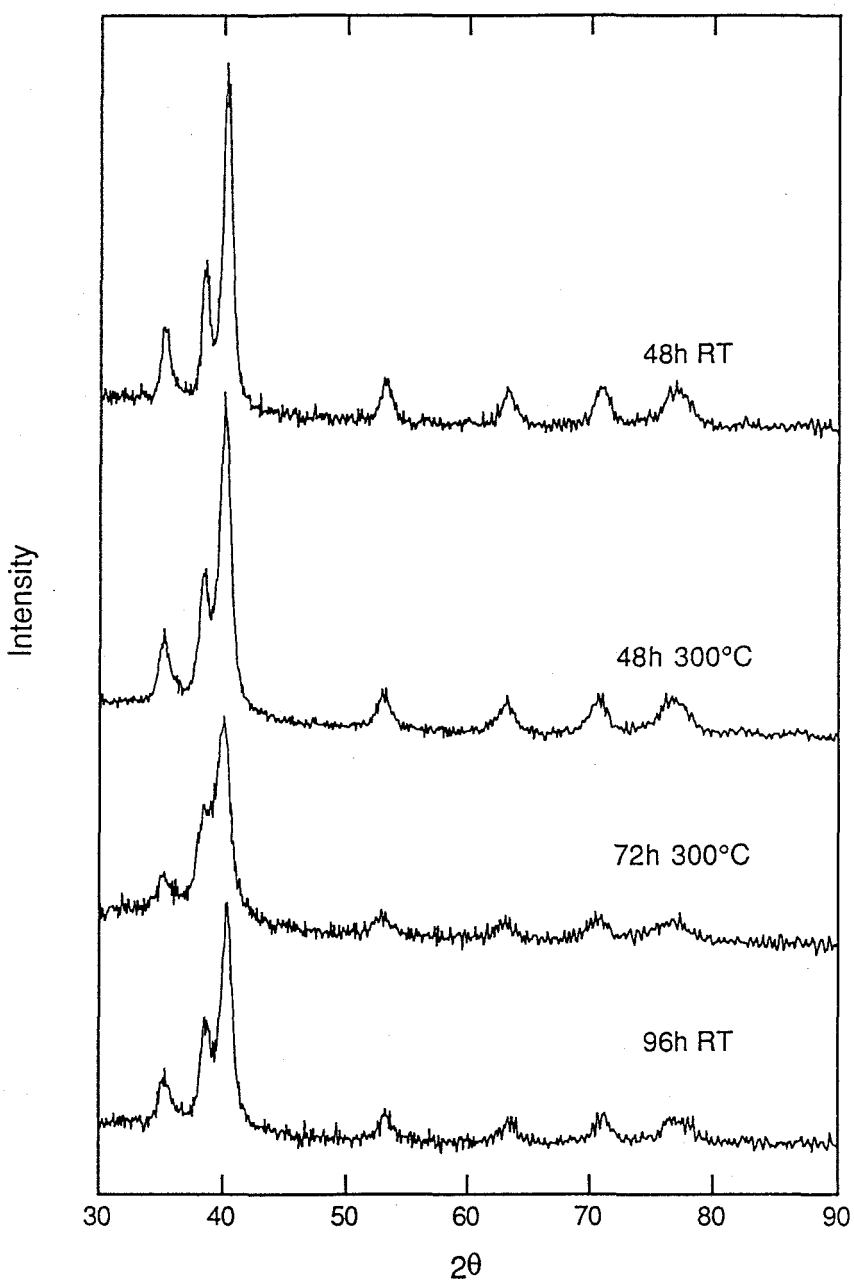

Fig. 5-1 XRD spectra of $Ti_{95}Cu_5$ synthesized by ball milling at various temperature.

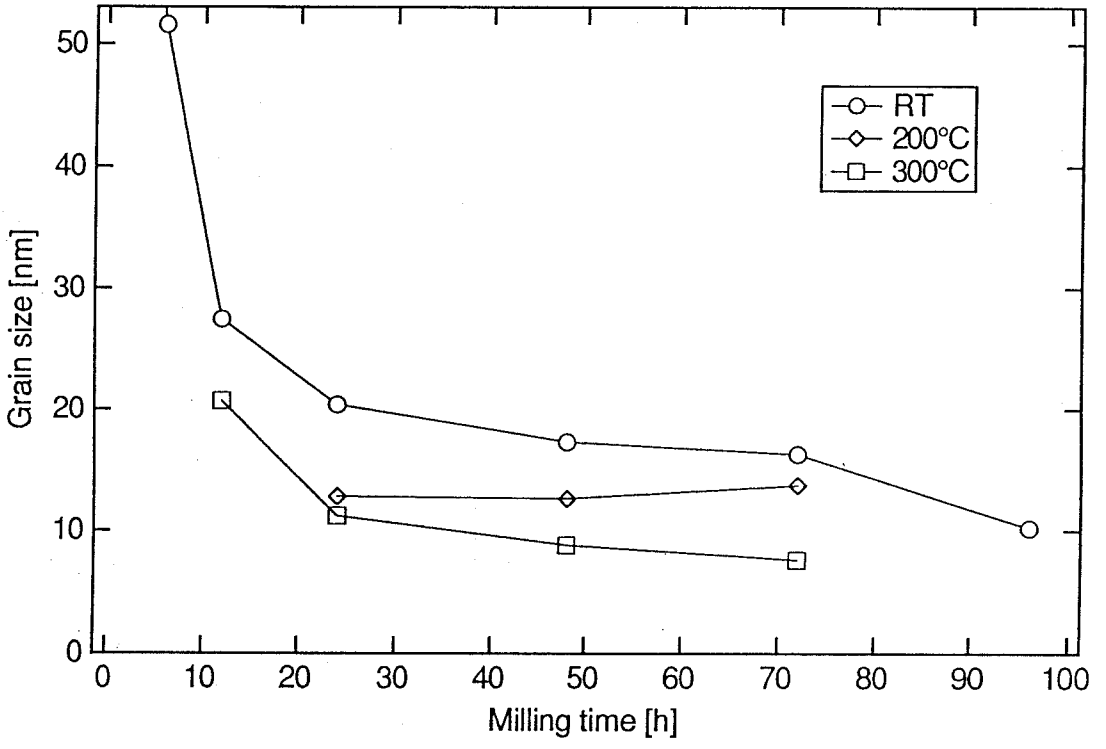

Fig. 5-2 Effect of milling temperature on the grain size of $Ti_{95}Cu_5$ synthesized by ball milling.

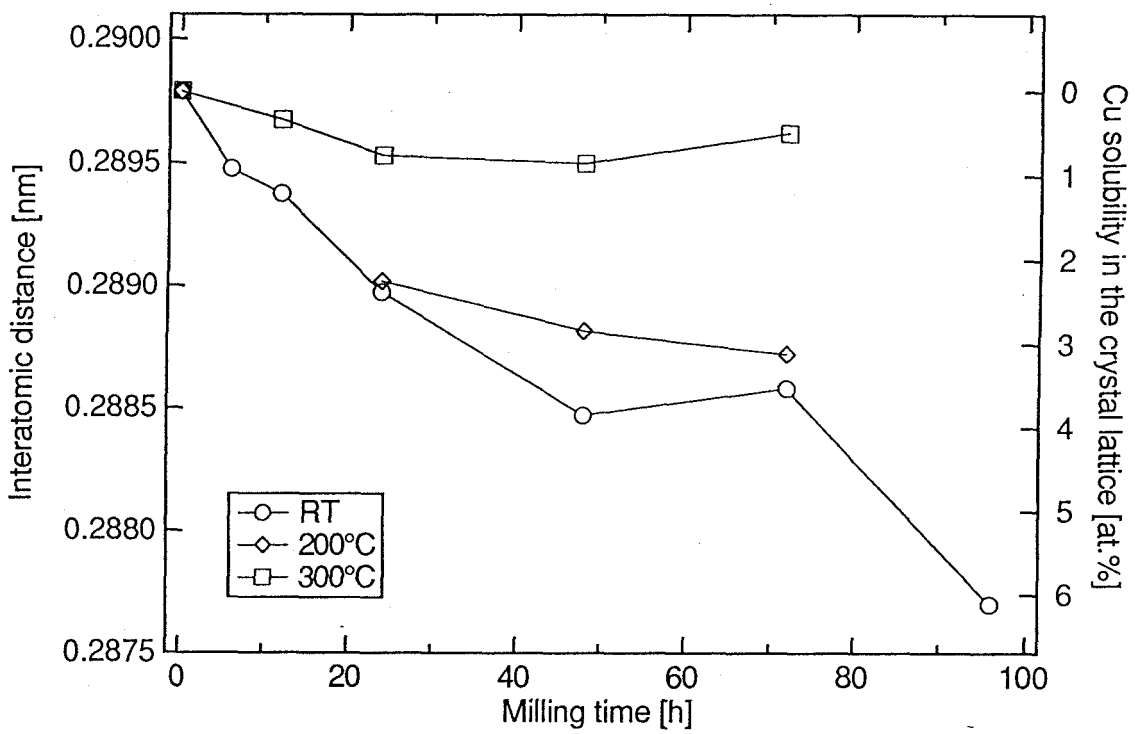

Fig. 5-3 Effect of milling temperature on the interatomic distance of $Ti_{95}Cu_5$ synthesized by ball milling.

Vegard's law, the interatomic distance have been converted to the solute concentration in the lattice. The fact that the nearest neighbor distance is larger than in the room temperature implies that the grain boundary segregation is more prominent than in the room temperature.

In HTBM, the Cu solubility in the crystal lattice is much less than in RTBM. After 72 hours of milling at 300 °C, the estimated lattice solubility is about 0.8 at.%, while in RTBM, the lattice solubility increases monotonously with milling time and most of the solute atoms are accommodated in solution in the crystalline lattice. The equilibrium solid solubility of Cu in α - Ti is much less than the observed value, in addition, its temperature dependence is almost negligible at temperatures of this range. The small lattice solubility in the early stage of ball milling suggests that in this period the mixing is incomplete and the structure is still inhomogeneous, as discussed in Chapter 3. After extended milling in RTBM, the calculated lattice solubility exceeds the overall solute concentration. This is probably due to the Fe contamination from the milling device. Even if this impurity effect is considered, the lattice solubility apparently decreases with milling time in HTBM.

5.5 Grain Growth Behavior

The microstructure evolution of ball-milled powder on heating and annealing was investigated. XRD spectra are shown in Fig. 5-4. Peak sharpening is significant at 350 °C and above. Figs. 5-5 and 5-6 indicate that the grain growth of the nanocrystalline structure takes place above 350 °C. A peak of Ti_2Cu is found in XRD spectrum at this temperature. No significant dependence on the milling temperature is observed for the grain growth behavior.

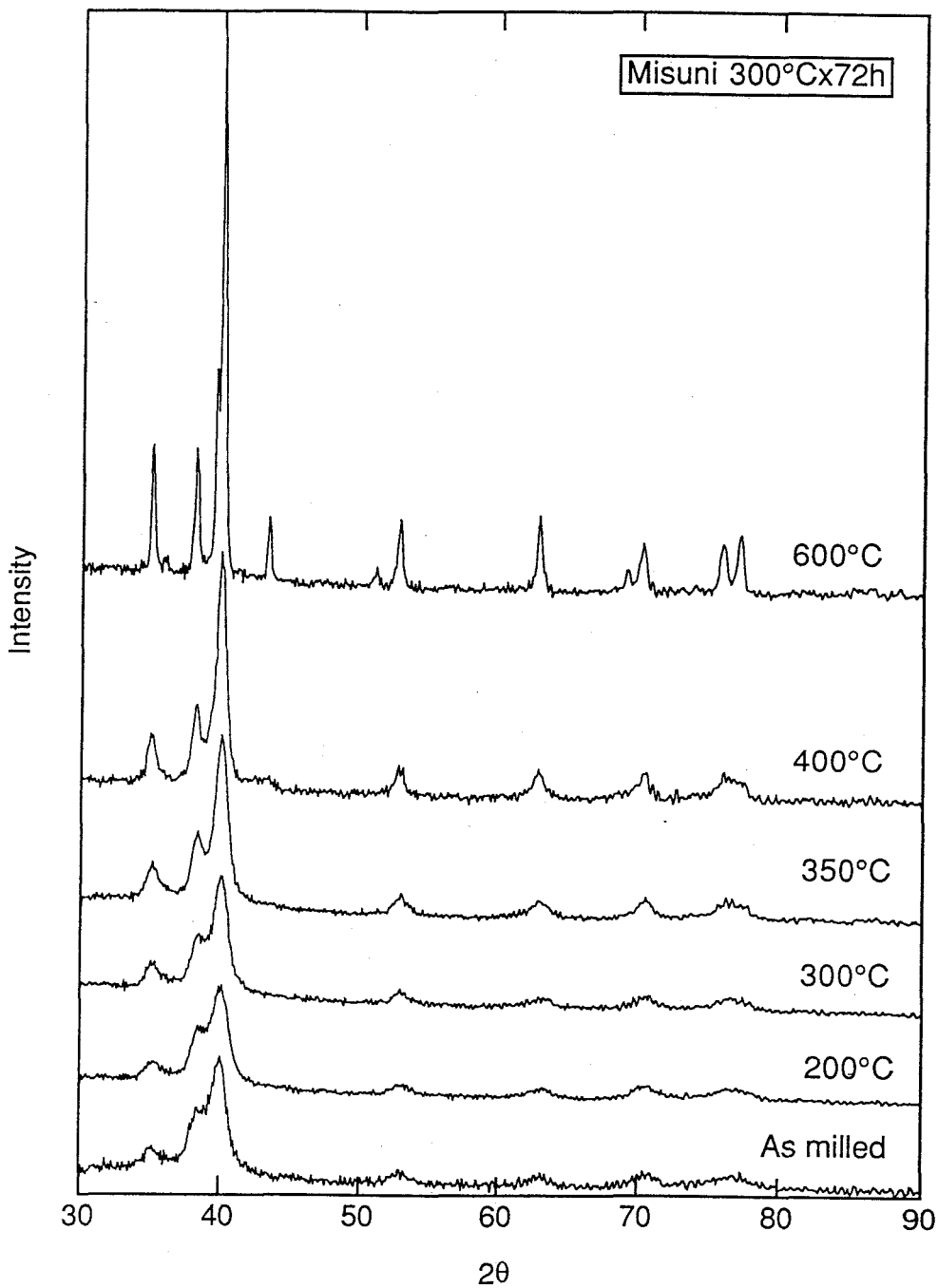

Fig. 5-4 XRD of $Ti_{95}Cu_5$ synthesized by ball milling at 300°C and heated at the indicated temperatures.

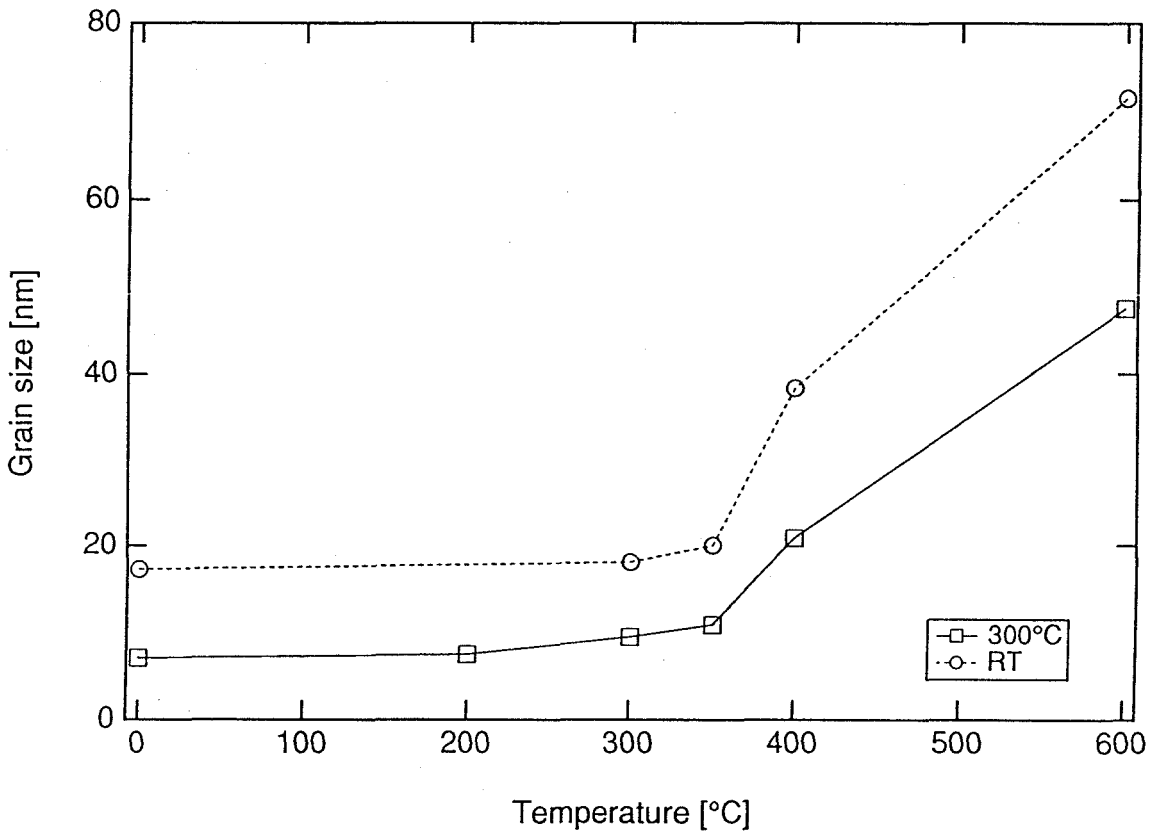

Fig. 5-5 Change of grain size of $Ti_{95}Cu_5$ synthesized by ball milling at 300°C and heated at the indicated temperatures.

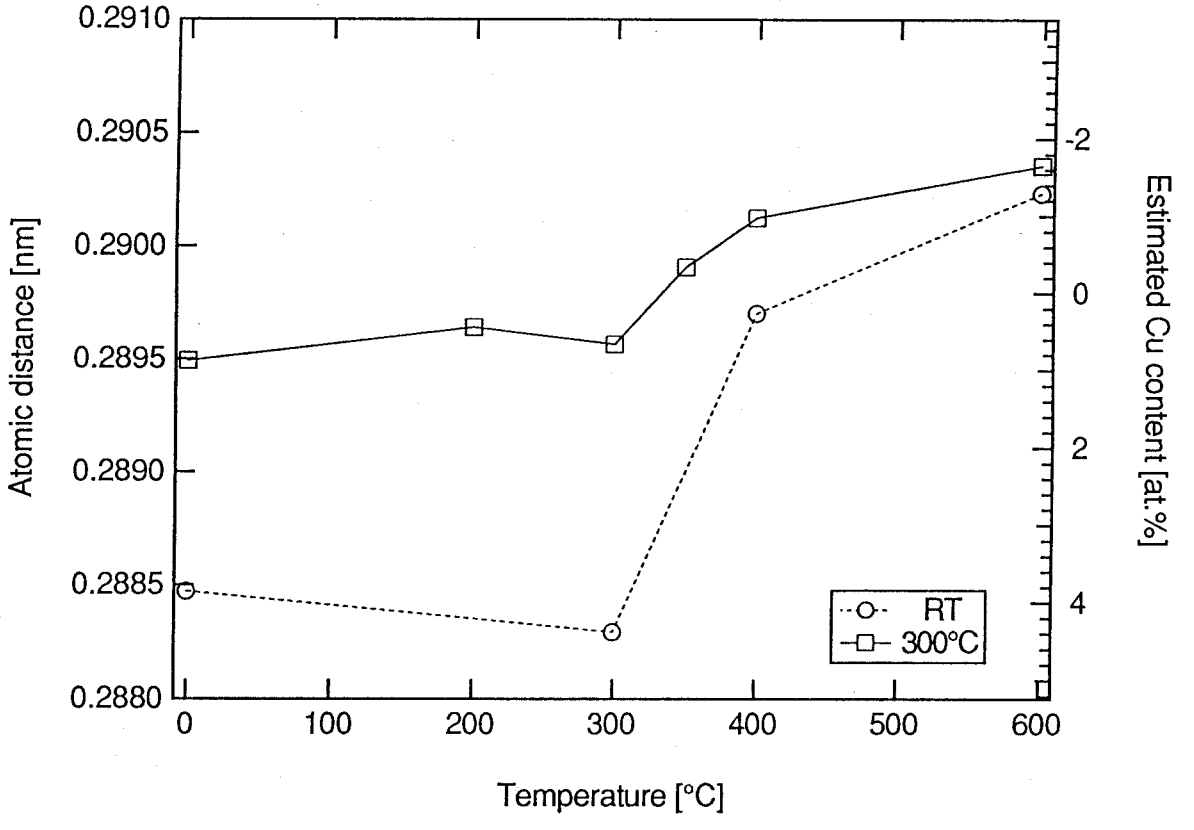

Fig. 5-6 Change of the nearest neighbor distance of $Ti_{95}Cu_5$ synthesized by ball milling at 300°C and heated at the indicated temperatures.

In contrast, annealing experiments revealed that the nanocrystalline structure produced in HTBM is more stable than in RTBM as demonstrated in Figs. 5-7 ~ 5-10. In XRD spectra, a clear difference is seen in the period of Ti_2Cu nucleation. The nucleation of Ti_2Cu is delayed by one order of magnitude in the HTBM sample. The arrows in Figs. 5-9 and 5-10 indicate the appearance of Ti_2Cu in XRD spectra, implying that the grain growth follows the nucleation of the intermetallic compound as observed in the previous study. However Fu and Johnson conducted HTBM experiments in the Zr - Al system and found that the grain growth is easier in samples produced by HTBM [102].

DSC experiments and Kissinger analysis were carried out to investigate the effect of milling temperature on the grain growth mechanism. DSC spectra in Fig. 5-11 indicate that the peak temperature shifts up in HTBM products. Kissinger plot in Fig. 5-12 demonstrates that the activation energy increases by 10 - 15 % in HTBM samples. As such, samples ball milled at 300 °C for 72 hours has high activation energy and grain growth temperature. Thus it is supposed that the nanocrystalline structure synthesized by HTBM carries high grain growth resistivity.

Similar to the result presented in Chapter 3, the activation energy of grain growth is much lower than that of homogeneous nucleation of Ti_2Cu, and higher than that of diffusion of Cu in Ti. However the heat and quench experiments demonstrated no grain growth at the peak temperature. Therefore the exothermic peak seen in DSC spectra is suspected to be due to the nucleation of Ti_2Cu rather than grain growth.

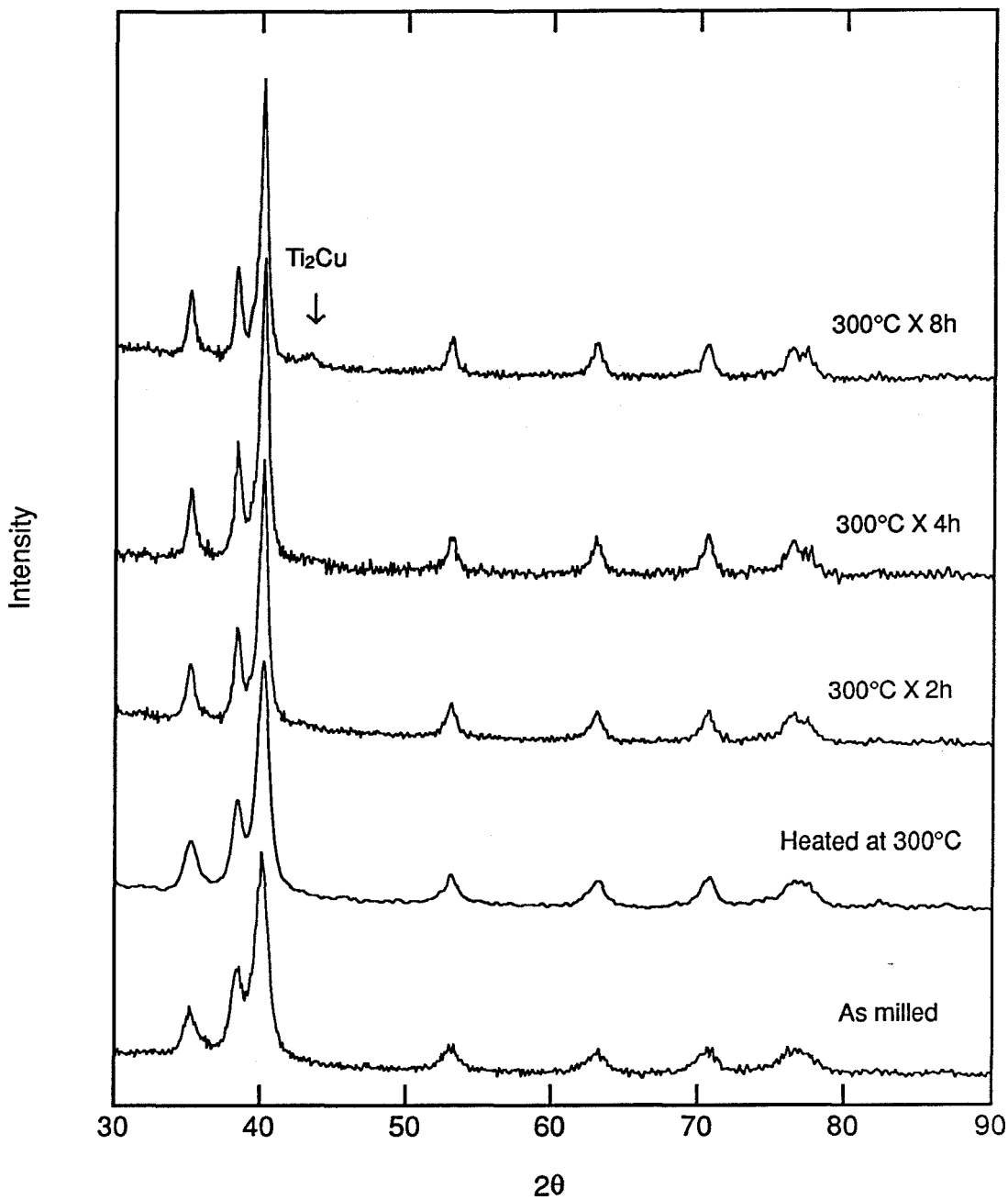

Fig. 5-7 XRD spectra of $Ti_{95}Cu_5$ synthesized by ball milling at 300 °C (with Misuni) and annealed at 300 °C for the indicated duration.

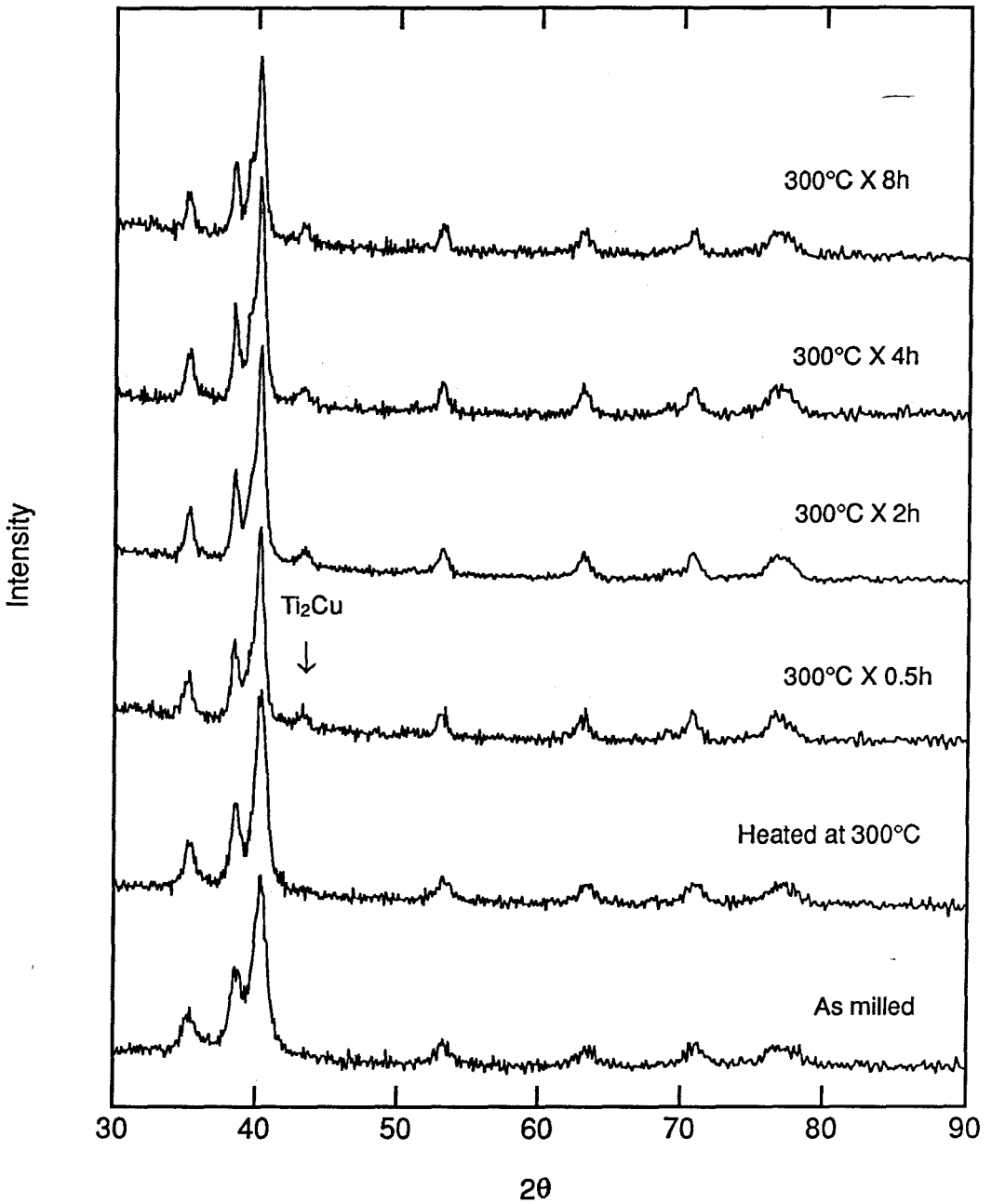

Fig. 5-8 XRD spectra of $Ti_{95}Cu_5$ synthesized by ball milling at room temperature (with Misuni) and annealed at 300 °C for the indicated duration.

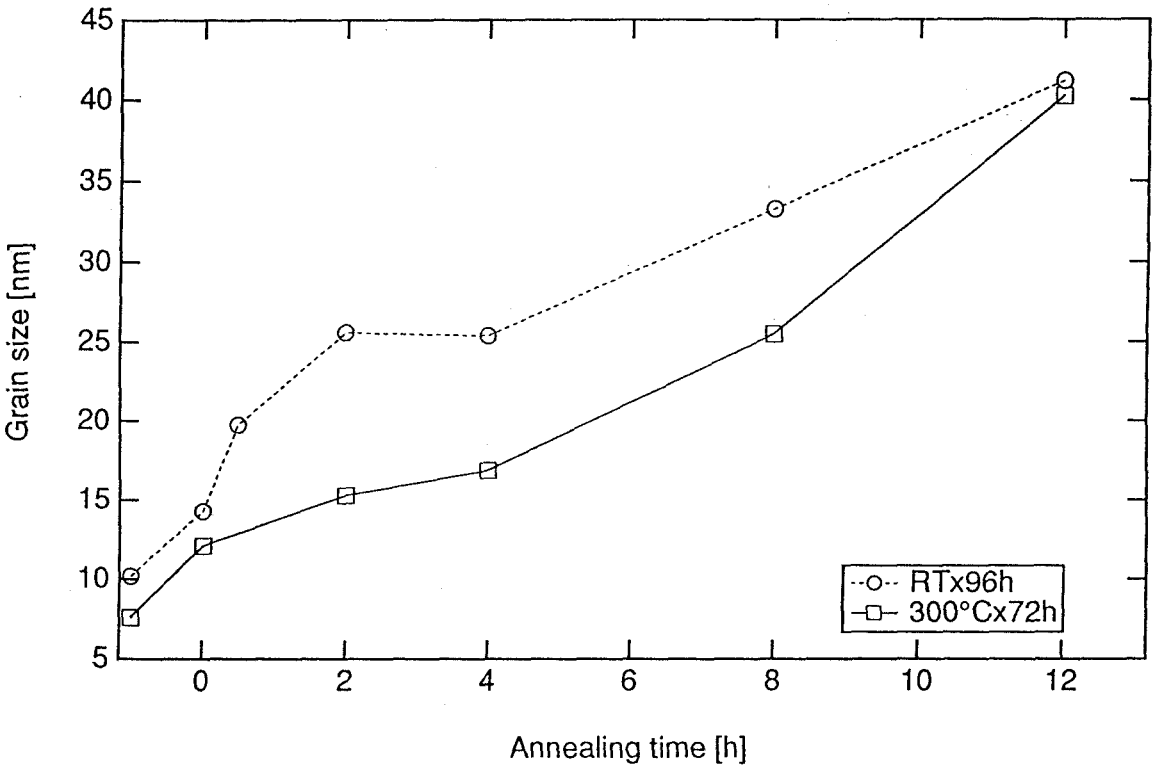

Fig. 5-9 Change of grain size of $Ti_{95}Cu_5$ synthesized by ball milling at 300°C and annealed at the indicated temperatures.

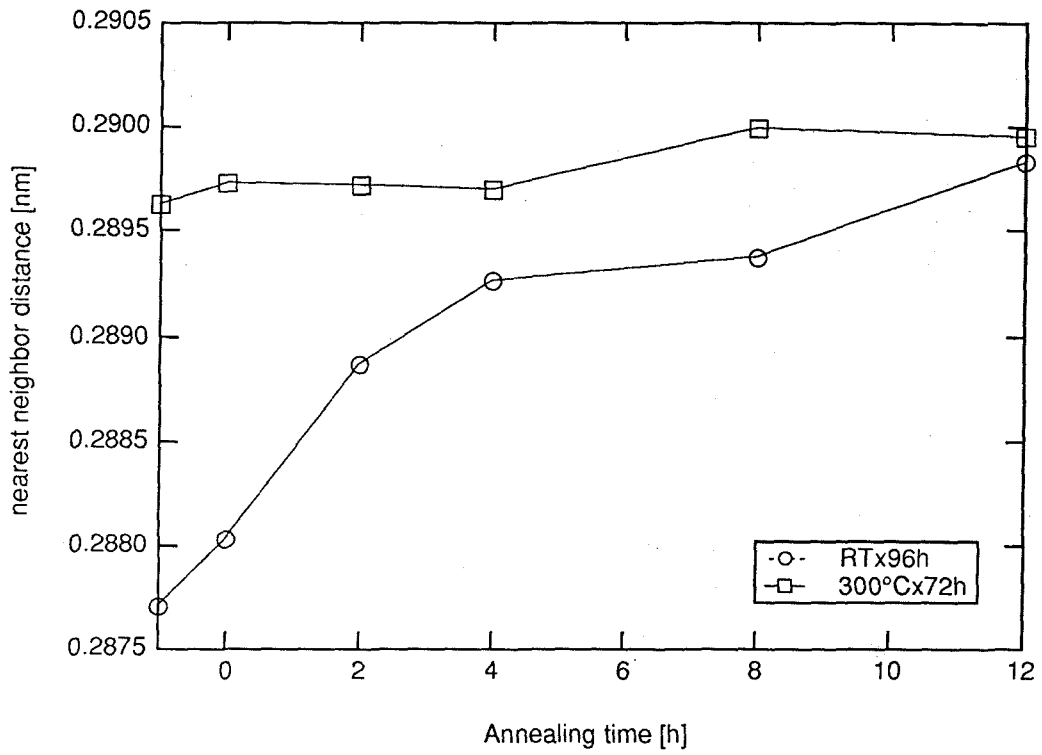

Fig. 5-10 Change of the nearest neighbor distance of $Ti_{95}Cu_5$ synthesized by ball milling at 300°C and annealed at the indicated temperatures.

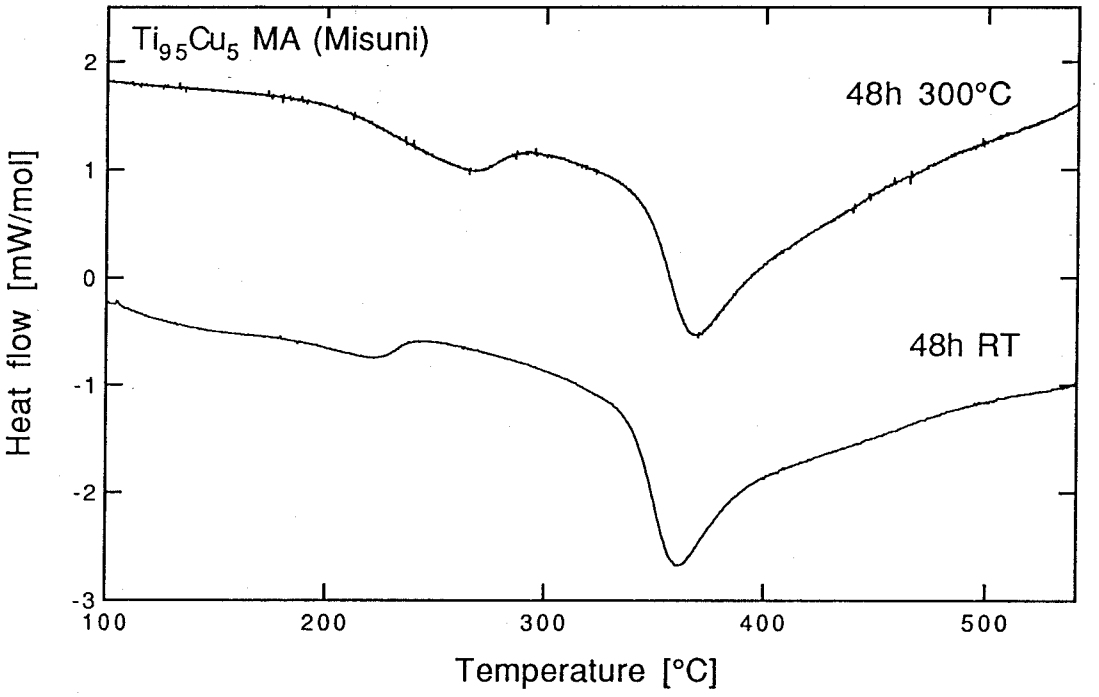

Fig. 5-11 DSC spectra of $Ti_{95}Cu_5$ synthesized by ball milling at various temperatures.

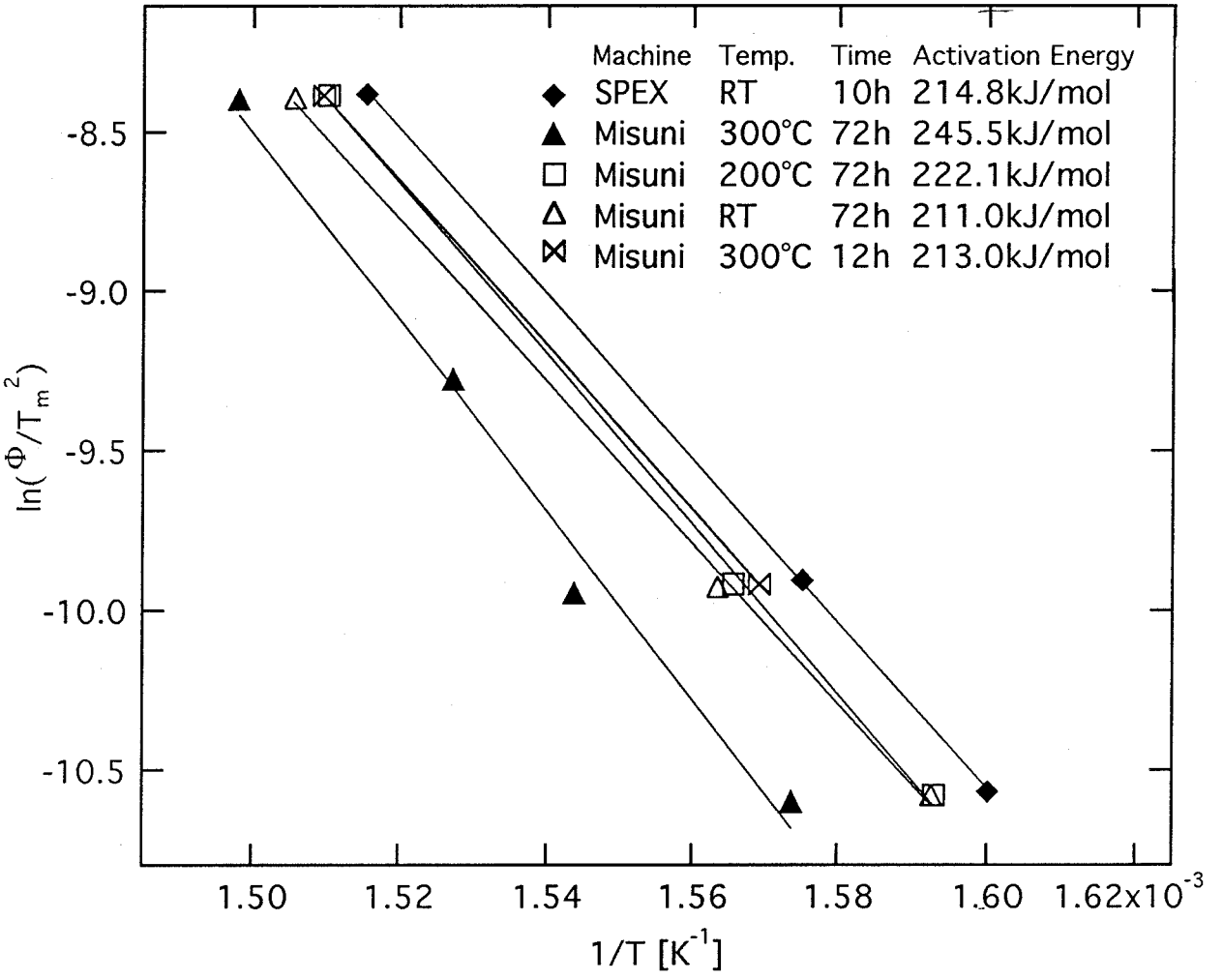

Fig. 5-12 Kissinger plot of $Ti_{95}Cu_5$ synthesized by ball milling at various temperatures.

5.6 Discussion

5.6.1 *Accelerated Nanocrystalline Structure Formation*

It has been reported that the solid-state amorphization reaction during ball milling is accelerated by high ambient temperature. Also nanocrystalline structure formation rate as the preliminary stage of amorphization is accelerated. This phenomenon is attributed to encouraged interdiffusion at the interfaces between two different species [97, 116].

A question why more grain boundaries are formed in HTBM immediately gives rise, although dynamic recovery effect is more significant in higher temperature. Lee *et al.* speculate on the SSAR that the defects of higher energy ($\sim k_B T$) created in HTBM (T > 200 °C) only play a major role in amorphization [99]. Nevertheless, the dislocation density should be lower in HTBM than in RTBM. A possible speculation is that a lot of dislocations are trapped in the crystal lattice in RTBM, while in HTBM they are all driven out of the crystal lattice and form grain boundaries. This idea may be reasonable because it has been known that solute atoms segregate along dislocations and constrain their smooth movement. In fact, solute concentration in the lattice is far less in HTBM samples.

5.6.2 *Why No Intermetallic Compound Nucleates?*

No intermetallic compounds are formed during milling at 300 °C for as long as 96 hours, although Ti_2Cu occurs by annealing at lower temperature for shorter duration. As high milling temperature increases diffusion rate, it may be likely that nuclei of critical scale form easier than in the room temperature. On the other hand, the nuclei might be destroyed during mechanical alloying. It is

evident that no nuclei remain since the grain growth in annealing is *slower* in HTBM samples. The observation that the solid-state amorphization of an intermetallic compound by mechanical grinding is also encouraged in high temperature [97] implies the destruction of crystalline nuclei might be important in the formation of nonequilibrium phases.

5.6.3 *Effect of High Temperature Milling*

It has been suspected that solute atoms tend to grain boundaries to segregate. However, chemical equilibrium is apparently not achieved at room temperature due to driving force for mixing. Indeed during RTBM, the grain boundary solute concentration is lower than during HTBM. As such, one expects a larger grain boundary energy for RTBM. During HTBM, the grain boundary energy is lowered by solute segregation and thus the grain boundary is stabilized. Consequently grain boundary formation is favored in HTBM, leading to a finer grain size.

The grain boundary is treated as a separate phase and appended in the schematic free energy diagram in Fig. 5-13. In the supersaturated solid solution, due to highly non-equilibrium condition, the chemical potential of Cu is raised to $\mu_{Cu}{}^{RT}$, hence the solid solubility is extended to $C_{Cu}{}^{RT}$ in RTBM. On the other hand, in HTBM, the decrease of solubility is interpreted in terms of the metastable equilibrium between the solid solution and the strongly segregated grain boundary phase. Note that the final lattice solubility in HTBM $C_{Cu}{}^{HT}$ is still larger than the equilibrium solubility $C_{Cu}{}^{eq}$.

In the mechanical alloying of a binary system, the atoms of the second element are driven into the crystal lattice. A supersaturated solid solution is formed unless an intermetallic compound or pure metal phase nucleates. On the

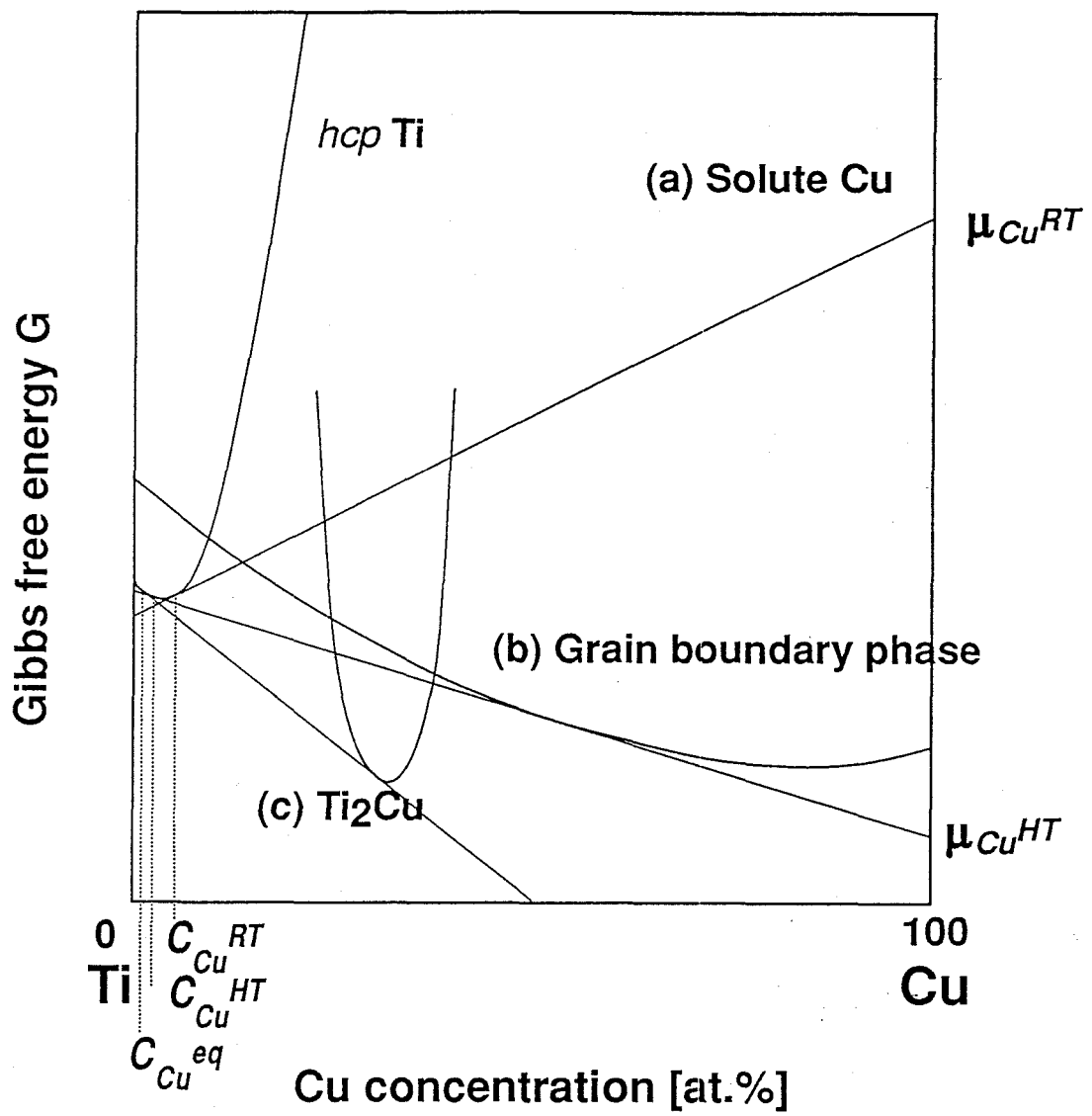

Fig. 5-13 Schematic Ti-Cu free energy diagram.

other hand, in the Ti-Cu system, strong equilibrium segregation is expected from the small solid solubility of Cu in Ti. Thus there occurs a driving force to expel the solute atoms from the matrix to the grain boundaries. This internal thermodynamic driving force may overcome the external driving force to form a supersaturated solid solution if the temperature is high enough to permit chemical diffusion. Furthermore, the mechanical breakdown of precipitate nuclei raise the free energy barrier for the nucleation of intermetallic compound or pure metal phases. Thus it is likely that in HTBM solute atoms diffuse to grain boundaries to achieve thermodynamic equilibrium. However, in RTBM, due to kinetic constraints, the mechanical driving force prevails and the system tends toward non-equilibrium supersaturation.

The enhanced stability of nanocrystalline structure prepared by the HTBM process compared with RTBM during the annealing process is interpreted as follows: solute atoms migrate to grain boundaries during heating, and form atomic clusters or the nuclei of intermetallic compounds during annealing. It is supposed in HTBM samples that the segregation is more uniform and the cluster formation is more difficult even though the initial grain boundary segregation before heating is greater. Furthermore, diffusion in fully segregated grain boundaries must be slower than in less segregated grain boundaries.

These results are somewhat counterintuitive however, because the recovery effect during milling is apparently bigger in HTBM, which implies that the defect density in the materials must be smaller in higher temperature. If grain boundaries are formed by piled up dislocations, the grain size should be bigger in HTBM samples. To interpret the present results, it is speculated that dislocations are trapped by solute atoms in the crystal lattice in RTBM, while at high temperature dislocations and solute atoms are mobile and tend to grain

boundaries. The observation that RTBM samples exhibit much larger lattice solid solubility than HTBM samples supports this idea.

5.7 Summary

By ball milling at high ambient temperature one can achieve nanocrystalline structure with a smaller grain size and greater thermal stability. We speculate that there is a metastable chemical equilibrium between the nanocrystalline phase and grain boundaries which is reached in HTBM. In contrast during RTBM, the solid solubility limit is much higher, which may imply that the external force to drive solute atoms into the crystal lattice leads to a non-equilibrium distribution of solute. The mechanism of HTBM has been discussed in terms of the potential balance to drive solute atoms either into the crystalline lattice or to grain boundaries, and it has been concluded that at high temperature the driving force to purge solute atoms to grain boundaries may prevail, and the grain boundary segregation becomes more prominent.

Chapter 6 Discussion

Global discussion on the mechanical alloying technique and nanocrystalline structure will be held in this chapter.

6.1 Mechanism of Nanocrystalline Structure Formation

The mechanism of formation of nanocrystalline structure has been investigated by Fecht *et al.* [44]. As discussed in Chap. 2, the deformation proceeds with the formation of shear bands. However the relationship between powder particle size and grain size and the effect of the deformation mode has not well been studied yet.

The mechanism of shear band formation and deformation involving shear bands have been well studied. The temperature rise in the shear bands is of great concern. Shear bands are formed at very high strain rate, when thermal softening is more significant than work hardening and strain rate hardening [117]. In titanium alloys, due to low thermal conductivity, shear band formation is not so difficult. In the Ti - 6 Al - 4 V alloy, shear band formation is reported to occur at the strain rate of 1100 s^{-1} [118]. As for the temperature rise, Me-Bar *et al.* [117] observed β transition in Ti alloys, so that the temperature rise is more than 950 °C.

In the ball milling process, the relative velocity at a ball - to - ball collision is estimated as 2 m/s [119]. Therefore high strain rate enough to form shear bands is expected. The width of shear bands is about 1 μm , much smaller than

those for conventional Ti alloys reported by Me-Bar *et al.* (3 - 40 μm) [117] and Lütjering *et al.* (~100 μm.) [118], therefore the temperature rise may be higher. However the density of shear bands may be much higher also, therefore the strain concentration can be smaller.

Yermakov *et al.* first regarded their result of solid - state amorphization as rapid melting and solidification [41]. However, later Schwarz *et al.* discussed the temperature rise during ball milling with respect to the pressure between balls, and concluded there is no melting involved [119]. So far no evidence of melting has been observed in ball milling products. There is still so much room for discussion in this topic.

The temperature shift may be a sharp thermal spike, with very high heating and cooling rates, maintaining high temperature for a very short time. No matter how high the peak is, probably no structural change by diffusion is expected. Therefore the structural evolution during collision is just mechanical mixing, and diffusional structure evolution follows as results of disorder introduced by the thermal spike, enhanced diffusion associated with high density of dislocation and overall temperature rise. In this point of view, it may be reasonable that the ambient temperature shift by 300 °C assists structural evolution effectively.

The mechanism of nanocrystalline structure formation is proposed as follows.

(1) At the early stage of ball milling, a random mixture of multiple species of atoms is produced. If, at least, one species is ductile, the original powder particles agglomerate each other and impacted, so that the product gets bigger and flaky.

(2) Atomic strain field occurs due to the intrusion of foreign atoms in the mother lattice. Then dislocations are pinned by the strain field.

(3) Shear bands start to form. The plastic deformation tends to concentrate in the shear bands. Due to heavy dislocation density, diffusion is enhanced, therefore the mixing is encouraged.

(4) Shear bands form a network. Some of them induce cracking, so that the fracture of particles is encouraged. Others may become grain boundaries. Also outside shear bands, a dislocation network is formed to be a cell structure, which finally becomes grain boundaries.

(5) As a result, grain boundary formation is accelerated and simultaneously powder formation is favored. Crashed powder particles agglomerate again into bigger particles, thus an equilibrium particle size distribution is reached.

(6) It is harder to form nanocrystalline structure of *fcc* alloys than *bcc* and *hcp* [51]. This is because dislocations are more mobile in *fcc* structure than in *bcc* or *hcp* structures, hence dislocation pinning is more unlikely in *fcc* structure.

6.2 Grain Boundary Structure of Nanocrystalline Materials

Interfaces such as surfaces, grain boundaries, phase boundaries, twin boundaries and antiphase boundaries have quite different properties as bulk materials. Therefore a lot of research has been conducted to study the interfaces. While surfaces are relatively easy to study, inner boundaries are not, and still numbers of studies are in progress.

In the previous chapters, a hypothesis that solute element segregates at grain boundaries and lowers the grain boundary energy, hence reduces grain size. Furthermore, the grain growth is hindered due to the difficulty in nucleation of intermetallic phases to eliminate segregation. In this section, the mechanism of grain growth and grain boundary structure are discussed.

6.2.1 *Grain Boundary As a Separate Phase*

There has been a concept to treat grain boundaries as a separate phase. Grain boundaries are treated as a mathematical interface with Gibbs adsorption theorem [120]. Guggenheim [121] introduced an idea to treat grain boundaries as a separate phase with finite thickness. The former approximation is mostly valid in equilibrium segregation because the influenced region by equilibrium segregation usually is not as thick as a few atomic layers [122]. However in non-equilibrium segregation, this is no more the case.

6.2.2 *Mechanism of Grain Boundary Segregation*

The mechanism of grain boundary segregation will be discussed in this section. Since neither intermetallic compound nor pure Cu phase is visible in the XRD spectrum of ball milled powder, all Cu atoms not trapped as solute in the crystal lattice most segregate to the grain boundaries.

1. Gibbs Adsorption Theorem

According to Gibbs adsorption theorem, for ideal solution, the equilibrium grain boundary energy depends on solute concentration as follows [120]:

$$\frac{d\gamma_{gb}}{dx_2} = -\Gamma_{2(1)}\left(\frac{d\mu_2}{dx_2}\right), \tag{6-1}$$

where γ_{gb} is the grain boundary free energy, $\Gamma_{2(1)}$ is the grain boundary excess of the solute, x_2 is the bulk solute concentration, and μ_2 is the chemical potential of the solute. The above equation indicates that the equilibrium grain boundary energy γ_{gb} is a monotonously decreasing function of solute concentration x_2, for stable systems ($d\mu_2/dx_2>0$) with positive adsorption ($\Gamma_{2(1)}>0$). Since solute excess is defined as the solute concentration at the interface, in short, solute elements that tend to segregate lower the grain boundary energy.

2. Mechanism of Grain Boundary Segregation

Along a grain boundary, undercoordinated atoms exist. A simple picture models the grain boundary as an array of broken bonds. The grain boundary energy is taken to be one half of total energy of the bonds broken to produce the interface [115]. Consequently, elements with less cohesive energy and weaker pair potentials will tend to occupy the sites at grain boundaries where bonds are missing. The surface free energy of solid Ti is 1.94 J/m^2 at 1300 °C, and that of Cu is 1.52 J/m^2 at 1000 °C and 1.78 J/m^2 at 925 °C [115]. Since surface energy increases as temperature decreases, Ti always has higher surface free energy than Cu at lower temperatures. As a result, Cu atoms in Ti matrix tend to segregate at the grain boundaries. On the other hand, the surface free energy of solid Nb is 2.15 J/m^2 at 2225 °C [123]. Therefore in the Nb - Cu system, it is likely that Cu tends to segregate to grain boundaries.

3. Estimated Grain Boundary Segregation

Actual tendency for segregation can be estimated from the equilibrium phase diagram. Langmuir-McLean equation was derived from entropic consideration as

$$\frac{x_b}{x_b^0 - x_b} = \frac{x_c}{1 - x_c} \exp \frac{-\Delta G}{RT}, \tag{6-2}$$

where x_c is the bulk solute molar fraction, x^0_b is the fraction of the grain boundary monolayer available for segregated atoms, x_b is the actual bulk solute fraction and ΔG is the free energy for segregation.

Seah and Hondros [124] applied gas adsorption theory by Brunauer [125] to solid- state and obtained

$$\frac{x_b}{x_b^0 - x_b} = \frac{x_c}{x_c^0} \exp \frac{-\Delta G'}{RT}, \tag{6-3}$$

where x^0_c is the solid solubility, $x^0_c = \exp(\Delta G_{sol}/RT)$, and

$$\Delta G' = \Delta G - \Delta G_{sol}. \tag{6-4}$$

Since $x_b^0 \approx 1$, one has grain boundary enrichment ratio β_b as

$$\beta_b = \frac{1}{x_c^0} \exp \frac{-\Delta G'}{RT}. \tag{6-5}$$

Furthermore, when the second phase is present, namely, $x^0_c < x_c$, then instead of Eqn. (6-3), one has

$$\frac{x_b}{x_b^0 - x_b} = \exp \frac{-\Delta G'}{RT}. \tag{6-6}$$

Eqn. (6-6) states that one can estimate equilibrium grain boundary segregation from the phase diagram. As shown in Fig. 6-1 [122], real segregation behavior is expressed pretty well with the above equation. $\Delta G'$ is derived as -10 ± 6 kJ/mol.

Actual segregation can be roughly estimated from the equilibrium phase diagram [125]. For Ti-Cu system, grain boundary enrichment of Cu in Ti-Cu solid

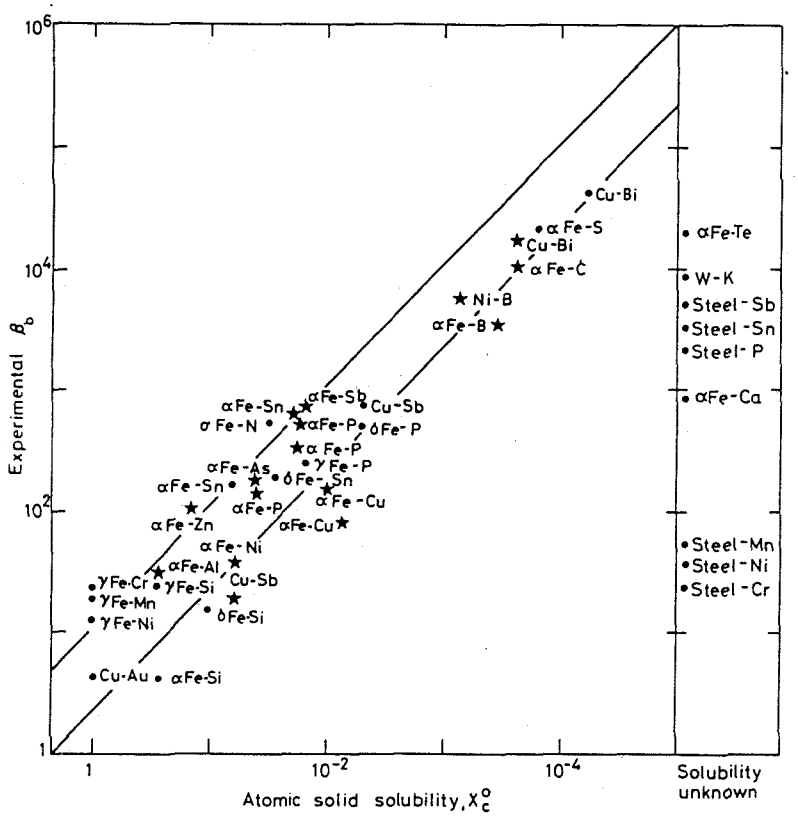

Fig. 6-1 Correlation of measured grain boundary enrichment ratios with the atomic solid solubility [122].

solution is estimated as about 10^3, for Nb-Cu system, grain boundary enrichment of Cu in Nb-Cu solid solution is roughly estimated as about 10^4 - 10^5, thus in both systems, heavily segregated grain boundaries must be expected.

4. Measured Grain Boundary Segregation

The grain growth behavior of nanocrystalline structure has been discussed in the previous chapters. It is revealed therein that, regardless of alloy system, atoms segregating at grain boundaries nucleate as intermetallic compounds or pure elemental phase to lower the free energy of the system. The grain growth immediately follows the purge of segregating atoms. This implies that there is a metastable thermodynamic equilibrium between strongly segregated grain boundaries and grains. Accordingly, it may be possible that there exists a metastable grain size as a function of overall solute concentration and temperature.

With the assumptions such that the grain boundary consists of a monatomic layer, that all the segregating atoms are accommodated in the boundary layers and that crystal grains are spherical, the solute concentration at grain boundary is estimated using measured grain size and interatomic distance. As shown in Fig. 6-2, in HTBM grain boundary solute concentration is almost constant, about 40 at.% and slightly decreases with milling time, while in RTBM it decreases with milling time monotonously. It may be due to incomplete homogenization that the measured interatomic distance is large so that the calculated solid solubility is low and the grain boundary solute concentration is estimated high. From this result it is speculated that there is an equilibrium between crystalline phase and grain boundaries, and it is gradually being reached in HTBM. On the other hand, in RTBM, the final grain boundary

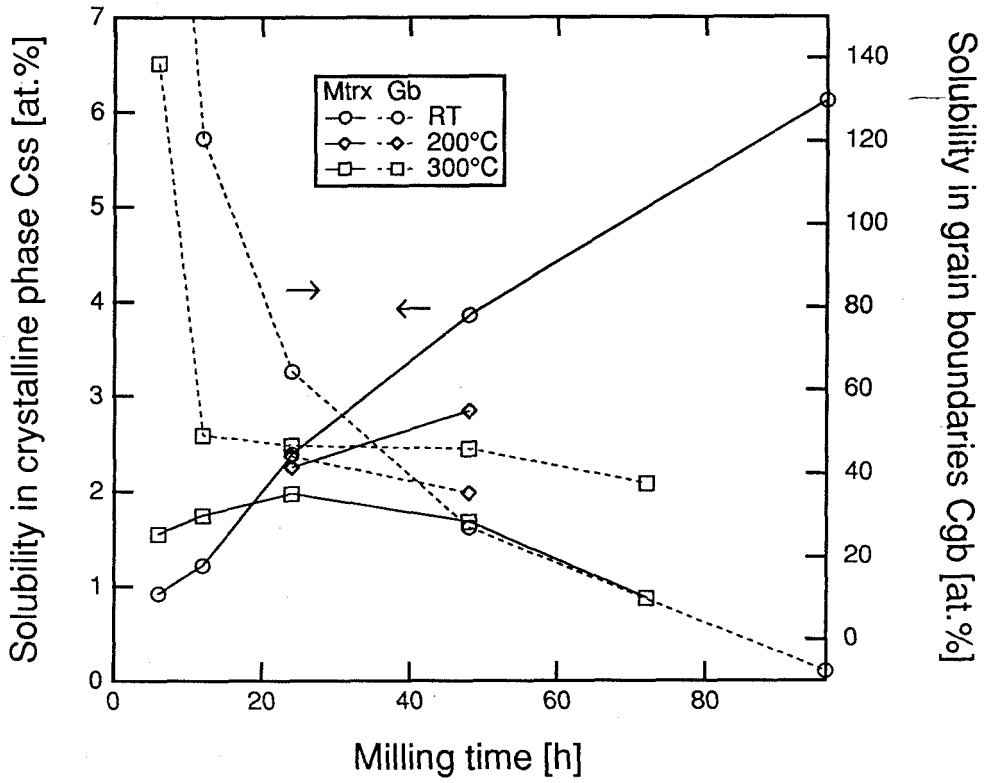

Fig. 6-2 Calculated solubility in the crystalline lattice and the grain boundaries of ball milled $Ti_{95}Cu_5$ powders. Grain boundary is assumed to be monolayer thick. Also crystal grain are assumed to be spheres.

concentration is less than this value, which may imply that the external force to drive solute atoms in the crystal lattice is still prevalent rather than equilibration.

5. Grain Boundary Thickness

Ouyang and Fultz investigated ball-milled *bcc* and *fcc* alloys with Mössbauer measurement and Monte Carlo simulation to find the grain boundary thickness of *bcc* and *fcc* alloys are 0.8 and 1.5 *nm*, respectively [127]. Fu and Johnson [102] conducted TEM observation in Zr - Al alloys synthesized by high temperature ball milling and found diffuse region between two adjacent grains.

The grain boundary thickness of nanocrystalline Ti - Cu alloys is estimated. Present results show that the Ti lattice parameters change by heating tending to the value of pure titanium. This implies that Cu atoms in the lattice either move out to boundaries or precipitate. However, rough approximation shows that some amount of Cu atoms may stay in the lattice, perhaps because grain boundaries are saturated by Cu atoms. For simplicity it is assumed that all grains are spheres with mean diameter d, and that a grain boundary is a layer with uniform thickness δ. Then the volume ratio between grain boundaries and grains is obtained as $\delta/6d$, and one can calculate the in-grain Cu concentration for a given grain size, grain boundary thickness and segregation coefficient. Note that this estimation gives a lower limit for the total grain boundary volume in a sample of a given grain size, that is, an upper limit for Cu concentration in the lattice.

The effect of grain boundary thickness and grain size on in-grain Cu concentration is shown in Fig. 6-3. The overall Cu concentration is fixed at 10 at.%, and the grain boundary Cu concentration is assumed to be 25 at.% based on the fact that the stable grain size of Ti - Cu alloys by ball milling is

extrapolated to be zero at about 19 at.% Cu composition, as demonstrated in Chapter 3 (see Fig. 3-9). Then in-grain Cu concentration is 4.7 at.% for 10 *nm* grains with 1.2 *nm* thick grain boundaries. Thus the Cu concentration in grains may still be higher than the equilibrium solubility since grain boundaries may be saturated. Accordingly the lattice expansion by heating is interpreted as the removal of Cu atoms out of the lattice.

Inversely, the grain boundary thickness of nanocrystalline $Ti_{95}Cu_5$ is estimated from observed grain boundary concentration presented in the previous section. With the grain size of 10 *nm* and almost no in-grain Cu concentration, Fig. 6-4 indicates relatively thin grain boundaries can accommodate segregating Cu atoms. This estimation agrees with the result of Ouyang *et al* [127].

6.2.3 *Liquid-like Phase at Grain Boundaries?*

It is not quite a far-fetched idea to assume a liquid-like phase at grain boundaries. Liquid phase sintering technology totally employs liquid phases penetrating solid materials along grain boundaries [128]. In recent publication *Materials Interfaces*, Clarke and Gee contributed a chapter on wetting of interfaces [129]. In engineering fields, it is not such a strange phenomenon. For instance, thin glass films are observed at room temperature in microstructure of ceramics [130]. Waseda *et al.* investigated the structure of nanocrystalline $FeZn_2O_4$ by means of anomalous X-ray scattering to find that $FeZn_2O_4$ monograin particles of 4 *nm* diameter are not contacting one another like rigid balls; instead, 0.2 *nm* wide amorphous films envelopes each particle [131].

In metals, such phenomena are seen at relatively high temperatures, for instance, when steel is annealed at high temperatures for very long time. Alloying elements lower the melting point of steels significantly. Therefore the

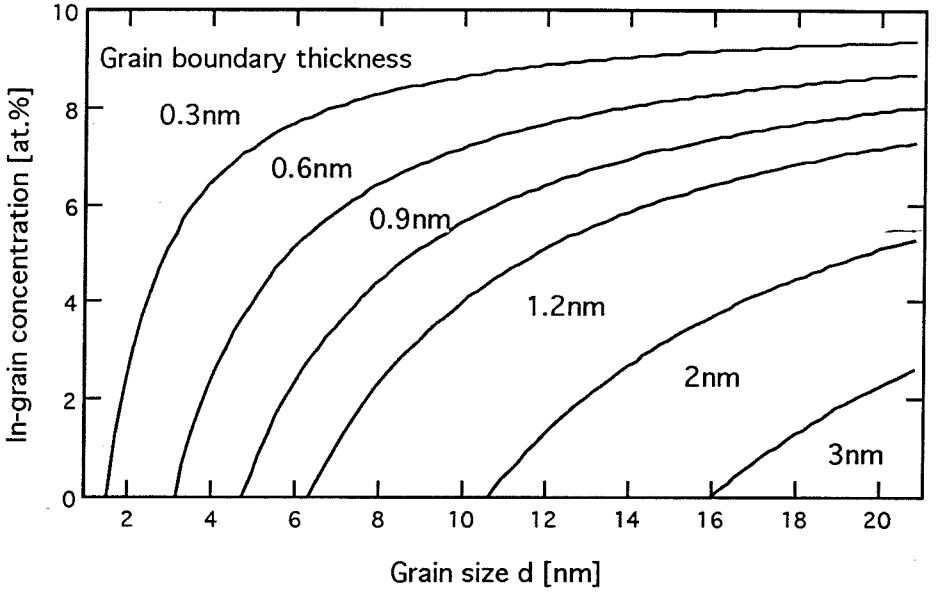

Fig. 6-3 In-grain Cu concentration in nanocrystalline $Ti_{90}Cu_{10}$ as a function of grain size, grain boundary thickness and grain boundary composition. Grain boundary accomodates 25 at.% Cu.

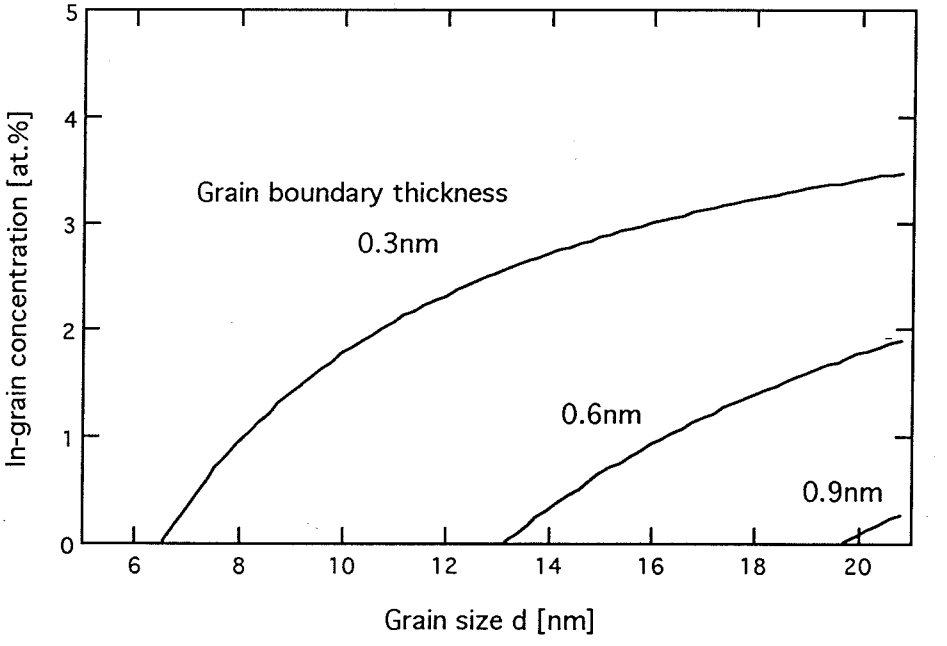

Fig. 6-4 Estimation of grain boundary thickness in nanocrystalline $Ti_{95}Cu_5$ using observed grain size(~10*nm*) and in-grain Cu concentration (almost none). Relatively thin (~0.5*nm*) grain boundaries can accomodate solute atoms.

liquid phase occurs at grain boundaries due to segregating alloying elements, and cause fracture at last [132]. Solidification segregation is usually discussed in terms of melting point and solute distribution between solid and liquid phases, however in thermodynamic point of view, it is interpreted that the liquid phase carries lower free energy than the surrounding solid phase, and the existence of liquid phase is favored because the interfacial energy of solid crystals are relatively large.

Two important phenomena must be noted: first, alloying elements or foreign species tend to interfaces such as grain boundaries or surfaces. They, in most cases, lower the interfacial energy [122], especially in the combination of strongly segregating species. Secondly, interfacial energy may be pretty smaller than grain boundary energy between the same phase if the grain boundary angle is quite large [115, 133]. Actually in some ceramics impurity segregation of hundreds of *ppms* at grain boundaries stabilizes glass phase which helps liquid-phase sintering [128].

The existence of a liquid or amorphous phase at a grain boundary possibly lowers the energy of the system. Machlin pointed out the possibility of existence of a liquid layer at a grain boundary, instead of a high-angle grain boundary [115]. Johnson pointed out that heterogeneous nucleation is favored at grain boundaries [134]. Also Spaepen [135] stated that, at grain boundaries, the nucleation of amorphous phase is easier than that of intermetallic phases. It is because an intermetallic phase nucleus at the grain boundary may form a coherent interface to one crystal, but hardly to the other.

Serebryakov [136] modeled grain boundaries as a disordered layer, and estimated grain boundary energy as a function of grain boundary thickness. He

found that the boundary free energy can take minimum at finite grain boundary thickness considering wetting effect at grain boundaries. He added that this effect is significant only in ultrafine grain structure.

The morphology of a liquid phase between two crystals strongly depends on the relative magnitude between grain boundary energy γ_{gb} and solid-liquid interface energy γ_{SL}, as drawn in Fig. 6-5 [130]. If $1 < (\gamma_{gb} / \gamma_{SL}) < \sqrt{3}$, the liquid phase occurs at grain boundary triple-points; if $\sqrt{3} < (\gamma_{gb} / \gamma_{SL}) < 2$, the liquid phase covers grain edges. Finally, if $2 < (\gamma_{gb} / \gamma_{SL})$, all grain boundary faces are covered by liquid phase [130].

Since the nanocrystalline structure consists of randomly oriented grains, the grain boundaries are mostly high-angle grain boundaries. Although neither the high-angle grain boundary energy nor the liquid-solid interface energy is known for Ti, usually the former is larger than the latter, even the angle dependence of grain boundary energy being taken into account. For example, for Cu, grain boundary energy is measured to be 0.625 J/m^2, and solid-liquid interface energy is 0.177 J/m^2 [115]. Thus, the liquid phase may occur easily at grain boundary triple points, furthermore, it may be favored for two adjacent grains to have two solid-liquid interfaces with a liquid-like disordered "phase" between them rather than to have a conventional large-angle grain boundary [115]. This liquid-like phase depicted in Fig. 6-6 has a higher free energy than the lattice structure. Accordingly its thickness, *i. e.* the grain boundary thickness, must be determined from minimizing the total energy, in the same manner as for stacking fault formation.

6.2.4 Nanocrystalline or Amorphous?

Solid-state amorphization reaction (SSAR) may be interpreted by the

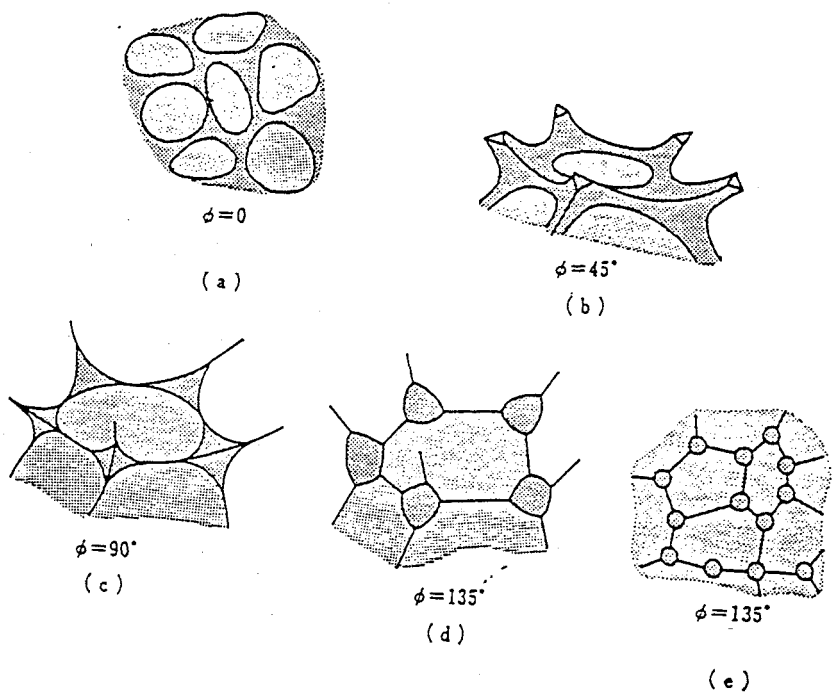

Fig. 6-5 Schematic picture of grain boundary wetting [130]. ϕ is given by $\gamma_{SS} = 2\gamma_{SL} \cos(\phi/2)$, where γ_{SS} and γ_{SL} are interfacial free energies between solid/solid and solid/liquid, respectively. (a) and (e) are cross section view, perspective view otherwise.

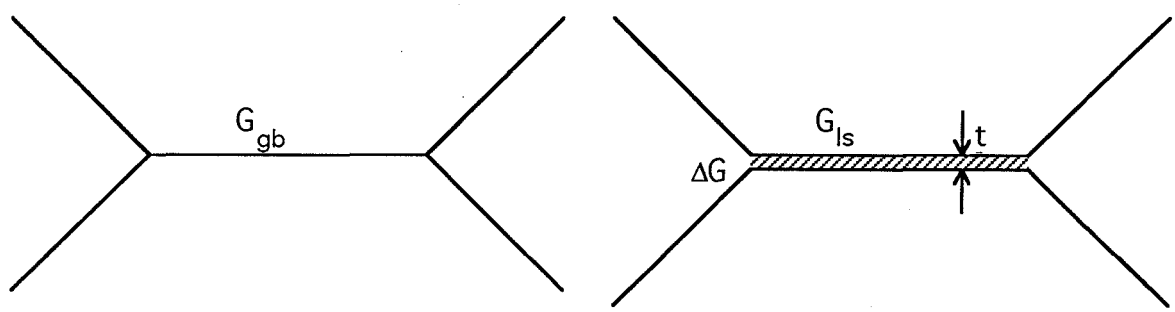

G_{gb} > $2G_{ls} + \Delta G\, t$

(a) high angle grain boundary (b) grain boundary with a liquid layer

Fig. 6-6 Schematic picture of "liquid-like" phase at a grain boundary. Liquid phase may be more stable than grain boundaries.

growth of grain boundary "phase" in thickness and grain size reduction to a certain threshold.

There are some evidences reported so far to show the relationship between grain boundaries and solid state amorphization phenomena. In Cu-Y system, amorphous phase is observed to form along Y-Y grain boundaries as a layered structure [137]. Meng *et al.* reported that no amorphous nucleation at the boundary between Ni single crystal substrate and sputtered polycrystalline Zr [138]. Ni grain boundaries are essential for amorphous phase to occur. Busch *et al.* studied Co - Zr double layers with Atom Probe Field Ion Microscopy, and found that amorphization occurs at Zr - Zr grain boundaries, where Co atoms are highly segregated [139].

Radial distribution function is a good measure to study short range order in amorphous materials. Recent studies with anomalous X-ray scattering revealed that the more bonds of same species are seen in amorphous alloys synthesized by solid state processes than those by rapid quenching [119, 140, 141]. Since the heat of mixing is usually large negative in amorphous-forming binary system, and since mechanical milling forces atomic random mixing rather than forming bonds of same species, it is natural to think that there is an unknown mechanism that favors bonds of same species. Suzuki suggested that the structure might be microscopically phase-separated [142]. This could be an evidence that amorphous structure is the extreme result of crystal size refinement by mechanical milling, with considering that nanocrystalline structure formation is the preliminary stage of the solid-state amorphization.

Jorra *et al.* [63] studied nanocrystalline Pd synthesized by gas condensation with small-angle neutron scattering and found that the structure

consists of densely packed non-spherical crystallites surrounded by medium made of incoherent low density interfaces. Their result implies that the grain boundary is rather a distinct bulky phase than a layer of uniform thickness. On the contrary, TEM study on nanocrystalline alloys produced by gas condensation demonstrated sharp and straight grain boundaries [3]. Trudeau *et al.* conducted high-resolution TEM study on ball-milled Fe alloys and reported sharp grain boundaries [143]. Thus Siegel [8] concluded that the disorder associated with grain boundaries ranges in less than 0.4 *nm*, for both gas condensation and ball milling.

Then what determines whether the system goes to amorphous, or stay in nanocrystalline state? A hypothesis that the free energy of grain boundary "phase" is thickness-dependent is proposed. The present result shown in Chap. 3 and the report by Eckert *et al.* [101] indicated that the stable grain size of nanocrystalline structure decreases with more solute concentration. These results imply that the grain boundary energy drops with more solute segregation. Hence the enthalpy of mixing of the grain boundary phases is negative, probably, like liquid phases.

Since disordered grain boundary structure is located adjacent to ordered lattice structure, gradual change of order in grain boundary is expected along thickness direction. Therefore the surface of the grain boundary phase might be influenced by the adjacent crystals. Fecht *et al.* argue that a crystalline state can be unstable under certain condition and polymorphically collapse to a liquid or amorphous phase. Then below the equilibrium temperature the crystalline solid can melt to the amorphous solid by addition of alloying element [144]. Hence the free energy difference between the ideal glass and crystalline state ΔG_{SL} reduces to zero. However, when the grain boundary layer is thin, it may not apply.

Liquid phase has higher free energy than crystalline phase, therefore $\Delta G_{SL} > 0$. Accordingly ΔG_{SL} must be thickness-dependent: it may be decreasing and reduces to zero at a certain thickness.

Consequently the above question is understood in the following manner. If the system can store energy enough to build grain boundaries thicker than the critical thickness, then no more energy is required to increase the thickness of the grain boundaries, thus the system becomes amorphous completely. Otherwise, the system settles in the nanocrystalline structure, the metastable equilibrium between crystals and grain boundaries with the maximum grain boundary thickness the system can achieve. However, no convincing proof has ever been obtained.

6.3 Future Prospect

In this thesis, I have discussed on the hypotheses that the grain boundary segregation hinders grain growth, ant that the grain boundaries in nanocrystalline alloys synthesized by mechanical milling has a liquid-like disordered structure. Various attempts have been made to verify them. However, no convincing proof has been obtained. In TEM study, the thin area enough for grain boundary observation may not be obtained easily. SAXS experiments are also bothered by the same trouble.

Recent progress in electron microscopy enables us to observe and conduct chemical analysis of very fine region as small as 1 nm using Field-Effect Analytical Electron Microscopy (FE-AEM) [145]. The electron probe size can be thinner than 1 nm.. Although this apparatus is neither so popular nor easy to reach, in a few years or so, it will be available for studying nanocrystalline

materials.

6.4 Summary

In order to interpret the nanocrystalline structure formation and grain growth behavior, a hypothesis that the grain boundary segregation has been proposed. Theoretical consideration and experimental study confirmed that the segregation can lower the grain boundary energy and thus stabilize the nanocrystalline structure against grain growth. Although inconclusive, the relationship between solid state amorphization and nanocrystalline structure formation has been discussed.

Chapter 7 Conclusion

Nanocrystalline alloys have been prepared with the ball milling technique. Structure consisting of nanometer-sized crystal grains were synthesized. The mechanism of deformation and nanostructure formation has been discussed. Diffuse grain boundaries found in a nanocrystalline Ti - Cu alloy synthesized by mechanical alloying suggests that a disordered structure is formed in grain boundaries.

Thermodynamic stability of the nanocrystalline structure has been studied. It was found that the grain growth is not normal grain growth but preceded by the nucleation of an intermetallic compound on heating or annealing.

These observations are interpreted in terms of a hypothesis that grain boundary segregation stabilizes grain boundaries. This hypothesis is supported by assuming a "liquid-like" grain boundary structure.

At last, a novel method to produce "more stable" nanocrystalline alloys by means of high temperature ball milling was proposed. The stability of nanocrystalline structure produced with this method can be interpreted with the above hypothesis. This technique provides a clue to control grain size as desired.

Appendix Small Angle X-ray Scattering: Theory

When a small homogeneous object is hit by X - ray beam, the scattered beam spreads and forms a central peak of width ε, which is given by

$$\varepsilon = \frac{\lambda}{d}, \tag{A-1}$$

where λ is the wavelength of the incident beam and d is the characteristic length of the object. This relation holds irrespective of the shape of the object.

The upper limit of the measurable object size with SAXS is given by this equation. Assuming a Cu - $K\alpha$ radiation X - ray source (λ = 1.54 Å) is used, then if the angular resolution of the detector is 0.001 rad, particles as big as 1540 Å can be detected. The lower limit is usually determined by other constraints, such as the geometry and the sensitivity of the detector. The smaller a particle is, the broader and lower the central peak becomes. Therefore the length of the detector determines the lower limit. In addition, it becomes difficult to distinguish the peak from the background. Usually the lower measurable limit of dimension is 10 Å. However, it has been known that SAXS is also affected by the roughness of the interface between two regions. Therefore it is difficult to separate these two effects.

In SAXS, as mentioned, electron density inhomogeneity is detected. The inhomogeneity may or may not be particulate, however it must be statistically isotropic, and with no long range order.

1. Scattering by an electron

When X-rays hit an electron, it vibrates and releases a spherical scattered wave. The intensity of the scattered wave $I(\theta)$ at scattering angle θ at the distance a is given by Thomson formula:

$$I(\theta) = \frac{I_e}{a^2}, \tag{A-2}$$

where,

$$I_e = \left(\frac{e^2}{mc^2} \right)^2 \frac{1+\cos^2\theta}{2} I_0 . \tag{A-3}$$

I_0 is the intensity of the primary beam. $(e^2/mc^2)^2 = 7.90 \times 10^{-26}$ cm^2 is the differential cross section of an electron, the square of the classical electron radius. As for small angle θ, $I(\theta)$ is almost constant, it will be omitted in the following equations for briefness.

2. Scattering by a matter

Assume the coherent scattering of a plane wave by a matter of volume V. Then the total scattering amplitude, referred to structure factor, F at angle θ is given by,

$$F(\boldsymbol{q}) = \int_V \rho(\boldsymbol{r}) e^{-i\boldsymbol{q}\cdot\boldsymbol{r}} dV, \tag{A-4}$$

where $\rho(\boldsymbol{r})$ is the electron density in the matter, λ is the wavelength of the incident beam. θ is replaced by $\boldsymbol{q}$, scattering vector, which is parallel to Δk,the change of the wavevector by the scattering, and given by

$$q = (4\pi/\lambda)\sin\theta. \tag{A-5}$$

The scattering intensity $I(\boldsymbol{q})$ is then obtained by:

$$I(\boldsymbol{q}) = FF^* = \iint \rho(\boldsymbol{r}_1)\rho(\boldsymbol{r}_2)e^{-i\boldsymbol{q}\cdot(\boldsymbol{r}_1-\boldsymbol{r}_2)}dV_1dV_2, \tag{A-6}$$

Defining autocorrelation function by

$$\tilde{\rho}^2(\boldsymbol{r}_1-\boldsymbol{r}_2) = \int \rho(\boldsymbol{r}_1)\rho(\boldsymbol{r}_2)dV_1 = \langle\rho(\boldsymbol{r}_1)\rho(\boldsymbol{r}_2)\rangle V, \tag{A-7}$$

then one has,

$$I(\boldsymbol{q}) = \int_V \tilde{\rho}^2(\boldsymbol{r})e^{-i\boldsymbol{q}\cdot\boldsymbol{r}}dV. \tag{A-8}$$

Note that $\boldsymbol{r}_1$ - $\boldsymbol{r}_2$ in the above equation has been replaced by $\boldsymbol{r}$.

For a statistically isotropic system, $\rho(\boldsymbol{r}) = \rho(r)$, likewise $e^{-i\boldsymbol{qr}}$ can be repalced by $\langle e^{-i\boldsymbol{qr}}\rangle = \sin qr/qr$ [146], thus the above equation becomes

$$I(q) = \int_V 4\pi r^2\tilde{\rho}^2(r)\frac{\sin qr}{qr}dr. \tag{A-9}$$

This simplification is indispensable for easy calculation. Hence the isotropy is one of the essential requirement for a SAXS sample. In the same fashion, by defining the electron density fluctuation $\Delta\rho(r) = \rho(r) - \langle\rho\rangle$, one has correlation function $\gamma(\boldsymbol{r})$ [147] such as

$$\gamma(r) = \langle\Delta\rho(r_1)\Delta\rho(r_2)\rangle, \tag{A-10}$$

where $r = |\boldsymbol{r}_1 - \boldsymbol{r}_2|$. Thus,

$$I(q) = V\int_0^\infty 4\pi r^2\gamma(r)\frac{\sin qr}{qr}dr. \tag{A-11}$$

By inverse Fourier transform,

$$\gamma(r) = \frac{1}{2\pi^2 V}\int_0^\infty q^2 I(q)\frac{\sin qr}{qr}dq. \qquad \text{(A-12)}$$

As seen in Eqn. (A-11), if the material has a long range order, $\gamma(r)$ does not vanish at high r region, therefore $I(q)$ does not converge. Thus the lack of long range order in the sample is also the essential requirement in SAXS.

From the definition of the correlation function and Eqn. (A-11), one has,

$$\gamma(0) = \frac{1}{2\pi^2 V}\int_0^\infty q^2 I(q)dq = (\Delta\rho)^2. \qquad \text{(A-13)}$$

As this quantity is a material constant and independent of the measurement, one may define an invariant Q as:

$$Q \equiv \int_0^\infty q^2 I(q)dq. \qquad \text{(A-14)}$$

To separate geometrical component, define the chord distribution function $\gamma_0(r)$ as

$$\gamma(r) = (\Delta\rho)^2 \gamma_0(r). \qquad \text{(A-15)}$$

Since the correlation function gives the spread of the region of dense electron, the width of the correlation function gives the size of the inhomogeneous region. This quantity is referred to correlation length lc, and given as follows:

$$l_c = 2\int_0^D \gamma_0(r)dr \qquad \text{(A-16)}$$

Using invariant Q, one can compute the correlation length only with

measured quantities,

$$l_c = \frac{\pi}{Q}\int_0^\infty I(q)qdq. \tag{A-17}$$

3. Guinier Approximation

Now assume an object containing particles. The particles may not be isometric but must have three orthonormal axes of symmetry. In addition, they have to be randomly oriented. The structure factor is calculated as,

$$F(\boldsymbol{q}) = \Delta\rho\int_V \cos(\boldsymbol{q}\cdot\boldsymbol{r})dV. \tag{A-18}$$

For the central part, cos $\boldsymbol{q}\cdot\boldsymbol{r}$ can be expanded as 1 - $(\boldsymbol{q}\cdot\boldsymbol{r})^2/2$+...., thus Eqn. (A-18) becomes for small $\boldsymbol{q}$,

$$F(\boldsymbol{q}) \cong \Delta\rho V\left\langle 1-\frac{(\boldsymbol{q}\cdot\boldsymbol{r})^2}{2}\right\rangle = \Delta\rho V\left(1-\frac{\langle(\boldsymbol{q}\cdot\boldsymbol{r})^2\rangle}{2}\right). \tag{A-19}$$

Note that higher order terms have been dropped. Guinier introduced an exponential form expression to approximate Eqn. (A-19) [148],

$$F(\boldsymbol{q}) \cong \Delta\rho V\exp\left\langle -\frac{(\boldsymbol{q}\cdot\boldsymbol{r})^2}{2}\right\rangle. \tag{A-20}$$

Then, the scattering intensity is

$$I(\boldsymbol{q}) \cong (\Delta\rho V)^2\exp\left\langle -(\boldsymbol{q}\cdot\boldsymbol{r})^2\right\rangle. \tag{A-21}$$

A quantity called radius of gyration R_G is defined by

$$R_G^2 = \frac{\int_V r^2 dV}{V}, \tag{A-22}$$

then as $\left\langle (\boldsymbol{q}\cdot\boldsymbol{r})^2 \right\rangle = \frac{q^2}{V}\int_V r^2 dV = \frac{q^2 R_G^2}{3}$ for fixed $\boldsymbol{q}$, thus, one has

$$I(\boldsymbol{q}) = (\Delta n)^2 \exp\left(-\frac{R_G^{\,2}}{3}q^2\right), \qquad \text{(A-23)}$$

where $\Delta n = \Delta\rho V$ is the number of excess electrons in the object. Thus SAXS spectrum tends to a straight line near $q = 0$ on a $\log I$ - q^2 plot.

Apparently from its definition, the radius of gyration provides the characteristic dimension of the object. In addition, note that this conception applies for particulate ststems only. The treatment for non-particulate systems will be discussed later.

4. Porod Approximation

Another approximation was proposed by Porod [149, 150] and later by Debye [151] independently. For small r, in a particulate system, the chord distribution function can be expanded as:

$$\gamma_0(r) = 1 - ar + br^2 + cr^3 + \cdots \qquad \text{(A-24)}$$

where a, b, c,... are constants. Porod showed that $a = S/4V$ graphically, hence,

$$\gamma_0(r) = 1 - \frac{S}{4V}r + br^2 + cr^3 + \cdots \qquad \text{(A-25)}$$

where S is the total area of the surface of the object. Then Eqn. (A-11) becomes:

$$I(q) \equiv (\Delta\rho)^2 V \int_0^D 4\pi r^2 \left(1 - \frac{S}{4V}r + br^2 + cr^3 + \ldots\right)\frac{\sin qr}{qr}\,dr. \qquad \text{(A-26)}$$

Here the upper limit of the integral is replaced by D, the largest dimension of the object where $\gamma(D)$ is non-negative. Computing this integral, as q increases, one has a fourth power relationship so-called Porod's law,

$$I(q) \to (\Delta\rho)^2 \cdot \frac{2\pi}{q^4} \cdot S. \qquad \text{(A-27)}$$

Thus SAXS spectrum tends to a straight line of slope -4 on a log$I$ - log$q$ plot.

Notice that when the internal surface in not smooth, this relation have to be modified. If the surface is a fractal with the fractal dimensionality D, then the surface area S is no more a constant, accordingly the surface area goes like $S \sim r^D$, where r is the characteristic length of the object. As $V \sim r^3$, in Eqn. (A-26), $S/V \sim r^{D-3}$, consequently Eqn. (A-27) becomes:

$$I(q) \sim (\Delta\rho)^2 \, q^{-(6-D)}. \qquad \text{(A-28)}$$

as q increases. Thus a smooth and sharp interface gives a Porod slope -4, however when the interface becomes dull and unclear, the final slope deviates from -4.

5. Anisometric Particles

Considering that $e^{iq\cdot r} = \exp\{iq(a\alpha + b\beta + c\gamma)\}$, where a, b, c are x, y, z components of $\boldsymbol{r}$, α, β, γ are cosines between each axis and $\boldsymbol{q}$. Then Eqn. (A-4) is written as

$$F(q) = \Delta\rho \iiint_V \frac{\sin qx\alpha}{qx\alpha} \cdot \frac{\sin qy\beta}{qy\beta} \cdot \frac{\sin qz\gamma}{qz\gamma} dxdydz. \qquad \text{(A-29)}$$

To estimate the contribution of z-component, ignoring the fact that a, b, c are not independent, one has for z-direction

$$\int_{-L/2}^{L/2} \frac{\sin qz\gamma}{qz\gamma} dz = L \frac{\sin(qL\gamma/2)}{qL\gamma/2}, \tag{A-30}$$

where L is the length of the particle. Consequently, z-component intensity contribution I_Z goes like:

$$I_z \propto L^2 \int_0^1 \left(\frac{\sin(qL\gamma/2)}{qL\gamma/2} \right)^2 d\gamma \approx \frac{\pi L}{q}. \tag{A-31}$$

For anisometric particles, the above assumption is valid. However, if L is extremely large, then Eqn. (A-31) becomes invalid and it reduces to 1. As a result, for an acicular particle elongated to z-direction, a factor of q^{-1} is removed from the expression Eqn. (A-27), and $I(q)$ goes like q^{-3} in the Porod region. Similarly, for plate-like particles, whose two dimensions are extremely larger than the other, then q^{-2} is eliminated from Eqn. (A-27), and Porod law becomes $I(q) \sim q^{-2}$.

6. Non-Particulate System

For a non-particulate system of a mixture of phase 1 and 2 with mole fractions of φ_1 and φ_2, respectively, the correlation function is:

$$\gamma(r) = \varphi_1 \varphi_2 (\Delta\rho)^2 \gamma_0(r), \tag{A-32}$$

and the scattering intensity goes:

$$I(q) = V\varphi_1 \varphi_2 (\Delta\rho)^2 \int_0^\infty 4\pi r^2 \frac{\sin qr}{qr} \gamma_0(r) dr. \tag{A-33}$$

Porod law is slightly modified into,

$$I(q) \to V\varphi_1 \varphi_2 (\Delta\rho)^2 \cdot \frac{2\pi}{q^4} \cdot S. \tag{A-34}$$

Thus the fourth power law remains valid for non-particulate systems. In addition, the modification for internal surface applies in the same fashion. Although, as mentioned, the radius of gyration loses its physical meaning in such a system, the correlation length still carries an importance as an index of the size of inhomogeneity.

References

[1] J. W. Cahn: *Nature*, 348 (1990) 389.

[2] H. Gleiter and P. Marquardt: *Z. Metall.*, 75 (1984) 263.

[3] H. Gleiter: *Prog. Mat. Sci.*, 33 (1989) 223.

[4] H. Gleiter: *NanoStructured Mater.*, 1 (1992) 1.

[5] R. Birringer: *Mat. Sci. Eng.*, A117 (1989) 33.

[6] R. Birringer, H. Gleiter and P. Marquardt: *Phys. Lett.* A, 102 (1984) 365.

[7] R. Birringer, U. Herr and H. Gleiter: *Trans. Jpn. Inst. Met.*, (Suppl.), 27 (1986) 43.

[8] R. W. Siegel: in *"Materials Interfaces"*, edited by D. Wolf and S. Yip, Ch. 16 (1992) [Chapman & Hall].

[9] W. L. Johnson: *Prog. Mat. Sci.*, 30 (1986) 81.

[10] R. W. Cahn: *Colloq. de Physique*, 51, (1990) C4-3.

[11] C.-P. P. Chou and D. Turnbull: *J. Non-Cryst. Solid*, 17 (1975) 169.

[12] D. Turnbull: Met. Trans., 12B (1981) 217.

[13] A. Inoue, T. Nakamura, N. Nishiyama and T. Masumoto: Mat. *Trans. JIM*, 33 (1992) 937.

[14] A. M. El-Sherik, K. Boylan, U. Erb, G. Palumbo and K. T. Aust: *Mat. Res. Soc. Symp. Proc.*, 238 (1992) 727.

[15] R. Birringer: in *"Nanophases And Nanocrystalline Structures"*, The Minerals, Metals & Materials Society, *to be published.*

[16] Y. Seki and W. L. Johnson: A. H. Clauer and J. J. deBarbadillo eds., in *"Solid State Powder Processing"*, (1990) 287 [The Minerals, Metals & Materials Society].

[17] M. Uda: *NanoStructured Mater.*, 1 (1992) 101.

[18] R. F. Bunshah: *Thin Solid Films*, 107 (1983) 21.

[19] J. J. Wu, H. V. Nguyen and R. C. Flagan: *Langmuir* 3 (1987) 266.

[20] R. C. Flagan: *Ceramic Transactions*, 1 (1988) 229.

[21] Y. Yoshizawa and K. Yamauchi: *J. Japan Inst. Metals*, 53 (1989) 241.

[22] T. Usami, T. Hasegawa and S. Asai: *J. Japan Inst. Metals, conf. abst.* 110 (1992) 245

[23] H. Bestgen: *Proc. 5th Int. Conf. on Rapidly Quenched Metals*, S. Steeb and H. Warlimont eds., (1985) 443, [Elsevier].

[24] I. A. Aksay and M. Sarikaya: in *"Nanophases and nanocrystalline structures"*, The Minerals, Metals & Materials Society, *to be published.*

[25] K. Uenishi, H. Koh, J. Hisayama, K. Hori, T. Yamamoto, K. N. Ishihara, P. H. Shingu, S. Imanaka and S. Nasu: *Jpn. Inst. Met. Proc. Abs.*, 105 (1989) 191.

[26] P. H. Shingu: *New Ceramics*, 5 (1992) 85.

[27] H. Kimura, S. Kobayashi, S. Sugawara and E. Fukazawa: *J. Jpn. Soc. Powder and Powder Metall.*, 40 (1993) 278.

[28] T. Morooka, E. Yuasa and A. Ishii: *J. Jpn. Soc. Powder and Powder Metall.*, 40 (1993) 311.

[29] D. K. Kim and K. Okazaki: *Mat. Sci. Forum*, 88-90 (1992) 551.

[30] T. Yamasaki, Y. Ogino, W. Wang, K. Fokuoka, T. Atou and Y. Shono: *J. Jpn. Soc. Powder and Powder Metall.*, 40 (1993) 324.

[31] H. Mori, M. Komatsu, K. Takeda and H. Fujita: *Phil. Mag. Let.*, 63 (1991) 173.

[32] S. Schumacher, R. Birringer, R. Strauss and H. Gleiter: *Acta Metall.*, 37 (1989) 2485.

[33] H. Gleiter: *Phys. Stat. Sol.* (b): 172 (1992) 41.

[34] W. L. Johnson: *Int. J. Rap. Solidif.*, 1 (1985) 331.

[35] O. D. Sherby and J. Wadsworth: *Prog. Mat. Sci.*, 33 (1989) 169.

[36] A. H. Chokski, A. Rosen, J. Karch and H. Gleiter: *Scripta Met.*, 23 (1989) 1679.

[37] J. S. C. Jang and C. C. Koch: *Scripta Met. Mat.*, 24 (1990) 1599.

[38] J. S. Benjamin and T.E. Volin, *Metall. Trans*, 5 (1974) 1929.

[39] P. S. Gilman and J. S. Benjamin: *Ann. Rev. Mater. Sci.*, 13 (1983) 279.

[40] A. Szegvari: U. S. Patent 2764359, (1956).

[41] A. Y. Yermakov, Y. Y. Yurichikov and V. A. Barinov, *Phys. Met. Metallogr.*, 52 (1981) 50.

[42] C. C. Koch, O. B. Cabin, C. G. McKamey and J. O. Scarbrough : *Appl. Phys. Lett.*, 43 (1983) 1017.

[43] E. Hellstern, H. J. Fecht, Z. Fu and W. L. Johnson: *J. Appl. Phys.*, 65 (1989) 305.

[44] H. J. Fecht, E. Hellstern, Z. Fu and W. L. Johnson: in *"1989 Advances in Powder Metallurgy"*, vol. 2 (1989) 111 [Metal Powder Industries Federation].

[45] J. Eckert, J. C. Holzer, C. E. Krill, III and W. L. Johnson: *Mater. Sci. Forum*, 88-90 (1992) 505.

[46] H. J. Fecht, G. Han, Z. Fu and W. L. Johnson: *J. Appl. Phys.*, 67 (1990) 1744.

[47] E. Ivanov, S. K. Makhlouf, K. Sumiyama, H. Yamauchi, K. Suzuki and G. Golubkova: *J. Alloys & Compounds*, 185 (1992) 25.

[48] E. Hellstern, H. J. Fecht, Z. Fu and W. L. Johnson: *J. Mater. Res.*, 4 (1989) 1292.

[49] E. Hellstern, H. J. Fecht, C. Garland and W. L. Johnson: *Mat. Res. Soc. Symp. Proc.*, 132 (1989) 137.

[50] Y. R. Abé and W. L. Johnson: *Mat. Sci. Forum*, 88-90 (1992) 513.

[51] H. J. Fecht, E. Hellstern, Z. Fu and W. L. Johnson: *Metall. Trans. A*, 21 (1990) 2333.

[52] J. Eckert, L. Shultz, E. Hellstern and K. Urban :*J. Appl. Phys*, 64 (1988) 3224.

[53] N. Burgio, A. Iasonna, M. Magini, S. Martelli and F. Padella: *Colloq. de Physique*, 51 (1990) C4-265.

[54] H. Hashimoto and W. Watanabe: *Mat. Sci. Forum*, 88-90 (1992) 89.

[55] G. Mazzone, A. Montone and M. Vittoni Antisari: *Phys. Rev. Lett.*, 65 (1990) 2019.

[56] H. Hashimoto, W. Watanabe: *Jpn. Inst. Met. Symp. Proc.*, 112 (1993) 182.

[57] C. Politis and W. L. Johnson: *J. Appl. Phys.*: 60 (1986) 1147.

[58] B. D. Cullity, in *"Elements of X-ray Diffraction"*, 2nd ed., (1978), [Addison-Wesley].

[59] H. P. Krug and L. E. Alexander: in *"X-ray Diffraction Procedures for Polycrystalline and Amorphous Materials"*, 2nd ed., (1974), [Wiley]

[60] P. Lamparter and S. Steeb, *J. Non-Cryst. Sol.*, 106 (1988) 137.

[61] A. Guinier and G. Fournet, translated by C. B. Walker : in *"Small-angle Scattering of X-rays"*, (1955) [Wiley].

[62] V. Gerold, *J. Appl. Cryst.*, 11 (1978) 376.

[63] E. Jorra, H. Franz, J. Peisl, G. Wallner, W. Petry, R. Birringer, H. Gleiter and T. Haubold: *Phil. Mag. B* , 60 (1989) 159.

[64] U. Bonse and M. Hart: *Z. Physik*, 189 (1966) 151.

[65] H. Matsuoka, K. Kakigami and N. Ise: *The Rigaku Denki Journal*, 22 (1991) 8.

[66] J. W. M. DuMond and H. A. Kirkpatrick: *Rev. Sci. Instruments*, 1 (1930) 88.

[67] H. H. Johann: *Z. Physik*, 69 (1931) 185.

[68] T. Johannson: *Z. Physik*, 83 (1933) 507.

[69] G. Fournet: *Bull. Soc. Franç. Mineral. et Cryst.*, 74 (1951) 39.

[70] P. W. Schmidt: *Acta Cryst.*, 8 (1955) 772.

[71] R. Perret and W. Ruland: *J. Appl. Phys.*, 1 (1968) 308.

[72] C. E. Krill, III: *private communications.*

[73] R. Messier, A. P. Giri and R. A. Roy: *J. Vac. Sci. Technol.*, A2, (1984), 500.

[74] J. L. Murray, in *"Binary Alloy Phase Diagrams"*, 2nd ed., edited by T. B. Massalski (Chief), H. Okamoto, P. R. Subramanian and L. Kacprzak, (1991) 1494, [ASM International].

[75] R. Ray, B. C. Giessen and N. J. Grant: *Scripta Met.*, 2 (1968) 357.

[76] M. Sakata, N. Cowlam and H. A. Davis: *Proc. 4th Int. Conf. on Rapidly Quenched Metals*, Sendai, Japan, vol. 1 (1981) 327.

[77] A. J. Maeland, in *"Hydrides for Energy Storage"*, A. F. Anderson and A. J. Maeland eds., (1978) 447 [Pergamon].

[78] K. H. J. Buschow: *Acta Met.*, 31 (1983) 155.

[79] J. Reeve, G. P. Gregan and H. A. Davis: *Proc. 5th Int. Conf. on Rapidly Quenched Metals*, S. Steeb and H. Warlimont eds., (1985) 203 [Elsevier].

[80] H. F. Rizzo, T. B. Massalski and E. D. McClanahan: *Metall. Trans. A*, 19A (1988) 5.

[81] D. E. Luzzi, H. Mori, H. Fujita and M. Meshii: *Scripta Metall.*, 18 (1984) 957.

[82] D. E. Luzzi, H. Mori, H. Fujita and M. Meshii: *Scripta Metall.*, 19 (1985) 897.

[83] P. D. Askenazy, E. A. Kamenetzky, L. E. Tanner and W. L. Johnson: *J. Less-Common Metals*, 140 (1988) 149.

[84] M. von Allmen and A. Blatter: *Appl. Phys. Lett.*, 50 (1987) 1873.

[85] A. L. Greer: *J. Lessc. Met.*, 140 (1988) 327.

[86] K. Osaka, E. H. Trinh, J. C. Holzer and W. L. Johnson: *Appl. Phys. Lett.*, 60 (1992) 1079.

[87] G. Cocco, L. Schiffini, I. Soletta, M. Baricco and N. Cowlam: *Colloq. de Physique*, 51 (1990) C4-175.

[88] G. Cocco, I. Soletta, S. Enzo, M. Magini and N. Cowlam: *ibid*, C4-181.

[89] Y. Gotanda and M. Nagumo: *Autumn Symp. Abs. Jpn. Soc. Powder and Powder Metall.*, (1992) 83.

[90] A. F. Marshall, Y. S. Lee and D. A. Stevenson: *Acta Metall.*, 35 (1987) 61.

[91] C.-H. Hwang, K. Cho and K. Kawamura: *Proc. 5th Int. Conf. on Rapidly Quenched Metals*, S. Steeb and H. Warlimont eds., (1985) 331 [Elsevier].

[92] T. Morooka, E. Yuasa, M. Kushida and Y. Morikawa: *J. Jpn. Soc. Powder and Powder Metall.*, 40 (1993) 251.

[93] R. B. Schwarz, P. Nash and D. Turnbull: *J. Mater. Res.*, 2 (1987) 456.

[94] L. Battezatti, M. Baricco, G. Rionito and I. Soletta: *Colloq. de Physique*, 51 (1990) C4-79.

[95] C. G. Woychik and T. B. Massalski: *Proc. Int. Conf. on Rapidly Quenched Metals*, S. Steeb and H. Warlimont eds., (1985) 211 [Elsevier].

[96] F. Sommer, K.-H. Klappert, I. Arpshofen and B. Predel: Z. *Mettalkd.* 73, (1982) 581.

[97] C. H. Lee, M. Mori, T. Fukunaga and U. Mizutani, *Jpn. J. Appl. Phys.*, 29 (1990) 540.

[98] H. E. Kissinger, *Anal. Chem.*, 29 (1957) 1702.

[99] J. M. Criado and A. Ortega: *J. Non-Cryst. Sol.*, 87 (1986) 302.

[100] T. Tanaka, S. Nasu, B. Huang, K. N. Ishihara and P. H. Shingu: *Nucl. Inst.* B, 76 (1993) 195.

[101] J. Eckert, Y. R. Abé, Z. Fu and W. L. Johnson: *Mat. Res. Soc. Symp. Proc.*, 272 (1992) 271.

[102] Z. Fu and W. L. Johnson: *in press.*

[103] T. B. Massalski: in *"Physical Metallurgy"*, 3rd. ed., R. H. Cahn and P. Haasen eds., vol. 1, Ch. 4, pp. 178 (1983) [Elsevier].

[104] M. A. Tenhover: Ph. D. Thesis, (1981), California Institute of Technology.

[105] Y. R. Abé: *unpublished result.*

[106] H. Kuwano, H. Morita and Y. Hamaguchi: *Autumn Symp. Abs. Jpn. Soc. Powder and Powder Metall.*, (1992) 88.

[107] C. G. Woychik and T. B. Massalski, S. Steeb and H. Warlimont eds.: *Proc. 5th Int. Conf. on Rapidly Quenched Metals*, (1985) 207 [Elsevier].

[108] C. M. Libatini and S. F. Dyment: *Acta Met*, 1963, 11, 1263.

[109] K. H. J. Buschow: *Scripta Met.*, 17 (1983) 1135.

[110] Y. R. Abé: *unpublished result.*

[111] D. J. Chakrabarti and D. E. Laughlin, in *"Binary Alloy Phase Diagrams"*, 2nd ed., edited by T. B. Massalski (Chief), H. Okamoto, P. R. Subramanian and L. Kacprzak, (1991) 1440 [ASM International].

[112] M. Schänzer and H. Mehrer, *J. de Physique*, 51 (1990) C4-87.

[113] L. U. A. Andersen, J. Bøttiger and K. Dyrbye, *Mat. Sci. Eng.*, A115 (1989) 126.

[114] J. Eckert, R. Birringer, J. C. Holzer, C. E. Krill, III and W. L. Johnson: *Mat. Res. Soc. Symp. Proc.*, 238 (1992) 739.

[115] E. S. Machlin: in *"An Introduction to Aspects of Thermodynamics and Kinetics Relevant to Materials Science"*, (1991) [Giro Press].

[116] C. H. Lee, T. Fukunaga and U. Mizutani: *Mat. Sci. Eng.*, A134 (1991) 1334.

[117] Y. Me-Bar and D. Shechtman: *Mat. Sci. Eng.*, 58 (1983) 181.

[118] L. W. Meyer and C. Y. Chiem: in *"Titanium, Science and Technology"*, G. Lütjering, U. Zwicker and W. Bunk eds., vol. 3 (1984) 1907.

[119] R. B. Schwarz, R. R. Petrich and C. K. Saw: *J. Non-Cryst. Solids*, 76 (1985) 281.

[120] J. W. Gibbs, in *"The Scientific Papers of J. Willard Gibbs"*, vol. 1, [Dover], (1961).

[121] E. A. Guggenheim, in *"Thermodynamics"*, (1967) [North Holland].

[122] E. D. Hondros and M. P. Seah: in *"Physical Metallurgy"*, 3rd. ed., R. H. Cahn and P. Haasen eds., vol. 1, Ch. 13, (1983) [Elsevier].

[123] L. E. Murr: in *"Interfacial Phenomena in Metals and Alloys"*, (1975) [Techbooks].

[124] M. P. Seah and E. D. Hondros: *Proc. Roy. Soc.*, A335 (1973) 191.

[125] S. Brunauer, L. S. Deming, W. E. Deming and E. J. Teller: *J. Am. Chem. Soc.* 62, (1940) 1723.

[126] J. J. Burton and H. S. Machlin: *Phys. Rev. Lett.*, 37 (1976) 1433.

[127] H. Ouyang, B. Fultz and H. Kuwano: *in press.*

[128] R. M. German: in *"Liquid Phase Sintering"*, Chap. 1, (1985) [Plenum].

[129] D. R. Clarke and M. L. Gee, in *"Materoals Interfaces,"*, edited by D. Wolf and S. Yip, Ch. 8, (1992) [Chapman & Hall].

[130] W. D. Kingery, H. K. Bowen, D. R. Uhlmann: in *"Introduction to Ceramics"*, 2nd ed., (1976) [Wiley].

[131] E. Matsubara, K. Okuda, Y. Waseda and T. Saito: Z. *Naturforsch.*, 47a (1992) 1023.

[132] H. G. Suzuki, T. Nishimura and S. Yamaguchi: *Iron and Steel*, 65 (1979) 2038.

[133] R. A. Swalin: in *"Thermodynamics of Solids"*, 2nd. ed., (1972) [Wiley]

[134] W. L. Johnson: in *"Materials Interfaces"*, edited by D. Wolf and S. Yip, Ch. 20, (1992) [Chapman & Hall].

[135] F. Spaepen, F.: *Adv. Cryog. Eng.*, (1986) 32 1019.

[136] A. Serebryakov: *Mat. Sci. Forum*, 88-90 (1992) 133.

[137] R. W. Johnson, C. C. Ahn and E. R. Ratner: *Appl. Phys. Lett.*, (1989) 54 795.

[138] W. J. Meng: Ph. D. Thesis, (1988), California Institute of Technology.

[139] R. Busch, S. Schneider and K. Samwer: Nachrichten der Akademie der Wissenschaften in Göttingen, II. *Mathematisch-Physikalische Classe*, Nr. 1, (1991) [Vandenhoeck & Ruprechtin Göttingen, Germany].

[140] T. Fukunaga, N. Hayashi, N. Watanabe and K. Suzuki: *Proc. 5th Int. Conf. on Rapidly Quenched Metals*, S. Steeb and H. Warlimont eds., (1985) 475, [Elsevier].

[141] H. U. Krebs, D. J. Webb and A. F. Marshall: *Phys. Rev. B*, 35 (1987) 5392.

[142] K. Suzuki: *Powder and Powder Metallurgy*, 36 (1989) 3.

[143] M. L. Trudeau, A. van Neste and R. Schultz: *Mater. Res. Soc. Symp. Proc.* 206 (1991) 487.

[144] H. J. Fecht, P. J. Desré and W. L. Johnson: *Phil. Mag. B*, 5 (1989) 577.

[145] Y. Ikematsu, R. Uemori, S. Funaki and H. Morikawa: *Electron Microscopy*, vol. 2, EUREM 92 (1992) 265.

[146] P. Debye: *Ann. Physik*, 46 (1915) 809.

[147] P. Debye and A. M. Bueche: *J. Appl. Phys.*, 20 (1949) 518.

[148] A. Guinier: in "*X-ray Diffraction*", 1963, Chap. 10 [Freeman].

[149] G. Porod: *Kolloid Z.*, 124 (1951) 83.

[150] G. Porod: in "*Small Angle X-ray Scattering*", O. Glatter and O. Kratky eds., Chap. 2, (1982) [Academic Press].

[151] P. Debye, H. R. Anderson, Jr. and H. Brumberger: *J. Appl. Phys.*, 28 (1957) 679.